



Michigan Technological University
Create the Future Digital Commons @ Michigan Tech

Dissertations, Master's Theses and Master's
Reports - Open

Dissertations, Master's Theses and Master's
Reports

2010

Energy harvesting from body motion using rotational micro-generation

Edwar. Romero-Ramirez
Michigan Technological University

Follow this and additional works at: <https://digitalcommons.mtu.edu/etds>



Part of the [Mechanical Engineering Commons](#)

Copyright 2010 Edwar. Romero-Ramirez

Recommended Citation

Romero-Ramirez, Edwar., "Energy harvesting from body motion using rotational micro-generation",
Dissertation, Michigan Technological University, 2010.
<https://doi.org/10.37099/mtu.dc.etds/404>

Follow this and additional works at: <https://digitalcommons.mtu.edu/etds>



Part of the [Mechanical Engineering Commons](#)

ENERGY HARVESTING FROM BODY MOTION
USING ROTATIONAL MICRO-GENERATION

By

EDWAR ROMERO-RAMIREZ

A DISSERTATION

Submitted in partial fulfillment of the requirements

for the degree of

DOCTOR OF PHILOSOPHY

(Mechanical Engineering-Engineering Mechanics)

MICHIGAN TECHNOLOGICAL UNIVERSITY

2010

Copyright © Edwar Romero-Ramirez 2010

This dissertation, "Energy Harvesting from Body Motion using Rotational Micro-Generation" is hereby approved in partial fulfillment of the requirements for the degree of DOCTOR OF PHILOSOPHY in the field of Mechanical Engineering-Engineering Mechanics.

DEPARTMENT
Mechanical Engineering-Engineering Mechanics

Signatures:

Dissertation Advisor

Dr. Robert O. Warrington

Co-Advisor

Dr. Michael R. Neuman

Department Chair

Dr. William W. Predebon

Date

Abstract

Autonomous system applications are typically limited by the power supply operational lifetime when battery replacement is difficult or costly. A trade-off between battery size and battery life is usually calculated to determine the device capability and lifespan. As a result, energy harvesting research has gained importance as society searches for alternative energy sources for power generation. For instance, energy harvesting has been a proven alternative for powering solar-based calculators and self-winding wristwatches. Thus, the use of energy harvesting technology can make it possible to assist or replace batteries for portable, wearable, or surgically-implantable autonomous systems. Applications such as cardiac pacemakers or electrical stimulation applications can benefit from this approach since the number of surgeries for battery replacement can be reduced or eliminated.

Research on energy scavenging from body motion has been investigated to evaluate the feasibility of powering wearable or implantable systems. Energy from walking has been previously extracted using generators placed on shoes, backpacks, and knee braces while producing power levels ranging from milliwatts to watts. The research presented in this paper examines the available power from walking and running at several body locations. The ankle, knee, hip, chest, wrist, elbow, upper arm, side of the head, and back of the head were the chosen target localizations. Joints were preferred since they experience the most drastic acceleration changes. For this, a motor-driven treadmill test was performed on 11 healthy individuals at several walking (1-4 mph) and running (2-5 mph) speeds. The treadmill test provided the acceleration magnitudes from the listed body locations. Power can be estimated from the treadmill evaluation since it is proportional to the acceleration and frequency of occurrence. Available power output from walking was determined to be greater than 1 mW/cm³ for most body locations while being over 10 mW/cm³ at the foot and ankle locations. Available power from running was found to be almost 10 times higher than that from walking.

Most energy harvester topologies use linear generator approaches that are well suited to fixed-frequency vibrations with sub-millimeter amplitude oscillations. In contrast, body motion is characterized with a wide frequency spectrum and larger amplitudes. A generator prototype based on self-winding wristwatches is deemed

to be appropriate for harvesting body motion since it is not limited to operate at fixed-frequencies or restricted displacements. Electromagnetic generation is typically favored because of its slightly higher power output per unit volume. Then, a non-harmonic oscillating rotational energy scavenger prototype is proposed to harness body motion. The electromagnetic generator follows the approach from small wind turbine designs that overcome the lack of a gearbox by using a larger number of coil and magnets arrangements.

The device presented here is composed of a rotor with multiple-pole permanent magnets having an eccentric weight and a stator composed of stacked planar coils. The rotor oscillations induce a voltage on the planar coil due to the eccentric mass unbalance produced by body motion. A meso-scale prototype device was then built and evaluated for energy generation. The meso-scale casing and rotor were constructed on PMMA with the help of a CNC mill machine. Commercially available discrete magnets were encased in a 25 mm rotor. Commercial copper-coated polyimide film was employed to manufacture the planar coils using MEMS fabrication processes. Jewel bearings were used to finalize the arrangement. The prototypes were also tested at the listed body locations. A meso-scale generator with a 2-layer coil was capable to extract up to $234\text{ }\mu\text{W}$ of power at the ankle while walking at 3mph with a 2cm^3 prototype for a power density of $117\text{ }\mu\text{W}/\text{cm}^3$.

This dissertation presents the analysis of available power from walking and running at different speeds and the development of an unobtrusive miniature energy harvesting generator for body motion. Power generation indicates the possibility of powering devices by extracting energy from body motion.

Acknowledgements

There are a number of people I would like to express my gratitude to for their contribution to this research work. Foremost, I would like to express my sincere appreciation to my advisor, Dr. Robert Warrington, and to my co-advisor, Dr. Michael Neuman, for their mentoring, encouragement, assistance, advice, patience, and valuable comments to endure this research and the writing of this dissertation. Thank you Bob and Mike, both of you have helped me to continue to learn and grow as a professional.

I am also grateful to my committee members, Drs. Craig R. Friedrich, Paul L. Bergstrom, Bruce E. Seely, and Khalil Najafi for sharing their technical and professional insights to shape this dissertation. Special thanks to Dr. Charles D. Van Karsen for the vibration testing facilities; Dr. Jeffrey Allen for the high speed camera facilities and Mr. Ezequiel Medici for his assistance; Mr. Michael Lacourt for the patience on the CNC machining assistance; Mr. Jerry Dion, Mr. Martin Toth, and Mr. Timothy Alholinna for the manufacturing help. I would like to thank Mr. William Knudsen for the microfabrication aid. I also would like to give special thanks to Ms. Laura Walz and Mr. Kumar Vanga for their constant coaching while training me in the laboratories, as well as Mr. Tzeno Galchev at University of Michigan for multiple discussions.

I would also like show my appreciation for the support of all the people I met during the period I was working on this dissertation. I owe a dept of gratitude to Mrs. Madeline Mercado-Voelker for her warm heart during the cold Keweenaw winters to all Hispanic/Latino students; she made us feel at home. I am also grateful to the Writting Center staff for their help in the preparation of this manuscript, especially to Ms. Rachael Barlock, and to Mrs. Nancy Barr at the Mechanical Engineering - Engineering Mechanics Department for her proofreading work. I would also like to thank the support of my friends, *Los Tertulianos*, and fellow graduate and undergraduate students.

Finally, I gratefully acknowledge the contribution of the Engineering Research Center for Wireless Integrated MicroSystems (WIMS) which provided financial support for this research through the National Science Foundation under Award Number EEC-0096866. I want also to recognize the financial support given at Michigan Technological University for the completion of this work by the Institute for Interdis-

ciplinary Studies, by the Biomedical Engineering Department, and by the Graduate School for the Summer Finishing Fellowship.

To Linita

*A mi esposa y compañera de toda mi vida, Lina, porque
has sido mi complemento, mi apoyo y ayuda incondicional
durante todo este largo y difícil proceso. Sin ti, hubiera
sido imposible culminar este proyecto*

*A mis padres Flor y Ciro por todo lo que he logrado
aprender y lo lejos que he podido llegar gracias a ustedes,
por su constante apoyo y consejos a pesar de la distancia,
de ustedes aprendí que el estudio es la mejor herencia*

Contents

Abstract	v
Acknowledgements	vii
Dedication	ix
Contents	xi
List of Figures	xv
List of Tables	xxi
1 Introduction	1
1.1 Motivation	1
1.2 Technology Trend	3
1.3 Research Objectives	6
1.4 Dissertation Overview	7
2 Energy Harvesting Background	9
2.1 Introduction	9
2.2 Energy Generation from the Human Body	9
2.3 Transduction Techniques	10
2.4 Human-Based Energy Harvesters	12
2.4.1 Electromagnetic Energy Generators	12
2.4.2 Piezoelectric Energy Generators	17
2.4.3 Electrostatic Energy Generators	21
2.5 Energy Generation Summary	23
3 Power from Body Motion	27
3.1 Introduction	27
3.2 Transduction Limits	28
3.3 Kinetic Energy Harvesting	31

3.4	Power Limits	33
3.4.1	Body Acceleration Measurement	36
3.4.2	Body Acceleration Results	38
3.4.3	Evaluation of Available Body Power	41
3.5	Power Generation from the Human Body	49
3.6	Power Generation Summary	58
4	Generator Design	63
4.1	Introduction	63
4.2	Design	63
4.3	Induced Voltage Model	65
4.3.1	Magnetic Field Model	69
4.3.2	Generator Kinematics	74
4.3.3	Coil Geometry	78
4.3.4	Power Evaluation	84
4.3.5	Induced Voltage	86
4.4	Generator Sizing	87
4.5	Summary	93
5	Generator Fabrication and Testing	97
5.1	Introduction	97
5.2	Fabrication	97
5.2.1	Photolithography	97
5.2.2	CNC Machining	100
5.2.3	Prototypes	100
5.3	Prototype Testing	103
5.3.1	First Prototype: μ VPG-0.5	103
5.3.2	Second Prototype: μ VPG-1.0	106
5.3.3	Third Prototype: μ VPG-1.1	107
5.3.4	Fourth Prototype: μ VPG-1.2	117
5.3.5	Fifth Prototype: μ VPG-1.3	119
5.3.6	Sixth Prototype: μ VPG-1.4	119
5.3.7	Seventh Prototype: μ VPG-1.5	123
5.4	Summary	125
6	Discussion of Results	129
6.1	Model and Experiment Comparison	129
6.1.1	Kinematics	130
6.1.2	Magnetic Field	135
6.1.3	Q factor	136
6.1.4	Power Loss by Eddy Currents	140

6.1.5	Summary	141
6.2	Evaluation	142
6.3	Challenges	143
6.3.1	Power Generation and Efficiency	143
6.3.2	Fabrication	144
6.3.3	Rectification	145
6.3.4	Energy Storage	145
7	Societal Implications	147
7.1	Introduction	147
7.2	The Environmental Battery Reality	148
7.3	Miniaturization, Pervasiveness, and Public Perception	151
7.4	Energy Harvesting Implications	154
8	Conclusion	159
8.1	Conclusion	159
8.2	Summary of Findings	160
8.3	Recommendations	164
	Bibliography	167

List of Figures

1.1	Portable computing improvements from 1990-2010.	4
1.2	Comparison of power sources	5
1.3	Comparison of power consumption vs. power generation	6
2.1	Oscillating rotational generators diagrams from commercial wristwatches.	13
2.2	Inertial linear-based generators	15
2.3	Linear electromagnetic generators	16
2.4	Knee-mounted biomechanical energy harvester	17
2.5	Piezoelectric generators patents for heart implants.	18
2.6	Shoe-mounted piezoelectric energy generators	19
2.7	Impact-based piezoelectric generators	20
2.8	Embedded piezoelectric generators	21
2.9	Electrostatic generators	22
2.10	Electret generators	23
2.11	Summary of energy scavengers by frequency of operation	24
2.12	Summary of energy harvesters by generator's volume	25
2.13	Summary of reported energy harvesters by power density	26
3.1	Transduction generation limits.	30
3.2	Energy harvester geometries	31
3.3	Kinetic energy harvester schematic.	32
3.4	Maximum power available for linear-vibration generators at resonance from human-based motion and machine-based vibration.	35
3.5	Body locations and coordinate system.	37
3.6	3-Axis ± 6 G MMA7260Q accelerometer on a breakout board on top of a Sun SPOT mote.	38
3.7	Comparison between the ± 3 G test sensor (3-axis ± 3 G ADXL335) and the Sun SPOT reference sensor (3-axis ± 2 G LIS3L02AQ).	39
3.8	Comparison between the ± 6 G test sensor (3-axis ± 6 G MMA7260Q) and the Sun SPOT reference sensor (3-axis ± 2 G LIS3L02AQ).	39

3.9	Comparison between the ± 18 G test sensor (2-axis ± 18 G ADXL-321) and the Sun SPOT reference sensor (3-Axis ± 2 G LIS3L02AQ).	40
3.10	Step frequency for the walking and running test on a treadmill	40
3.11	Acceleration readings from the walking test at each body location in G	42
3.12	Acceleration readings from the running test at each body location in G	42
3.13	Acceleration readings comparison from the walking and running test at each body location in G	43
3.14	Average acceleration distribution for treadmill walking in G	44
3.15	Average acceleration distribution for treadmill running in G	45
3.16	Average acceleration distribution and comparison for treadmill walking and running in G	46
3.17	Energetic figure of merit for each body location while walking.	47
3.18	Energetic figure of merit for each body location while running.	48
3.19	Energetic figure of merit comparison for each body location while walking and running	48
3.20	Available power at different body locations from walking	50
3.21	Available power at different body locations from running	50
3.22	Available power comparison at different body locations from walking and running	51
3.23	Available power density at different body locations from walking	51
3.24	Available power density at different body locations from running	52
3.25	Available power density comparison at different body locations from walking and running	52
3.26	Resultant acceleration in G for the walking and running tests.	54
3.27	Resultant figure of merit σ_ω for the walking and running tests.	55
3.28	Available power from the resultant acceleration for the walking and running tests	55
3.29	Available power density from the resultant acceleration for the walking and running tests	56
3.30	Available power density for average walking conditions along the vertical axis.	60
3.31	Available power density for average walking conditions along the forward axis.	60
3.32	Available power density for average walking conditions along the lateral axis.	61
3.33	Available power density for average walking conditions along from the resultant acceleration from vertical and forward axes.	61
4.1	Simplified schematic of the proposed design.	65
4.2	Coil designs vs. contact pads.	66

4.3	Layout of a coil sector corresponding to one PM pole-pair with 5 wires depicted.	68
4.4	Diagram of the simplified coil design.	69
4.5	Axial flux permanent magnet (AFPM) machine topology.	69
4.6	Magnetic flux distribution for a single wire and one pole-pair under a sinusoidal field.	70
4.7	Magnetic field distribution for a one-rotor design at a distance locate at 0.5 mm over the surface for one pole-pair arrangement	71
4.8	Magnetic field distribution in between a two-rotor design separated by 1 mm for one pole-pair arrangement.	72
4.9	Magnetic field distribution for a one-rotor design at a point located at 0.5 mm over the surface for one pole-pair sector-shaped area	72
4.10	Magnetic field distribution in between a two-rotor design separated by 1 mm for one pole-pair sector-shaped area	73
4.11	Magnetic flux distribution at 0.5 mm over 1-layer of sector-shaped PM and 11 mm of radius	73
4.12	Ideal Pendulum.	75
4.13	Variation of the pendulum period T against the period T_0	77
4.14	Pendulum model for a proof mass released from a 90° angle.	79
4.15	Simplified coil design geometry.	82
4.16	Comparison of coil designs with varying pole-pairs for the same number of radial wires (40 radial segments) and the same outer and inner diameter dimensions.	82
4.17	Optimal radial length for a generator with a diameter of 25 mm.	83
4.18	Optimal radial length as a function of rotor diameters.	83
4.19	Variation of coil resistance, ratio of coil-end length to radial-wire length, and number of turns for varying pole-pair numbers of a 25 mm diameter generator with 5 mm long radial wires.	84
4.20	Variation of coil resistance, ratio of coil-end length to radial-wire length, and number of turns for varying pole-pair numbers of several optimized generator dimensions (Fig. 4.18) vs. a non-optimized generator (25mm diameter, 5mm radial wires) with 100 μm wire linewidth.	85
4.21	Generator diagram.	85
4.22	Induced voltage for a proof mass released at a 90° angle with the generator configuration of Table 4.1.	86
4.23	Proof mass location.	87
4.24	Proof mass location nomenclature.	88
4.25	Frequency and torque evaluation for a 25mm diameter rotor with a stacked mass and various proof mass densities.	91
4.26	Solutions for the 1.9 Hz and 2.5 Hz target frequencies.	92

4.27	Modeling results for a stacked proof mass generator design for several dimensions.	92
4.28	Three solutions for the stacked proof mass model presented in Fig. 4.27.	93
4.29	Protruded proof mass solutions of 20 mm, 25 mm and 30 mm diameter of PM ring for the design frequency of 1.9 Hz.	94
4.30	Protruded proof mass solutions of 20 mm, 25 mm and 30 mm diameter of PM ring for the design frequency of 2.5 Hz.	95
5.1	Planar coil fabrication process.	98
5.2	Detail of a 200 μm linewidth and 4 turns copper planar coil on polyimide substrate	99
5.3	Coil iterations for 20 pole-pairs arrangements.	99
5.4	A 430 μm thick 10-layer coil assembly (L100U51M8T-2L).	100
5.5	CNC-machined components.	101
5.6	$\mu\text{VPG} - 0.5$ prototype	102
5.7	$\mu\text{VPG} - 1.0$ prototype	102
5.8	Coil nomenclature example.	103
5.9	Test results for the $\mu\text{VPG}-0.5$ prototype on a laboratory shaker. . . .	104
5.10	Instantaneous voltage for the $\mu\text{VPG}-0.5$ prototype on a laboratory shaker at 5 Hz and 12 Ω load.	105
5.11	Commercial self-winding wristwatch generator.	105
5.12	Test results from a commercial wristwatch on a laboratory shaker. . .	105
5.13	Voltage output results for the $\mu\text{VPG}-1.0$ prototype on a laboratory shaker.	107
5.14	Laboratory shaker setup.	107
5.15	Power output results for the $\mu\text{VPG}-1.0$ prototype on a laboratory shaker.	108
5.16	Acceleration peak variation in G for the $\mu\text{VPG}-1.0$ prototype	108
5.17	$\mu\text{VPG}-1.1$ prototype photos.	109
5.18	Voltage output results for the $\mu\text{VPG}-1.1$ prototype on a laboratory shaker for varying frequency and loading conditions.	110
5.19	Results for the $\mu\text{VPG}-1.1$ prototype on a laboratory shaker for a load of 15 Ω with 0.5 Hz frequency increments.	110
5.20	Results for the $\mu\text{VPG}-1.1$ prototype while free walking.	112
5.21	Voltage output results for the $\mu\text{VPG}-1.1$ prototype on a laboratory shaker for varying frequency and loading conditions.	113
5.22	Power output results for the $\mu\text{VPG}-1.2$ prototype on a laboratory shaker.	113
5.23	Shaker acceleration in G for the $\mu\text{VPG}-1.1$ prototype using the L100U20M9T-2L coil (1 G=9.8 m/s ²).	113
5.24	$\mu\text{VPG}-1.1$ prototype using the L100U20M9T-2L coil.	114
5.25	Power output for the test 3 with a load of 28 Ω	115

5.26	Voltage output results for the $\mu VPG-1.1$ prototype on a laboratory shaker for the L200U20M4T-10L coil with varying frequency and a 44Ω load.	116
5.27	Power output results for the $\mu VPG-1.1$ prototype on a laboratory shaker for the L200U20M4T-10L coil with varying frequency and a 44Ω load.	116
5.28	$\mu VPG-1.2$ prototype photo.	117
5.29	$\mu VPG-1.2$ prototype results while free walking.	118
5.30	Open-circuit results for the $\mu VPG-1.3$ prototype while free walking.	120
5.31	$\mu VPG-1.3$ prototype generation results with a 10Ω load while free walking.	121
5.32	$\mu VPG-1.4$ prototype generator photo	121
5.33	Micrograph analysis for a L200U20M4T coil, 5X magnification.	122
5.34	RMS voltage output results for the treadmill test of the $\mu VPG-1.4$ prototype.	123
5.35	Power output results for the treadmill test of the $\mu VPG-1.4$ prototype.	124
5.36	Results for the generator located at the ankle while walking at 3 mph.	124
5.37	Free walking results for the $\mu VPG-1.5$ prototype at the leg and chest locations.	126
5.38	Free walking results for the $\mu VPG-1.5$ prototype at upper body locations.	127
6.1	Comparison for a proof mass released at 45° with the developed model.	131
6.2	Detail of the comparison for a proof mass released at 45° with the developed model.	131
6.3	Comparison for a proof mass released at 90° with the developed model.	132
6.4	Detail of the comparison for a proof mass released at 90° with the developed model.	132
6.5	Comparison of variable vs. constant frequency for a proof mass released at 90°	133
6.6	Pendulum oscillations from a proof mass released at a 90° angle compared against the nonlinear pendulum and the harmonic oscillator model.	134
6.7	Coil evaluation at constant speeds for two different wire lengths.	137
6.8	Coil evaluation at constant speeds for four and six layer stacks.	138
6.9	Coil evaluation at constant speeds for a 6-layer coil (TC200U51M4T-6L coil).	138
6.10	Energy versus frequency plot.	139
6.11	FFT analysis of the acceleration (forward axis) at the ankle location while walking (1-4 mph).	140
7.1	Relative environmental score vehicle battery technologies	149

List of Tables

1.1	Percentage of population over 65-years old	1
3.1	Piezoelectric material properties.	29
3.2	Estimated power density limits for different transduction methods during human walking generation.	31
3.3	$ASTF$, or σ_ω values, calculated from various motion sources.	34
3.4	Energetic figure of merit, σ_ω , for the average walking speed of 1.4 m/s (3.1 mph) and for the moderate running speed of 2.2 m/s (5 mph). . .	49
3.5	Available power for the average walking speed of 1.4 m/s (3.1 mph) and for the moderate running speed of 2.2 m/s (5 mph)	53
3.6	Available power density for the average walking speed of 1.4 m/s (3.1 mph) and for the moderate running speed of 2.2 m/s (5 mph)	53
3.7	Energetic figure of merit for the resultant acceleration	56
3.8	Available power for the resultant acceleration	57
3.9	Available power density for the resultant acceleration	57
4.1	Generator configuration	78
4.2	Modeling results for the induced voltage of a proof mass released at a 90° angle.	87
4.3	Stacked brass proof mass solutions for one-rotor design.	91
4.4	Protruded brass proof mass solutions for one-rotor design with 180°.	93
5.1	$\mu VPG-0.5$ prototype parameters.	103
5.2	Power generation from Fig. 5.35 for the average walking speeds. . .	125
6.1	Eddy current loss parameters.	141
6.2	Eddy current loss for various coil configurations at constant rotational speed.	141

Chapter 1

Introduction

1.1 Motivation

Health care services are facing a variety of challenges as the world's population ages due to increased longevity and declining birth rates [36]. The US alone will have 20% of the population over the age of 65 by 2050. In contrast, Europe will see rates close to 30% while Japan will arise to almost 40%, as shown in Table 1.1¹. It is anticipated that in the near future specialized health care services will be in higher demand due to this increase. This demand will be characterized not only by medical resources to attend to this segment of the population but to keep them active as well. Therefore, the monitoring of physiological responses as well as specialized drug or other therapy delivery applications will be needed for portable, wearable, or implantable biomedical autonomous devices. In addition, wireless communication promises new medical applications such as the use of wireless body sensor networks for health monitoring [50, 134, 44].

These biomedical devices, however, come with their own issues, mainly power

¹Population Division of the Department of Economic and Social Affairs of the United Nations Secretariat, World Population Prospects: The 2008 Revision, <http://esa.un.org/unpp>

Table 1.1: *Percentage of population over 65-years old*¹.

Region	1950	2000	2050
USA	8.3	12.4	21.6
Europe	8.2	14.8	27.4
Japan	4.9	17.2	37.8
World	5.2	6.8	16.2

¹Population Division of the Department of Economic and Social Affairs of the United Nations Secretariat, World Population Prospects: The 2008 Revision, <http://esa.un.org/unpp>

source challenges. Batteries are commonly used to energize most of these applications, but they have a finite lifetime. As biomedical devices tend to be relatively power hungry, a trade-off between battery capacity and size has governed the lifespan, dimensions, and capabilities for battery-powered devices. New technologies such as energy harvesting have the capability to effectively power electronic instruments. Harnessing energy from sources such as motion, sunlight, and temperature changes has been employed respectively on electronic self-winding wristwatches, solar-powered calculators, and thermal-powered wristwatches. Therefore, energy harvesting is an alternative to batteries for energizing electronic devices.

Energy harvesting was the main technology used before the advent of the internal combustion engine, the power grid, or batteries. For instance, wind turbine farms and hydroelectric plants are the successors of windmills and water wheels. Small electrical generators were also used in radios and flashlights operated by hand cranking in the 1940s. Other recent examples include the bicycle dynamo (capable of producing up to 3 W of power) and lever-driven mobile phone chargers (up to 2 W of power) [30, 133]. Industrial applications for recent vibration energy harvesters have been developed to power autonomous wireless sensor nodes (Ferro Solutions Inc.², Perpetuum Ltd.³). Energy scavenging of water flow in oceans and rivers are exploited as well [125] (similar to an eel swimming, one device uses the traveling vortices in water to strain piezoelectric polymers). One of the most well-known examples of energy harvesting from body motion is the self-winding wristwatch mechanism that evolved from being entirely mechanical (wind-up) to use a hybrid approach (using a miniature electromagnetic generator to charge a battery).

Wearable microinstruments for environmental monitoring of humidity, temperature, pressure, and acceleration with data processing capabilities have been successfully implemented as watch-sized devices [71, 145, 80]. Such systems are commonly powered by batteries, and sometimes the battery is larger than the entire system. This is normally the case for devices that need to be functional for long periods of time. For example, batteries for cardiac pacemakers occupy half the device's volume [68], while their average lifetime is between 5 to 12 years [52]. Implantable biomedical devices, such as neural prostheses [49, 34, 85] are also dependant on microsystems for their operation. The use of radio frequency (RF) induction for power and radio telemetry is the best alternative when wires or batteries are not an option, which is the case for some integrated neural stimulation microsystems [80]. This approach uses an external flat antenna and an implanted on-chip antenna. These types of microsystems could also benefit from energy harvesting to avoid battery limitations. To address the need for more efficient technology, researchers have tried to employ energy harvesters for powering biomedical devices, as evidenced by the investigations

²<http://www.ferrosi.com>

³<http://www.perpetuum.co.uk>

of automatic self-winding wristwatches for powering pacemakers [43, 42, 41] or by using generators placed in shoes for powering artificial organs [6].

The decrease in power consumption by electronic devices has been well documented in recent years. A custom digital signal processing (DSP) unit consumed about $18\mu\text{W}$ of power by 1998 [3]. An updated version from the same group presented a power consumption of 500nW by 2005 [4], while another group in 2008 presented a processor called Phoenix using only 30pW of power [112]. Therefore, low-power electronics are making progress to extend battery life or even use energy harvesting as the sole energy source. If electronic self-winding wristwatches can harness body motion to power themselves, in the near future hybrid approaches using energy harvesters and rechargeable batteries could power more portable applications or even implantable devices. It is anticipated that hybrid power supplies will be critical for a wide range of autonomous micro systems [45, 15].

Another concern is the environmental panorama of battery disposal around the world. Millions of batteries are discarded into sanitary landfills where heavy metals can result in groundwater contamination. Therefore, solutions that minimize or avoid battery disposal will certainly provide an environmental advantage.

1.2 Technology Trend

Computer technology has progressed aggressively over the last two decades as shown in Fig. 1.1, but it is also clear that battery technology has not kept the same pace. This energy source, although increased in capacity over the years, seems to slow down the progress for portable electronics to gain a wider adoption. It is evident that advances in computational capabilities outpace the battery development; hence more applications could be envisioned if batteries followed the trend of computer technology. For instance, the cost of battery replacement prohibits a wider deployment of wireless sensor networks. As a result, other energy sources are needed to cover the increasing demands of new electronic applications. Energy harvesting can be an option to solve this problem.

Fig. 1.1 represents the increase in performance for several technologies compared against those available in 1990, for instance disk capacity increased by a factor of 10,000 between 1990 and 2010 while battery energy density increased only 5X. This graph is an extension of the one presented by Starner and Paradiso [121] that covered the period from 1990 to 2003. The reference point for the comparisons was kept the same as [121]: a high-end portable computer from 1990, with a 80386 processor running at 16 MHz, 8 MB of RAM and 40 MB of hard disk capacity, using a nickel-cadmium battery. The latest technologies were compared for each year as multiples of the reference laptop. Only disk capacity and available RAM data were kept from Starner and Paradiso from the years 1990-2003 [121]. Specialized computer magazines

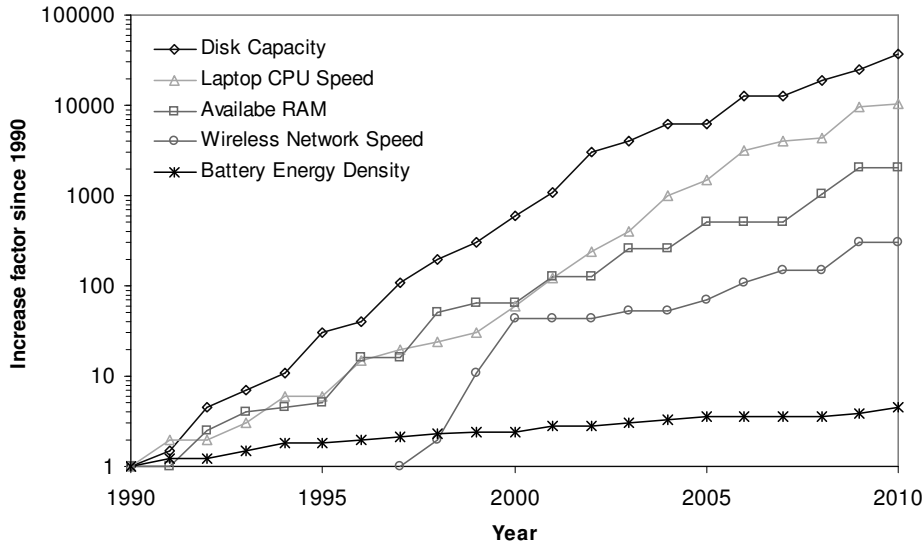


Figure 1.1: *Portable computing improvements from 1990-2010. Wireless connectivity only considers the IEEE 802.11 standard released in 1997. Partial data from [121] and from specialized computer magazines.*

over the internet were used to obtain most of the information. Since there are several Central Processing Unit (CPU) benchmarking comparisons, the number of million instructions per second (MIPS) for Intel processors was used as a reference providing a similar trend line as the one from the work of Starner and Paradiso. The battery energy density was based on the volumetric energy density (Wh/L) data gathered from Panasonic⁴ for nickel-cadmium, nickel-metal hydride, and lithium-ion battery chemistries, because it was readily available until 2010. Although Starner and Paradiso calculated the energy density using J/kg the results are nearly identical. The IEEE 802.11 standard released in 1997 was included for the wireless network speed trend.

On the other hand, energy sources other than batteries exist with even higher power densities, as shown in Fig. 1.2, but most of them are designed for macro-scale systems and/or require a combustible to operate. The human body is also an alternative energy source that can provide power densities under 1 W/kg (1 mW/g) or 1 W/L (1 mW/cm³) as shown in Fig. 1.2. Due to the decrease in power consumption of electronic devices mentioned previously, the available power density levels of 1 mW/cm³ or 1 mW/g are an interesting option for low-power applications. Since the power is generated by body motion, the applications that can directly benefit for this approach are portable electronics and biomedical devices (wearable or surgically-implantable).

⁴www.panasonic.com

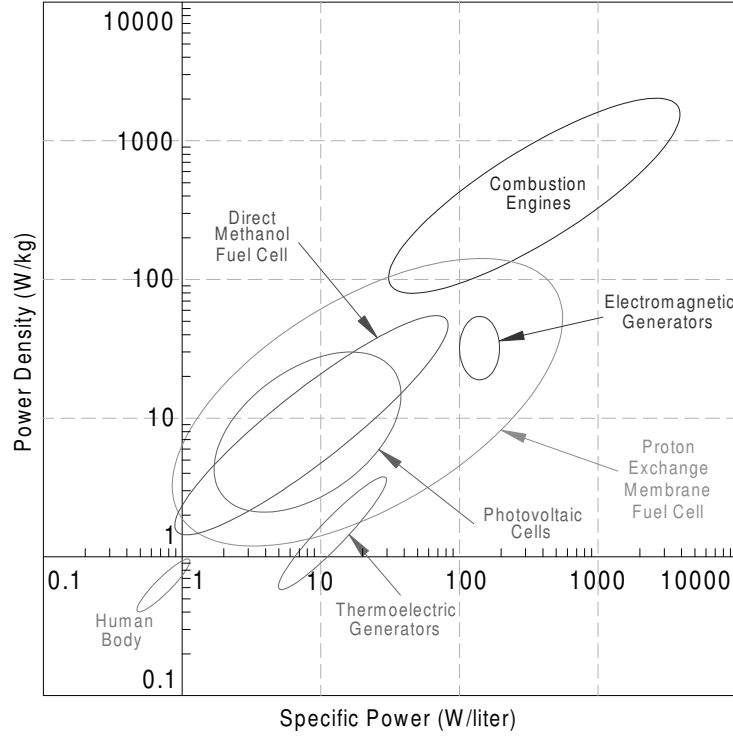


Figure 1.2: Comparison of power sources, chart adapted from [30].

Fig. 1.3 highlights the power budget for some electronic applications within the human body generation range. For example, using the previous reference of 1 mW/cm^3 (or 1 mW of power in a volume of 1 cm^3) only a few miniature low-power applications (such as pacemakers, hearing aids, watches, and some consumer devices) can directly use the energy harvesting approach. However, larger generator volumes can produce higher power outputs. Continuing with the reference of 1 mW/cm^3 , a relatively small generator with a volume of 10 cm^3 could produce up to 10 mW . According to the chart in Fig. 1.3, 10 mW can be used to power some remote controls and communication devices (pagers). Taking as a reference the shoe generator presented by Kymissis et al [58] with a power generation over 200 mW , some radios and cell phones can be powered by energy harvesting.

Fig. 1.3 describes the power requirements of several electronic products ranging from medical devices to consumer products (power consumption from one microwatt up to several watts). This figure also includes the power output of one energy harvester (a shoe generator) and several human-operated generators for comparison purposes. Although human-operated generators have a power output enough to energize power-hungry devices (such as notebook computers), they require active generation.

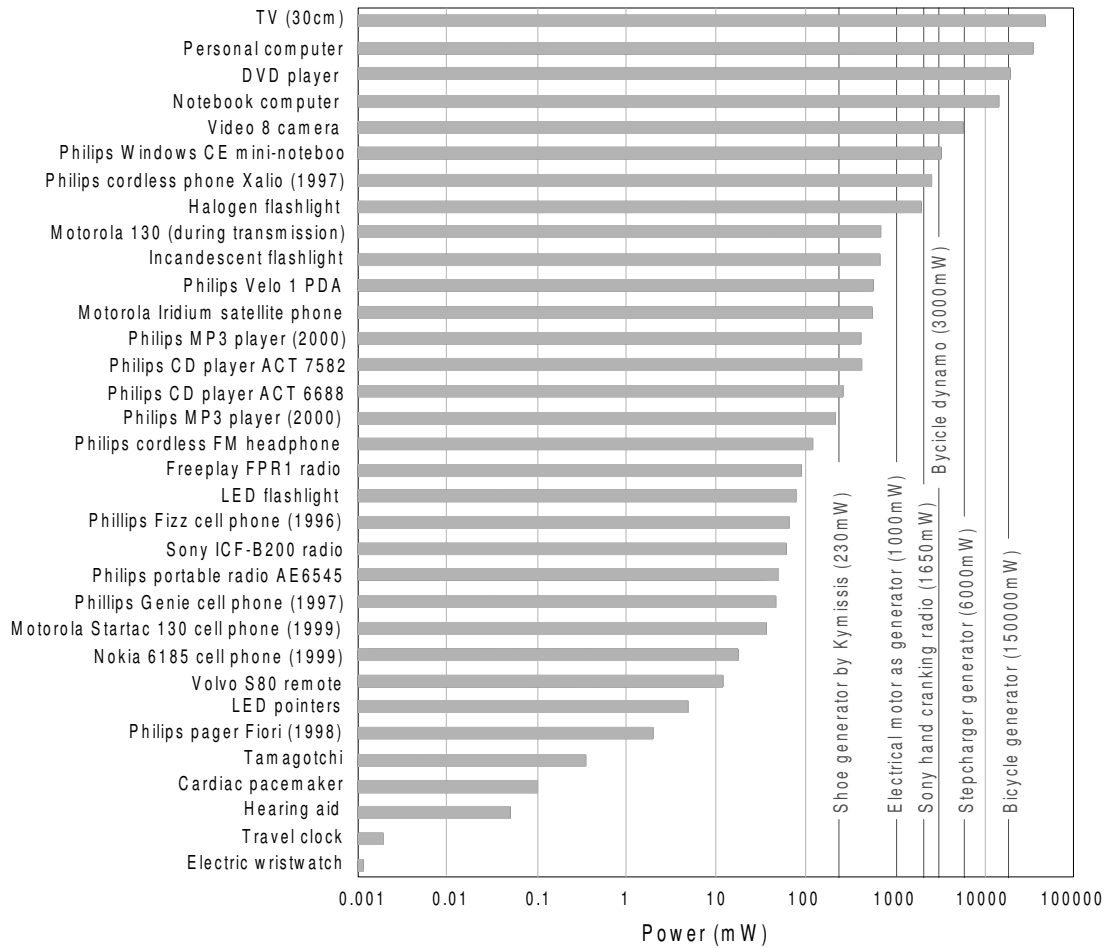


Figure 1.3: Comparison of power consumption (horizontal bars) against power generation (vertical lines) for some electronic devices, chart adapted from [31].

On the other hand, passive generation, although producing a lower power output, produces an adequate amount to energize low-power electronic applications, including some medical devices. Therefore, it is clear that energy harvesting from body motion has the potential to power some biomedical applications and other low-power devices.

1.3 Research Objectives

Since there is little research that focuses on energy harvesting from body motion, and considering the potential uses for such portable, embedded, or surgically-implantable

devices, this investigation will concentrate on energy scavenging from human activities. This dissertation considers the potential and limitations of energy harvesting from low-frequency vibrations. The field, as portrayed in the scientific and technical literature, will be reviewed for energy harvesting from motion and vibration and specifically from human body motion. Based on this review and mathematical modeling, a prototype device will be designed and evaluated. The main objective of this dissertation is to investigate methods for harvesting energy from normal human body movements and choose a technology that allows the generation of electrical energy.

Recognizing how much energy is available and how it can be harnessed is essential for developing energy harvesters, therefore the specific goals are:

- *Evaluate energy harvesters for body motion:* A background on state-of-the-art energy harvesters is needed to learn their potential and limitations. Generator designs based on several possible mechanisms will be considered and an approach for further development will be chosen.
- *Determine the available power from body motion:* A literature review will be carried out to learn what previous work has been done. Models that estimate how much energy is available from body motion need to be elaborated in order to understand the limits of energy generation from this source. A human subject investigation will be required to determine body locations and evaluate the energy generation potential.
- *Design, fabricate, and evaluate a chosen approach:* Based on the evaluation of energy harvesters and possibilities of generation from the human body, a prototype generator will be designed, fabricated, and evaluated to determine if the predicted performance can be achieved. This evaluation will require human subject investigation.

1.4 Dissertation Overview

This dissertation is divided into eight chapters that correspond to the motivation behind it; the societal implications; background on energy harvesting generation and generators; an estimation of how much power is available from body motion; a generator design, fabrication, setup, and testing; an analysis and discussion of the prototype generator; and a conclusion chapter.

Chapter 2 (Energy Harvesting Background). This section reviews the different approaches presented by researchers on energy harvesting for human-based architectures.

Chapter 3 (Power from Body Motion). This part describes the analysis for available power from motion and vibration energy harvesting. It also includes recordings

of acceleration from various body locations while performing different activities. The results serve to estimate the available power that can be obtained from body motion.

Chapter 4 (Generator Design). This chapter includes generator architecture, modeling of a pendulum-based electromagnetic mechanism, magnetic flux distribution, simulation of the voltage output, and optimization of the device for several topologies.

Chapter 5 (Generator Fabrication and Testing). This section provides the description of the fabrication processes employed to manufacture miniature prototype devices and results of the testing.

Chapter 6 (Discussion of Results). This chapter presents the analysis and evaluation of the investigation and discussions of the results of previous sections.

Chapter 7 (Societal Implications). This section discusses the societal implications, both positive and negative, that this kind of technology can pose in society. What are the worries that people could face when a new technology intended to replace a previous one is introduced? Will society be concerned with the miniaturization and pervasiveness of technology? What is the future of this technology? What are the implications in the developed and developing world? These are only some of the questions that are analyzed in this section.

Chapter 8 (Conclusion). This chapter provides the summary of this research, including the prototype generators, while providing recommendations for future work.

Chapter 2

Energy Harvesting Background

2.1 Introduction

Energy harvesting is a research area that is gaining relevance for powering electronic devices because of the almost infinite lifetime potential. Energy generation from motion, solar light, and temperature changes has proven to be a viable alternative to batteries for commercial products, such as hand-cranking radios and flashlights, solar-powered calculators, and thermal-powered wristwatches. Energy scavenging also addresses the feasibility of using body motion to power portable, wearable, or implantable systems, such as biomedical applications. On the other hand, the increasing use of miniature low-power electronics and wireless technologies for new medical monitoring applications, such as body sensor networks for health-monitoring [50, 44, 134], will challenge present technologies due to battery finite lifetime and size. A trade-off between battery size and battery capacity has typically dominated the final size, lifetime, and capabilities of a system.

This chapter reviews the energy scavenging literature. Energy generation will be covered for human-based energy harvesters and machine-based scavengers.

2.2 Energy Generation from the Human Body

One of the first reviews on energy generation from the human body was made by Starner in 1996 [120]. The description included analysis for available power from body heat (0.2-0.3 W on the neck, 0.6-1.0 W on the head, and 3-5 W on the entire body surface), respiration (~1 W for breathing, ~0.8 W from chest movement), blood pressure (~1 W), and other activities, such as typing (0.007-0.02 W), bicep curls exercising (~20 W), arm lifting (~60 W), and walking (~70 W). Although those numbers and locations represent an expected average power limit, devices harnessing those power levels could interfere severely with everyday activities, but devices harvesting

a small percentage of those levels would be a feasible option.

Active power generation produces significantly higher power output, as evidenced by bicycle generators powering small TV sets. For example, an occasional cyclist can produce close to 150 W, but a professional can output on average up to 700 W [30]. Some studies in this area have covered the power outputs expected from some activities, such as cranking, shaking, and pedaling, as well as the comfort of sustained generation. In 1999, Jansen and Stevels [48] reported active power generation levels using lever-driven generators (~ 6 W), crank-driven generators (~ 21 W), and bicycle pedaling (~ 100 W). Later work from this group [115] studied the power generation from sustained one-hand cranking. It was presented that power output drops close to 40 W from a peak of 150 W after 10 minutes of continuous cranking. It was concluded that 28 W on average can be obtained from sustained cranking for 30 minutes, and that 14 W could be converted into electricity if assuming a conversion mechanism efficiency of 50%. Other examples studied include the peak power from cycling and rowing as 600 W and 800 W respectively, but they are reduced to near 20% after 5 minutes of continuous activity¹.

Biomechanical motion analysis for energy harvesting from walking at the joints was examined by Niu et al [83]. The evaluation of a 1 Hz gait cycle (\sim two steps per second on average) showed that movements from the elbow, knee, and ankle have a potential for energy harvesting. The negative work required to decelerate the limbs can be as high as 40% at the ankle and elbow, and 90% at the knee. Then, an electric generator can reduce the body metabolic load if it assimilates this negative work while producing energy. Li et al [60] demonstrated this using a knee brace that harnessed energy only when the limbs decelerated, producing an output close to 5 W.

Generator designs based on linear motion (linear generator architecture) have also been studied. Von Buren et al [135] estimated that a generator with a 1g proof mass having an oscillation amplitude of 5 mm could produce up to 200 μ W. Further work found that these generators can produce up to four times more power if placed on the lower limbs rather than on upper body locations [136]. It was also mentioned that a device with a 0.3 g proof mass and a vibration amplitude of 0.5 mm can produce close to 3 μ W, but if a 2 g mass oscillating 10 mm is used instead, the power produced can be as high as 1.5 mW.

2.3 Transduction Techniques

Energy harvesting makes use of several transduction techniques to produce energy. Generation commonly involves the use of electromagnetic induction, piezoelectric generation, or electrostatic transduction. Other practical methods include the use of

¹<http://web.kyoto-inet.or.jp/people/kazuho/manasle/manasle.htm>

thermal gradients, photovoltaic cells, or a combination of the above techniques. A brief description is given for each of these.

Electromagnetic generation is based on the induced voltage in a coil when a magnet moves relative to it. This is produced by the changing magnetic flux as described by the Faraday's law of induction (Eq. 2.1):

$$|E| = |d\phi_B/dt| \quad (2.1)$$

where $|E|$ is the magnitude of the electromotive force (EMF) in volts, and ϕ_B is the magnetic flux in webers. This change is either due to having a fixed magnet and a moving coil, or the opposite, a fixed coil and a moving magnet. For a coil, the EMF depends on the number of coil turns, the strength of the magnetic flux, and the rate of change of the magnetic flux. A typical architecture might be a magnet attached to a cantilever beam or spring that oscillates with respect to a coil, or a free sliding magnet within a helical coil that surrounds the magnet.

Piezoelectric transduction for energy harvesting is based on the produced voltage when a piezoelectric material is subject to mechanical deformation. The amount of voltage produced is dependent on the properties of the material, the amount of deformation, and the direction of the applied forces. A common arrangement for piezoelectric generators is the cantilever beam architecture. The cantilever beam is either subject to mechanical deformation, or subject to an external vibration. The cantilever beam is typically designed with the objective to match its natural resonant frequency to that of the external vibration.

Energy generation from electrostatic transduction is based on the charging of capacitor plates. The separation of charged capacitor plates is varied by environmental motion or vibration, changing the capacitance of the capacitor structure. The change in capacitance changes the voltage across the capacitor according to the fundamental capacitor relationship (Eq. 2.2):

$$Q = CV \quad (2.2)$$

where the charge on the capacitor Q is equal to the capacitance C times the voltage V . When the capacitance is decreased (by an increasing separation of the capacitor plates) the voltage through the capacitor increases (because there is a charge on the capacitor). Therefore, the mechanical energy due to vibrations or motion that increases the plate separation is converted into electrical energy.

2.4 Human-Based Energy Harvesters

The scavenging of body motion for powering portable mechanical devices was first reported in 1770 when the Swiss watchmaker Abraham Louis Perrelet² invented the self-winding mechanism for pocket watches. The mechanism was designed to wind the watch's mainspring as the person walked. This was achieved using an oscillating weight inside the watch mechanism. By 1924, John Harwood adapted a similar mechanism for wristwatches [24]. His design allowed the mainspring to wind only when the weight oscillated in one direction. Since spring bumpers limited the swinging to less than 360°, this design is now known as a *bumper* wristwatch. By the 1960s, self-winding wristwatches without spring bumpers, for full rotations, became common, but it wasn't until 1986³ when the Japanese company Seiko made an updated version that included a tiny electrical generator.

2.4.1 Electromagnetic Energy Generators

Oscillating rotational generators originated from wristwatch companies. The Japanese company Seiko presented the Automatic Generating System (AGS) in 1986. This self-winding mechanism was used on wristwatches under the Kinetic brand name. The design consisted of a rotating pendulum mass, a gear box train (ratio 1:100), and a small permanent magnet generator, Fig. 2.1a. Due to wrist position changes, one oscillation from the pendulum mass produced 100 rotations on the generator. According to Paradiso and Starner [87], 5-10 μW of power was estimated to be produced when worn, and 1 mW could be obtained when forcibly shaken. Swiss company ETA later introduced the Autoquartz with a different approach. The pendulum mass wound a spring connected to a small generator using a gear box train, Fig. 2.1b. Once the spring was fully wound, it unwound making the generator rotate at 5-15 krpm for a short time (50 ms), generating more than 15 V and 6 mA (90 mW) [87].

Researchers have also investigated commercial wristwatch generators to determine if it is possible to use them for implantable biomedical applications. For example, Goto et al. [43, 42] exploited the Seiko's generator for powering a circuit to pace the heart of a dog. The generator, when placed for a 30-minute period on the right ventricular wall of a dog's heart beating at 200 beats per minute (bpm), was able to store 80 mJ of energy in a capacitor. Another test using a charged capacitor was capable of pacing a dog's heart at 140 bpm for 60 minutes consuming 420 mJ. The actual energy requirement of 210 mJ for 30 minutes was higher than the energy produced in the same amount of time, 80 mJ. The 13 μJ of energy produced was

²<http://www.hautehorlogerie.org/en/players/famous-watchmakers/18th-century/abraham-louis-perrelet.html> Retrieved September 29 2009

³http://www.seikowatches.com/baselworld/2007/press/details/070412_07.html Retrieved September 29 2009

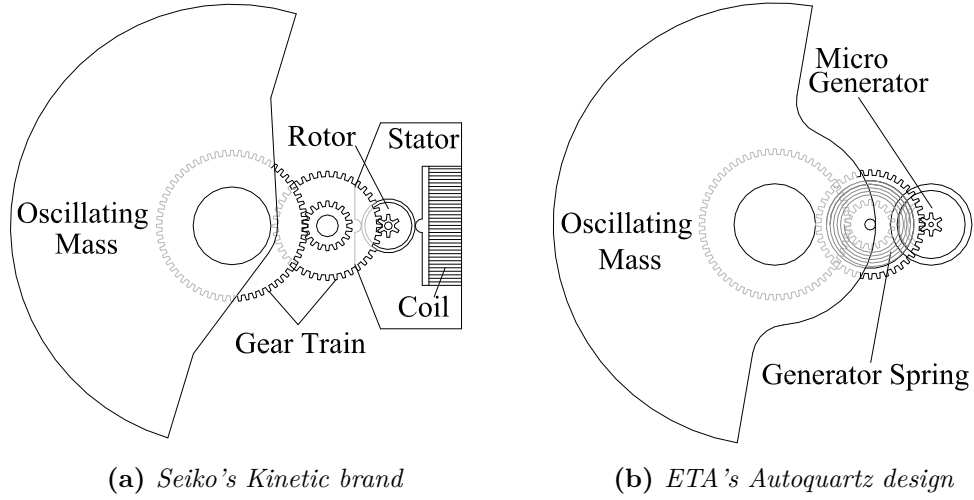


Figure 2.1: *Oscillating rotational generators diagrams from commercial wristwatches.*

compared against a cardiac pacemaker requiring only $5 \mu\text{J}$ (2.5 V , 0.4 ms and 500Ω load). This showed the feasibility of generating the power needed for the stimulation. No long-term studies were presented considering the possible effects of the generator on the heart wall. Later work from Gorge et al. [41] tried to determine how much power could be generated using the Seiko's generator taped to the chest of individuals working in an office environment. It was concluded that, over a period of 8 hours, the power generated varied from 0.2 to $2.1 \mu\text{W}$, with a mean value of $0.5 \mu\text{W}$. This power level was considered to be 10 to 100 times less than required for charging a cardiac pacemaker battery.

Further studies employing the Seiko generator have also been undertaken. The analysis performed by Sasaki et al. [109] found that if the right conditions are given to keep the rotations, this generator can produce up to 10 times more energy than from swinging motion alone. A swinging motion at 1 Hz was found to produce $15 \mu\text{W}$ while self-excited rotations were able to produce up to $170 \mu\text{W}$ at 2 Hz . The conditions to maintain these rotations were described as:

$$|\dot{\theta}|_{t=0} > \omega \quad (2.3)$$

$$\frac{2c}{Ama\omega} < 1 \quad (2.4)$$

where θ is the rotation angle, ω is the angular speed, c is the electromagnetic damping, A is the amplitude of the external oscillation, m is the pendulum mass, and a is the distance between the center of gravity and the axis of rotation. Another promising linear generator was also presented by this group. It was composed of a permanent

magnet mass suspended by springs and surrounded by a 400-turn coil. Although the linear generator had an overall volume of 500 cm^3 , it was reported that it produced up to 90 mW when excited at its natural resonant frequency of 6 Hz with a vibration amplitude of 5.5 mm.

Wang et al [139] have also improved upon the original Seiko design. Their objective was to increase the power output density from about 7.5 mW/cm^3 to 50 mW/cm^3 . This group fabricated a miniature eight-pole permanent magnet generator using an imbricated-pole stator with a single wire-wound coil to be driven at high speed. A prototype generated 15 mW at 6000 rpm (100 Hz) after rectification by a Schottky-diode bridge for a volume slightly larger than 1 cm^3 .

In addition to the rotational design from wristwatches, linear displacement generators, similar to the commercial shake-driven flashlights, have also been investigated for body motion. Duffy and Carroll [25] described one such design situated inside a shoe sole. The generator was composed of two opposing magnets attached together inside a container with three wrapped coils, about 45 mm long and 13 mm in diameter, Fig. 2.2a. The shoe generator produced 8.5 mW when tested at a frequency of 5 Hz. A second generator design consisting of a set of fixed magnets facing a moving magnet with a coil in between was also tested. This set was able to produce up to $230\text{ }\mu\text{W}$ of power at a frequency of 5 Hz. Further work [21] evaluated different rectification circuits: half-wave and full-wave designs versus doubler and quadrupler voltage multipliers. The doubler was found to produce a higher voltage and power output. A six-coil design with sliding magnets produced peak-to-peak voltages of 4 V (400 mV_{rms}) when tested at 2 Hz. The voltage doubler offered a rectified power output close to 1 mW when using a 0.1 F double-layer capacitor, although up to 2 mW was expected. It was assumed that this was due to the capacitor taking longer to charge.

Backpacks have also been used for energy generation. Rome et al. [102] employed the up-and-down movement of backpack loads to generate energy. This backpack design was divided in two frames, a vertical-moving structure where the load was placed, and a fixed frame attached to the individual. A toothed rack on the moving frame was connected to a gear box on the fixed structure, which was attached to a DC generator, Fig. 2.2b. When the movable structure traveled 4.5 cm the generator could rotate up to 5000 rpm due to the gear box. Power generation up to 7.4 W was reported when carrying heavy loads (38 kg). In addition, the load peak force from the movable design decreased up to 12% when compared to a fixed cargo. This decrease in the metabolic cost increased the efficiency of the overall energy generation process.

Other studies made by Niu and Chapman [82] evaluated arm swinging, foot movement, and trunk displacement as potential locations for energy harvesting. Their proposed design, as shown in Fig. 2.3a, used a linear electromagnetic generator tested on the mentioned body locations. An average power output of 10 mW and an open-circuit peak voltage of 7 V were reported for the device placed on the arm. A

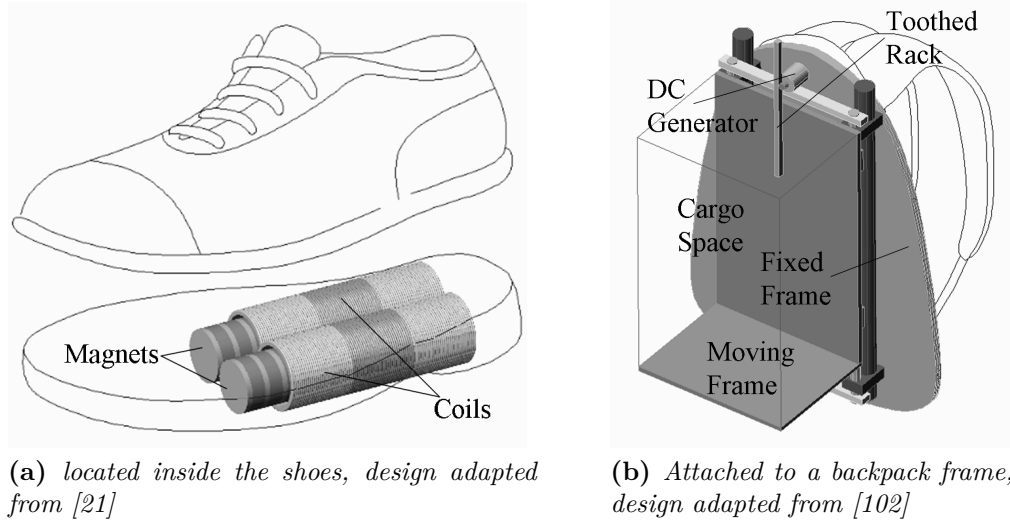


Figure 2.2: Inertial linear-based generators

backpack-situated generator produced 50-80 mW with a peak voltage of 20 V (open-circuit), while the power output for the harvester worn on a shoe was 80 mW for an open-circuit peak voltage close to 27 V. Power was measured after rectification while charging a battery. It was reported that impedance matching would increase the power by a factor of three.

Linear electromagnetic generators have also been optimized for energy harvesting while walking, as performed by von Büren and Tröster [137]. The generator consisted of an air-core tubular structure having a flexure bearing, and a free-sliding magnet stack surrounded by coils, Fig. 2.3b. Energy harvesters having a volume of 0.25 cm^3 were analyzed with different quantities of magnets (6-9) and coils (6-10). The power output varied according to the body location, but on average 2-25 μW were recorded. A comparison was offered with a lithium-ion battery having an energy density of 0.3 Wh/cm^3 . The battery would be depleted in a 4-year period if 2 μW is drawn, or its energy would be completely consumed in 4 months if the power drain is 25 μW . A prototype with a volume of 0.5 cm^3 (15 mm long, 6 mm diameter) having 6 magnets and 5 coils was tested below the knee while walking for an average output power of 35 μW and a peak power of 1 mW (electrical efficiency of 66% on a 10Ω load).

Another study employing a linear electromagnetic generator (55 mm long, 17 mm diameter) using a free sliding magnet surrounded by coils was presented by Saha et al. [107]. Two different configurations using *magnetic springs* (magnets located at the ends to repel the free-sliding magnet) were presented. A first configuration having fixed magnets at the ends (top and bottom of the tubular structure) was placed in a backpack. It provided 0.3 mW when walking and 2.46 mW when slowly running.

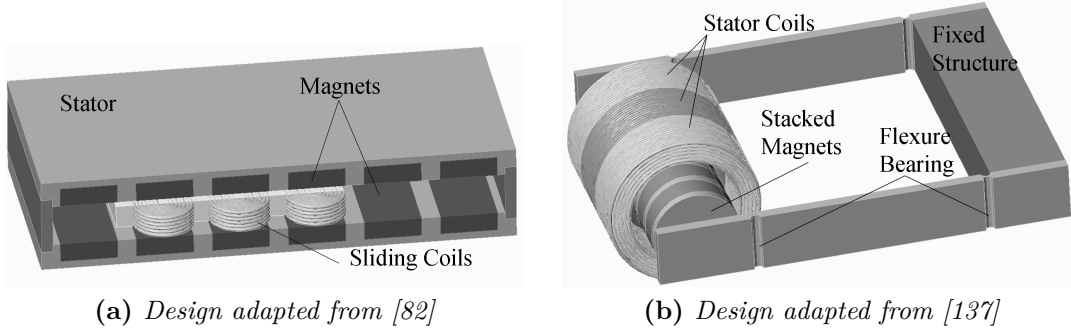


Figure 2.3: *Linear electromagnetic generators*

A second configuration with the top fixed magnet removed produced 0.95 mW when walking and 2.46 mW when slowly running. The second arrangement had a higher sliding magnet displacement for a 300% increase in power output while walking and 32% increase while slowly running. The energy stored in a Li-MnO₂ coin cell battery reached 3.54 J after one hour of walking. The energy generated exceeded the power consumption of 700 μ W (2.5 J in 1hr) for a wearable system composed of a light sensor, microphone, accelerometer, microprocessor, and RF transceiver.

McCarthy et al. [72] optimized a shake-driven flashlight design for energy harvesting while walking. The optimization was performed varying the coil number of turns for a fixed length and the length of the coil for a fixed number of turns. The alternative coil shapes given by the optimization process offered at least a 10% increase in energy generation while increasing the length by 17%. Combining the optimal coil and magnet length the energy generation improves over 18%. A test at 4 Hz for the optimized model provided energy levels close to 0.14 J.

Li et al. [60] presented a knee-mounted brace for biomechanical energy harvesting during walking. A gear-train and a small permanent magnet generator were fitted on a custom knee brace, as shown in Fig. 2.4. This generator was designed to harness the energy from leg deceleration rather than for continuous generation, similar to the generative braking process of hybrid cars. The gait process is divided into two stages: swing and stance. At the swing phase when the leg is moved forward, the body uses energy to decelerate the limb. This generator, when operated under the right conditions, was able to produce a power peak close to 20 W and an average power output of 4.8 ± 0.8 W. This generative braking was reported to use less than one watt of metabolic power to produce one watt of electrical power, while if used continuously more than two watts of body work are needed to generate only one watt of usable power.

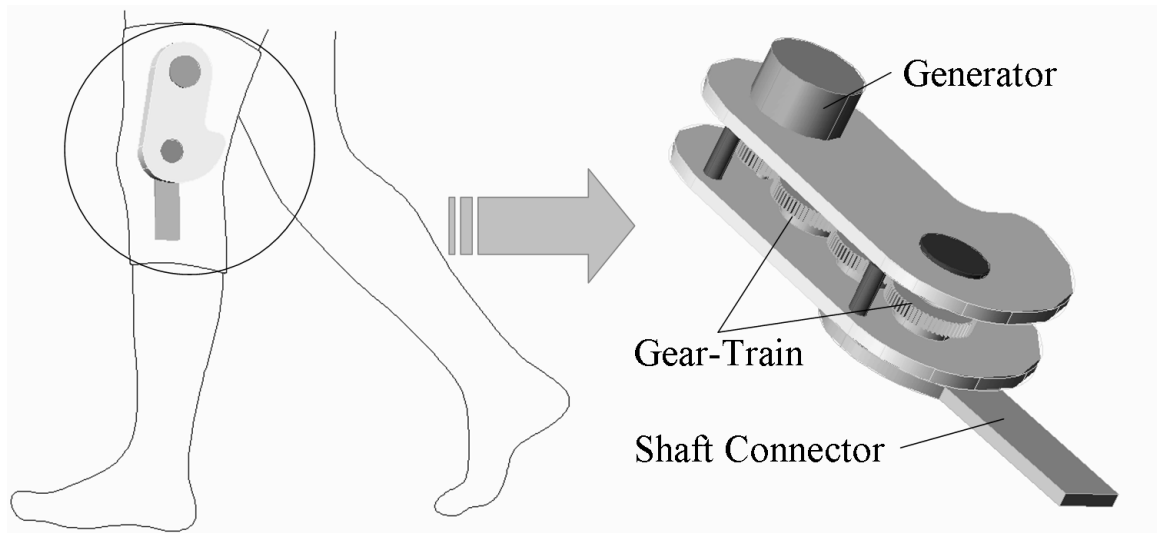


Figure 2.4: *Knee-mounted biomechanical energy harvester with generator details, design adapted from [60].*

2.4.2 Piezoelectric Energy Generators

Electronic implants with piezoelectric generators for energy harvesting have also been studied. A patent granted in 1969 to Wen H. Ko described one of the first attempts to harness heart motion for electric generation⁴. This generator described by Professor Ko was a piezoelectric rectangular-shaped cantilever beam with an added weight at its free end, Fig. 2.5a. The structure when vibrating at a suitable frequency produced a signal rectified by a voltage doubler. This design was intended to power an electrical implant such as a cardiac pacemaker. This piezoelectric device was tested on a dog's heart beating at 80 bpm producing a 4 V output voltage on a $105\ \Omega$ load for $160\ \mu\text{W}$ of power. Edward A. Schroepfel's patent described a different approach when trying to harness the heart motion to power a cardiac pacemaker circuit⁵. This patent described a piezoelectric strip inside a catheter for human heart insertion, Fig. 2.5b.

⁴Ko, W. H. 1969, Piezoelectric energy converter for electronic implants, U.S. Patent 3,456,134. The image in this patent was not identified as copyrighted material according to the United States Patent and Trademark Office, Manual of Patent Examining Procedure (Latest Revision July 2008), Appendix R Patent Rules, found at http://www.uspto.gov/web/offices/pac/mpep/documents/appxr_1_71.htm, retrieved in July 10, 2010.

⁵Schroepfel, E. A., 1987, Pacing lead with piezoelectric power generating means, U.S. Patent 4,690,143. The image in this patent was not identified as copyrighted material according to the United States Patent and Trademark Office, Manual of Patent Examining Procedure (Latest Revision July 2008), Appendix R Patent Rules, found at http://www.uspto.gov/web/offices/pac/mpep/documents/appxr_1_71.htm, retrieved in July 10, 2010.

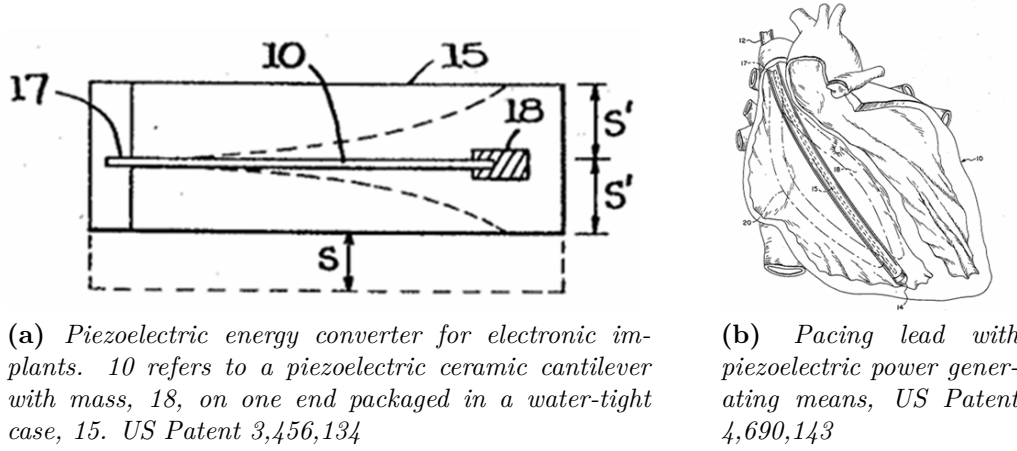


Figure 2.5: *Piezoelectric generators patents^{4,5} for heart implants.*

When the heart is beating it bends the catheter which stresses the piezoelectric strip generating an output signal.

Another piezoelectric generator for powering artificial organs harnessing the foot fall during gait was presented by Antaki et al. [6]. This generator consisted of two hydraulic cylinders placed in a shoe insole containing lead zirconate titanate (PZT) piezoelectric stacks, Fig. 2.6a. The hydraulic cylinders had pulse-amplifiers beneath the toes and heel region for transforming the low-frequency footfall into high-frequency pulses. A 1/17 scale prototype was evaluated producing 150-675 mW for walking ($5.7 \pm 2.2 \text{ mWkg/L}$) and 675-2100 mW ($23.6 \pm 11.6 \text{ mWkg/L}$) for simulated jogging, while up to 6.2 W could be expected from a 75 kg individual.

Another generator to be placed inside the shoe using the bending of piezoelectric materials was developed by Kymissis et al. [58]. They have introduced the concept of parasitic power generation capturing the energy that otherwise would be wasted or dissipated. For example, a 68 kg individual walking at 1 Hz with a 5 cm vertical displacement represents 67 W of power employed [121]. Trying to harvest all the energy would severely interfere with the gait process, but using the deformation that a sports shoe suffers (<1 cm) seemed practical. Kymissis et al. presented two different piezoelectric designs to be compared against an electromagnetic generator, Fig. 2.6b. The first configuration was made of a stack of Polyvinylidene fluoride (PVDF) sheets shaped similar to a shoe sole to be stressed under bending (the outside layers were stretched while the inner layers were compressed). This arrangement provided $\pm 60 \text{ V}$ with an average power output of 1.1 mW. The second configuration was designed to harness the heel strike using a unimorph strip (steel spring bonded to a PZT piezoelectric material sheet). The steel was bent stressing the PZT when there was a heel strike, generating peak voltages up to 150 V and power outputs up to

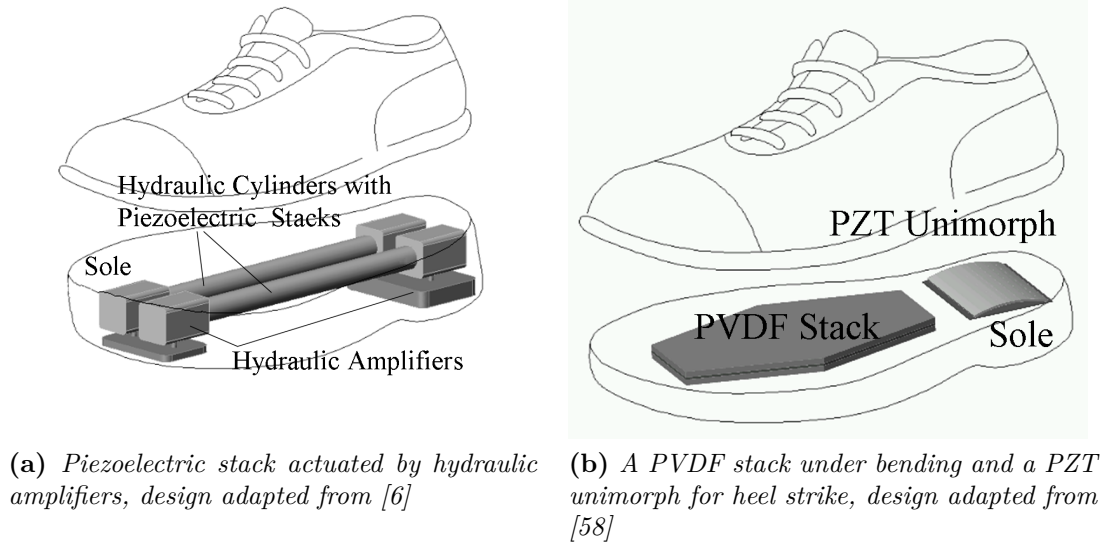


Figure 2.6: *Shoe-mounted piezoelectric energy generators*

1.8 mW. The electromagnetic design was made from a lever-driven flashlight generator mounted in a shoe. A hinged plate attached to the flashlight lever exploited 3 cm of walking stroke producing an average power output of 230 mW, although interfering with the normal gait. The piezoelectric shoe generators were also used as RFID transmitters sending a 12-bit serial ID at 310 MHz every 3-6 steps up to a 20 m distance. Later work described a power output of 1.3 mW for the PVDF stack, and 8.4 mW for two back-to-back unimorphs [113]. Similar work from this group used push buttons with piezoelectric materials. These push buttons (commercial piezoelectric strikers connected to amorphous-core transformers) produced 0.5 mJ of energy at 3 V for transmitting 12-bit ID code over 30 m several times [86].

Impact forces have also been used for energy harvesting with piezoelectric materials. For example, a linear impact-based generator was proposed by Renaud et al. [97] for harnessing limb motion. This design consisted on a free-sliding mass (750 mg) with piezoelectric cantilever beams at the ends for 10 mm displacement, Fig. 2.7a. When the sliding-mass impacts the cantilever beams they resonate generating energy for an estimated power output of 40 μ W. Further work [96] tested a prototype (25 cm³, 60 g sliding-mass) that produced 47 μ W when turned over every second, and generated 600 μ W at 10 Hz for a 10 cm linear displacement amplitude. A similar approach was also presented by Cavallier et al. [22] but using tin balls and several PZT cantilever beams in a circular package (2 mm high, 14 mm diameter), Fig. 2.7b. In spite of the fact that the objective was to compare the efficiency of PZT cantilever beams versus stacks of PZT-Silicon-PZT, the study demonstrated the use of low frequencies

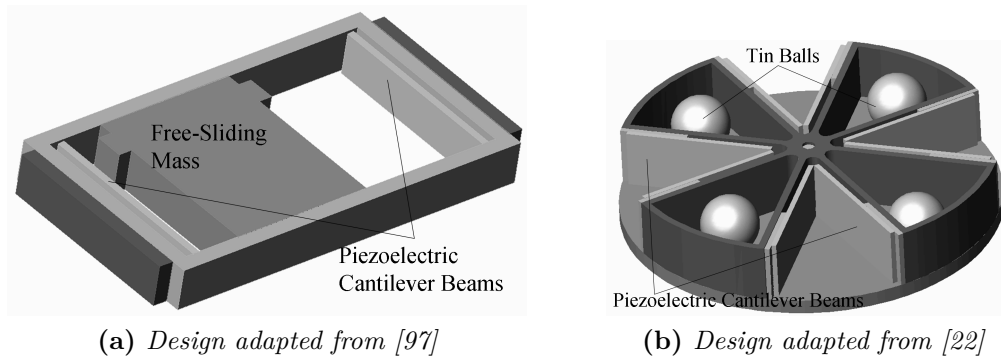


Figure 2.7: *Impact-based piezoelectric generators*

to excite vibrations in structures at higher frequency without the need of frequency tuning. The evaluation of the prototype was performed using one element tested at a frequency of 6 Hz generating 62 nW (the complete generator with all the elements could generate around 0.5 μ W).

Prosthetic knee implants is another area where piezoelectric generation has been studied, as evaluated by Platt et al. [92, 91]. Piezoelectric transduction benefits from the knee location because forces can be up to three times higher than body weight. A laboratory test was elaborated using three piezoelectric stacks (1x1x2 cm), Fig. 2.8a. The prototype was capable of producing 850 μ W of continuously regulated power (19% electrical efficiency, 20% electromechanical efficiency).

A study of backpack straps as locations for piezoelectric stacks was undertaken by Feenstra et al. [27]. The tension force on the straps, with the stacks placed in series, was mechanically amplified and converted into compressive load, Fig. 2.8b. 176 μ W of power was reported when walking on a treadmill with a 40 lb load, while the maximum power output is expected to be on the order of 400 μ W.

Muscle-powered piezoelectric generation was presented by Lewandowski [59]. The generator was devised to be positioned in series with a muscle-tendon to use the muscle contraction for piezoelectric stack compression. Power generation would benefit more from electrically-stimulated muscle rather than natural muscle contractions. Hence, individuals with extensive paralysis are preferable since electrically-stimulated muscle would not interfere with natural muscle movement or other activities. In addition, the power needed to electrically stimulate the muscles is minimal in comparison with the power that a muscle can generate when using this generator. The forearm muscle (brachioradialis), the dorso-lateral muscle on the trunk (latissimus dorsi), and the calf muscle (gastrocnemius) are capable of forces of 50 N, 100 N, and 250 N respectively. These forces on a piezoelectric stack (5x5 mm cross-sectional area, 1 Hz, and 250 ms) can produce power outputs of 8 μ W (2.5 cm long, at brachioradialis), 54 μ W (4 cm long, at latissimus dorsi), and 690 μ W (8 cm long, at gastrocnemius). A

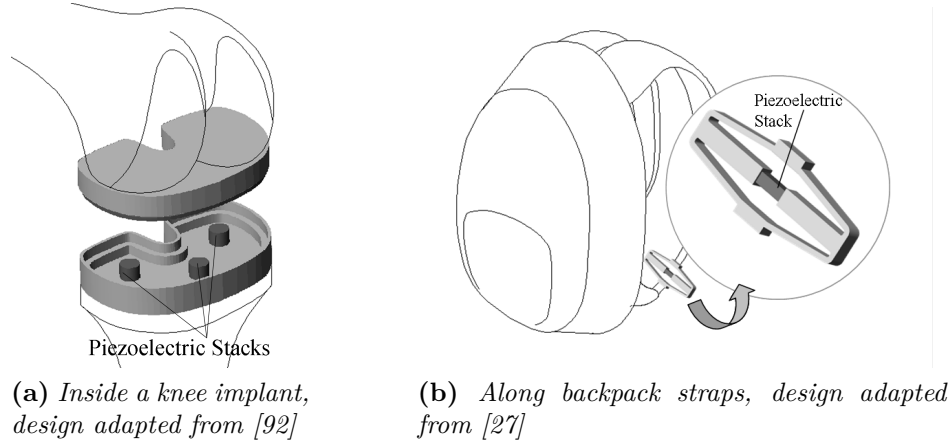


Figure 2.8: *Embedded piezoelectric generators*

PZT stack prototype (5x5x18 mm) produced up to 80 μW for a 250 N force. Muscle, tendon, and bone attachments were not mentioned in this investigation.

ZnO nanowires have also been suggested for energy generation [61, 142, 143]. Gao et al. [35] indicated that the use of flexible substrates would enable the use of piezoelectric nano arrays for bendable power sources in implantable biosensors. 50 mV are known to be generated by a single nanowire, thus arrays of nanowires could produce enough from energy harvesting. Such nano arrays have reported power densities of 100-200 $\mu\text{W}/\text{cm}^2$ [35]. Power densities close to 83 nW/cm² for nanowires stimulated by ultrasonic waves have also been reported [60].

2.4.3 Electrostatic Energy Generators

Tashiro et al. [124] developed a variable-capacitance-type electrostatic generator for harnessing the ventricular wall motion of a dog's heart using a honeycomb structure, as shown in Fig. 2.9a. The motion of the left ventricular wall was measured for testing a prototype resonating at 6 Hz. This prototype was made of stacked strips (50 layers, 20 cells per layer) of corrugated polyester film with evaporated aluminum (50 mm x 30 mm x 30 μm) and a mass (780 g) on top. An accelerometer placed on a dog's heart was used to drive a test setup with the same motion. The power output from the generator driven with the replicated heart motion was employed to pace the dog's heart at 180 bpm for over two hours. 36 μW of power on average was obtained while 18 μW was required for the stimulation pulse.

Mitcheson et al. [77] reported an electrostatic non-resonant prototype employing a variable-gap parallel-plate capacitor. Two hundred fifty Volts were generated for a pre-charge of 30 V producing 0.3 μJ per cycle. This arrangement followed the coulomb-force parametric-generator (CFPG) architecture (using the contact force to

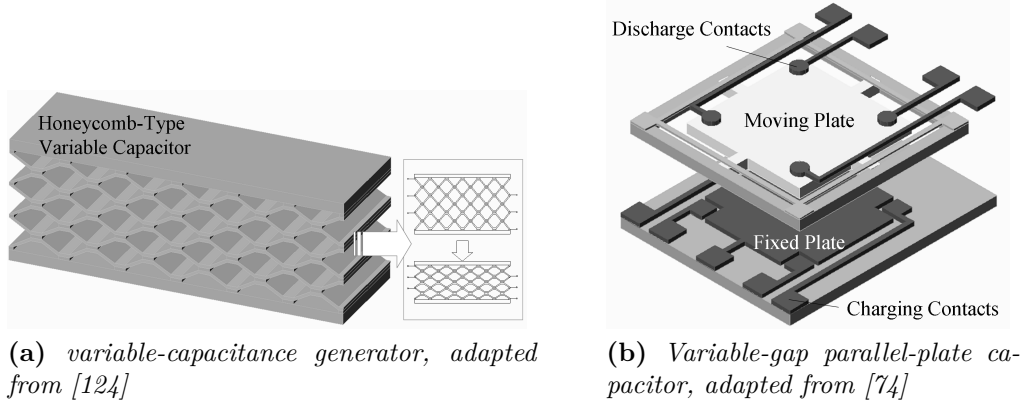


Figure 2.9: *Electrostatic generators*

damp the movement) described in [76] and was reported as suitable for large amplitudes and low frequencies. Energy is produced only when the inertial force is larger than the damping force. A capacitor plate (200 mm^2) with a proof mass made of stacked silicon plates ($10 \times 11 \times 0.4 \text{ mm}$) was fabricated for a maximum displacement of $450 \mu\text{m}$. The final discharge of 250 V was produced by a capacitance change from 15 pF to 127 pF (11 pF parasitic capacitance). Other work from this group presented a modified version of this parallel-plate capacitor, as shown in Fig. 2.9b. 120 nJ of energy and voltages up to 220 V were reported per cycle (using 30 V of charging voltage), although up to $2.6 \mu\text{J}$ per cycle could be obtained for an optimized device ($80 \mu\text{W}$ of power at 30 Hz). It is expected that if using gold as the proof mass material, the power output could be increased up to 10 times.

Arakawa et al. [7] used an electret-based approach to avoid the need of pre-charging. An overlapped area capacitor using amorphous perfluoropolymer (CY-TOP), as the electret, was presented. This electret material choice presented a charge density up to 0.68 mC/m^2 which produced $6 \mu\text{W}$ with a sinusoidal input oscillation of 1 mm at 10 Hz . Later work from this group was presented by Tsutsumino et al. [130]. They were able to reach a charge density as high as 1.37 mC/m^2 using corona discharging on a $15 \mu\text{m}$ film with 1000 V of average surface voltage. Thirty eight microwatts of power output was achieved at 20 Hz and 2 mm_{p-p} vibration amplitude (150 V sinusoidal peak-to-peak waveform). When compared against Teflon AF, CY-TOP presents a surface charge density, σ , about 3 X larger. A 9 X increase in power generation could be expected since power output is proportional to σ^2 . The surface charge density was sustained for more than 100 days, and it was stable up to its glass transition temperature, $\sim 108^\circ\text{C}$. The capacitor plates consisted of rectangular areas ($10 \times 20 \text{ mm}$) covered with electrodes (1 mm wide, $30 \mu\text{m}$ gap) and separated by an air gap ($100 \mu\text{m}$), Fig. 2.10a. One milliwatt of power can be generated for a prototype

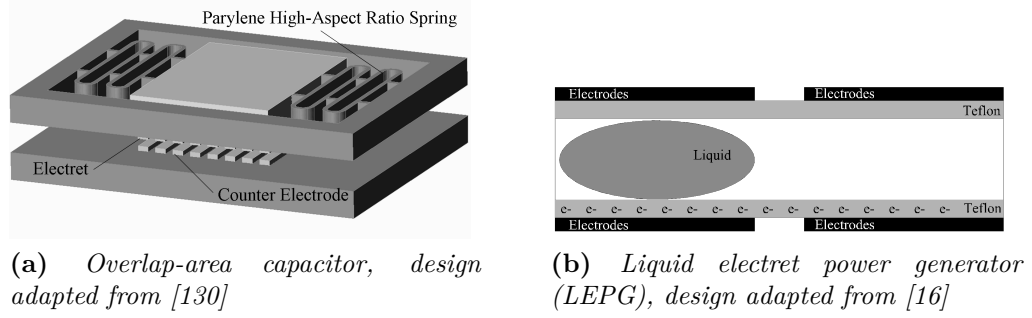


Figure 2.10: *Electret generators*

having $200\ \mu\text{m}$ wide electrodes ($50\ \mu\text{m}$ gaps) and oscillations of 1mm_{p-p} at 20 Hz.

Boland et al. [16] used fixed electret plates with liquid droplets in between, called a liquid electret power generator (LEPG). The electret plates were covered with Teflon, and the dielectric was made of liquid droplets in addition to air, Fig. 2.10b(b). Polar liquids present high dielectric constants producing large capacitance changes when air is replaced by droplets. When the generator vibrates, the liquid droplets change the capacitance of this arrangement producing energy. The prototype was reported to produce $0.11\ \mu\text{W}$ of power at 60 Hz, although it could produce up to $10\ \mu\text{W}$ of power.

2.5 Energy Generation Summary

Figures 2.11, 2.12, and 2.13 summarize the findings of energy harvesters for body motion. Fig. 2.11 shows a review of energy generators by the frequency of operation, whereas Fig. 2.12 provides a representation of the energy harvesters by volume. Fig. 2.11 is mainly dominated by electromagnetic and piezoelectric transduction generators at frequencies close to 1 Hz, making them preferable over electrostatic generators. Filled symbols show the trend that larger devices are able to produce a higher power output. Devices operating at 1 Hz were reported to produce from less than $1\ \mu\text{W}$ up to 7 W of power, at the expense of the generator's size. Fig. 2.12 describes better this trend where larger devices were reported to produce a larger power. According to this chart, devices on the order of $1\ \text{cm}^3$ were reported to produce from less than $1\ \mu\text{W}$ up to $\sim 1\ \text{mW}$ for generators operating at frequencies close to walking. Fig. 2.13 summarizes that generators operating at 1 Hz presented power densities between $\sim 1\ \mu\text{W}/\text{cm}^3$ up to $\sim 1\ \text{mW}/\text{cm}^3$.

The shaded area in Fig. 2.11 represents the range of frequencies commonly associated with body motion activities. Those generators that are found inside this region are potential candidates for portable devices and/or biomedical applications. Although piezoelectric generators presented a relatively large power output, a per-

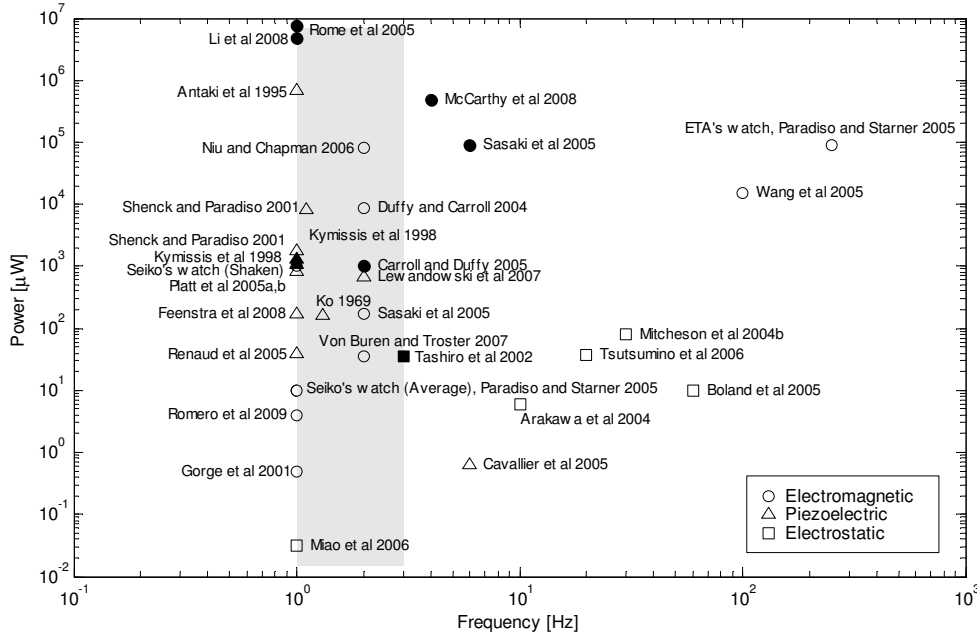


Figure 2.11: Summary of energy harvesters by frequency of operation. Shapes represent the transduction technology with the filled symbols for generators with volume greater than 10 cm^3 and the open symbols representing generators with volumes less than 10 cm^3 . The shaded area represents frequencies associated with body motion from 1 to 3 Hz.

centage of them were designed to be placed inside shoes which might not be the most desirable location. The clear-shaded area in Fig. 2.12 corresponds the zone for miniature systems with energy harvesters smaller than 1 cm^3 ($1 \mu\text{W}$ - 1 mW power output). The designs from von Buren and Tröster [137] and Renaud et al [97] are suitable solutions for portable or implantable devices in that size range, although power output is below $50 \mu\text{W}$, whereas Feenstra et al [27] device produced a higher output it is designed to be placed in backpack straps. The darker-shaded region encompasses devices with volumes in between 1 - 10 cm^3 , which is populated with a larger variety of energy harvesters. Generators in this region can be selected according to the application constraints since power output goes from less than one microwatt to several milliwatts. Devices with volumes over 10 cm^3 seem to be more appropriate for portable or wearable systems because of the larger dimensions.

Fig. 2.13 describes better the energy generation panorama for generators operating at frequencies between 1 - 3 Hz . The chart does not include all the reviewed generators since not all publications provided the power output or the device's volume to estimate the power density values. It can be appreciated that generators are capable of producing power densities as high as $1 \text{ mW}/\text{cm}^3$ for devices with a

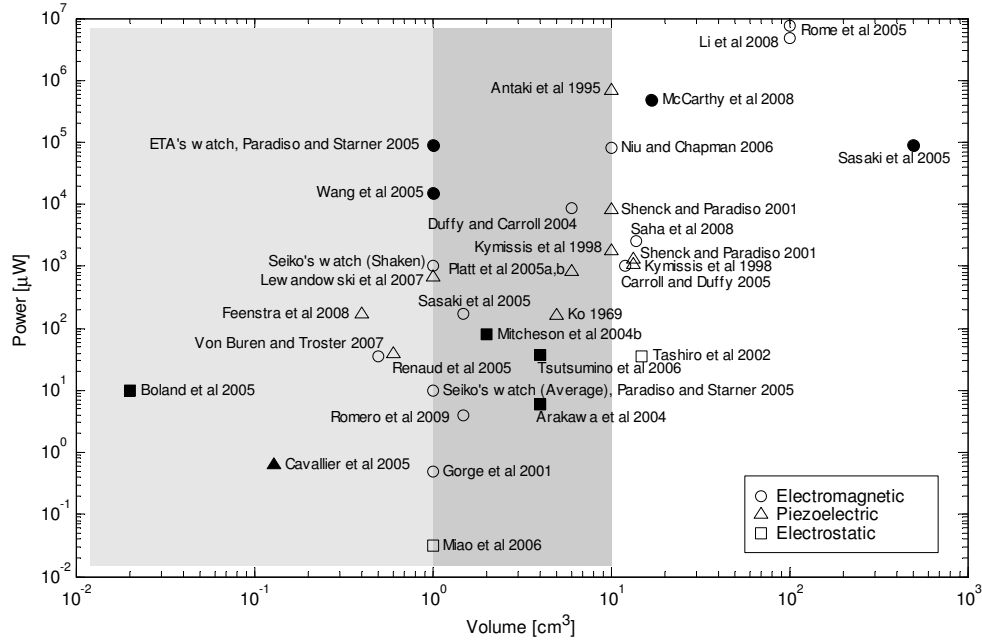


Figure 2.12: Summary of energy harvesters by generator's volume. Shapes represent the transduction technology with the filled symbols for generators with operating frequencies greater than 3 Hz and the open symbols representing generators operating at frequencies less than 3 Hz. The clear shaded area represents volumes smaller than 1 cm^3 while the darker area is for volumes between 1 to 10 cm^3 .

volume smaller than 10 cm^3 , while most devices were found in the range of 100 to $1000 \mu\text{W}/\text{cm}^3$. From this chart, most electrostatic energy harvesters were found to produce less than $100 \mu\text{W}/\text{cm}^3$, making this transduction technique less competitive in comparison to electromagnetic or piezoelectric generation. Therefore, the power density chart makes it easier to design systems for a given set of constraints.

From the charts, electromagnetic and piezoelectric generators were found to provide the largest amount of power per unit volume, with electromagnetic devices having a relatively higher output. Most of the evaluated harvesters were generators with linear displacement, whereas human motion is three dimensional presenting linear displacements and rotations. Thus, generator designs that harvest energy from more than one direction or that harness the joint rotations could be better suited for body motion. In this case, electromagnetic generation with rotational architectures could have an advantage over piezoelectric devices with linear designs. Only the impact-based piezoelectric design from Cavallier et al [22] takes advantage of a three dimensional motion approach, but its power output was too low ($<0.1 \mu\text{W}$).

These charts can help to determine technologies and constraints for different ap-

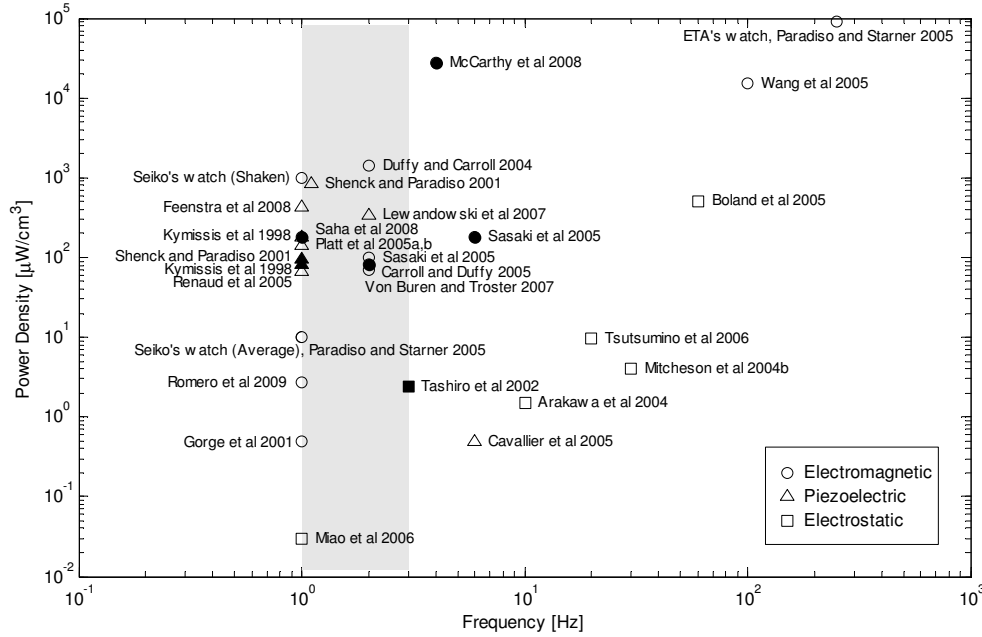


Figure 2.13: Summary of reported energy harvesters by power density. Shapes represent the transduction technology with the filled symbols for generators with volume greater than 10 cm^3 and the open symbols representing generators with volumes less than 10 cm^3 . The shaded area represents frequencies associated with body motion from 1-3 Hz.

plications. Although devices with volumes over 10 cm^3 can produce milliwatts of power, devices with dimensions on the order of 1 cm^3 present potential applications due to their reduced sizes for embedded or surgically-implantable applications. Actual technology limits power output for the latter to hundreds of microwatts.

As summarized in Fig. 2.13, electromagnetic generators with rotational designs were found to have high power densities (ETA's watch, Seiko's watch, Wang et al design[139]) in small volumes ($<10 \text{ cm}^3$). Since the size of generators can be reduced by means of MEMS technology, smaller energy harvesters for body motion can be fabricated with high power density using rotational electromagnetic generation.

Chapter 3

Power from Body Motion

3.1 Introduction

Energy harvesting is the process in which energy is produced from external sources, such as air or water flow, vibrations or motion, solar energy, or thermal gradients. The term is usually applied to power generation for small, portable, wearable, or autonomous devices. Kinetic or inertial energy harvesting uses external vibration or motion to generate energy. This external vibration can be in the form of engine or machine-based vibrations (constant frequency vibrations), while motion can be associated with human activities, environment movement, or oscillations with low-frequency, large amplitude, and broad frequency spectra. Energy scavenging from kinetic generators uses the external vibration or motion to produce electricity. The kinetic energy is transferred to a proof mass where several transduction techniques can be employed to transform it to electrical energy. These devices are typically designed to match their natural resonant frequency with that of the energy source to maximize their power output. Linear-based energy harvesters are found to be well suited for machine vibrations because mechanical vibrations are relatively uniform (constant frequency) with a main vibration axis.

Mechanical vibration has an energetic content in the form of kinetic energy. A better estimation of the available energy leads to a better match of energy harvesters for a given external source. One of the questions that needs to be solved is how much energy is available in order to determine how it can be harvested. In order to solve that question, the transduction generation (how to transform one form of energy into another) needs to be analyzed to determine if there are generation limits. Kinetic energy harvesting is studied later to define the parameters that need to be considered for this evaluation.

Body motion has a high kinetic energy content due to the relatively abrupt movements, acceleration changes, and relatively large displacements. In order to analyze

how much energy is available from human activities, a walking and running tests were performed at several treadmill speeds. Acceleration and step frequency were recorded to evaluate how much energy is available at different body locations. Energy harvesters can then be designed to scavenge this energy for powering portable electronics or implantable biomedical devices.

3.2 Transduction Limits

Transduction generation limits are defined as energy per volume, or energy density, and expressed with the lower case letter u . Maluf and Williams [69] offered one of the first descriptions for the transduction limits for thermal, electromagnetic, piezoelectric, and electrostatic generation. The thermal approach is based on the thermal expansion u_{te} (for one dimension) defined as

$$u_{te} = \frac{1}{2} Y (\alpha \Delta T)^2 \quad (3.1)$$

where Y is the Young's modulus, α is the coefficient of thermal expansion (the volumetric thermal expansion is approximately 3α), and ΔT is the temperature difference. Different materials will have different energy densities based on their properties, this is shown in Fig. 3.1a. This energy density can reach values near 400mJ/cm³ depending on the material considered for a temperature difference of 25°C. A temperature difference between the 37°C from the human body and a 22°C environment leads to a 15°C gradient. This gradient still provides energy densities of tens of mW/cm³. However, the requirement of a thermal gradient limits where such a generator can be placed. Generators placed against the skin use the difference in temperature between the body and the surrounding environment. Inside the human body such a generator would be severely limited since it is estimated that gradients will never exceed 0.2°C [65]. In addition, harvesting the thermal expansion of a material is not a simple task.

Thermoelectric energy conversion makes use of a temperature gradient to create an electric potential for thermoelectric materials. The Carnot efficiency η_c ($\eta_c = (T_{high} - T_{low})/T_{high}$) provides a limit for this generation. If body temperature (37°C) and a cool room (25°C) are considered, the efficiency of the generation is only 5.5%. Yet, commercial thermoelectric generators are able to produce 60μW/cm² for a temperature gradient of 5°C from body heat waste [87].

The energy density for an electromagnetic generator [69] is defined as

$$u_{em} = \frac{1}{2} \frac{B^2}{\mu_0} \quad (3.2)$$

where B is the magnetic field, and μ_0 is the permeability of free space ($\mu_0 = 4\pi \times 10^{-7}$ H/m). Assuming a maximum value of 1T for the magnetic flux B yields to a maximum the-

Table 3.1: *Piezoelectric material properties.*

Material	Y (GPa)	σ_y (MPa)	d_{33} (p m/V)	k_{33} (CV/Nm)	ε/ϵ_0
PZT-701 ¹	90	80	153	0.52	425
PZT-502 ¹	62	80	450	0.65	1950
PZT-507 ¹	62	80	820	0.75	4400
PMN-PT28 ¹	300	80	1700	0.9	5500
PMN-PT30 ¹	210	80	2200	0.94	7000
PZN-8%PT ²	8.3	80	2200	0.94	5100

¹Morgan Electro Ceramics plc²[99]

oretical of 400 mJ/cm³, as shown in Fig. 3.1b. A modest value of 0.1 T has an energy density of 4 mJ/cm³, which can be considered as a practical obtainable value.

The maximum energy density for a piezoelectric material [105] is given as

$$u_{pe} = \frac{1}{2} \frac{\sigma_y^2 k^2}{Y} \quad (3.3)$$

where σ_y is the yield strength of the material, k is the electromechanical coupling coefficient, and Y is the modulus of elasticity. The previous expression is also presented as

$$u_{pe} = \frac{1}{2} \frac{\sigma_y^2 d^2}{\varepsilon} \quad (3.4)$$

where d is the piezoelectric charge constant, and ε is the permittivity or dielectric constant. Using the properties of a high performance piezoelectric material, such as the single crystal PZN-8%PT (Pb(Zn_{1/3}Nb_{2/3})O₃- PbTiO₃, [99]) the theoretical maximum value is 343 mJ/cm³. Employing the properties of a common piezoelectric material, such as PZT-5H (Pb(Zr,Ti)O₃, PZT-501 from Morgan Electro Ceramics plc) with a safety factor of 2, an energy density of 19 mJ/cm³ can be considered as a practical value. The trend for the piezoelectric materials of Table 3.1 is shown in Fig. 3.1c.

The energy density for electrostatic generation [69], such as a capacitor, is defined as

$$u_{es} = \frac{1}{2} \epsilon E^2 \quad (3.5)$$

where ϵ is the dielectric constant, and E is the electric field. Using the permittivity of the free space ($\epsilon_0 \approx 8.85 \times 10^{-12} \text{A}^2 \text{s}^4 / (\text{kgm}^3)$) and a maximum electric field of 100 MV/m (or a field of 100 V over 1 μm) gives a theoretical maximum value of

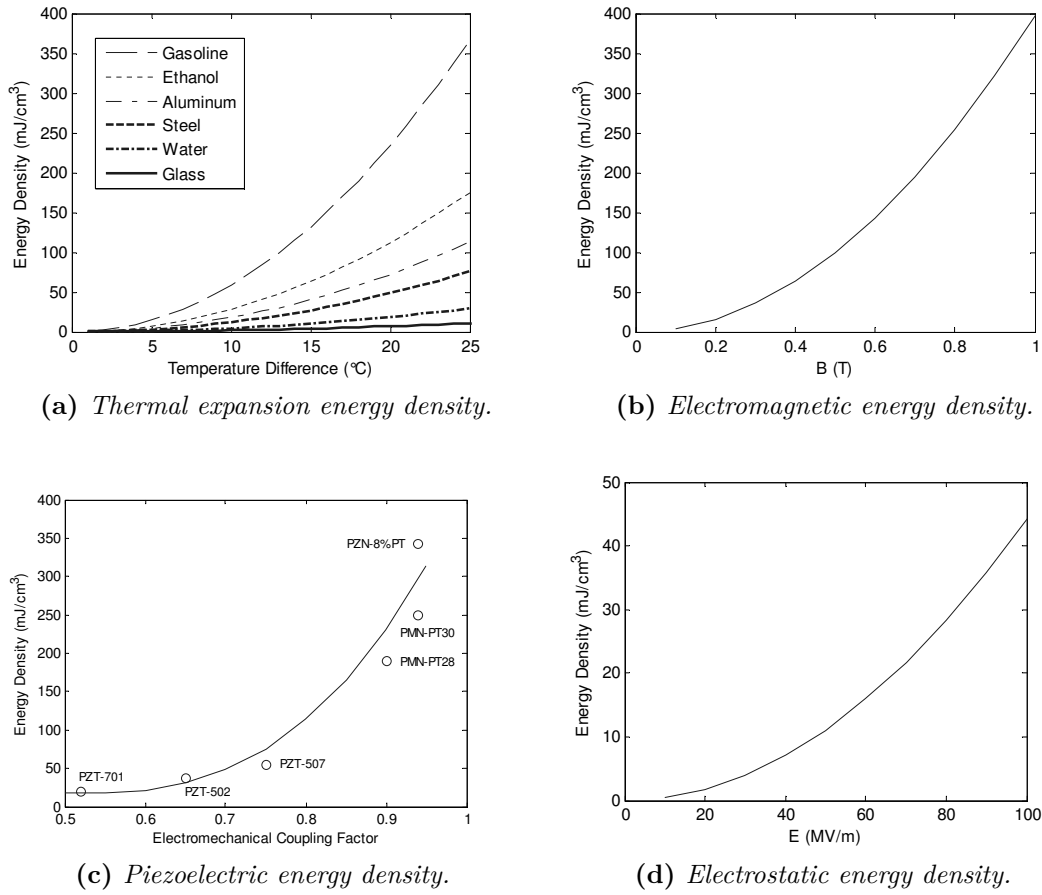


Figure 3.1: Transduction generation limits.

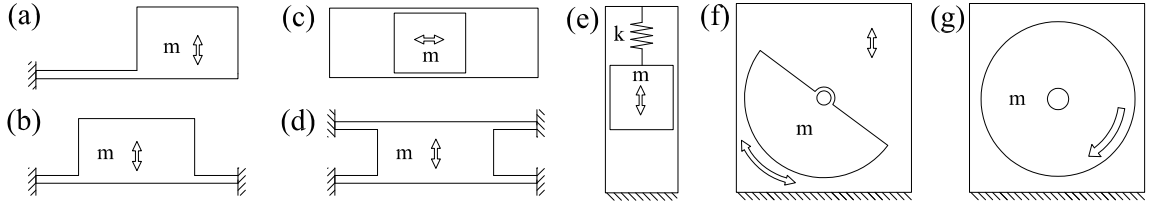
44 mJ/cm³, as shown in Fig. 3.1d. A modest E of 30 MV/m produces of 4 mJ/cm³, which can be considered as a practical value.

In summary, assuming a frequency of 1 Hz (similar to human walking), the electromagnetic transduction is limited to a maximum theoretical value of 400 mW/cm³ (4 mW/cm³ practical value), piezoelectric generation can be as high as 343 mW/cm³ (19 mW/cm³ practical), while electrostatic transduction is limited to 44 mW/cm³ (4 mW/cm³ practical), see Table 3.2. These findings were also presented earlier by Roundy [106] in terms of energy as mJ/cm³.

The transduction technology does not limit how much energy can be harvested since over 1 mW of power can be produced by walking from a 1 cm³ generator (according to Table 3.2). Therefore, the next questions to answer are: How much energy is actually available and how much can be scavenged?

Table 3.2: *Estimated power density limits for different transduction methods during human walking generation.*

Transduction technique	Maximum estimated value (mW/cm ³)	Practical value (mW/cm ³)
Electromagnetic	400	4
Piezoelectric	343	19
Electrostatic	44	4

**Figure 3.2:** *Energy harvester geometries: (a) cantilever beam, (b) out-of-plane plate, (c) free-sliding mass, (d) in-plane plate, (e) spring-mass system, (f) oscillating rotational, and (g) continuous rotation generator. Designs adapted from [147, 8].*

3.3 Kinetic Energy Harvesting

Energy harvesting generators typically follow a cantilever-beam architecture with a proof mass at the end of the beam, although several other geometries are also known, as shown in Fig. 3.2. The transduction from kinetic energy to electrical energy usually consists of electromagnetic, piezoelectric, or electrostatic techniques. Electromagnetic generation uses the relative displacement between a magnet and a coil to induce a voltage, piezoelectric generation uses the straining of the material to produce a voltage, whereas electrostatic transduction uses the changing distance of the parallel plates of a capacitor (or change of dielectric properties) to increase the voltage (potential energy) of a charged capacitor. Mitcheson et al. [76] classified the kinetic generators according to the damping mechanism used. Hence, generators are classified according to the damping by a force proportional to the velocity, velocity-damped resonant-generators (VDRG), or by a constant force, Coulomb-damped resonant-generators (CDRG). Coulomb-force parametric-generators (CFPG) is the category for non-resonant generators damped by a constant force. Electromagnetic and piezoelectric transduction are the common methods for VDRGs, while CDRGs and CFPGs usually employ electrostatic transduction.

A typical schematic of a kinetic energy generator is shown in Fig. 3.3. This arrangement, a spring-mass system, consists of a proof mass m , a spring with constant k , and a damper d (that encompasses frictional and energy generation damping

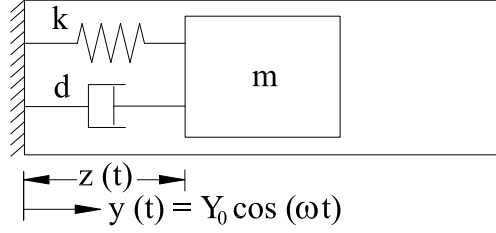


Figure 3.3: *Kinetic energy harvester schematic.*

terms). The spring-mass system is represented as

$$m\ddot{z}(t) + d\dot{z}(t) + kz(t) = -m\omega^2 Y_0 \sin(\omega t) \quad (3.6)$$

where z is the relative displacement, ω is the frequency in rad/s, and Y_0 is the vibration amplitude. The steady state solution, as presented by Rao [95], for a sinusoidal-driven input function is

$$z(t) = Z \sin(\omega t - \phi) \quad (3.7)$$

where the amplitude Z is

$$Z = Y_0 \frac{\omega_r}{\sqrt{(1 - \omega_r^2)^2 + (2\zeta_t \omega_r)^2}} \quad (3.8)$$

where ω_r represents the ratio of input frequency to natural resonant frequency $\omega_r = \omega/\omega_n$, ω_n is the natural resonant frequency ($\omega_n = \sqrt{km}$), ζ_t is the total damping ratio ($\zeta_t = d_t/(2m\omega_n)$), d_t represents the total damping, and ϕ is the phase angle

$$\phi = \tan^{-1} \left(\frac{d_t \omega}{k - m\omega^2} \right) \quad (3.9)$$

The power dissipated from the system represented in Fig. 3.3 into the damper is [26]

$$P_d = \frac{m\zeta_t Y_0^2 \omega_r^2 \omega^3}{[1 - \omega_r^2]^2 + [2\zeta_t \omega_r]^2} \quad (3.10)$$

For Eq. 3.10, the maximum power is found when the vibration frequency matches the natural resonant frequency ($\omega_r = 1$). The previous expression becomes

$$P_d = \frac{1}{2} m Y_0^2 \omega_n^3 \frac{1}{2\zeta_t} \quad (3.11)$$

Using the expression $a = Y_0 \omega^2$, where a is the acceleration of the system, the Eq. 3.11 can be rewritten as

$$P_d = \frac{1}{2}m \frac{a^2}{\omega} \frac{1}{2\zeta_t} \quad (3.12)$$

where the last term is also known as the Q factor

$$Q = \frac{z}{Y_0} = \frac{1}{2\zeta} \quad (3.13)$$

The equation 3.12 can also be written as

$$P_d = \frac{1}{2}m \frac{a^2}{\omega} Q \quad (3.14)$$

If considering that the total damping is composed of the electrically produced (ζ_e) and the mechanically produced (ζ_m), $\zeta_t = \zeta_e + \zeta_m$, the Eq. 3.12 can be written for the electrical component as

$$P_e = \frac{1}{2}m \frac{a^2}{\omega} \frac{\zeta_e}{2(\zeta_m + \zeta_e)} \quad (3.15)$$

3.4 Power Limits

Using the simplified model from Fig. 3.3, the available power from a system vibrating at resonance is [76]

$$P_{available} = \frac{1}{2}Y_0^2\omega^3m\frac{z}{Y_0} \quad (3.16)$$

The expression from Eq.3.16 is also equivalent to Eq. 3.11 using Eq. 3.13,

$$P_{available} = \frac{1}{2} \frac{a^2}{\omega} m Q \quad (3.17)$$

which is basically Eq. 3.14.

Yeatman et al. [146] described four limiting parameters for energy generation: the proof mass m , the input displacement amplitude Y_0 , the proof mass displacement z , and the vibration frequency ω . For example, from Eq. 3.16, high-frequency vibrations would produce a higher power output, but high-frequency acceleration is commonly related to small displacements and relatively low accelerations. In considering the inherent relationship between acceleration a , frequency ω , and displacement Y as $a = \omega^2 Y$, the limiting parameters are further restricted. Since the acceleration, frequency and displacement are given by the external vibrating source, rather than being of free selection, the energy generation parameters are reduced to three. Using Eq. 3.19 the relevant factors are the acceleration-squared-to-frequency (which is an

Table 3.3: *ASTF, or σ_ω values, calculated from various motion sources.*

Vibrating Source	σ_ω (m^2/s^3)
Base of a 3-axis machine tool ¹	0.230
Blender casing ¹	0.054
Cloth dryer machine ¹	0.016
Washing machine ¹	0.0004
Small microwave oven ¹	0.007
Home breadmaker ¹	0.001
HVAC vents in office building ¹	0.0001-0.006
Walking (measured on the head) ²	0.5-3.0

¹Calculated from [106]²Calculated from [46]

input source constraint), the proof mass m (a sizing factor), and the Q factor (a generator design constraint).

The acceleration-squared-to-frequency term will be referenced as *ASTF* or σ_ω , which will also be considered as a figure of merit for the energetic content of the source (m^2/s^3 units), and equal to

$$\sigma_\omega = \frac{a^2}{\omega} \quad (3.18)$$

The Q factor is a dimensionless parameter that relates the total energy stored to the energy lost in a single cycle. The Q factor is then a measure of the quality of an energy harvester. Conversely, the *ASTF* or the σ_ω term represents the energy level from the source. Therefore, energy harvesters are ultimately limited by the level of energy from the source (σ_ω) and by the energy generation process (Q factor). Thus, Eq. 3.19 can be written as

$$P_{available} = \frac{1}{2}m\sigma_\omega Q \quad (3.19)$$

Roundy [106] provided some examples of the peak acceleration and its corresponding frequency for several applications, these results are tabulated for σ_ω values and summarized on Table 3.3. A study by Hirasaki et al. [46] provided values from acceleration and frequency from human walking to tabulate the σ_ω term presented in Table 3.3. From these results, the *ASTF* (or σ_ω values) for machine-based vibrations are relatively low ($\ll 1$). In contrast, σ_ω values from body activities, such as walking, are relatively high (> 1).

Stephen [122] reported that electromagnetic energy harvesting can deliver a maximum power that corresponds to 50% of the maximum available power. Therefore, the expression for maximum power that can be delivered into the electrical load is

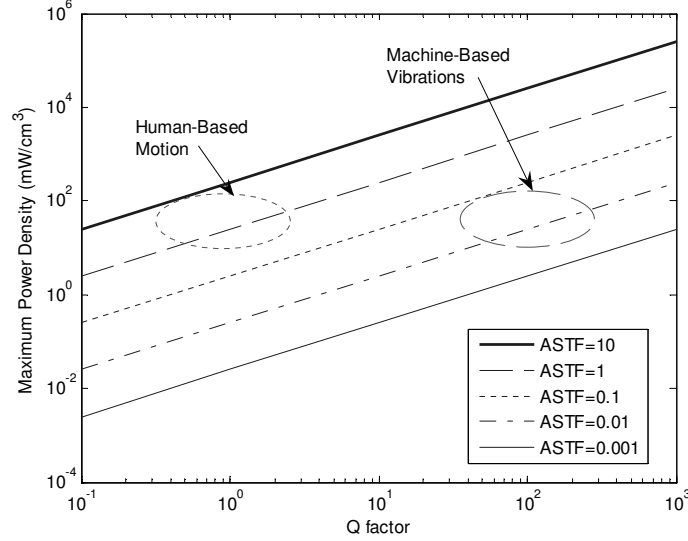


Figure 3.4: Maximum power available for linear-vibration generators at resonance from human-based motion and machine-based vibration.

$$P_{max\ elect} = \frac{1}{4} m \sigma_{\omega} Q \quad (3.20)$$

Arranging the Eq. 6.4 to be divided by the generator volume V to obtain volumetric power density from $\rho = m/V$, where ρ is the proof mass density, leads to

$$\frac{P_{max\ elect}}{V} = \frac{1}{4} \rho \sigma_{\omega} Q \quad (3.21)$$

A plot of Eq. 3.21 is shown in Fig. 3.4. A proof mass density of 10 g/cm^3 was used (for simplicity and because it is similar to that of molybdenum). Two distinct zones are displayed, the first is for the human-based motion harvesters assuming $Q \sim 1$ and $\sigma_{\omega} \sim 1$, while the second is for machine-based vibration generators assuming $Q \sim 100$ and $\sigma_{\omega} \sim 0.01$. The σ_{ω} values from Table 3.3 served as reference for the Fig. 3.4.

Figure 3.4 indicates the maximum power that can be delivered into an electric load for a system vibrating at its resonant frequency. If the energy from body motion can be harnessed by operating at resonance, then power densities comparable to generators from machine vibrations can be reached. From the Fig. 3.4, it seems reasonable to generate power from body motion with power densities on the order of mW/cm^3 . Therefore, human-based generators are still an untapped source of kinetic energy.

3.4.1 Body Acceleration Measurement

A test to evaluate σ_ω was performed to determine how much power can be generated from body motion. Walking and running were chosen as the most representative body motion activities. The test conducted measured acceleration and frequency values at several body locations from walking and running at different speeds. These acceleration and frequency readings are needed to estimate σ_ω , and then to estimate the maximum available power.

In order to proceed, a human investigation protocol was approved by the Michigan Technological University Institutional Review Board. The test was performed on 11 healthy individuals while walking and/or running on a motor-driven treadmill (Stairmaster 2100 Treadmill). Ten individuals agreed to perform the walking test (5 women, 5 men, age 29.4 ± 5.8 , weight 62.9 ± 12.8 kg, height 1.68 ± 0.1 m) and 10 subjects agreed to participate on the running test (5 women, 5 men, age 28.7 ± 7.0 , weight 63.2 ± 12.4 kg, height 1.69 ± 0.1 m). The motorized treadmill was run at speeds of 1.0, 1.5, 2.0, 2.5, 3.0, 3.5 and 4.0 mph (0.45, 0.67, 0.89, 1.12, 1.34, 1.56, 1.79 m/s) for the walking test, and to 2.0, 2.5, 3.0, 3.5, 4.0, 4.5, and 5.0 mph (0.89, 1.12, 1.34, 1.56, 1.79, 2.01, 2.24 m/s) for the running test.

As a comparison, average walking speed has been reported to be 3.4 mph (~ 1.5 m/s) for younger pedestrians and 2.8 mph (~ 1.3 m/s) for older pedestrians (over 65 years old), while the 15th-percentile was 1.25 m/s for younger pedestrians and 0.97 m/s for older pedestrians [56]. Long distance jogging speed was found to be 7.7 mph (~ 3.4 m/s) for men and 6.5 mph (~ 2.9 m/s) for women [123]. For simplicity, 3.1 mph (~ 1.4 m/s) will be considered as the average walking speed, while 7.4 mph (~ 3.3 m/s) will be the average running speed. In contrast, top runners can go as high as 23 mph (~ 37 kph, ~ 10.3 m/s). Therefore, the tested walking speeds varied from relatively slow (1 mph) to moderately fast (4 mph), while running speeds were relatively slow (2-5 mph).

The body locations chosen, as shown in Fig. 3.5, were: ankle, knee, hip, wrist, elbow, upper arm near the joint at the shoulder (will be called shoulder for simplicity), chest, back of the head, and side of the head. Joint locations were preferred because of the large acceleration changes they experienced [83]. For example, normal walking accelerations are usually below 5 G for the foot, and up to 10 G while running (1G = 9.8 m/s^2) [53]. The earth's gravitational acceleration G (upper case letter) is used to avoid confusion with g as a mass unit. Runners experience different vertical peak accelerations at different body locations: between 0.8-4.0 G at the head, 0.9-5.0 G at the back, and from 3.0-12.0 G at the ankle [17]. Gait-related motion is also found to consist mainly of low frequencies (< 50 Hz). For instance, physiological tremor is under 25 Hz and shock transmissibility of biomaterials is in between 25-60 Hz [53]. Thus, accelerometers with a frequency sensitivity of up to 50 Hz, and a range of ± 5 G for walking, and ± 12 G for running were used for the tests.

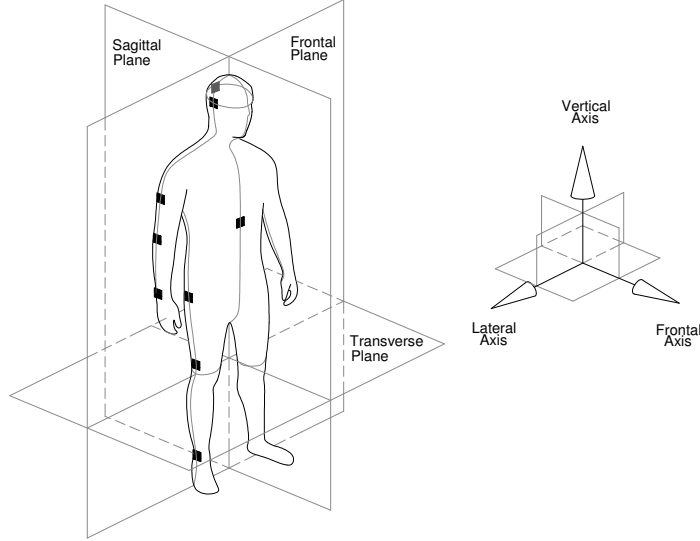


Figure 3.5: *Body locations and coordinate system.*

A wearable sensor platform was assembled using a portable data logger and data acquisition system (DATAQ DI-710-ULS) placed in a small backpack. Accelerometers were chosen according to the previous considerations and commercial availability. The chosen accelerometers were: 3-Axis ± 3 G ADXL335 (Analog Devices), 3-Axis ± 6 G MMA7260Q (Freescale Semiconductor), and 2-Axis ± 18 G ADXL321 (Analog Devices). The accelerometers were connected to the data logger and sampled at a frequency of 960 Hz per channel. A 50 Hz lowpass filter was used to avoid aliasing. Based on preliminary tests, the 3-Axis ± 6 G MMA7260Q was used at the leg locations (ankle, knee, and hip) for walking while the 2-Axis ± 18 G ADXL321 was employed at the same locations for running. The 3-Axis ± 3 G ADXL335 was placed at the other body locations for the walking and running tests. The accelerometers were contained inside small rigid plastic packages (3.4x4x0.8 cm). These units were fixed with Velcro strips and an elastic bandage wrapped on the body. Accelerometer X, Y, and Z axes were oriented respectively into forward, vertical, and lateral directions, as shown in Fig. 3.5. Acceleration measurements were recorded for periods of 60 seconds for each treadmill speed.

The acceleration waveforms from the custom sensor system were compared against a reference accelerometer to verify the accuracy of the recordings. A Sun SPOT (Sun Small Programmable Object Technology by Sun Microsystems) sensor node unit, or mote, with an integrated 3-axis ± 2 G LIS3L02AQ accelerometer was used as a reference. Since the Sun SPOT mote has the accelerometer built inside the unit, the test accelerometer was not affixed at the same point, but placed in close proximity



Figure 3.6: 3-Axis ± 6 G MMA7260Q accelerometer on a breakout board on top of a Sun SPOT mote. AA battery is included for size comparison.

(~ 5 mm on top of the Sun SPOT accelerometer, as shown in Fig. 3.6). Fig. 3.7 shows the results of the comparison between the test sensor (3-axis ± 3 G ADXL335) and the reference sensor (3-axis ± 2 G LIS3L02AQ) when manually shaking them. The signals were recorded independently using the Sun SPOT for the ± 2 G LIS3L02AQ sensor and the DATAQ DI-710-ULS for the ± 3 G ADXL335 accelerometer. The acceleration waveforms were later synchronized and plotted on the same axis. The two waveforms were found to match closely, as shown in the Fig. 3.7. The reference sensor presented a cutoff acceleration at 2 G because of the ± 2 G limit from the Sun SPOT unit. The Z-axis test readout had also a slight variation in response to the 5mm offset mounting distance. The 3-Axis ± 6 G MMA7260Q and 2-Axis ± 18 G ADXL321 sensors were also compared against the reference accelerometer, as shown in Fig. 3.8 and Fig. 3.9. The output signals from these two accelerometers were also found to match well, which verifies the accuracy of the custom sensor system.

3.4.2 Body Acceleration Results

The stride frequency results are presented in Fig. 3.10 for the walking and running tests (error bars represent one standard deviation). Step frequencies for the walking test varied relatively linearly from 1.2 to 2.2 Hz (1-4 mph). A 1% variation in the step frequency was found when this test was compared against that of Hirasaki et al [46], as shown in Fig. 3.10. The average walking velocity of 1.4 m/s (~ 3.1 mph) was found to have an associated step frequency of 1.9 ± 0.1 Hz, while the running test showed an almost constant step frequency of 2.5 Hz. The shaded regions were added for comparison purposes for older and younger pedestrian average walking speeds.

The acceleration results for the different body locations are presented in Fig. 3.11 for the walking test and in Fig. 3.12 for the running test for each individual axis.

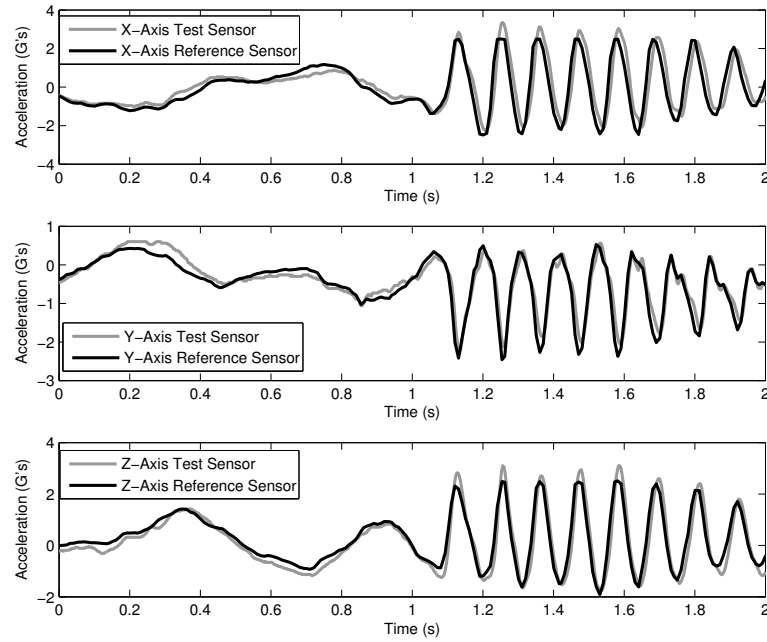


Figure 3.7: Comparison between the $\pm 3\text{ G}$ test sensor (3-axis $\pm 3\text{ G}$ ADXL335) and the Sun SPOT reference sensor (3-axis $\pm 2\text{ G}$ LIS3L02AQ).

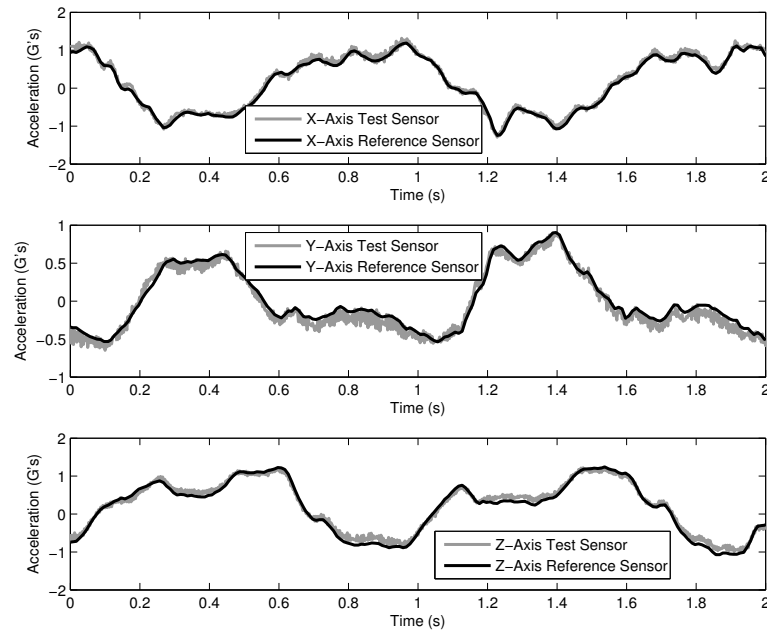


Figure 3.8: Comparison between the $\pm 6\text{ G}$ test sensor (3-axis $\pm 6\text{ G}$ MMA7260Q) and the Sun SPOT reference sensor (3-axis $\pm 2\text{ G}$ LIS3L02AQ).

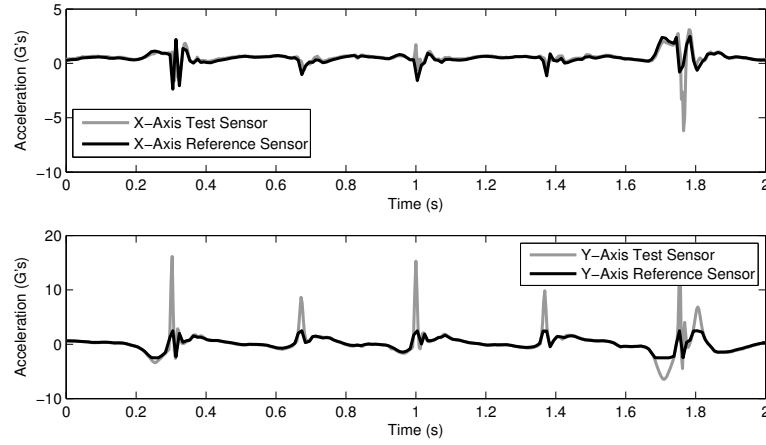


Figure 3.9: Comparison between the ± 18 G test sensor (2-axis ± 18 G ADXL-321) and the Sun SPOT reference sensor (3-Axis ± 2 G LIS3L02AQ).

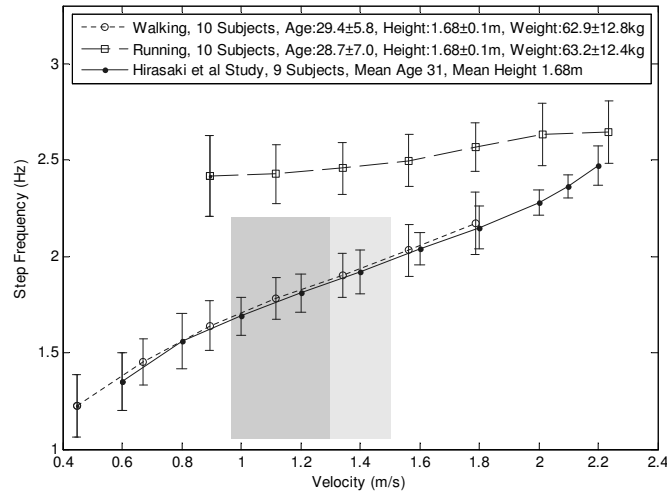


Figure 3.10: Step frequency for the walking and running test on a treadmill. Error bars represent one standard deviation. Darker-shaded area represents the 15th-percentile up to the average walking speeds for older pedestrians (over 65 years old), while the clear-shaded area includes for the 15th-percentile up to the average walking speeds for younger pedestrians (14-64 years old). Average walking speeds of older and younger pedestrians from [56].

Fig. 3.13 compares the results of both tests. It is shown that high energetic locations (those that undergo abrupt movements, such as the ankle and knee) exhibit larger accelerations than other body locations.

The larger accelerations were seen on the knee (~ 1 to ~ 3 G) and ankle (~ 2 G to ~ 4.5 G) locations for the forward direction while walking, Fig. 3.11. The vertical axis acceleration variation for the same locations ranged from ~ 1 to ~ 2.5 G for the ankle, and from ~ 0.5 to ~ 2.5 G for the knee (walking test). Most other body locations had accelerations while walking ranging from ~ 0.3 G up to about 0.5-1 G. These values are similar in magnitude at most locations of the vertical and lateral axis (except ankle, knee, and the hip to some extent). Lower body locations (ankle, knee, and hip) had a larger acceleration component along the vertical axis. Acceleration for the average walking velocity of 1.4 m/s (~ 3.1 mph) was close to 0.5 G for most body locations (except the ankle and knee).

Acceleration readings were larger for running than for walking, Fig. 3.13. Forward and vertical axes presented larger accelerations than the lateral axis. While running, lateral axis accelerations (0.2-1.2 G) exhibited little variation at all speeds, Fig. 3.12. The forward direction had acceleration readings from ~ 4 -7 G for the ankle, and from ~ 2 -3.5 G for the knee and wrist. The other body locations ranged from ~ 0.7 to ~ 1.5 G along the forward axis, while varying from ~ 1.5 to ~ 2.5 G for the vertical direction. The higher accelerations were found along the vertical direction rather than the forward axis, except for the ankle.

Figures 3.14 and 3.15 show the individual acceleration variation with error bars representing one standard deviation. Fig. 3.16 compares the acceleration variation between the walking and running tests. The larger acceleration variation for the running test can be mainly explained by the different foot-strike patterns and reaction force distributions [55], by the difference in test subject's height and weight (ranging from 1.50-1.83m and from 44-78.9 kg, respectively), and by the running shoe type.

3.4.3 Evaluation of Available Body Power

The acceleration and the step frequency results from the walking and running tests are essential to evaluate the energetic figure of merit σ_ω for each body location at different speeds. Once the σ_ω is known, an estimation of the maximum available power can be determined for the body locations at different speeds. The evaluation of σ_ω for the walking test is shown in Fig. 3.17, while the running test is in Fig. 3.18. The energetic figure of merit, σ_ω , comparison for walking and running is shown in Fig. 3.19, and this factor is found to increase with increasing walking and running speeds and is below 1 for most body locations. The ankle location during walking presents σ_ω values over 5 for the forward axis, between 1-4.5 for the vertical direction, and between 0.5-1.5 for the lateral axis, while the knee presents slightly lower values in some cases, Fig. 3.17. The running test provided larger values of the energetic

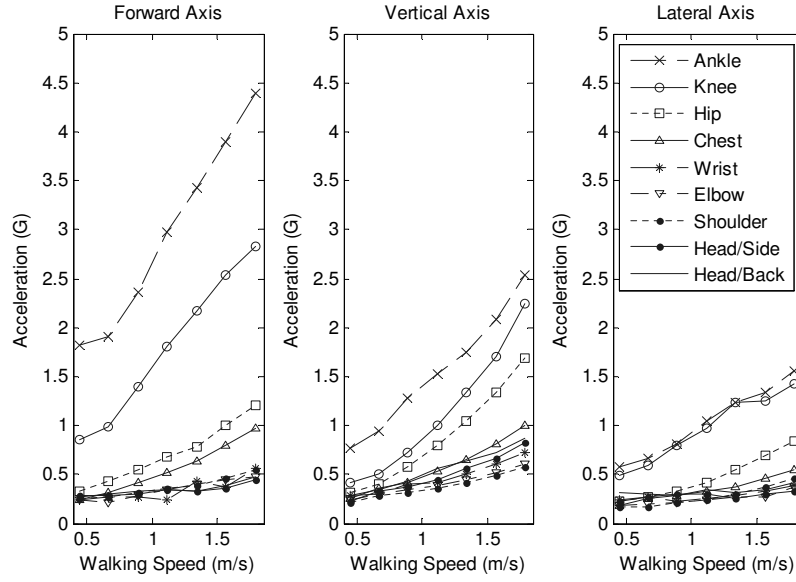


Figure 3.11: Acceleration readings from the walking test at each body location in G ($1 G = 9.8 m/s^2$). Walking test: 10 subjects, age: 29.4 ± 5.8 , height: $1.68 \pm 0.1 m$, weight: $62.9 \pm 12.8 kg$.

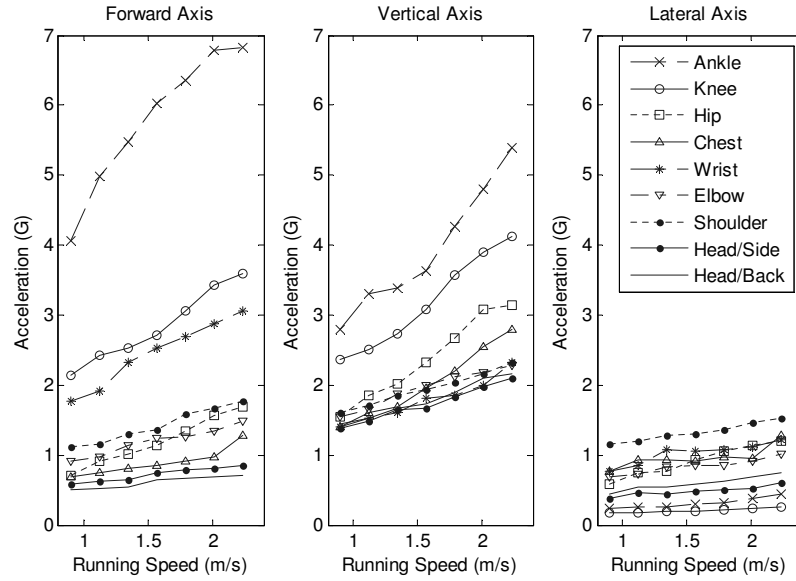


Figure 3.12: Acceleration readings from the running test at each body location in G ($1 G = 9.8 m/s^2$). Running test: 10 subjects, age: 28.7 ± 7.08 , height: $1.68 \pm 0.1 m$, weight: $63.2 \pm 12.4 kg$.

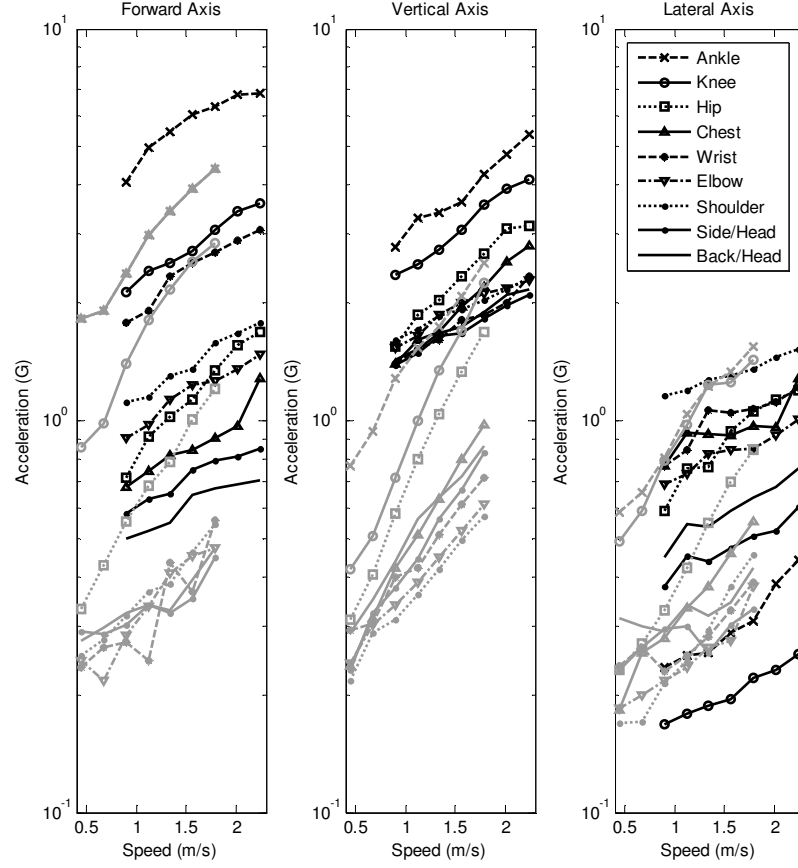


Figure 3.13: Acceleration readings comparison from the walking (gray color lines) and running (black color lines) test at each body location in G ($1\text{ G} = 9.8\text{ m/s}^2$). Walking test: 10 subjects, age: 29.4 ± 5.8 , height: $1.68 \pm 0.1\text{ m}$, weight: $62.9 \pm 12.8\text{ kg}$. Running test: 10 subjects, age: 28.7 ± 7.08 , height: $1.68 \pm 0.1\text{ m}$, weight: $63.2 \pm 12.4\text{ kg}$.

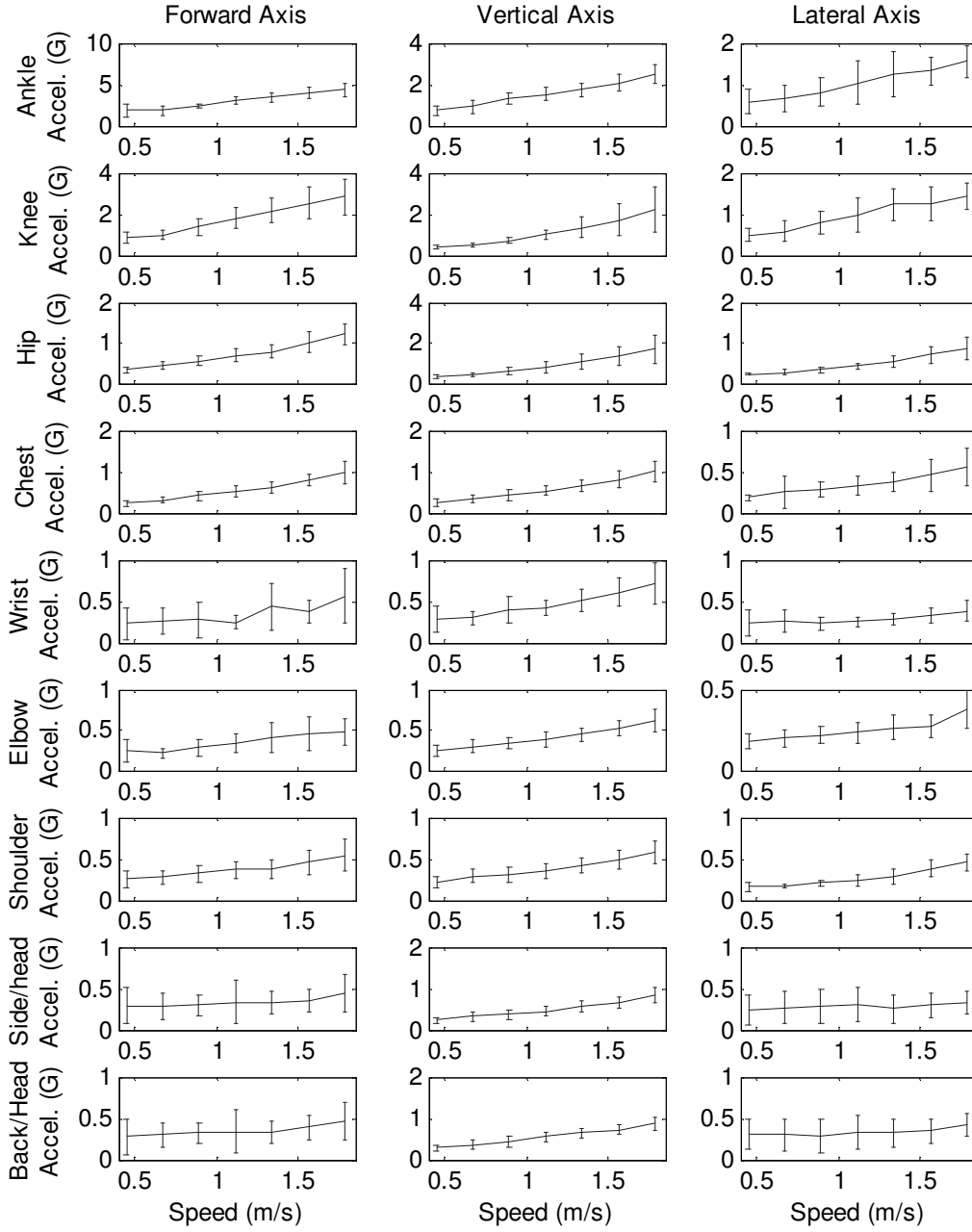


Figure 3.14: Average acceleration distribution for treadmill walking in G ($1\text{ G} = 9.8\text{ m/s}^2$). Error bars represent one standard deviation. Walking test: 10 subjects, age: 29.4 ± 5.8 , height: $1.68 \pm 0.1\text{ m}$, weight: $62.9 \pm 12.8\text{ kg}$.

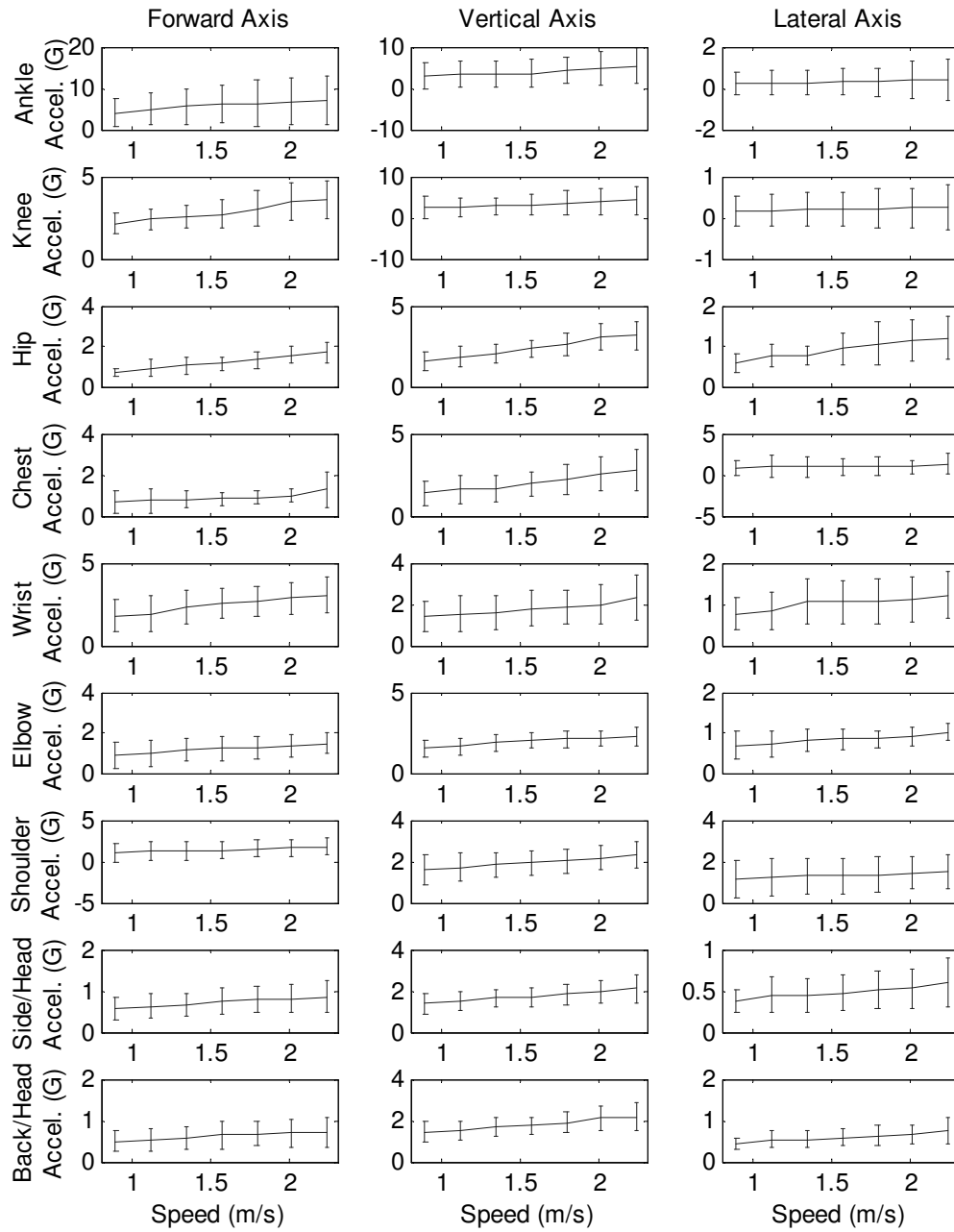


Figure 3.15: Average acceleration distribution for treadmill running in G ($1\text{ G} = 9.8\text{ m/s}^2$). Error bars represent one standard deviation. Running test: 10 subjects, age: 28.7 ± 7.08 , height: $1.68 \pm 0.1\text{ m}$, weight: $63.2 \pm 12.4\text{ kg}$.

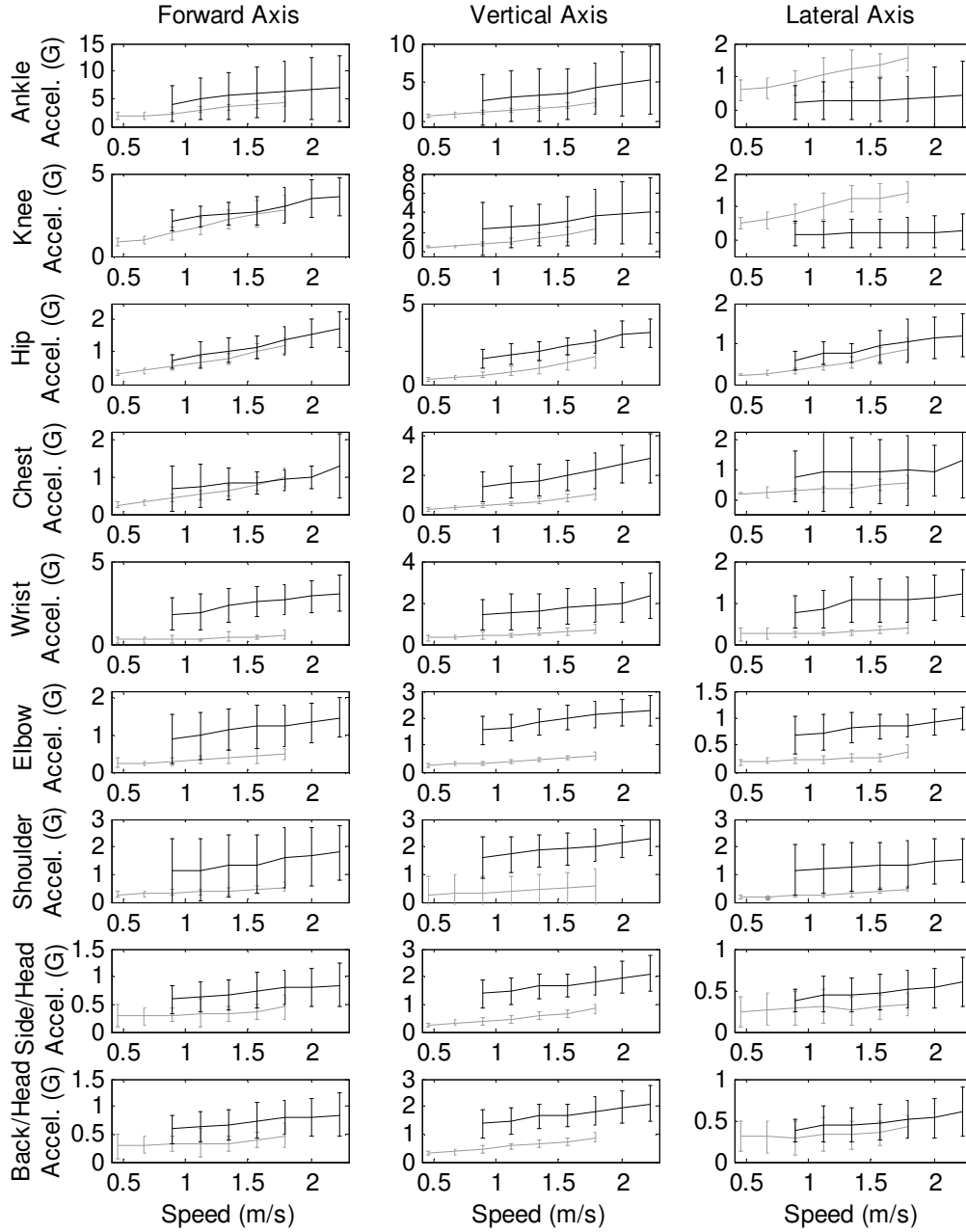


Figure 3.16: Average acceleration distribution and comparison for treadmill walking (gray color lines) and running (black color lines) in G ($1\text{ G} = 9.8\text{ m/s}^2$). Error bars represent one standard deviation. Walking test: 10 subjects, age: 29.4 ± 5.8 , height: $1.68 \pm 0.1\text{ m}$, weight: $62.9 \pm 12.8\text{ kg}$. Running test: 10 subjects, age: 28.7 ± 7.08 , height: $1.68 \pm 0.1\text{ m}$, weight: $63.2 \pm 12.4\text{ kg}$.

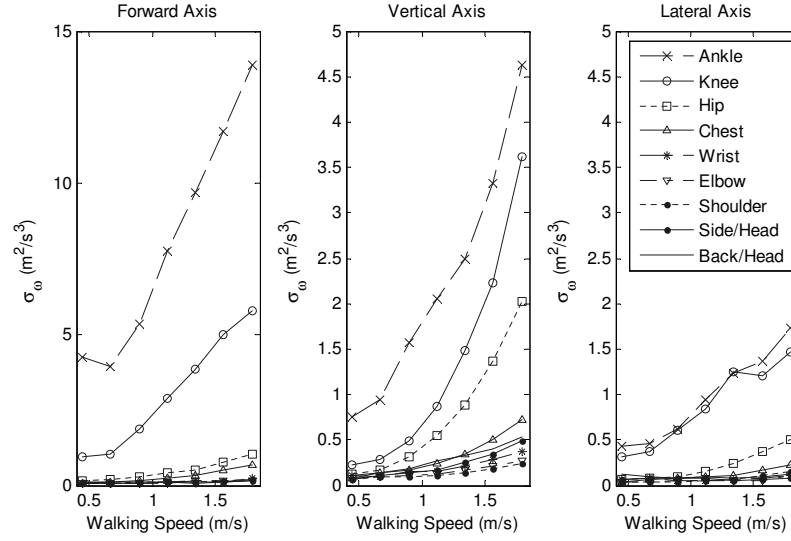


Figure 3.17: *Energetic figure of merit for each body location while walking.*

figure of merit: over 5 at the ankle, knee, and wrist for the forward and vertical axis (except the wrist). The other locations for the forward and vertical axes present σ_ω smaller than 1, while the vertical axis registers values over 2. Locations with a higher energetic figure of merit will present a higher available power, as described by Eq. 6.4. Table 3.4 summarizes the σ_ω for the average walking speed of 1.4 m/s (~ 3.1 mph) and the moderate running speed of 2.2 m/s (5 mph) at different body locations.

Available power can be estimated from Eq. 6.4 using the findings from the energetic figure of merit σ_ω . A first estimation is made assuming a generator with a 1g proof mass and a Q factor of 1, as shown in Figures 3.20 and 3.21. Fig. 3.22 exhibits a comparison between the walking and running results. From the walking test, available power levels below 0.5 mW are expected for most body locations, while the ankle and knee positions are able to provide power levels over 0.5 mW, as shown in Fig. 3.20. During the running test, the available power increases to over 0.5 mW for most of the body locations along the vertical axis, while the ankle and knee present significantly higher values. Table 3.5 summarizes the calculated available power for the average walking speed of 1.4 m/s (~ 3.1 mph) and the moderate running speed of 2.2 m/s (5 mph) at the body locations evaluated (assuming 1g mass and Q factor of one).

A second estimation is based on the power density metrics from Eq. 3.21 assuming a proof mass density of 10 g/cm³ and a Q factor of one. Figures 3.23 and 3.24 shows the power densities for each body location at the different walking and running speeds. Fig. 3.25 presents a comparison between the power densities of walking (gray color lines) and running (black color lines). Table 3.6 summarizes the available power

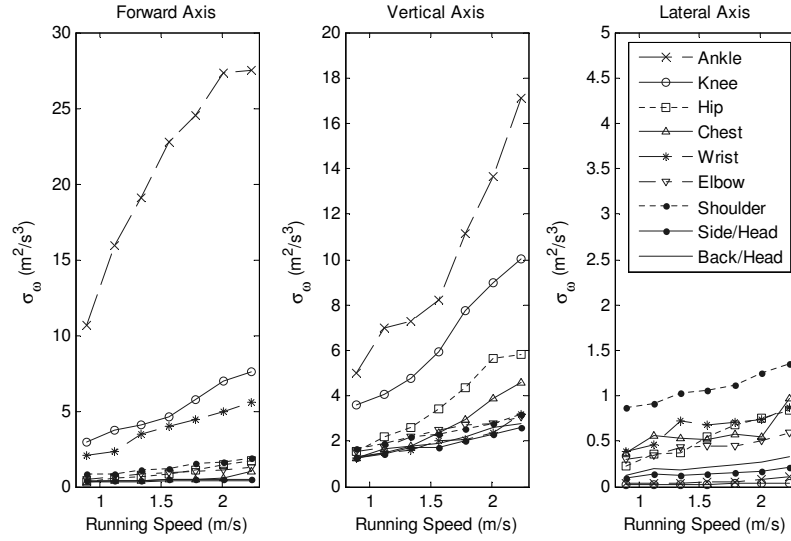


Figure 3.18: Energetic figure of merit for each body location while running.

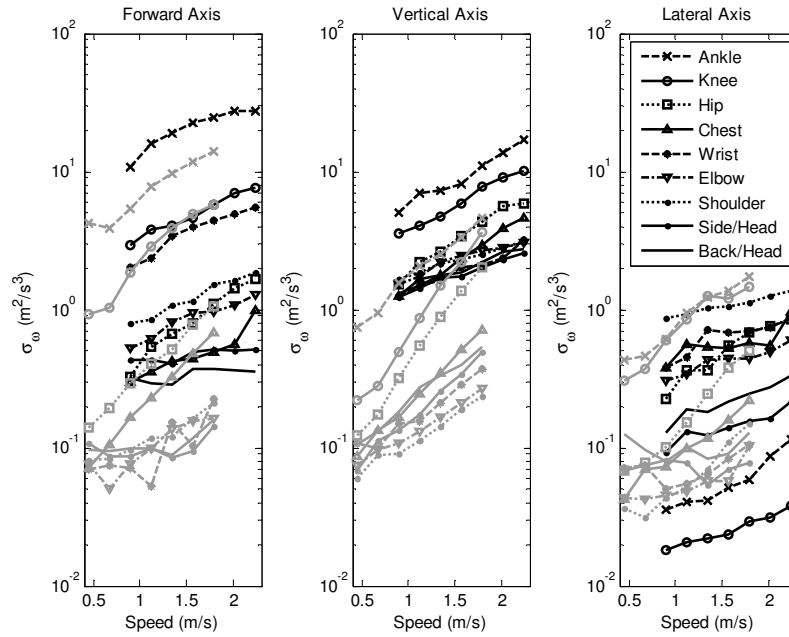


Figure 3.19: Energetic figure of merit comparison for each body location while walking (gray color lines) and running (black color lines).

Table 3.4: Energetic figure of merit, σ_ω , for the average walking speed of 1.4 m/s (3.1 mph) and for the moderate running speed of 2.2 m/s (5 mph).

Body Location	Walking			Running		
	Forward	Vertical	Lateral	Forward	Vertical	Lateral
	Axis (m ² /s ³)	Axis (m ² /s ³)	Axis (m ² /s ³)	Axis (m ² /s ³)	Axis (m ² /s ³)	Axis (m ² /s ³)
Ankle	10	2.7	1.3	27	17	0.2
Knee	4	1.6	1.3	7	10	0.1
Hip	0.6	1.0	0.3	1.7	6	0.8
Chest	0.4	0.4	0.1	1	5	1
Wrist	0.15	0.23	0.07	6	3	0.8
Elbow	0.15	0.18	0.05	1.3	3	0.6
Shoulder	0.15	0.15	0.05	2	3	1.3
Side of Head	0.1	0.28	0.05	0.5	2.5	0.3
Back of Head	0.1	0.32	0.08	0.4	2.7	0.3

density from Eq. 6.4 assuming a density of 10 g/cm³ and a $Q=1$. From these results, most body locations provide under 1 mW/cm³ from walking, while supplying over 1 mW/cm³ from running. The ankle location has an associated power density as high as 25 mW/cm³ from walking, and as high as 68 mW/cm³ from running.

3.5 Power Generation from the Human Body

A linear energy harvester could use the forward, vertical, or lateral motion of a walking or running individual to generate power according to the analysis in the previous section. Larger amounts of power output can be achieved if energy is harvested from several axes at the same time. A generator design employing the three acceleration components for energy generation would be relatively difficult to accomplish while remaining small in size (with relatively large dimensions along the three axes). An energy harvester using two of the acceleration axes would benefit from a planar design which is more appropriate for surgical implantation or for portable electronics. A planar topology can be accomplished by using two individual linear generators, one linear generator aligned to the resultant acceleration vector, or a rotational approach.

Since the lateral axis has smaller acceleration components, a resultant vector formed by the forward and vertical axis will have a larger magnitude. This resultant acceleration is shown in Fig. 3.26. The results exhibit an increase between 10-50% in magnitude when compared to the acceleration component from the forward axis

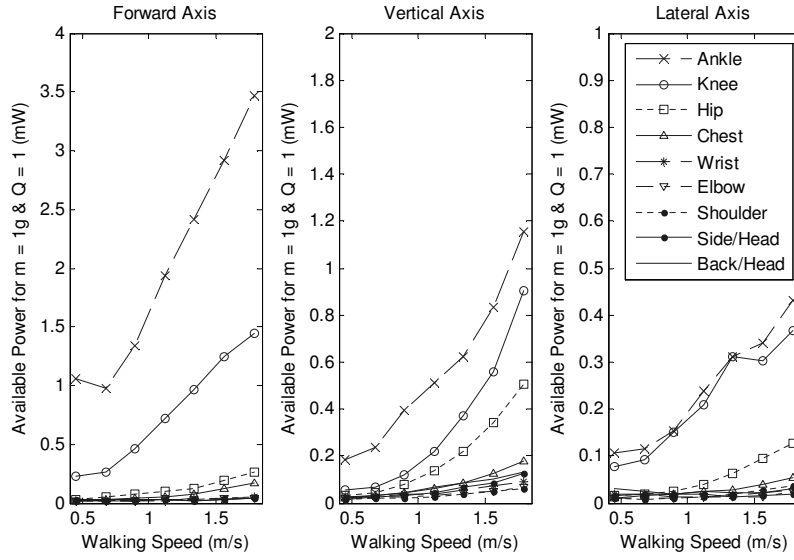


Figure 3.20: Available power at different body locations from walking for an energy harvester with 1g proof mass and Q factor of one.

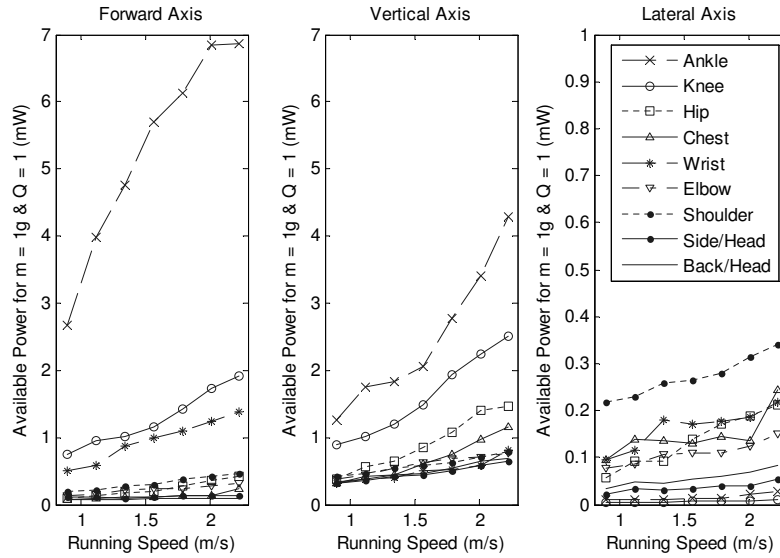


Figure 3.21: Available power at different body locations from running for an energy harvester with 1g proof mass and a Q factor of one.

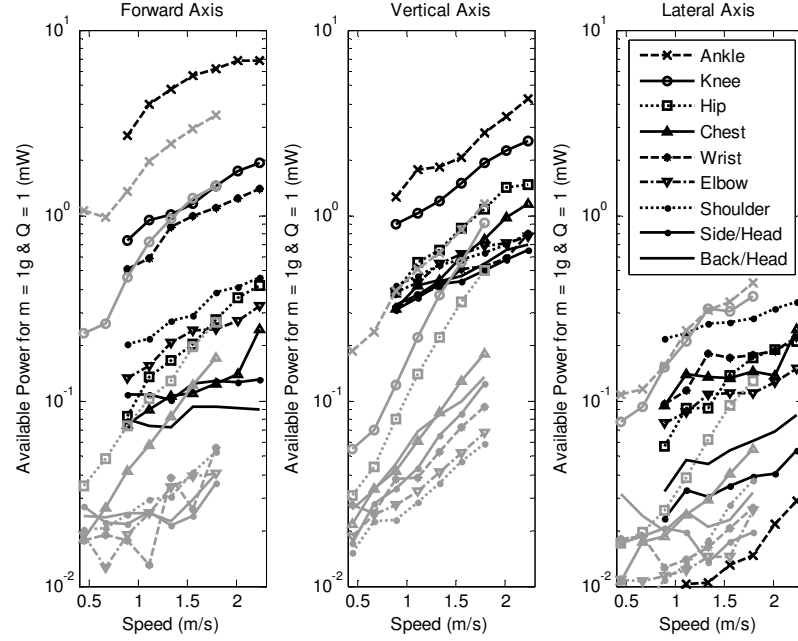


Figure 3.22: Available power comparison at different body locations from walking (gray color lines) and running (black color lines) for an energy harvester with 1g proof mass and a Q factor of one.

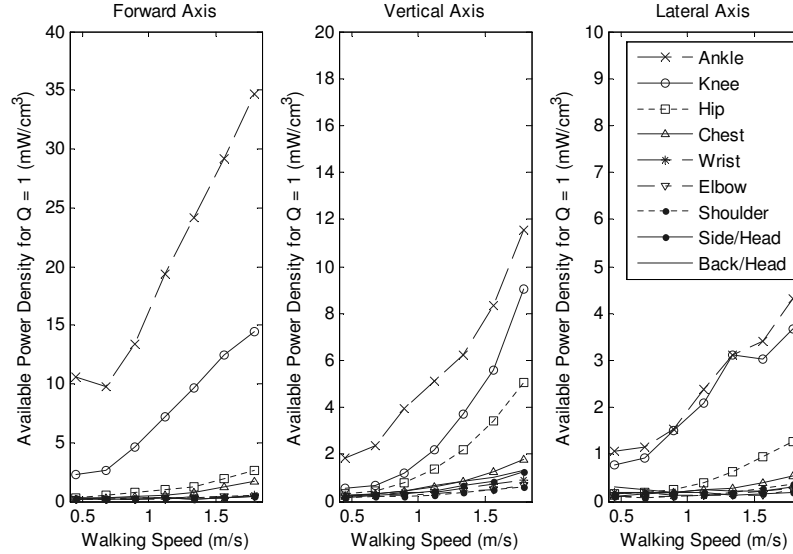


Figure 3.23: Available power density at different body locations from walking for an energy harvester with $\rho = 10\text{g/cm}^3$ and a Q factor of one.

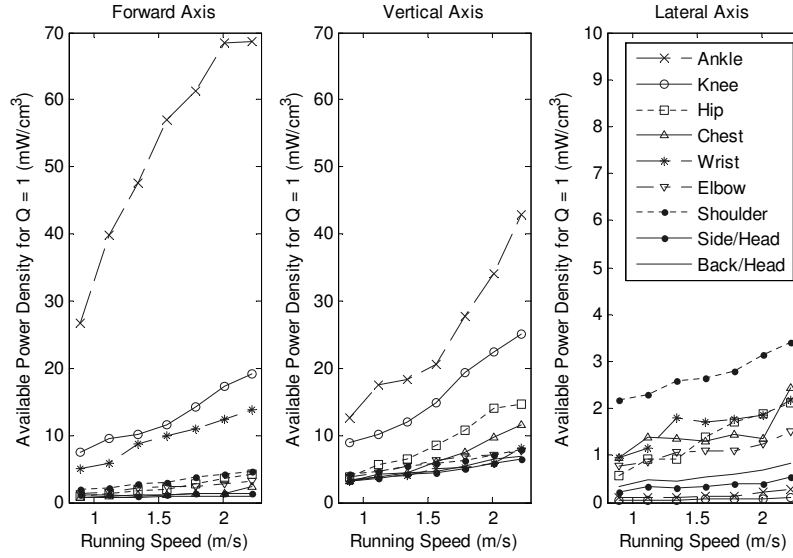


Figure 3.24: Available power density at different body locations from running for an energy harvester with $\rho = 10\text{g/cm}^3$ and a Q factor of one.

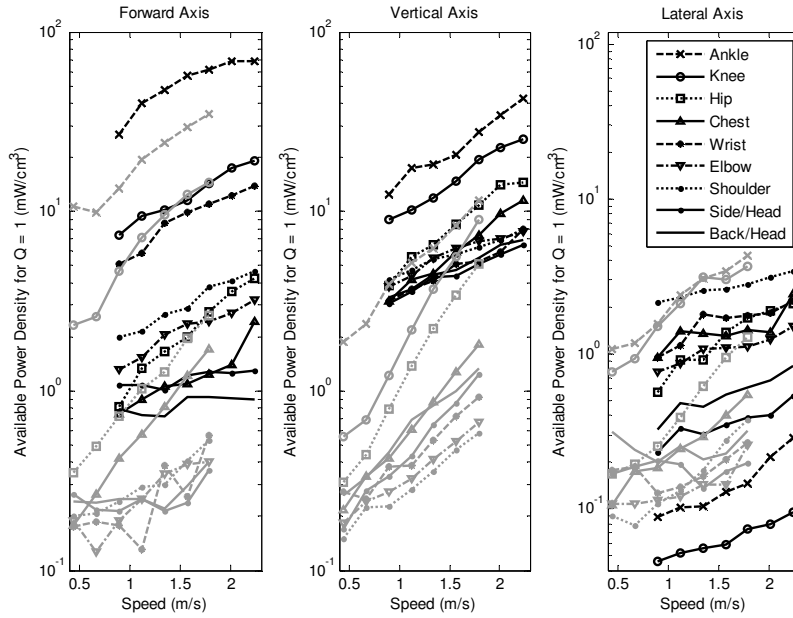


Figure 3.25: Available power density comparison at different body locations from walking (gray color lines) and running (black color lines) for an energy harvester with $\rho = 10\text{g/cm}^3$ and a Q factor of one.

Table 3.5: Available power for the average walking speed of 1.4 m/s (3.1 mph) and for the moderate running speed of 2.2 m/s (5 mph) assuming 1 g mass and a Q factor of 1.

Body Location	Walking			Running		
	Forward Axis (mW)	Vertical Axis (mW)	Lateral Axis (mW)	Forward Axis (mW)	Vertical Axis (mW)	Lateral Axis (mW)
Ankle	2.5	0.7	0.3	6.8	4.3	0.05
Knee	1	0.4	0.3	1.8	2.5	0.03
Hip	0.15	0.3	0.08	0.4	1.5	0.2
Chest	0.1	0.1	0.03	0.3	1.3	0.3
Wrist	0.04	0.06	0.02	1.5	0.8	0.2
Elbow	0.04	0.05	0.01	0.3	0.8	0.2
Shoulder	0.04	0.04	0.01	0.5	0.8	0.3
Side of Head	0.03	0.07	0.01	0.1	0.6	0.08
Back of Head	0.03	0.02	0.02	0.1	0.7	0.08

Table 3.6: Available power density for the average walking speed of 1.4 m/s (3.1 mph) and for the moderate running speed of 2.2 m/s (5 mph) assuming a density of 10 g/cm³ a Q factor of 1.

Body Location	Walking			Running		
	Forward Axis (mW/cm ³)	Vertical Axis (mW/cm ³)	Lateral Axis (mW/cm ³)	Forward Axis (mW/cm ³)	Vertical Axis (mW/cm ³)	Lateral Axis (mW/cm ³)
Ankle	25	6.8	3	68	43	0.5
Knee	10	4	3	18	25	0.3
Hip	1.5	2.5	0.8	4	15	2
Chest	1	1	0.3	2.5	13	2.5
Wrist	0.4	0.6	0.2	15	8	2
Elbow	0.4	0.5	0.1	3	8	1.5
Shoulder	0.4	0.4	0.1	5	8	3
Side of Head	0.3	0.7	0.1	1	6	0.8
Back of Head	0.3	0.2	0.2	1	7	0.8

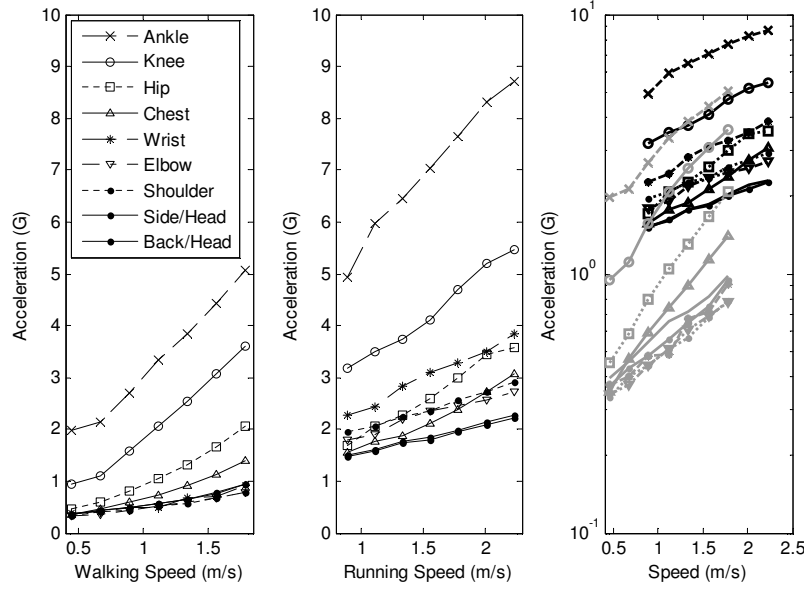


Figure 3.26: Resultant acceleration in G for the walking and running tests ($1 G = 9.8 m/s^2$). The last image includes a comparison between walking (gray color lines) and running (black color lines).

(Figures 3.11, 3.12, and 3.13). As a result, this also increases the magnitudes of the energetic figure of merit, the available power ($m = 1 g$ and $Q = 1$), and the available power density ($\rho = 10 g/cm^3$ and $Q = 1$), as shown in Figures 3.27, 3.28, and 3.29.

Tables 3.7, 3.8, and 3.9 summarize the energetic figure of merit, available power (assuming $m = 1 g$ and $Q = 1$), and available power density (assuming $\rho = 10 g/cm^3$ and $Q = 1$) for the average walking speed of $1.4 m/s$ (~ 3.1 mph) and the moderate running speed of $2.2 m/s$ (5 mph) at the different body locations. Thus, if a generator employs the resultant acceleration, the available power increases significantly when compared to one-axis linear generators. Using average walking and assuming a generator with $m = 1 g$ and $Q = 1$, the available power is estimated to be over $0.1 mW$ for most body locations, while the ankle and knee locations can have power levels over $1 mW$. While running, the power output increases to over $1 mW$ for most of the body locations. Available power density is found to be over $0.5 mW/cm^3$ for most body locations while walking (ankle and knee present higher magnitudes). Running gives power density levels over $3 mW/cm^3$ for all body locations (the ankle location can be over $100 mW/cm^3$). Some biomedical devices have power requirements similar to what is theoretically available (Cardiac pacemakers require an average of $0.1 mW$, while hearing aids consume around $0.05 mW$ [29]). Therefore, some biomedical applications can benefit directly from this energy harvesting approach for their power

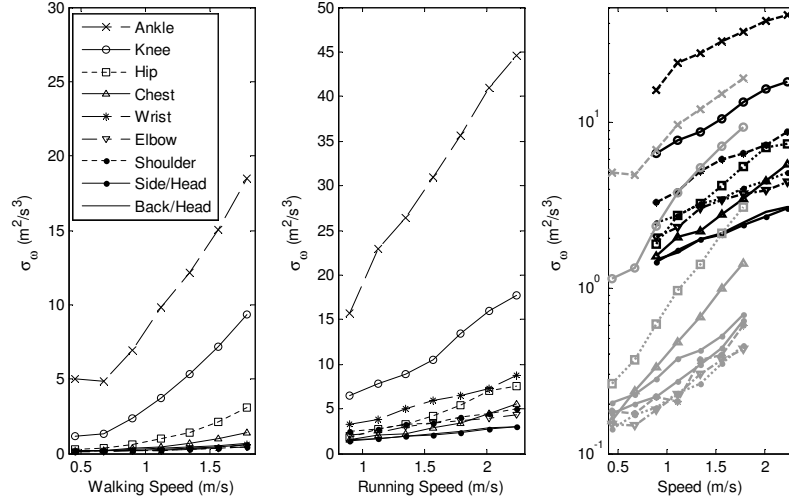


Figure 3.27: Resultant figure of merit σ_ω for the walking and running tests. The last image includes a comparison between walking (gray color lines) and running (black color lines).

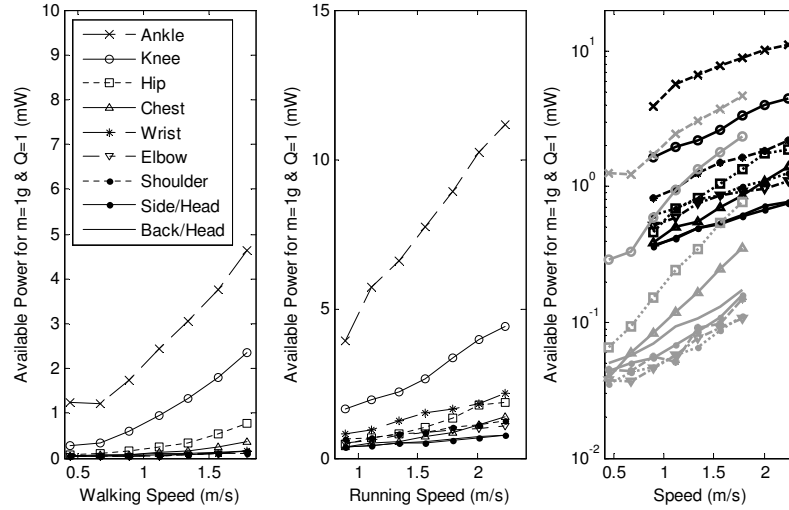


Figure 3.28: Available power from the resultant acceleration for the walking and running tests. The last image includes a comparison between walking (gray color lines) and running (black color lines).

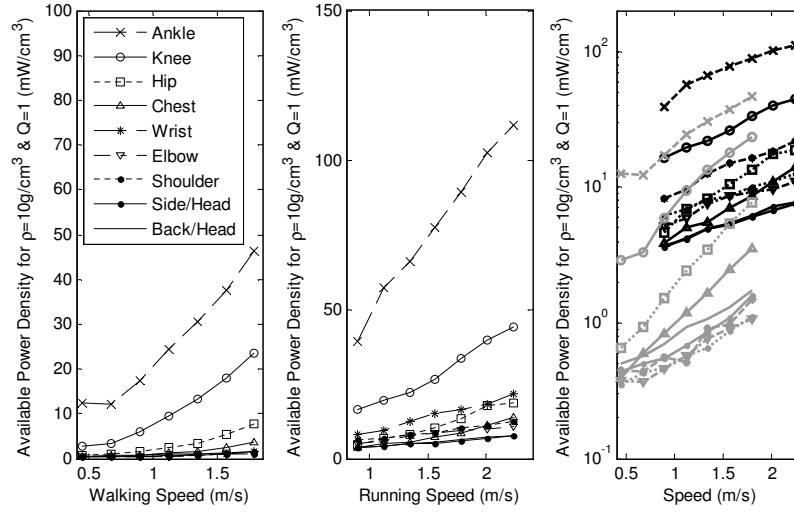


Figure 3.29: Available power density from the resultant acceleration for the walking and running tests. The last image includes a comparison between walking (gray color lines) and running (black color lines).

Table 3.7: Energetic figure of merit, σ_ω , for the resultant acceleration at the average walking speed of 1.4 m/s (3.1 mph) and in parentheses for the moderate running speed of 2.2 m/s (5 mph).

Body Location	σ_ω from Walking (m ² /s ³)	σ_ω from Running (m ² /s ³)
Ankle	13	45
Knee	6	18
Hip	1.6	7.5
Chest	0.8	5.5
Wrist	0.4	9
Elbow	0.3	4.5
Shoulder	0.3	5
Side of the Head	0.4	3
Back of the Head	0.4	3

Table 3.8: Available power for the resultant acceleration at the average walking speed of 1.4 m/s (3.1 mph) and in parentheses for the moderate running speed of 2.2 m/s (5 mph), assuming $m = 1\text{ g}$ and $Q = 1$.

Body Location	Available Power from Walking (mW)	Available Power from Running (mW)
Ankle	3.2	11
Knee	1.5	4.5
Hip	0.4	1.9
Chest	0.2	1.4
Wrist	0.1	2.2
Elbow	0.07	1.1
Shoulder	0.07	1.2
Side of the Head	0.1	0.8
Back of the Head	0.1	0.8

Table 3.9: Available power density for the resultant acceleration at the average walking speed of 1.4 m/s (3.1 mph) and in parentheses for the moderate running speed of 2.2 m/s (5 mph), assuming $\rho = 10\text{ g/cm}^3$ and $Q = 1$.

Body Location	Power Density from Walking (mW/cm ³)	Power Density from Running (mW/cm ³)
Ankle	3.3	110
Knee	15	45
Hip	4	19
Chest	2	14
Wrist	1	22
Elbow	0.7	11
Shoulder	0.7	12
Side of the Head	1	8
Back of the Head	1	8

source.

This approach is also found to be in agreement with the results presented by the suspended-load backpack generator from Rome et al [102]. This backpack used a 38 kg load that generated up to 7.4 W of power. Based on Eq. 6.4 and assuming $\sigma_\omega \sim 1$ (Table 3.4) and $Q \sim 1$ could provide a maximum power of 9.5 W. The difference between the reported and estimated value can be explained by the efficiency of the generator, and the actual Q and σ_ω values. As it could be expected, larger energy harvesters can produce a larger power output, thus generators can be sized according to the power required for implantable or portable electronics.

As a comparison, power can be estimated using the mechanical work W and the frequency f as

$$P = Wf \quad (3.22)$$

where the work W of a mass m along a distance d against the Earth's gravity g is $W = mgd$. Considering the average vertical displacement while walking to be 5 cm [102], the work done by a 1 g mass is ~ 0.5 mJ. Then, the power associated at a walking frequency of 2 Hz is ~ 1 mW, but only half of that can be converted into electricity [122]. This result is at the same power level as the one presented in Table 3.5. In summary, a 1 g proof mass generator traveling 5 cm at 2 Hz has an available power content of ~ 0.5 mW. Thus a larger device would produce more than 0.5 mW, and a smaller energy harvester would produce only a fraction of that.

The power evaluation was elaborated assuming a proof mass of 1 g, a proof mass density of 10 g/cm³, and a Q factor of 1. A larger proof mass or material density provides a larger power output, but power generation is also limited by the Q factor and the energetic figure of merit σ_ω . The Q factor for a linear generator is also the ratio of the proof mass displacement to the source displacement, as mentioned in Eq. 3.13. A Q factor of 1 implies that the proof mass translation is equal in magnitude to the external displacement. A 5 cm vertical displacement for a generator does not seem unreasonable for a Q of 1, but having a Q of one for a 1 m stride distance in a cm-sized generator is unrealistic. A linear generator would have a reduced Q factor in such conditions since it has limited displacement, but a rotational device could have larger Q factors since it does not have that constraint. Therefore, actual power output can differ from that summarized in Tables 3.8 and 3.9, and Figures 3.28 and 3.29.

3.6 Power Generation Summary

Energy generation is summarized for walking conditions of older (over 65 years old) and younger (14-64 years old) pedestrians in Figs. 3.30, 3.31, 3.32, and 3.33. Average walking speed for older pedestrians was reported as 1.3 m/s with the 15th-percentile

as 0.97 m/s, while for average walking speed was described as 1.5 m/s with the 15th-percentile as 1.25 m/s. [56]. In the figures, darker-shaded area represents the 15th-percentile up to the average walking speeds for older pedestrians, while the clear-shaded area includes from the 15th-percentile up to the average walking speeds for younger pedestrians. Although the treadmill test included the average walking speeds for older pedestrians, it might not accurately represent this segment of the population.

Fig. 3.30, 3.31, and 3.32 represent the available power density for generators moving along the vertical, forward, and lateral axes, respectively. Fig. 3.33 shows the available power density for a generator combining the vertical and forward axes. The available power density from walking is mainly concentrated in two distinctive zones, one for lower body locations (ankle, knee, and hip) and the other for the upper body locations (chest, wrist, elbow, shoulder, and head). For the vertical axis the available power density presented the largest values, from ~ 0.2 -1 mW/cm³ for the upper body and ~ 1 -10 mW/cm³ for the lower body. In contrast, the forward axis has three distinct regions with available power density values from ~ 0.1 -0.2 W/cm³ for the upper body (excluding the chest), from ~ 0.5 -1 mW/cm³ for the chest and hip, and from ~ 5 -20 mW/cm³ for the ankle and knee locations. The upper body locations for the lateral axis were found to have power densities with little change from ~ 0.1 -0.2 mW/cm³, while the leg locations (excluding the hip) were from ~ 2 -3 mW/cm³. When analyzing the available power density for the combined axes from Fig. 3.33, the upper body is found to offer from ~ 0.5 -1 mW/cm³, while the leg locations increase the power density as much as from ~ 1 -5 mW/cm³ for the hip, from ~ 6 -15 mW/cm³ for the knee, and from ~ 20 -40 mW/cm³.

These figures indicates that while walking at average speeds the upper body locations can provide power densities on the order of hundreds of μ W/cm³, while the leg locations can provide 10X higher power densities for linear generators. The analysis for the running test showed that the power density can be as high as 10X larger when compared against the same locations while walking (Fig. 3.25). However, actual available power can differ from the theoretical model. A combined axis generator should be able to produce as much as twice those values. Therefore, a generator design harnessing motion from two axes, or the rotational design found in self-winding wristwatches, can provide a better power output than a single axis design.

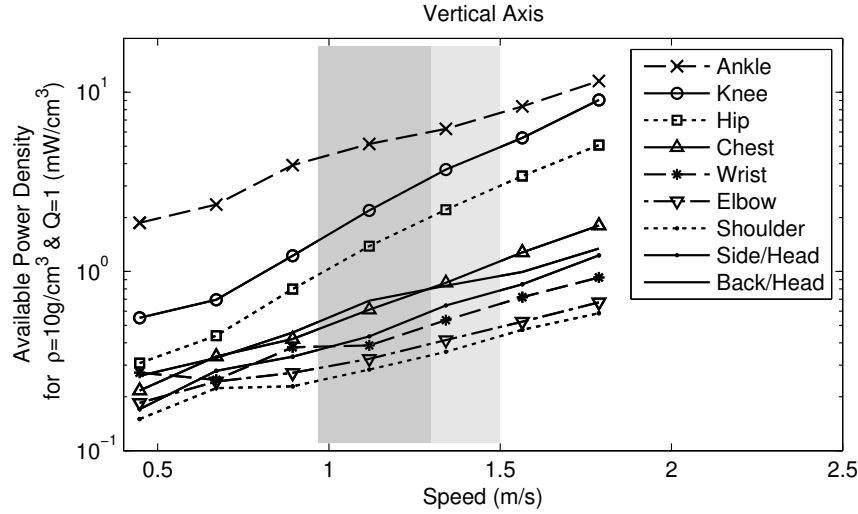


Figure 3.30: Available power density for average walking conditions along the vertical axis. Darker-shaded area represents the 15th-percentile up to the average walking speeds for older pedestrians (over 65 years old), while the clear-shaded area includes from the 15th-percentile up to the average walking speeds for younger pedestrians (14-64 years old). Average walking speeds of older and younger pedestrians from [56].

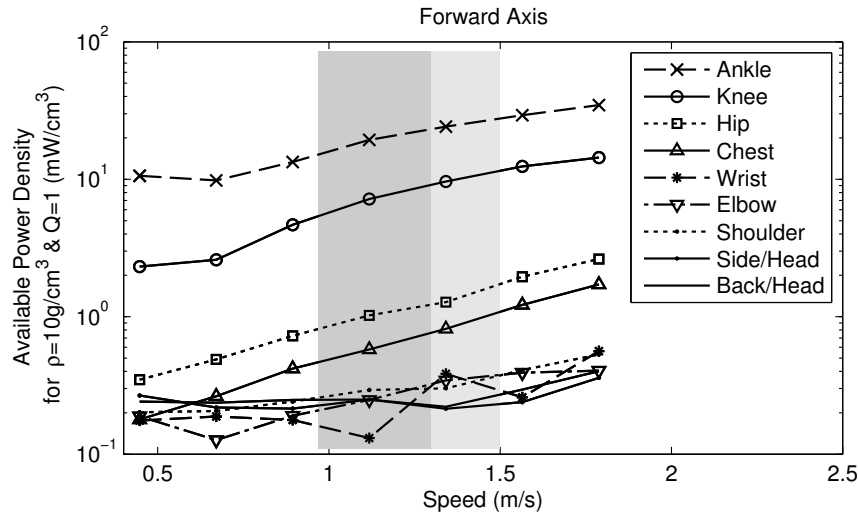


Figure 3.31: Available power density for average walking conditions along the forward axis. Darker-shaded area represents the 15th-percentile up to the average walking speeds for older pedestrians (over 65 years old), while the clear-shaded area includes from the 15th-percentile up to the average walking speeds for younger pedestrians (14-64 years old). Average walking speeds of older and younger pedestrians from [56].

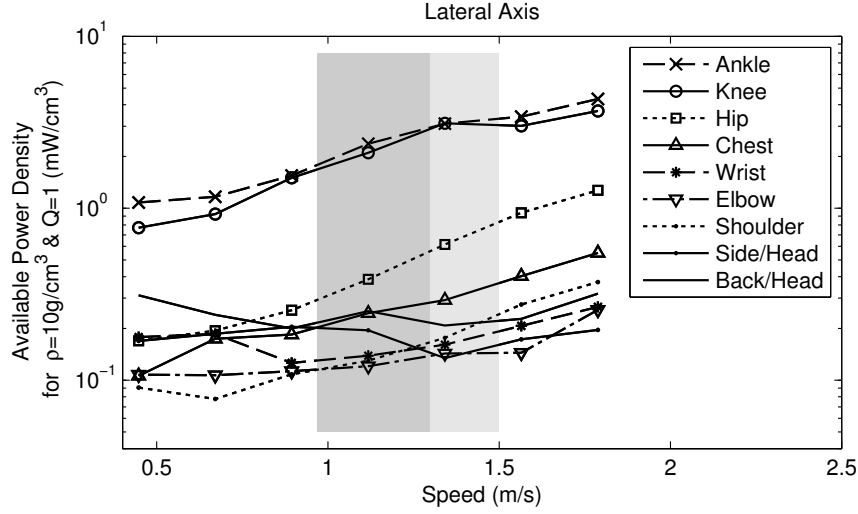


Figure 3.32: Available power density for average walking conditions along the lateral axis. Darker-shaded area represents the 15th-percentile up to the average walking speeds for older pedestrians (over 65 years old), while the clear-shaded area includes from the 15th-percentile up to the average walking speeds for younger pedestrians (14-64 years old). Average walking speeds of older and younger pedestrians from [56].

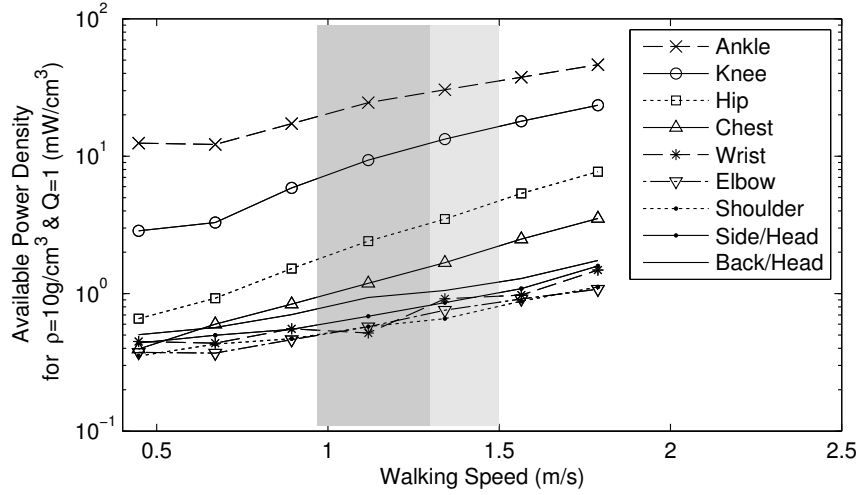


Figure 3.33: Available power density for average walking conditions along from the resultant acceleration from vertical and forward axes. Darker-shaded area represents the 15th-percentile up to the average walking speeds for older pedestrians (over 65 years old), while the clear-shaded area includes from the 15th-percentile up to the average walking speeds for younger pedestrians (14-64 years old). Average walking speeds of older and younger pedestrians from [56].

Chapter 4

Generator Design

4.1 Introduction

The design of kinetic energy harvesters for body motion is challenge because traditional generator architectures typically use the cantilever beam design, which is well-suited for high-frequency environments (>100 Hz) and small displacement applications (<1 mm). In addition, this type of generator relies on large quality (Q) factors that are tuned to a fixed frequency range. On the other hand, human activities are characterized by large amplitudes and low frequency content (<10 Hz). This kind of motion source makes it difficult to design a small generator that matches a person's broad frequency content while doing everyday activities (walking, jogging, office work, etc) with large Q -factors.

4.2 Design

The proposed design resembles the mechanism found in automatic self-winding wristwatches which is a proven design for powering them. In order to produce energy, this kind of input mechanism is connected to a small generator through the use of a gearbox. The gearbox is used to increase the rotational speed of the generator, similar to some electric self-winding wristwatches or large turbine for wind farms. To simplify the entire mechanism, sometimes the gearbox is omitted (as in small wind turbines) at the expense of having a larger generator (a larger number of magnets and coils). The size of the generator can be reduced by means of MEMS technology to a large number of magnets and coils in a reduced space for small applications at the meso-scale. Therefore, it seems natural to integrate the decades-old technology of self-winding wristwatches with recent MEMS-technology for some applications where the space is limited. In addition, some electric self-winding wristwatches are limited

by the cogging torque¹ (torque due to the interaction between the magnets on the rotor and the iron, or soft-magnetic material, on the stator). This reduces the sensitivity of the device, generating power only when there is enough energy to overcome this cogging torque.

Since wristwatch-based electromagnetic generators were found to provide large power densities from body motion (as described in Section. 2.5 on page 23) and generator designs harnessing motion from more than a single axis should provide a larger power output (last chapter, Section 3.6), then, the non-resonant planar rotational design presented here was determined to be satisfactory for body motion,

The proposed generator is composed of an eccentric weight rotor with multiple NdFeB permanent magnet (PM) pole-pairs and stacks of planar coils on the stator (ironless to avoid the cogging torque), as shown in the exploded view in Fig. 4.1. This eccentric rotor induces a voltage on the coil when it swings (or rotates) due to an external movement, a behavior akin to self-winding wristwatches. Although broad research has been carried out for energy harvesting activities; little has been presented for rotational generators that convert energy from human-based activities [103, 8, 12]. The advantages from this design are:

- *Pendular mechanism:* A rotational or pendular design is sensitive to a change of position or to an external motion if used as an electrical generator. In addition, planar coils can be used as the stator while permanent magnet materials can be accommodated in the rotor making a flat design. A rotational mechanism requires less traveling space than a linear design.
- *Planar geometry:* A planar design, such as the pendular mechanism, occupies less space and is suitable for portable devices and/or surgically implanted devices due to its low profile.
- *Electromagnetic transduction:* A rotational design is easier to implement with electromagnetic transduction. As evaluated from the Energy Harvesting Background Chapter, piezoelectric transduction uses the material deformation to induce a electrical potential which is difficult to achieve with an rotational architecture, and electrostatic energy generation produces a smaller amount of power. Planar coils and axially magnetized magnets are easier to implement for a planar architecture.
- *Planar coil:* A planar stator having planar coils are simpler to fabricate, less costly, and can be mass produced with intricate geometries using standard photolithography techniques. The proposed gear-shaped pattern is found suitable

¹Cogging torque is caused by be disruption of the magnetic circuit in a moving rotor by the variation of the energy stored in the magnet and armature.

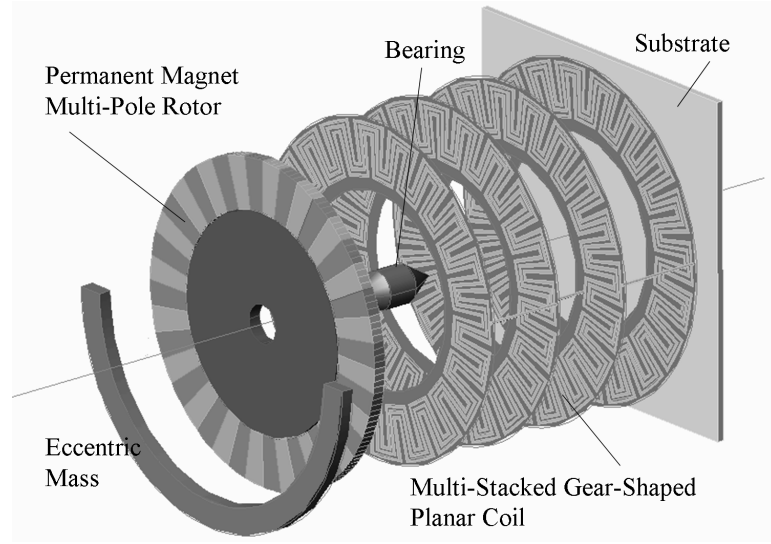


Figure 4.1: *Simplified schematic of the proposed design.*

to be elaborated with microfabrication technologies. The simplicity of this design makes it possible to fabricate coils by stacking several layers of flexible films. Although, planar coils can be stacked in order to achieve a better performance they have less wire-density as traditional wire-wound coils.

- *Iron-less stator:* Since the stator does not use a soft-magnetic material there is no cogging torque (due to the attractive force between the permanent magnet and the soft-magnetic material) while simplifying the coil fabrication process. This in addition increases the movement sensitivity of the pendular-mechanism since small changes in position from the external motion causes the generator to oscillate. However, a coreless design has a weaker magnetic field and larger leakage flux when compared against a design with a soft-magnetic material.

4.3 Induced Voltage Model

The modeling for the voltage simulation is based on the geometry of the coil area under one permanent magnet (PM) pole-pair. The coil pattern is based on a design resembling a gear shape. For simplicity, the number of coil sectors matches the number of PM pole-pairs, that is, a sector-shaped area corresponds to one PM pole-pair. This pattern is presented in Fig. 4.2a. This coil pattern has the added advantage, in contrast of the standard coil patter from Fig. 4.2b, of minimizing the electrical wiring to only two connection pads for electrical connections. This simplifies the fabrication process for stacking multiple coils while keeping a simple design.

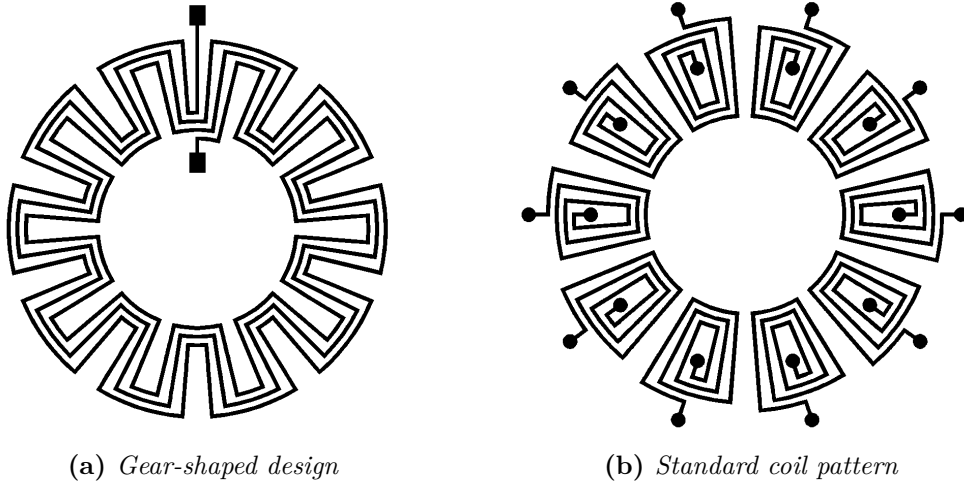


Figure 4.2: *Coil designs vs. contact pads.*

The model for the voltage modeling is based on the analysis of one coil segment under one PM pole-pair, as shown in Fig. 4.3. For instance, the analysis is elaborated for the coil segment $\overline{123456}$ (darker colored segment from Fig. 4.3). Current is induced on the coil segment $\overline{123456}$ when the generator oscillates (or rotates) with an angular velocity ω (rad/s) under a magnetic flux distribution B_z (T). Using Fleming's right-hand rule (for generators) the current direction is depicted as shown in the diagram. Since segments $\overline{12}$, $\overline{34}$, and $\overline{56}$ are parallel to the rotor tangential velocity there is no voltage induced on them. Thus, voltage is induced only on the radial coil segments ($\overline{23}$ and $\overline{45}$) when the magnets from the rotor pass over the coil. This geometry also allows the coil to be designed with radial segments of equal length. Hence, the analysis of the radial segments $\overline{23}$ and $\overline{45}$ follows as

$$e = \oint \vec{v} \times \vec{B} \quad (4.1)$$

where the expression for a radial segment is

$$e_{ba} = \int_{r_a}^{r_b} (r\omega\hat{e}_t) \times (-B\hat{e}_z) \cdot (dr\hat{e}_r) \quad (4.2)$$

then, the induced voltage e_{32} and e_{54} are

$$e_{32} = \omega B \int_{r_2}^{r_3} r dr = -\frac{1}{2}\omega B_z (R_{max}^2 - r^2) \quad (4.3)$$

$$e_{54} = \omega B \int_{zr_4}^{r_5} r dr = \frac{1}{2} \omega B_z (r^2 - R_{max}^2) = -\frac{1}{2} \omega B_z (R_{max}^2 - r^2) \quad (4.4)$$

the induced voltage in the coil segment $\overline{123456}$ becomes then $e_{61} = e_{32} + e_{54}$

$$e_{61} = -\omega B_z (R_{max}^2 - r^2) \quad (4.5)$$

where $R_{max} = r + l + \delta(N - 1) = r + d$, and N is the number of coil turns, therefore

$$R_{max}^2 - r^2 = (r + d)^2 - r^2 = d^2 + 2dr \quad (4.6)$$

for the previous loop ($N=2$)

$$(R_{max} - \delta)^2 - (r - \delta)^2 = (r + d - \delta)^2 - (r - \delta)^2 = d^2 + 2d(r - \delta) \quad (4.7)$$

thus, for the loop N

$$(R_{max} - (N - 1)\delta)^2 - (r - (N - 1)\delta)^2 = d^2 + 2d(r - (N - 1)\delta) \quad (4.8)$$

The induced voltage for the coil sector area having N turns follows as $e = e_1 + e_2 + \dots + e_N$

$$\begin{aligned} e_1 &= -\omega B_z [d^2 + 2dr] \\ e_2 &= -\omega B_z [d^2 + 2d(r - \delta)] \\ &\vdots \\ e_N &= -\omega B_z [d^2 + 2d(r - (N - 1)\delta)] \end{aligned} \quad (4.9)$$

$$e = -\omega B_z [d^2 + 2dr + d^2 + 2dr - 2d\delta + \dots + d^2 + 2dr - 2d(N - 1)\delta] \quad (4.10)$$

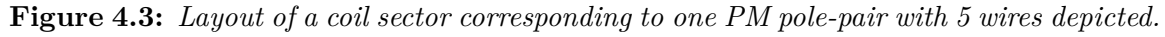
$$e = -\omega B_z [Nd^2 + 2Ndr - 2d\delta - \dots - 2d(N - 1)\delta] \quad (4.11)$$

$$e = -\omega B_z [Nd^2 + 2Ndr - 2d\delta(1 + 2 + \dots + (N - 1))] \quad (4.12)$$

using the triangular number² definition

$$T_n = 1 + 2 + 3 + \dots + (n - 1) + n = \frac{n(n + 1)}{2} \quad (4.13)$$

²A triangular number is a number that can be represented in the form of a triangular grid of dots where the first row contains a single point and each subsequent row contains one more point than the previous one.


$$e = -\omega B_z \left[Nd^2 + 2Ndr - 2d\delta \left(\frac{(N-1)N}{2} \right) \right] \quad (4.14)$$

Then, the induced voltage expression for p pole-pairs of permanent magnets and L number of coil layers finally become

A simpler analysis corresponds to a coil design where the magnets only cover the radial segments segments of the coil which have equal lengths, as shown in Fig. 4.4. For instance, modifying Eq. 4.5 to include the N turns, the p pole-pairs, and the L number of coil layers leads to this expression

Therefore, from Eq. 4.16 or Eq. 4.17 the induced voltage will be proportional to the angular speed, the magnetic field, the number of pole-pairs, the number of turns per coil, the number of stacked coil layers, and the radial segment length. The

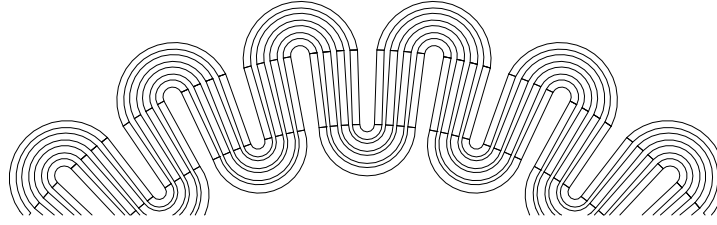


Figure 4.4: *Diagram of the simplified coil design.*

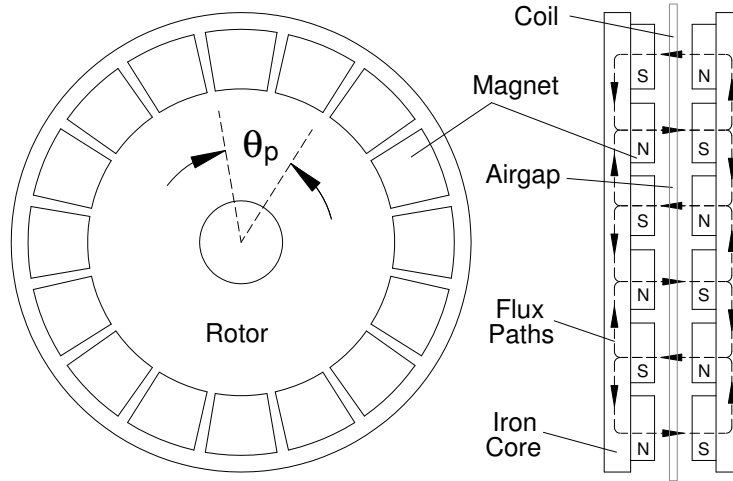


Figure 4.5: *Axial flux permanent magnet (AFPM) machine topology.*

following sections will analyze the magnetic field modeling, the kinematics of the generator, and the coil geometry to optimize the induced voltage generation.

4.3.1 Magnetic Field Model

This magnetic flux model analysis is based on the axial flux permanent magnet (AFPM) machine design with ironless stator at the macro scale. This design is used to obtain a relatively large magnetic flux in machines with large air gaps [62]. Fig. 4.5 shows the topology and distribution of the magnetic flux in such a design. One advantage of this approach is the shorter axial length for planar machines, where designs can be stacked for a higher power delivery. Another advantage is the elimination of the cogging torque since the stator is ironless, increasing the sensitivity of the generator to external motion sources.

The simplified model for the magnetic flux distribution using a single rotor, as shown in Fig. 4.6, represents one pole-pair of permanent magnets on top of a single

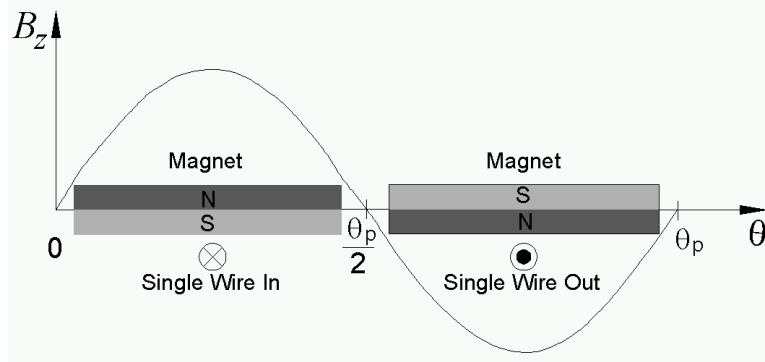


Figure 4.6: Magnetic flux distribution for a single wire and one pole-pair under a sinusoidal field. The image represents a lateral view of a permanent magnet pole-pair over a perpendicular wire loop for one pole-pair angle θ_p . The sinusoidal shape describes the distribution of the magnetic field.

wire loop (or turn coil). Pole-pair refers to a set of two magnets with opposing orientations of magnetic poles. A sinusoidal distribution for the magnetic flux (Fig. 4.6) in the air gap has been assumed for the modeling as suggested by [51, 62, 140, 141] since the waveform for a similar machines was found to be quasi-sinusoidal. The pole-pair angle θ_p refers to the angular distribution of one permanent magnet pole-pair as $\theta_p = 360^\circ/p$, where p is the number of pole-pairs.

Therefore, the axial distribution of the magnetic flux can be represented by this model

$$B_z = B_r \sin(p\theta(t)) \quad (4.18)$$

where B_r is the remanent magnetization, or magnetic field of the magnets measured in Teslas (T), p is the number of pole-pairs, and $\theta_i(t)$ is the angular position of the generator. Eq. 4.18 shows that the magnetic flux distribution is position dependent.

In order to understand the spatial distribution of the magnetic flux, finite element analysis (FEA) simulations using ANSYS were performed for several permanent magnet (PM) arrangements. A 3D model of the magnetic flux was produced for pole-pairs composed of discrete PM (2x1x1 mm) and for a sector-shaped PM. The modeling was performed for 20 pole-pairs (40 individual magnets for the discrete case), with a mean radius of 11 mm, and for single and double rotor (single and double permanent magnet layers). NdFeB (N50 Grade) permanent magnets were used as these were available (1x1x1 mm). Fig. 4.7 shows the results at a distance of 0.5 mm over the surface of the PM for one-rotor configuration with a maximum magnetic flux of 0.25 T (and in between 0.08-0.2 T for most of the area). In contrast, a two-rotor arrangement of discrete PM provides a 100% increase in magnetic flux (0.5 T peak, and between 0.17-0.39 T for most of the area) in between layers separated by 1mm (at a point

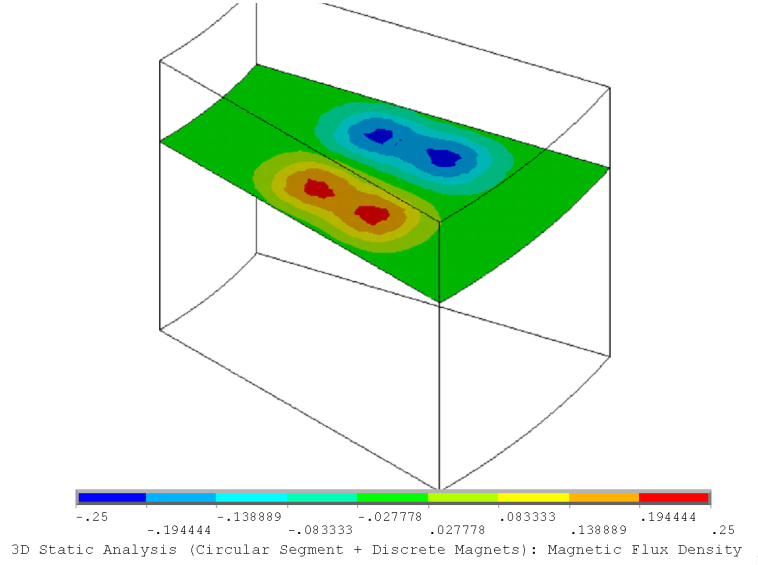


Figure 4.7: *Magnetic field distribution (Teslas) for a one-rotor design at a distance located at 0.5 mm over the surface for one pole-pair arrangement (two discrete permanent magnets, 2x1x1 mm).*

located 0.5 mm in between the rotors where the planar coil is to be situated). The one-rotor sector-shaped PM area shows that it can provide a maximum flux density of 0.3 T, while a two-rotor configuration reaches up to 0.6 T. Hence, the 3D modeling reveals that if a sector-shaped PM is used, a 20% increase in magnetic flux can be expected when compared to the discrete PM.

Fig. 4.11 shows the result of modeling the magnetic flux distribution at a point located 0.5 mm over the magnet surface for a one-rotor sector-shaped PM along the perimeter of 11 mm radius arc. The vertical component of the magnetic flux is seen with a sinusoidal shape as suggested previously for similar AFPM machines in [51, 62, 140, 141].

In summary, a two-rotor design separated by 1 mm provides twice the magnetic field in between the rotors (at a distance of 0.5 mm) than the magnetic field at a distance of 0.5 mm for one-rotor design. A rotor design that uses sector-shaped areas for the permanent magnets offers 20% higher magnetic field than a rotor design made of prismatic magnetic pieces. Although this model does not include leakage flux or field fringing effects due to adjacent magnets, it provides a clear distinction between the use of a single and or dual rotor and the difference when using a sector shaped magnetic area as opposed to prismatic-shaped magnetic materials.

Therefore, a generator with sector-shaped permanent magnets will have 20% increase in magnetic flux when compared to prismatic permanent magnets, and a double-rotor design should benefit of having twice the magnetic field of a single-rotor

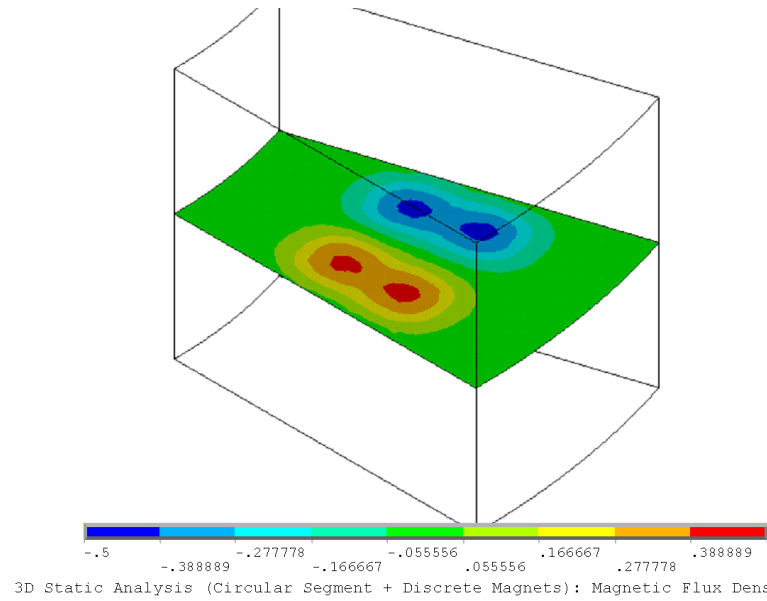


Figure 4.8: Magnetic field distribution (Teslas) in between a two-rotor design separated by 1 mm for one pole-pair arrangement (two discrete PM, 2x1x1 mm).

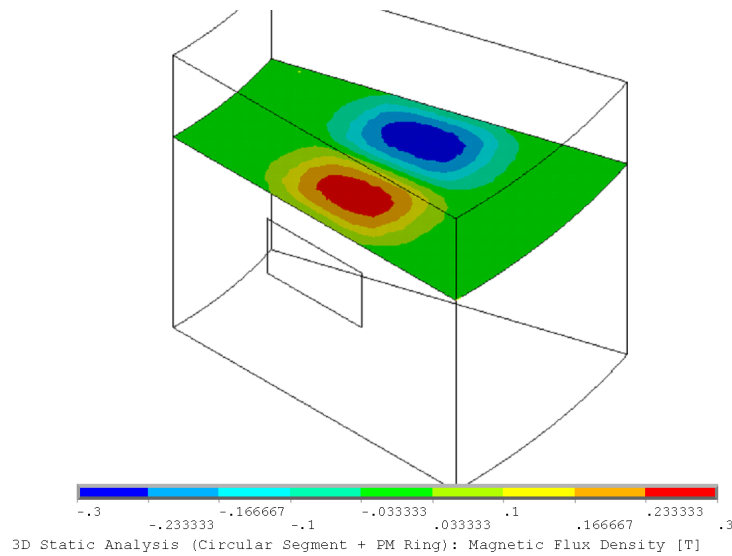


Figure 4.9: Magnetic field distribution (Teslas) for a one-rotor design at a point located at 0.5 mm over the surface for one pole-pair sector-shaped area.

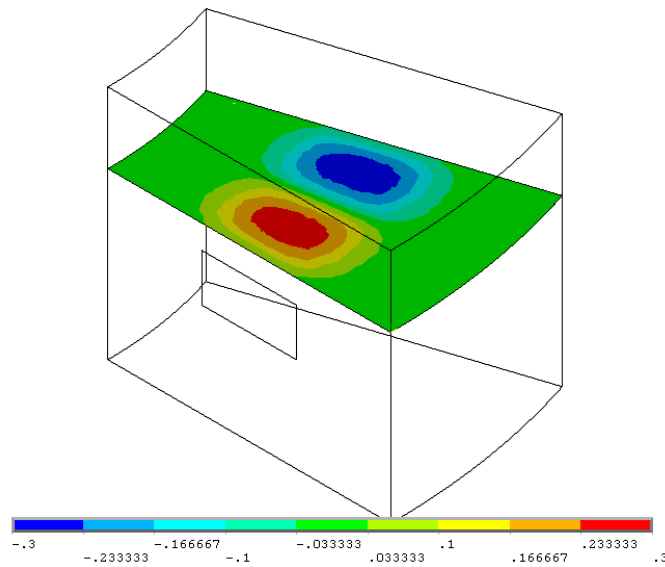


Figure 4.10: Magnetic field distribution (Teslas) in between a two-rotor design separated by 1 mm for one pole-pair sector-shaped area.

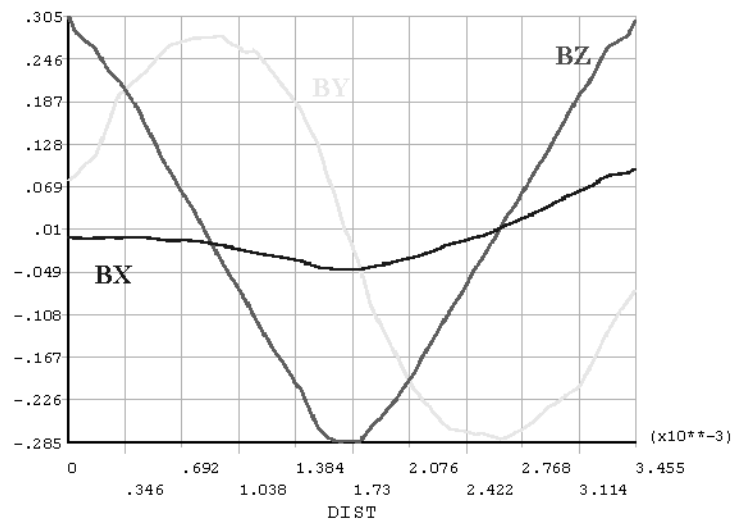


Figure 4.11: Magnetic field distribution at 0.5 mm over one-rotor design of a sector-shaped PM and 11 mm of radius. The vertical axis is the magnetic field in Teslas while the horizontal axis is the distance along the middle region in mm.

design for twice the induced voltage, according to the Eq. 4.16 or Eq. 4.17.

4.3.2 Generator Kinematics

The proposed generator has a mechanism that resembles an oscillating pendulum. While the mathematics of pendulums can be quite complex, some assumptions can be made to simplify the modeling. For example, a simple pendulum is an ideal model where a pendulum is assumed to be composed of a bob (proof mass) that is connected to a massless rod or cord, and there is no friction while in motion. From Fig. 4.12 and from Newton's second law, the pendulum equation can be written as $F = ma = -mg \sin\theta$ (where m is the mass, and g is the acceleration due to gravity, and θ is the angular position). Considering the relation between the angle θ and the arc length s ($s = l\theta$), where $v = ds/dt = l d\theta/dt$, and $a = d^2s/dt^2 = l d^2\theta/dt^2$, this results in

$$-mg \sin\theta = ml \frac{d^2\theta}{dt^2} \quad (4.19)$$

as the equation of motion, which can also be rewritten as

$$\frac{d^2\theta}{dt^2} + \frac{g}{l} \sin\theta = 0 \quad (4.20)$$

For the conservation of energy for this ideal system, the potential energy ($\Delta U = mgh$) must equal the kinetic energy ($\Delta K = 1/2mv^2$). Then, $1/2mv^2 = mgh$ or

$$v = \sqrt{2gh} = l d\theta/dt \quad (4.21)$$

From Fig. 4.12 $h = y_1 - y_0 = l(\cos\theta - \cos\theta_0)$, thus, when replacing h in the previous equation leads to

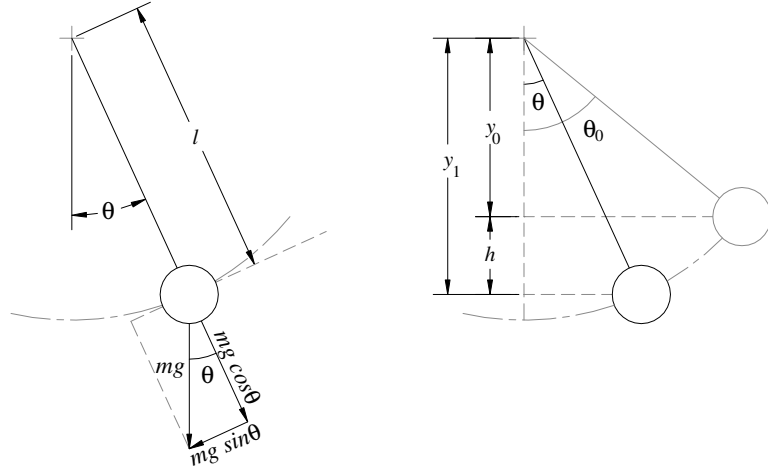
$$\frac{d\theta}{dt} = \sqrt{\frac{2g}{l} (\cos\theta - \cos\theta_0)} \quad (4.22)$$

The solution for the Eq. 4.22 is not straightforward, but if using the traditional approach of the small angle approximation ($\theta \ll 1$ or $\sin\theta \approx \theta$), the solution becomes

$$\theta(t) = \theta_0 \cos\left(\sqrt{\frac{g}{l}}t\right) \quad (4.23)$$

where the natural frequency for the ideal pendulum (ω_0) is expressed as the term $\sqrt{g/l}$, with units of rad/sec, and of period T in sec as

$$T_0 = 2\pi\sqrt{l/g} \quad (4.24)$$

**Figure 4.12:** *Ideal Pendulum.*

The proposed generator, however, does not behave as an ideal pendulum. Real operation has a damping component (due to friction and energy harvesting), forced oscillation (due to external forces), as well as large amplitude oscillations and non-harmonic content if used for body motion or other high energetic energy sources.

The modeling of a compound (real or physical) pendulum still gives insight about the kinematics. To estimate the induced voltage for an electrical generator, the angular speed must be known. Therefore, the kinematic analysis will help to determine the best parameters for its design.

A compound pendulum can be used as the model for an arbitrarily-shaped pendulum. The natural frequency for a compound pendulum is

$$\omega_0 = \sqrt{(mgL)/I} \quad (4.25)$$

where L is the distance from the pivot to the center of mass, and I is the moment of inertia.

The simplest case of a damped harmonic oscillator resembles partially the pendulum behavior. The equation that represents a damped harmonic oscillator is

$$\frac{d^2x}{dt^2} + 2\zeta\omega_0\frac{dx}{dt} + \omega_0^2x = 0 \quad (4.26)$$

where ω_0 is the undamped angular frequency of the system with mass m , and ζ is the damping ratio ($\zeta = c/(2m\omega_0)$). The underdamped case ($0 \leq \zeta < 1$) has the solution [95]

$$x(t) = e^{-\zeta\omega_0 t} [A \cos(\omega_d t) + B \sin(\omega_d t)] \quad (4.27)$$

where ω_d is the natural damped frequency ($\omega_d = \omega_0\sqrt{1-\zeta^2}$), and A and B are determined by the initial conditions as $A = x(0)$ and $(\zeta\omega_0x(0) + \dot{x}(0))/\omega_d$.

One of the main differences between the ideal pendulum (linear model) and a large amplitude oscillating pendulum (nonlinear model) is the frequency variation. While for the ideal pendulum (small amplitude oscillations) the period is constant (constant ω_0) a pendulum under large amplitude oscillations has a period that increases with increasing amplitude (variable ω). Re-writing Eq. 4.22, as explained by [9], produces

$$\frac{dt}{d\theta} = \frac{1}{\sqrt{2}}\sqrt{\frac{l}{g}} \frac{1}{\sqrt{\cos\theta - \cos\theta_0}} \quad (4.28)$$

The solution for Eq. 4.29 is found after integrating over one complete cycle for

$$dt = \frac{1}{\sqrt{2}}\sqrt{\frac{l}{g}} \frac{1}{\sqrt{\cos\theta - \cos\theta_0}} d\theta \quad (4.29)$$

Since the pendulum period T oscillates through one complete cycle as $T = (\theta_0 \rightarrow 0^\circ \rightarrow -\theta_0 \rightarrow 0^\circ \rightarrow \theta_0)$, or using twice the half-cycle simplification as $T = 2(\theta_0 \rightarrow 0^\circ \rightarrow -\theta_0)$, or by further simplification using four times the quarter-cycle as $T = 4(\theta_0 \rightarrow 0^\circ)$. Then, the integration of Eq. 4.29 is performed over four times the quarter of a period, leading to

$$T = 4 \frac{1}{\sqrt{2}}\sqrt{\frac{l}{g}} \int_0^{\theta_0} \frac{1}{\sqrt{\cos\theta - \cos\theta_0}} d\theta \quad (4.30)$$

that can be rewritten in terms of elliptic function of the first kind (Jacobi's elliptic function) as

$$T = 4\sqrt{\frac{l}{g}} \int_0^{\pi/2} \frac{1}{\sqrt{1 - k^2 \sin^2(\varphi)}} d\varphi \quad (4.31)$$

or more simply as

$$T = 4\sqrt{\frac{l}{g}} F\left(\sin\frac{\theta_0}{2}, \frac{\pi}{2}\right) \quad (4.32)$$

where $F(k, \varphi)$ is the Legendre's elliptic function of the first kind. Using Eq. 4.24 in to Eq. 4.32 leads to the simplified expression

$$T = 4T_o F(k, \varphi) \quad (4.33)$$

Eq. 4.32 can also be expanded in a series as [9]

$$T = 2\pi\sqrt{\frac{l}{g}} \sum_{n=0}^{\infty} \left[\left(\frac{(2n)!}{(2^n \cdot n!)^2} \right)^2 \cdot \sin^{2n}\left(\frac{\theta_0}{2}\right) \right] \quad (4.34)$$

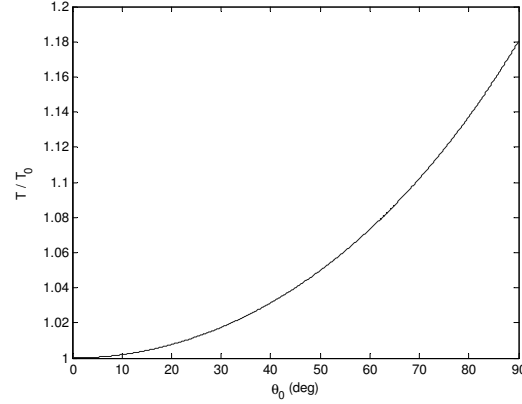


Figure 4.13: Variation of the pendulum period T (from large amplitude oscillations) against the period T_0 (from the small angle approximation).

Fig. 4.13 shows the deviation of T (for large amplitude oscillations) from T_0 (for the small amplitude pendulum, with constant Period T_0). At 30° the deviation is 1.7%, at 60° the deviation is 7.3%, but at 90° the deviation reaches 18%. Then, the pendulum period T can be up to 20% larger than the ideal pendulum period T_0 when modeling the kinematics of the generator as a compound pendulum³ (instead of an ideal pendulum with a concentrated mass) moving with amplitudes larger than 10° .

Since the proposed generator is intended to be used on the human body and subject to irregular motion it is difficult to anticipate the device performance. Then, a design approach based on basic kinematics is used to avoid the complex nonlinear behavior of a compound pendulum moving with large oscillations. Generators can be modeled with the proof mass released from an angle until the oscillations decay. For this, the angular speed for the design modeling can be determined using the damped harmonic oscillator approach from Eq. 4.27, while the induced voltage from Eq. 4.16 or Eq. 4.17 will have a shifting period as presented in Eq. 4.33. A generator configuration is presented in Table 4.1 for this model. The resonant frequency for this system was calculated as 2.4Hz.

The modeling of the angular position and angular velocity of the prototype based on the configuration from Table 4.1 is presented in Fig. 4.14a. This simplified model was based on Eq. 4.27. Fig. 4.14b shows the change in frequency for large amplitude oscillations. At a small initial amplitude angle the frequency is 2.41 Hz; at a 30° angle the frequency is 2.37 Hz (1.7% deviation); at a 60° angle the frequency is 2.24 Hz (7.3% deviation); and at a 90° angle the frequency changes to 2.04 Hz (18% deviation). At 45° there is only a 3.4% deviation, while a 5% change happens at around 55° , and

³A compound pendulum differs from the ideal pendulum model since it can be an arbitrarily shaped rigid body swinging by a pivot.

Table 4.1: *Generator configuration*

Element	Symbol	Value
Pole-Pairs	p	20
Coil Turns	N	4
Number of Layer	L	2
Coil Linewidth	w	200 μ m
Wire Radial Length	d	3.3mm
Generator Radius	R_{max}	12.7mm
Proof Mass	m	3.2g
Magnetic Field	B_r	0.2T

a 10% change happens at 75° . Therefore, when comparing the model against the experimental results some differences will be evident.

A model that describes accurately the large amplitude pendulum include three damping terms (quadratic, linear, and velocity independent terms) was presented by Squire [119] as

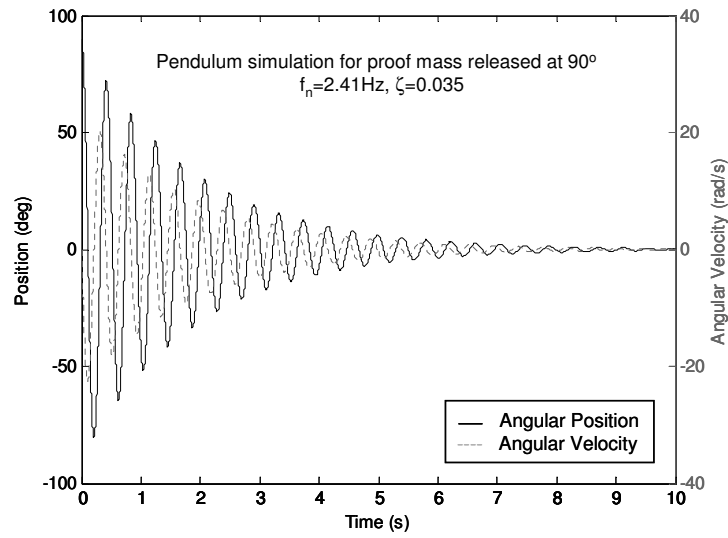
$$\frac{d^2\theta}{dt^2} + a \left| \frac{d\theta}{dt} \right| \frac{d\theta}{dt} + b \frac{d\theta}{dt} + c \operatorname{sign} \left(\frac{d\theta}{dt} \right) + \omega_0^2 \left(\theta - \frac{1}{6}\theta^3 \right) \quad (4.35)$$

where θ is the pendulum vertical angle, t is time, a (quadratic term), b (linear term), and c (velocity independent term) are the damping coefficients (other publications use β and γ such as $\beta = a$ and $2\gamma = b$), sign represents "the sign of", and $\omega_0^2 (\theta - 1/6\theta^3)$ is the restoring term (a simplification of $\omega_0^2 \sin(\theta)$ from Eq. 4.20). The linear and quadratic terms are associated respectively with the viscous (low Reynolds number) and turbulent (high Reynolds number) components of the damping force [40], while electromagnetic damping is also associated with the linear term [119]. The velocity independent term is included due to the dry friction (Coulomb damping) of the bearings [119].

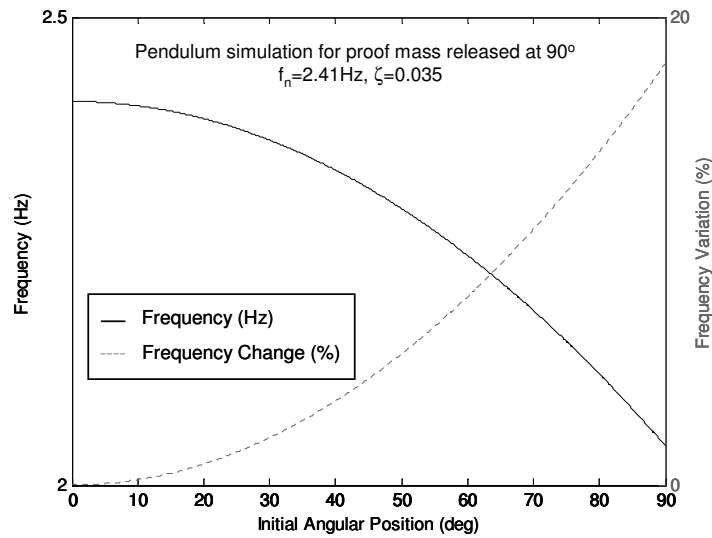
4.3.3 Coil Geometry

In order to determine the internal resistance for the power generation analysis the geometry needs to be determined. For this, the coil pattern shown in Fig. 4.3 depicting one pole-pair (sector-shaped) needs to be analyzed. For the arrangement provided in Fig. 4.3, the number of turns N is either constrained by the maximum number of turns that can be placed in a given space (maximum possible perimeter) or constrained by physical restrictions in the coil dimensions. One of these parameters is the arc length per pole-pair (C_{min}) as follows

$$C_{min} = 2(g/2 + \delta(N - 1) + w + g/2) = 2N\delta \quad (4.36)$$



(a) Angular position and angular velocity variation.



(b) Frequency variation.

Figure 4.14: Pendulum model for a proof mass released from a 90° angle.

where g is the gap distance, w is the linewidth dimension, δ is the minimal wire separation (linewidth + gap), and N the number of turns, as shown in Fig. 4.3. The perimeter length C ($C = pC_{min}$), where p is the number of pole-pairs, must match the perimeter of a minimum radius r_{min} , as $C = 2\pi r_{min}$, where $r_{min} = r - \delta(N_{max} - 1)$ where r is the base radius (Fig. 4.3) and N_{max} is the maximum number of turns per coil, the relation becomes

$$N_{max} = \frac{\pi(r + \delta)}{\delta(p + \pi)} \quad (4.37)$$

where the maximum number of turns N is the integer value of N_{max} .

The radial segments are designed to be of equal length, and each segment has a length equal to $l + \delta(N - 1)$, where N is the number of turns per coil per layer L . The total length of the radial segments l_r of one pole-pair is

$$l_r = 2(l + \delta(N - 1)) \quad (4.38)$$

The arc segments are calculated based on the angles α_i and γ_i ($\theta_p = \alpha_i + 2\gamma_i = \alpha_i + \beta_i$), where θ_p is the angle describe by one pole pair, and α and β follow the description from Fig. 4.3. The individual outer arc lengths ($C_{\alpha i}$) are calculated as $C_{\alpha i} = R_i \alpha_i$ while the individual inner arc length ($C_{\beta i}$) as $C_{\beta i} = R_i \beta_i$. The total length of the arc segments (l_c) of one pole-pair is

$$l_c = \left(\sum_{i=1}^N (C_{\alpha i} + C_{\beta i}) \right) \quad (4.39)$$

while the total wire length (L_{tot}) per p pole-pairs and L layers is $L_{tot} = pNL(L_r + l_c)$. Therefore, if the planar coil has a cross-sectional area A_{wire} with a wire resistivity ρ_{wire} in Ωm , then the total internal resistance of the planar coil (R_{coil}) in ohms is

$$R_{coil} = \frac{\rho_{wire} L_{tot}}{A_{wire}} \quad (4.40)$$

The geometry analysis for the coil in Fig. 4.4 assumes a circular coil-ends design. Since the radial segments are of equal magnitude, the estimation of the coil-ends arc segment lengths is needed to calculate the internal coil resistance. Following the Fig. 4.15 nomenclature, the length of an outer arc segment s_o is $s_o = \Omega_o r_o$, while the inner arc segment length s_i is $s_i = \theta_i r_i$. The angles are calculated as

$$\alpha = \tan^{-1} \left(\frac{r}{2\sqrt{R^2 - r^2/4}} \right) \quad (4.41)$$

$$\beta = \pi/2 - \alpha \quad (4.42)$$

$$\theta = \pi - 2\tan^{-1}(r/\sqrt{4R^2 - r^2}) \quad (4.43)$$

$$\Omega = \pi + 2\tan^{-1}(r/\sqrt{4R^2 - r^2}) \quad (4.44)$$

The variation of the inner radius r_i and outer radius r_o follow as

$$\begin{aligned} r_{i1} &= \delta - \delta/2 \\ r_{i2} &= r_{i1} + \delta = 2\delta - \delta/2 \\ &\vdots \\ r_{in} &= n\delta - \delta/2 \end{aligned} \quad (4.45)$$

while the outer radius expression follows the previous form as

$$r_{on} = n\delta_o - \delta_o/2 \quad (4.46)$$

but with an outer gap distance δ_o calculated as

$$\delta_o = s_{max}/(2N + 3) \quad (4.47)$$

where the s_{max} term was obtained from

$$s_{max} = \pi 2R/p \quad (4.48)$$

therefore, the arc-segment lengths for inner arcs (s_{in}) and outer arcs (s_{on}) are

$$s_{in} = \delta(n - 1/2)(\pi - 2\tan^{-1}(r/\sqrt{4R^2 - r^2})) \quad (4.49)$$

$$s_{on} = \delta_o(n - 1/2)(\pi + 2\tan^{-1}(r/\sqrt{4R^2 - r^2})) \quad (4.50)$$

while the total wire length (L_{tot}) per p pole-pairs and L layers is

$$L_{tot} = pL \left(2Nd + \sum (s_{in} + s_{on}) \right) \quad (4.51)$$

Coils can have different configurations for varying number of pole-pairs with the same number of radial segments and same overall dimension as shown in Fig. 4.16. A relatively large number of pole-pairs (PP) produces smaller coil-end lengths generating smaller electrical resistance, but at the expense of having smaller magnetic regions with a reduced magnetic field. On the other hand, a smaller number of pole-pairs suggests a larger magnetic region which provides larger magnetic gradients but at the expense of having larger electrical resistance, as shown schematically in Fig. 4.16.

Since voltage is only induced on the radial wire segments (perpendicular to the velocity component), there is an optimal radial wire length (or minimal permanent

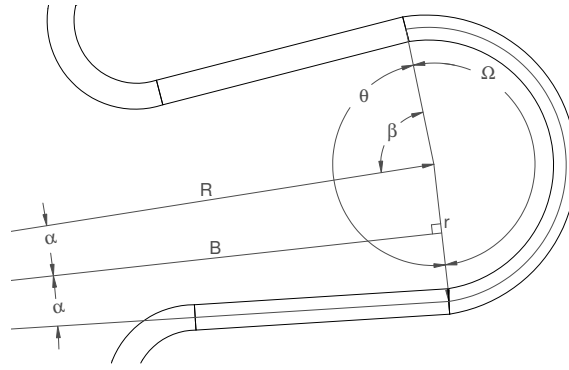
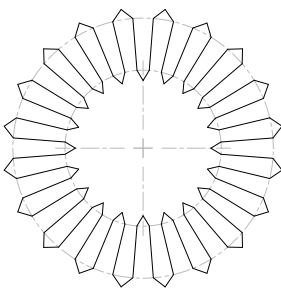
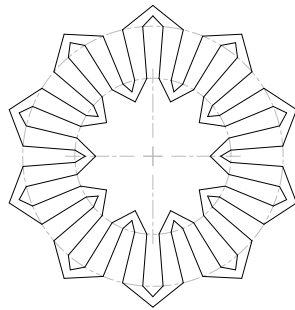


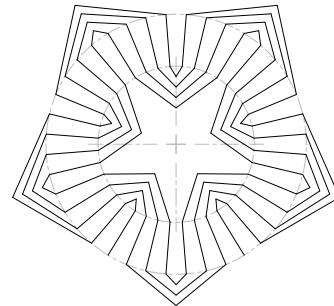
Figure 4.15: *Simplified coil design geometry.*



(a) 20 pole-pairs schematic.



(b) 10 pole-pairs schematic.



(c) 5 pole-pairs schematic.

Figure 4.16: *Comparison of coil designs with varying pole-pairs for the same number of radial wires (40 radial segments) and the same outer and inner diameter dimensions.*

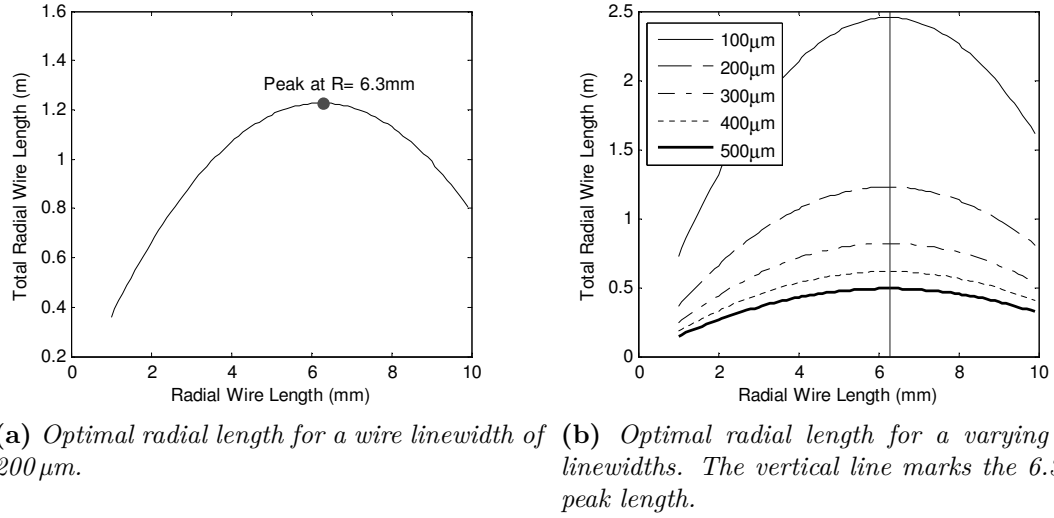


Figure 4.17: Optimal radial length for a generator with a diameter of 25 mm.

magnet radial length) that maximizes the length of radial wire segments for a given configuration. Fig. 4.17a depicts an example for a generator with a diameter of 25 mm. Fig. 4.17b shows that the wire linewidth does not influence the optimal radial length but it does affect the total radial wire length. Fig. 4.18 indicates the optimal radial length for several rotor diameters.

Based on the Eq. 4.51 and Eq. 4.40, the estimation of the coil resistances is presented in Fig. 4.19. From the figure, a larger number of pole-pairs leads to a smaller internal coil resistance. The ratio of coil-ends length to radial-wire length illustrates what was described in Fig. 4.16. The coil resistance increases almost exponentially for pole-pair numbers smaller than 10, or when the ratio of the end-

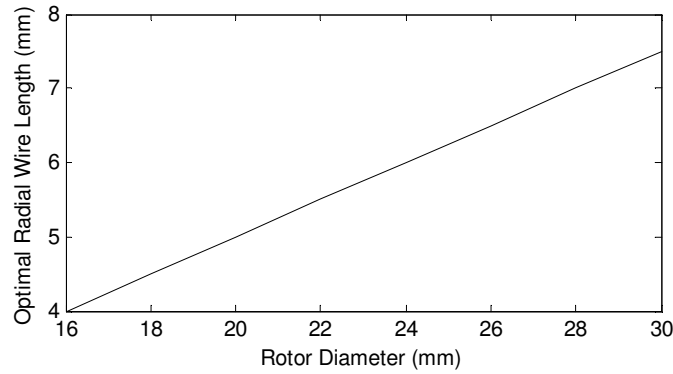


Figure 4.18: Optimal radial length as a function of rotor diameters.

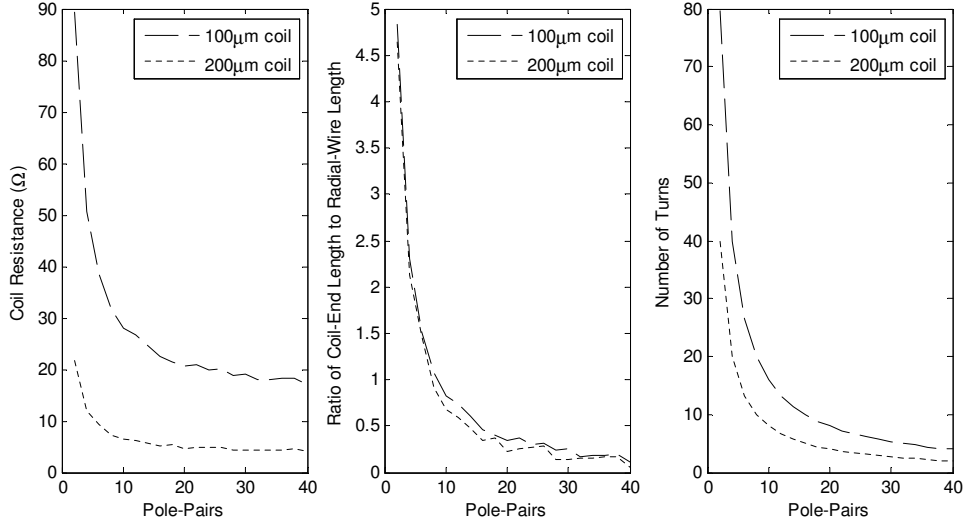


Figure 4.19: Variation of coil resistance, ratio of coil-end length to radial-wire length, and number of turns for varying pole-pair numbers of a 25 mm diameter generator with 5 mm long radial wires.

coils to radial-wires becomes larger than one. Thus, this ratio should be kept as small as possible to minimize coil internal resistance. Fig. 4.20 presents a comparison of several optimized dimensions with the one presented in Fig. 4.19. It can be observed that while the non-optimized generator gets the ratio of coil-end to radial-wire length close to 1, the optimized iterations are closer to 0.5 for the 10 pole-pair designs.

4.3.4 Power Evaluation

Power can be calculated from the diagram presented in Fig. 4.21 as a simplification of the generator circuit, the resulting current I can be found by Ohm's law as

$$I = \frac{V}{R_C + R_L} \quad (4.52)$$

where R_C is the coil electrical resistance and R_L is the load resistance, then, the power dissipated into the load R_L is equal to

$$P_L = I^2 R_L = \left(\frac{V}{R_C + R_L} \right)^2 R_L \quad (4.53)$$

The previous equation helps to determine the power produced by the generator. If applying the maximum power transfer theorem (which establishes that in order to

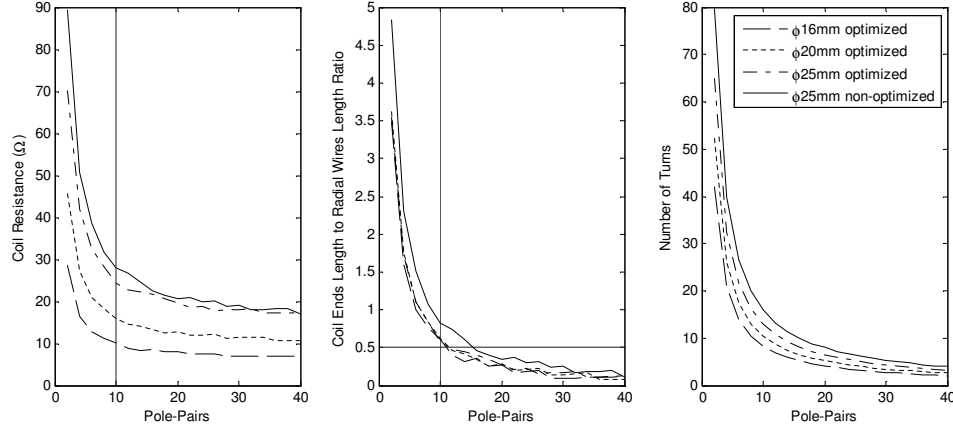


Figure 4.20: Variation of coil resistance, ratio of coil-end length to radial-wire length, and number of turns for varying pole-pair numbers of several optimized generator dimensions (Fig. 4.18) vs. a non-optimized generator (25mm diameter, 5mm radial wires) with $100\mu\text{m}$ wire linewidth.

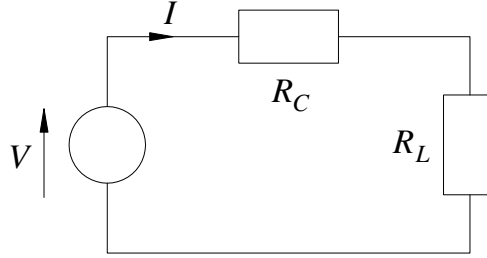


Figure 4.21: Generator diagram.

obtain maximum power the resistance of the load must match the internal resistance, this is $R_C = R_L$) then the power delivered is equal to $P_L = V^2/(4R_L)$.

Iron-cored permanent magnet machines (motors and generators) have core losses due to the flux pulsations between the magnets and the iron. Core-less designs, such as the one presented, do not suffer from this but are subject to eddy current losses. Eddy currents depend on the geometry of the wire cross-section and the magnetic flux variation [51]. A basic approach considers the eddy current loss (P_e) in a single round conductor with a transverse alternating field as [140]

$$P_e = \frac{\pi l d^4 B_{max}^2 \omega^2}{32\rho} \quad (4.54)$$

where l is the length, d the diameter, B_{max} is the peak value of the magnetic field,

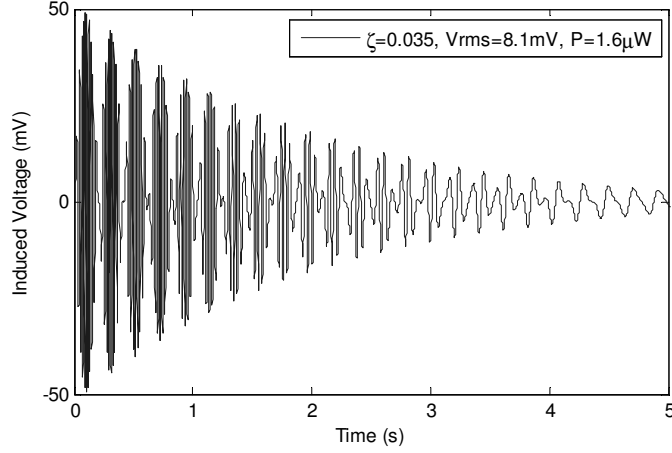


Figure 4.22: *Induced voltage for a proof mass released at a 90° angle with the generator configuration of Table 4.1.*

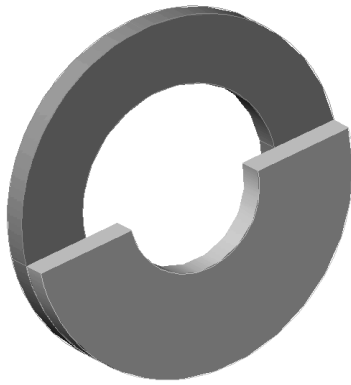
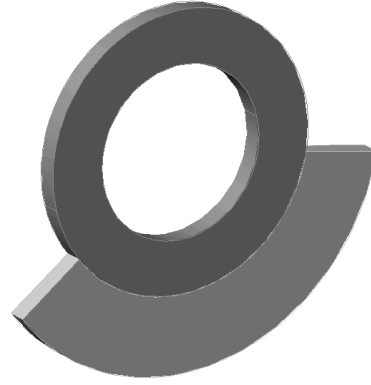
ω is the electrical angular frequency, and ρ is the conductor resistivity. However, a coreless winding arrangement with magnetic axial flux has a tangential component of flux density which can lead additional eddy-current loss [20]. Finite element analysis is usually performed in order to make a better estimation of the eddy current loss, as presented in [20, 140]. The estimation of this parameter will help to determine the performance of this generator design in operation. As stated in Eq. 4.54 reducing the diameter d (using a smaller wire) diminishes this loss for a given configuration, but at the expense of increasing the coil resistance.

4.3.5 Induced Voltage

Using the Eq. 4.16, the data from Table 4.1, and the model from Fig. 4.14 a model for a mass released at a 90° can be modeled as show in Fig. 4.22. The configuration given in Table 4.1 was also used to model the induced voltage for a 10-layer coil with varying wire linewidth and to estimate the power output assuming a matching load (Eq. 4.53). The results are summarized in Table 4.2. The $50\text{ }\mu\text{m}$ wire linewidth although providing a higher induced voltage has a higher internal coil resistance. The main advantage of the $50\text{ }\mu\text{m}$ wire linewidth over the other designs is the larger voltage output that makes it easier to use AC rectification for motion sources other than decaying oscillations from a 90° angle release. Therefore, planar coils should be fabricated with the smaller wire linewidth in order to induced a higher voltage.

Table 4.2: Modeling results for the induced voltage of a proof mass released at a 90° angle.

Coil Configuration	Induced Voltage (mVrms)	Power Output (μ W)
200 μ m linewidth, 10 layers	40.5	8.2
100 μ m linewidth, 10 layers	81	8.2
50 μ m linewidth, 10 layers	162	8.2

(a) *Stacked proof mass.*(b) *Protruded proof mass.***Figure 4.23:** Proof mass location.

4.4 Generator Sizing

Previous section found the optimal wire length for a given rotor diameter (as shown in Fig. 4.18) determines the rotor dimensions but not the proof mass size. Since the rotor is composed of two components, the multiple pole permanent magnet ring and the proof mass, an optimization of the dimensions is needed. Two basic geometries will be analyzed for the proof mass location on this generator, as shown in Fig. 4.24: placing the proof mass on top of the multi-pole (PM) ring or a protruding proof mass placed on the PM ring periphery. The proof mass diameter is the same as the PM ring diameter for the stacked design while the outer ring diameter is the inner proof mass diameter for the protruding design. Stacking the proof mass provides a smaller area but a thicker device, while a protruding mass allows for a thinner design but with a larger footprint. Therefore, the selection of the proof mass location and dimensions are critical for this design.

The generator dimensions are ultimately constrained by the pendulum frequency and pendulum torque. The generator frequency in Hz is based on the description of Eq. 4.25 as

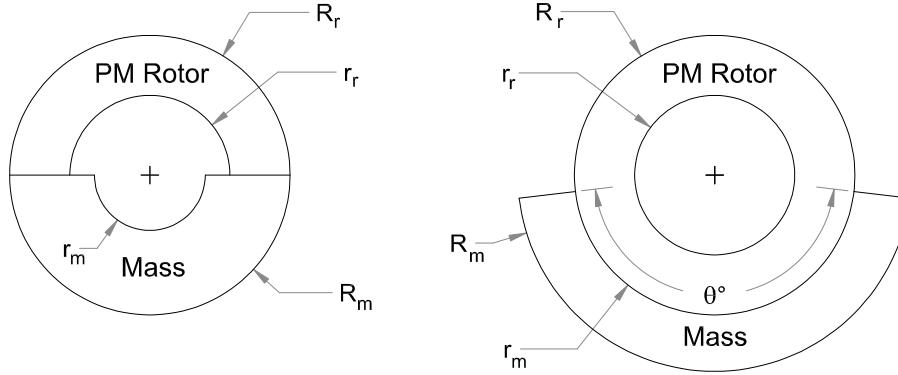


Figure 4.24: Proof mass location nomenclature.

$$f_0 = \frac{1}{2\pi} \sqrt{\frac{mgy_c}{I}} \quad (4.55)$$

where the mass of the system (m), the distance to the centroid of mass (y_c), and the moment of inertia (I) are intrinsically related to the dimensions and material properties. The power generation capabilities from rotational systems is related to the torque (τ) and the angular velocity (ω) as

$$P_g(t) = \tau(t) \cdot \omega(t) \quad (4.56)$$

Therefore, determining an operational frequency and available torque helps for the optimization of the generator. Using the nomenclature in Fig. 4.24 to evaluate the terms from Eq. 4.55 leads to the moment of inertia for the multi-pole PM ring (I_r) as

$$I_r = \frac{1}{2} \pi h_r \rho_r (R_r^4 - r_r^4) \quad (4.57)$$

where ρ indicates the material density, h the thickness, R_r is the external ring radius, and r_r is the internal ring radius (r subscripts are used for the ring while m subscripts are used for the proof mass). Similarly, the moment of inertia (I_m) for the stacked proof mass (4.23a) is

$$I_m = \frac{1}{4} \pi h_m \rho_m (R_m^4 - r_m^4) \quad (4.58)$$

whereas for the protruded mass (Fig. 4.23b) is

$$I_m = \frac{1}{4} h_m \rho_m \theta_m (R_m^4 - r_m^4) \quad (4.59)$$

where θ_m is the proof mass angle for a more general case. The total moment of inertia is

$$I = I_r + I_m \quad (4.60)$$

The multi-pole PM ring mass (m_r) is

$$m_r = \pi \rho_r h_r (R_r^2 - r_r^2) \quad (4.61)$$

while the proof mass (m_m) for the stacked design is

$$m_m = \frac{1}{2} \pi \rho_m h_m (R_m^2 - r_m^2) \quad (4.62)$$

and the proof mass for the protruded design is

$$m_m = \frac{1}{2} \rho_m h_m \theta_m (R_m^2 - r_m^2) \quad (4.63)$$

whereas, the total mass (m) is found as

$$m = m_r + m_m \quad (4.64)$$

The evaluation of the proof mass centroid distance (y_m) is needed to determine the center of mass of the compound system, this can be found for the stacked mass as

$$y_m = \frac{4}{3} \frac{1}{\pi} \left(\frac{R_m^3 - r_m^3}{R_m^2 - r_m^2} \right) \quad (4.65)$$

while for the protruding mass is

$$y_m = \frac{4}{3} \frac{1}{\theta_m} \sin \left(\frac{\theta_m}{2} \frac{R_m^3 - r_m^3}{R_m^2 - r_m^2} \right) \quad (4.66)$$

then, the center of mass of the system can be calculated from

$$y_c = \frac{y_m m_m}{m} \quad (4.67)$$

The above expressions can be replaced in Eq. 4.55 to determine the resonant frequency. The torque evaluation can be obtained from

$$\tau = m y_c \quad (4.68)$$

replacing Eq. 4.67 in Eq. 4.68 leads to the simplified expression

$$\tau = y_m m_m \quad (4.69)$$

Therefore, the evaluation of the Eq. 4.55 and 4.69 will follow to determine the generator sizing.

Traditional linear-based generators are designed with a frequency that matches the driving frequency in order to optimize the energy generation process. Then, it is convenient to design the generator with a target frequency because the chosen mechanism is based on a pendulum design. Although a body motion generator will operate on a broad frequency range, a dominant frequency mode for the most common body activity can produce the most energy. Since the most consistent activities for the frequency content are walking and running, they are analyzed for this purpose. Based on the treadmill test results, summarized in Fig. 3.10 on page 40, an average frequency of 1.9 Hz is associated with average walking speeds in between 1.3-1.4 m/s while 2.5 Hz was found to be associated for the moderate running speeds (it varied from 2.4 to 2.6 Hz while running in between 2-5 mph). Therefore, 1.9 Hz was chosen as the generator target frequency for walking whereas 2.5 Hz was the target frequency for running activities.

The evaluation of Eq. 4.55 and Eq. 4.69 was initially done for a 25 mm stacked mass design with various proof mass densities (1mm ring and proof mass thicknesses). Material properties for a permanent magnet ring made of neodymium (NdFeB) and proof mass made of steel, brass, lead, and tungsten is modeled in Fig. 4.25. The models were done for a single rotor (single PM ring and a single proof mass) and for one double-rotor made of brass. The available torque for power generation was found to be proportional to the material density. A design with double-rotor was found to have the same resonant frequency as a one-rotor design but double the available torque at the expense of a thicker device. Then, high density materials are the most adequate for the power generation.

The line at 1.9 Hz helps to determine the inner radius dimension for this design, which translates it to a 6.3 gfmm available torque for the brass mass. The torque is expressed in grams-force millimeters because it is easier to understand the physical meaning. Assuming that the generator can rotate at a constant speed equal to the resonant frequency of 1.9 Hz, the 6.3 gfmm available torque gets converted in 737 μ W of rotational mechanical power. This available torque sets a limit for the electrical generation, a higher mechanical power available means that more electrical power can be converted. Thus, a design using two-rotors or using tungsten as the proof mass material will double the available mechanical power.

Solutions of the Eq. 4.55 and Eq. 4.69 for the 1.9 Hz and 2.5 Hz design frequencies are presented in Fig. 4.26. Points that lie on the 1.9 Hz and 2.5 Hz lines are possible radii combinations that satisfy the first optimization condition. This solution is plotted on the three dimensional results shown in Fig. 4.27a. Points that lie below

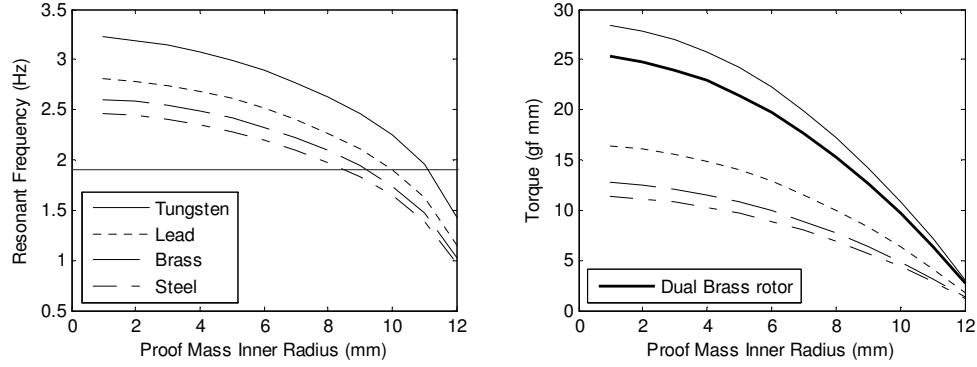


Figure 4.25: Frequency and torque evaluation for a 25mm diameter rotor with a stacked mass and various proof mass densities.

Table 4.3: Stacked brass proof mass solutions for one-rotor design.

PM Ring Diameter (mm)	1.9 Hz (Walking) Available Torque (gf mm)	2.5 Hz (Running) Available Torque (gf mm)
20	2.3	4.5
25	6.3	11.5
30	12.5	-

the lines in Fig. 4.27a are designs with resonant frequencies smaller than the design frequency while points above the lines represent designs with frequencies higher than the target frequency. Solutions were later analyzed for those producing a higher torque, as shown in Fig. 4.27b. This topology of a stacked proof mass can provide for a walking generator (1.9 Hz) more than twice the torque of a running generator design (2.5 Hz).

Since it is difficult to appreciate the results on the 3D model, solutions for 20, 25, and 30 mm rotor diameters are presented in Fig. 4.28. For the stacked proof mass geometry, smaller rotor diameters produce relative higher frequency designs and larger rotor diameters provide a larger available torque, this is summarized in Table 4.3. A 5mm increment in the rotor diameter produces close to twice the available torque. Therefore, larger rotor diameters will be preferred but the generator design will depend then on the available space for a given application. As described previously, dual-rotor designs can double this available torque as well as having a higher density material for the proof mass.

Solutions for the protruding proof mass model (Fig. 4.23b) were also analyzed for the 1.9 Hz and 2.5 Hz design frequencies, as shown in Fig. 4.29 and Fig. 4.30. Solutions showed that a 180° semi-circles presented a higher available torque than

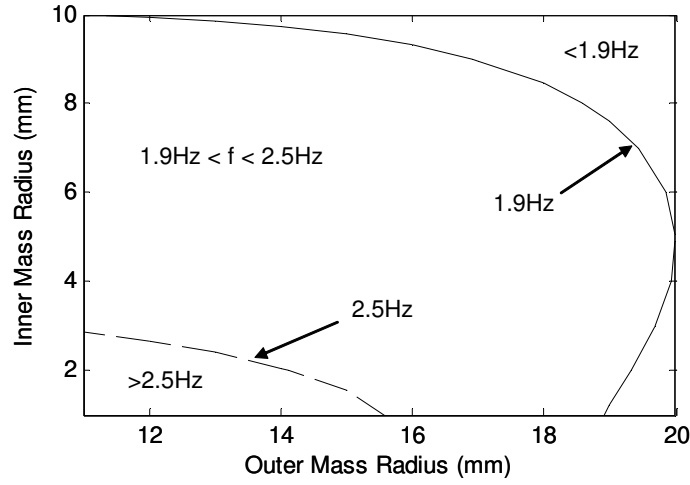
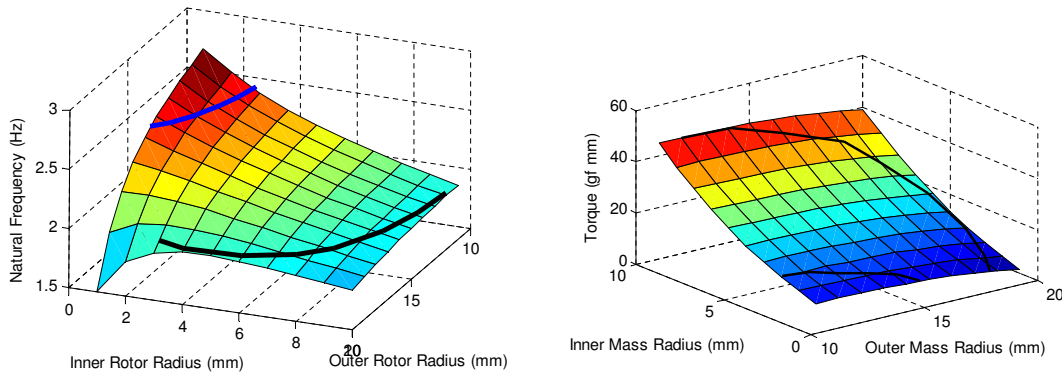


Figure 4.26: Solutions for the 1.9 Hz and 2.5 Hz design frequencies. Combinations of inner and outer radii that lie on the lines represent solutions for the 1.9 Hz and 2.5 Hz designs.



(a) Frequency results. Upper curved line on the 3D surface marks the 2.5 Hz designs while the bottom curved line represents the 1.9 Hz designs. (b) Torque results. Largest curved line marks the 1.9 Hz designs while the shortest curved line represents the 2.5 Hz designs.

Figure 4.27: Modeling results for a stacked proof mass generator design for several dimensions. The thick lines represent the solutions for the 1.9 Hz and 2.5 Hz target frequencies. The model corresponds to generators with a 1 mm thick neodymium PM ring and a 1 mm thick brass proof mass. The surface coloring represents the vertical axis results with red representing the highest results and blue representing the lower results.

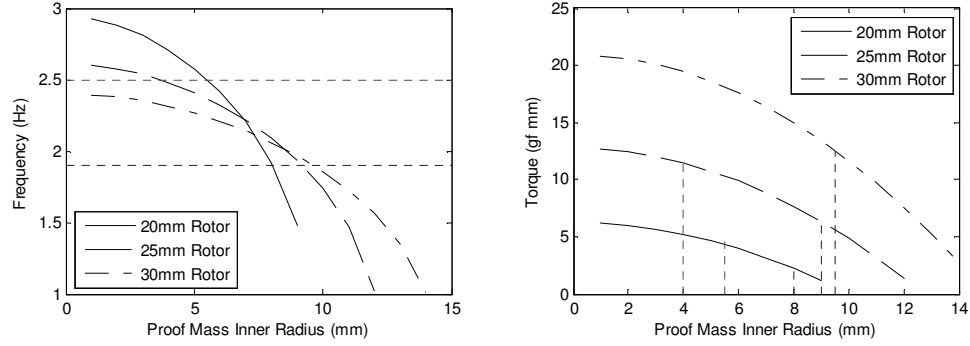


Figure 4.28: Three solutions for the stacked proof mass model presented in Fig. 4.27. Horizontal dotted lines represent the 1.9 Hz and 2.5 Hz design frequencies while the vertical lines represent the available torque for the 1.9 Hz and 2.5 Hz designs.

Table 4.4: Protruded brass proof mass solutions for one-rotor design with 180° .

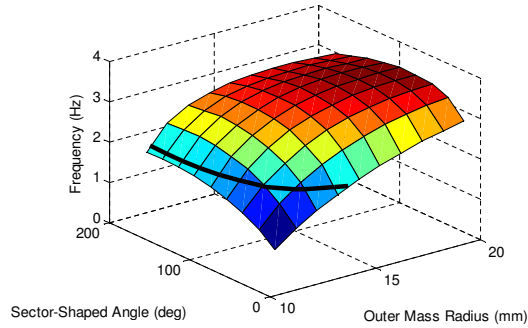
PM Ring Diameter (mm)	1.9 Hz (Walking) Available Torque (gf mm)	2.5 Hz (Running) Available Torque (gf mm)
20	2.5	5.3
25	6.5	16.5
30	13	68

designs with smaller sector-shaped angles, as shown in Fig.4.29 and Fig. 4.30. Results from the protruded proof mass model were found to be comparable to the stacked proof mass model as summarized in Table 4.4. Although the torque model for the 25 mm protruded mass was found to be 50% higher than the 25 mm stacked model for the design frequency of 2.5 Hz.

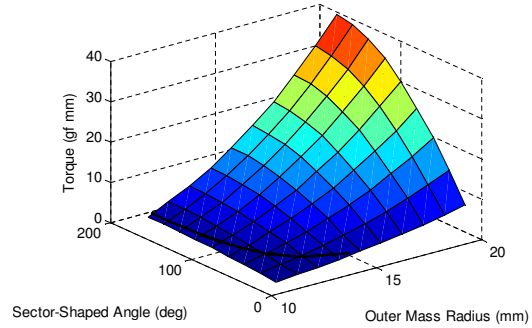
Both proof mass placements (stacked and protruded) were found to produce similar torques for their optimal dimensions. A higher available torque was found to be a practical design choice since the higher the torque the higher the possibilities of converting the mechanical power into electrical energy. The choice for the proof mass placement depends on the physical application constraints: a protruded model is best suited for a thinner profile while a smaller footprint can be achieved with a stacked design.

4.5 Summary

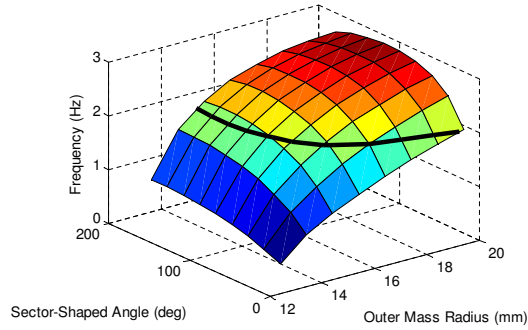
The induced voltage was found to be proportional to the device angular speed, the magnetic field strength, and the geometry of the planar coil. Models for stacked and



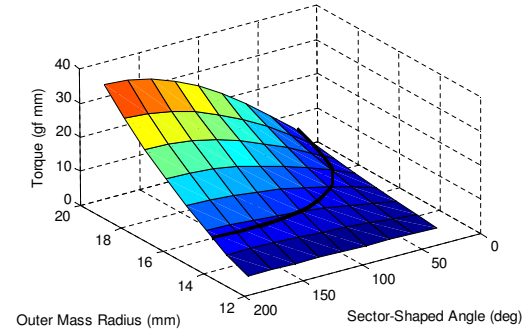
(a) Frequency solution for the 20 mm diameter PM ring



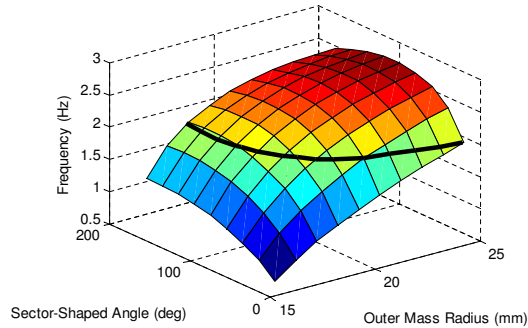
(b) Torque solution for the 20 mm diameter PM ring.



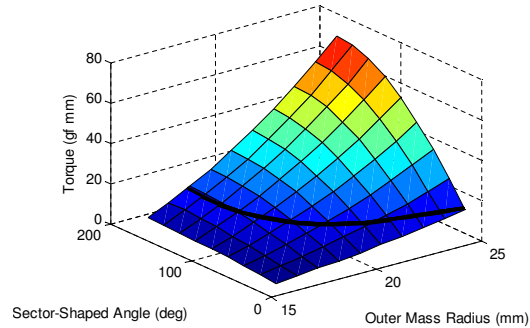
(c) Frequency solution for the 25 mm diameter PM ring



(d) Torque solution for the 25 mm diameter PM ring

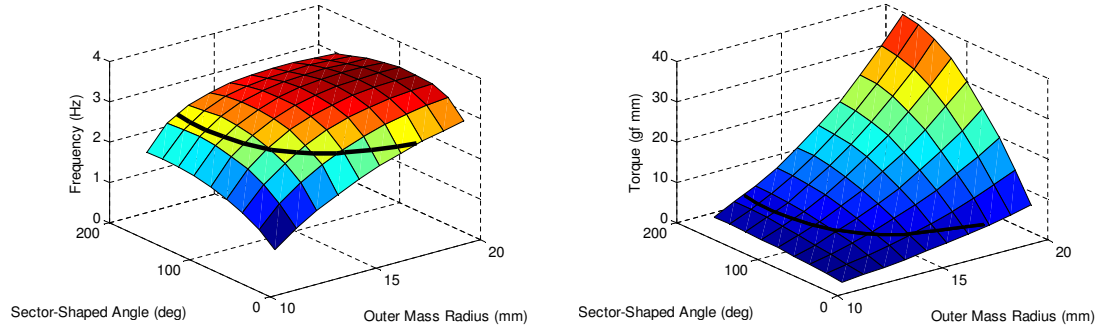


(e) Frequency solution for the 30 mm diameter PM ring



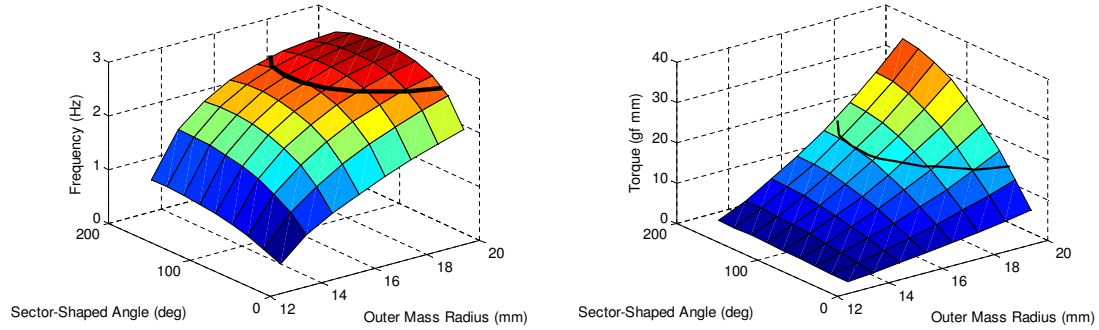
(f) Torque solution for the 30 mm diameter PM ring

Figure 4.29: Protruded proof mass solutions for 20 mm, 25 mm and 30 mm of PM ring diameter for the design frequency of 1.9 Hz. Curved line is the 1.9 Hz solution for each design.



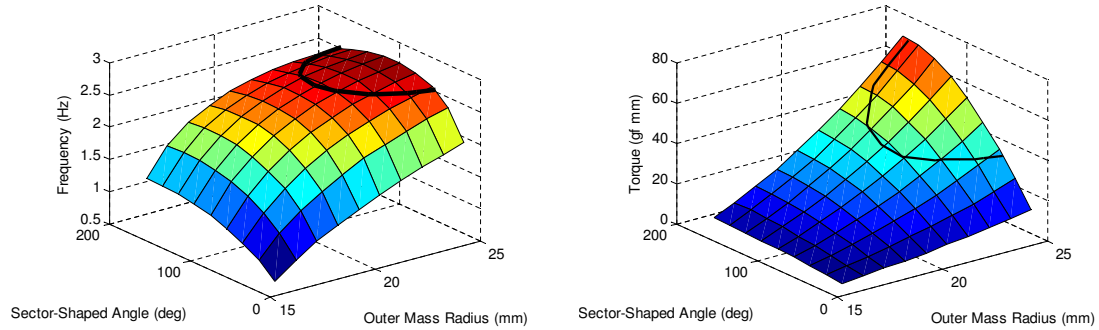
(a) Frequency solution for the 20 mm diameter PM ring

(b) Torque solution for the 20 mm diameter PM ring.



(c) Frequency solution for the 25 mm diameter PM ring

(d) Torque solution for the 25 mm diameter PM ring



(e) Frequency solution for the 30 mm diameter PM ring

(f) Torque solution for the 30 mm diameter PM ring

Figure 4.30: Protruded proof mass solutions for 20 mm, 25 mm and 30 mm of PM ring diameter for the design frequency of 2.5 Hz. Curved line is the 2.5 Hz solution for each design.

protruded proof mass were elaborated with design frequencies of 1.9 Hz and 2.5 Hz. 1.9 Hz was determined as the average walking speed from the results presented in the Section 3.4.2 (on page 38), while 2.5 Hz was the average walking speed for the performed treadmill test.

Next chapter will fabricate and evaluate several prototypes to determine their performance. Devices will be fabricated at the meso-scale and evaluated in laboratory environment as well as on human subjects. The prototypes will be evaluated to validate the models presented in this chapter.

Chapter 5

Generator Fabrication and Testing

5.1 Introduction

Prototypes were fabricated at the meso-scale (cm-sized) to provide a set of testbeds where the designs could be analyzed. The meso-scale fabrication comprised the rotor, stator, and casing elements. CNC machining (a traditional manufacturing technique for prototyping) was employed mostly for the structural elements, while photolithography (a MEMS-based fabrication technique) was used for the planar coil fabrication.

5.2 Fabrication

Two main techniques employed for the fabrication of prototypes were photolithography and CNC machining.

5.2.1 Photolithography

The planar coil was made of commercial copper-clad polyimide film using photolithography. Fig. 5.1 illustrates the clean room fabrication steps. SC1827 photoresist, EVG620 mask aligner, and MF319 developer were used for this process. The copper-clad polyimide employed had 18 μm thick copper on top of 20 μm or 25 μm thick polyimide. Masks were fabricated by photo plotting, limiting the coil dimensions to feature sizes of 100 μm . The Fig. 5.2 shows details of one of the fabricated planar coils.

Three different coil iterations were fabricated, as shown in Fig. 5.3. The first coil iteration was done with 200 μm linewidth to test the coil design and the manufacturing process. The second coil iteration was made with 2 mm nominal radial length wires (100 μm and 200 μm linewidth) to match the radial dimension of the test magnets (2x1x1 mm). The third version was elaborated with 5.1 mm nominal radial length

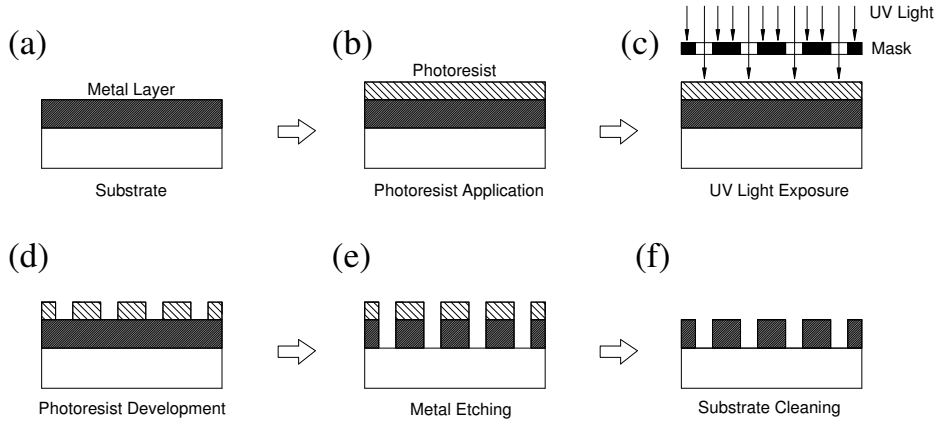


Figure 5.1: *Planar coil fabrication process.*

wires in order to match the permanent magnet length (5.1x1.1x1.1 mm). The copper-clad was not entirely etched for second iteration as it was for the first iteration in order to simplify the fabrication process. This was reverted for the third coil iteration since this can produce eddy currents¹ that increase the system damping.

Multi-layer coils were fabricated by stacking several layers of planar coils and bonding them with cyanoacrylate while applying pressure to ensure a compact assembly. This technique provided a relatively stiff 2-layer coil assembly with the gluing agent being as thin as 2 μm . In contrast, commercial bonding films were found to be as thin as 12.5 μm . This process provided 6X thinner assemblies. A 10-layer coil was constructed with this technique for a thickness of 430 μm by using 20 μm thick polyimide substrates with 18 μm copper-clad. Fig. 5.4 shows one of the 10-layer coil fabricated.

Coil nomenclature is based on the geometry of the coil ends of the planar coil (linear, triangular, or circular ends), coil linewidth, radial length ($R-r$, from Fig. 4.3), number of turns, and number of layers. For example, a coil labeled as L200U20M4T-2L represents a straight-end (linear ends) coil with 200 μm linewidth, 20 mm radial length, 4 turns, and 2 stacked layers. Fig. 5.8 provides a coil nomenclature example. The stator nomenclature includes the number of pole-pairs, the number of stators used and magnet dimensions. For instance, a stator represented as 20P2R5X1MM has 20 pole-pairs, 2 rotors, with individual magnets of 1.1x1.1x5.1 mm (5X1MM for simplicity).

¹Eddy currents are induced electrical currents in conductors when exposed to a changing magnetic field due to relative motion; or due to variations of the field with time, such as a moving magnet and a fixed coil.

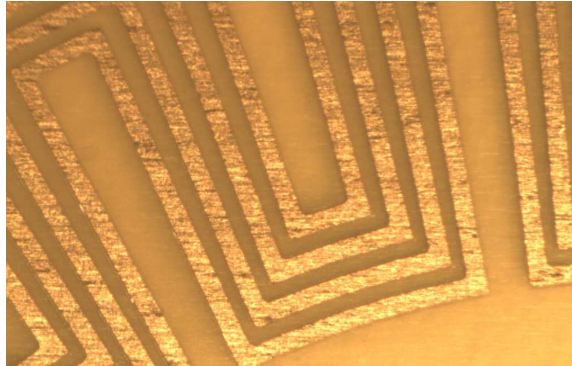
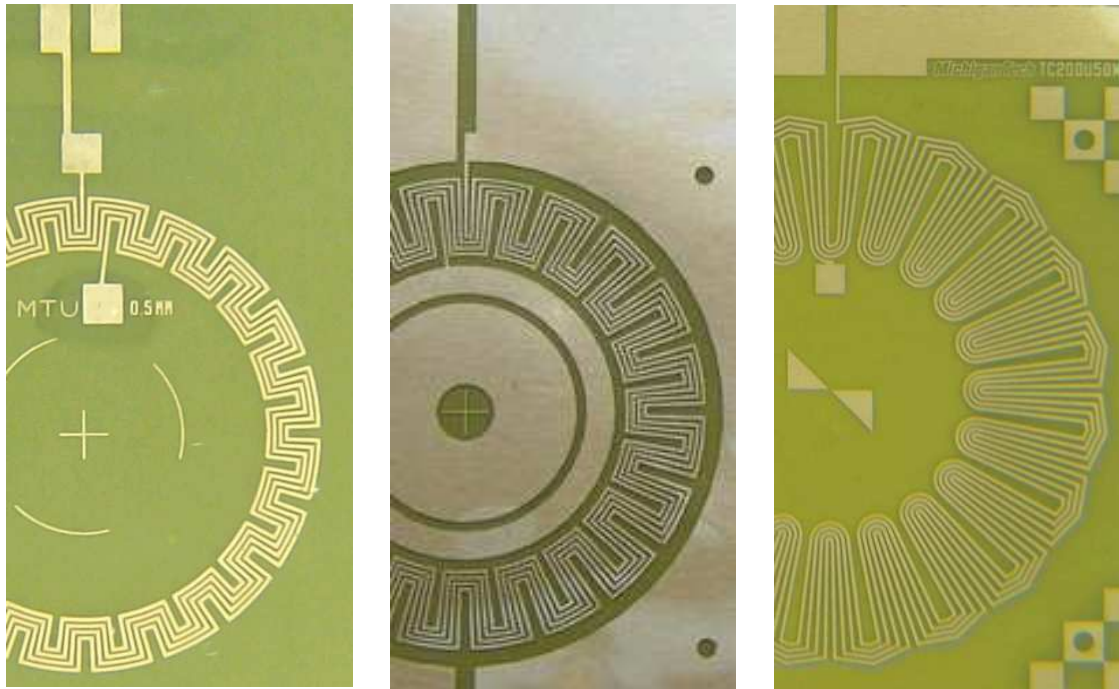


Figure 5.2: Detail of a $200\mu\text{m}$ linewidth and 4 turns copper planar coil on polyimide substrate, (L200U20M4T).



(a) First coil iteration, 0.5 mm nominal radial wire length. (b) Second coil iteration, 2 mm nominal radial wire length. (c) Third coil iteration, 5.1 mm radial wire length

Figure 5.3: Coil iterations for 20 pole-pairs arrangements.

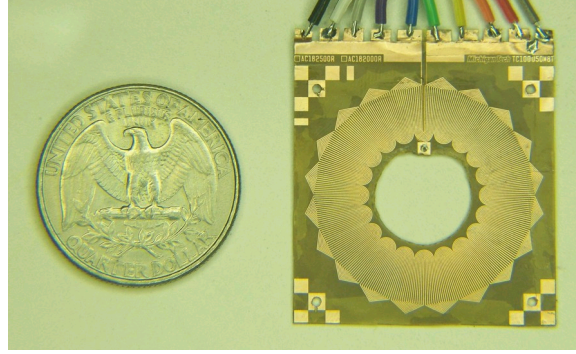


Figure 5.4: A $430\mu\text{m}$ thick 10-layer coil assembly (L100U51M8T-2L). A 25 cents coin was added for size comparison purposes.

5.2.2 CNC Machining

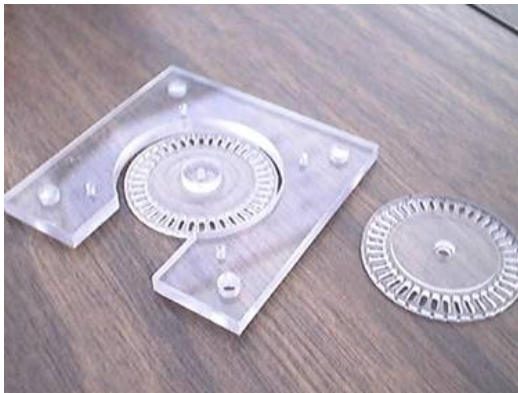
The rotor and the casing for the meso-scale prototypes were CNC machined using commercial PMMA and/or polycarbonate. Fig. 5.5 shows a picture of CNC machined rotors and casing structure. The rotors depicted were machined with slots for the insertion of individual magnet pieces. The observed casing structure has a set of alignment holes in addition to orifices for bolted assembly on this particular prototype. Commercially-available neodymium (NdFeB) permanent magnets (PM) were used. Eccentric mass elements were added to the rotor disc to complete the assembly. Ball bearings or jewel bearings finalized the design.

5.2.3 Prototypes

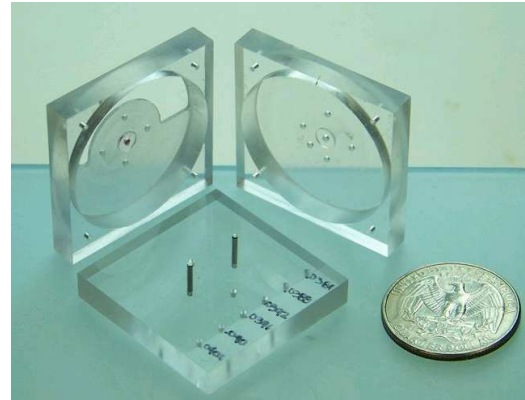
Micro Vibrational Power Generator or μVPG is the acronym termed for this generator design. Prototypes have an additional nomenclature due to several iterations of the devices, including different planar coils and stator assemblies. A first test-of-concept iteration ($\mu VPG - 0.5$) used a wire-wound coil, half rotors, and ball bearing design. The half rotor design was used to avoid an additional proof mass. This design is shown in Fig. 5.6.

Later iterations employed planar coils and full rotors. The iteration $\mu VPG - 1.X$ was used for the following designs:

- $\mu VPG - 1.0$, single rotor with 20 pole-pairs (individual $1 \times 1 \times 1$ mm PM and 2 mm radial-length coil) and single ball bearing, Fig. 5.7.
- $\mu VPG - 1.1$, single rotor with 20 pole-pairs (individual $1 \times 1 \times 1$ mm PM and 2 mm radial-length coil) and dual ball bearings.
- $\mu VPG - 1.2$, single rotor with 20 pole-pairs (individual $1 \times 1 \times 1$ mm PM and 2 mm radial-length coil) and jewel bearings.



(a) 25mm rotors for the 1mm cube magnets.



(b) Packaging enclosure and alignment fixture. A 25 cents coin was added for size comparison purposes.

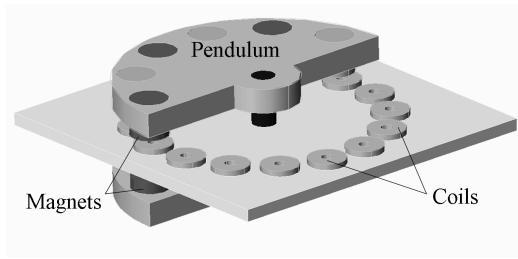


(c) Two rotors for the 1.1x1.1x5.1mm magnets (2 magnets shown), one rotor for the 1x1x2mm magnet configuration (middle rotor, assembled with 1mm cube magnets). A 25 cents coin was added for size comparison purposes.

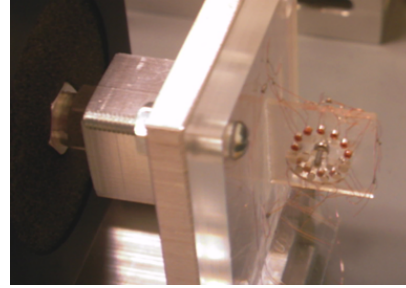


(d) Packaging, 10-layer coil, brass mass, and rotor with 1.1x1.1x5.1mm magnets. A 25 cents coin and a AA battery were added for size comparison purposes.

Figure 5.5: CNC-machined components.

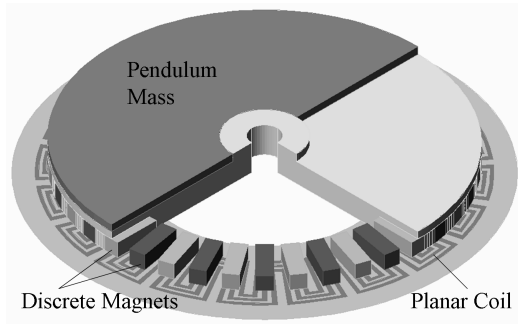


(a) Diagram

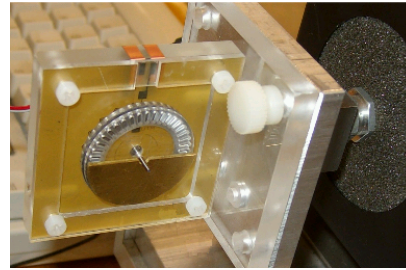


(b) Photo

Figure 5.6: $\mu VPG-0.5$ prototype (2 half-rotors, 6 round magnets per rotor, 12 wire-wound coils, and ball bearing).



(a) Diagram



(b) Photo

Figure 5.7: $\mu VPG-1.0$ prototype (1 rotor, 20 pole-pairs, 80 $1 \times 1 \times 1$ mm PM, ball bearing design).

- $\mu VPG-1.3$, single rotor with 20 pole-pairs (individual $5.1 \times 1.1 \times 1.1$ mm PM and 2 mm radial-length coil) and jewel bearings.
- $\mu VPG-1.4$, dual rotor with 20 pole-pairs (individual $5.1 \times 1.1 \times 1.1$ mm PM and 2 mm radial-length coil) and jewel bearings.
- $\mu VPG-1.5$, dual rotor with 20 pole-pairs (individual $5.1 \times 1.1 \times 1.1$ mm PM and 5.1 mm radial-length coil) and jewel bearings.

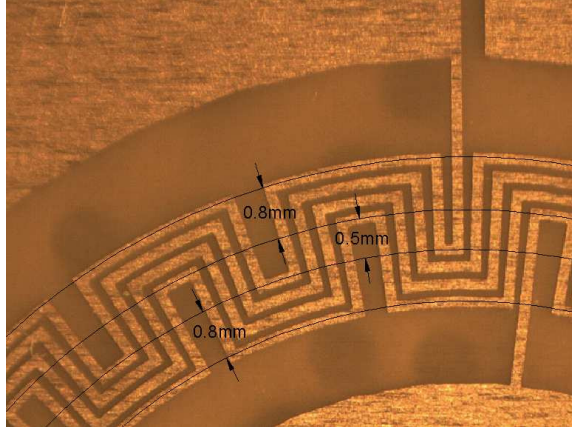


Figure 5.8: Coil nomenclature example. *L200U05M₄T* coil: linear ends, 200 μm linewidth, 0.5 mm nominal radial length (1.3 mm radial length including the coil ends), and 4 turns.

Table 5.1: $\mu\text{VPG-0.5}$ prototype parameters.

Element	Description
Permanent Magnet	12 (NdFeB N48) PM, $\phi 1/16'' \times 1/32''$
Wire-Wound Coil	12 coils, $\phi 80 \mu\text{m}$ (AWG 40) \times 80 turns, 13 Ω total
Pendulum Length	5 mm
Proof Mass	0.35 g
Resonant Frequency	5.8 Hz

5.3 Prototype Testing

5.3.1 First Prototype: $\mu\text{VPG-0.5}$

The $\mu\text{VPG-0.5}$ prototype, shown in Fig. 5.6, was the first design tested for a proof-of-concept generator with arbitrarily-chosen dimensions. This design had generator volume of 0.68 cm^3 (6mm radius) made of CNC-machined PMMA and assembled with ball bearings, 12 NdFeB PM (Grade N48, $1/16''$ diameter \times $1/32''$) for two semi rotors, and 12 wire-wound copper coils (80 turns, enameled copper wire, 40 AWG, $\sim 80 \mu\text{m}$ diameter, coil resistance 13 Ω). Rotor separation was 2 mm. The natural resonant frequency was calculated to be 5.8 Hz, for a proof mass of 0.35 g. The natural frequency (ω_n) was calculated from $\omega_n = \sqrt{mgl_{eq}/I}$, where m is the proof mass, g is the acceleration due to gravity, l_{eq} is the equivalent length for a compound pendulum, and I the moment of inertia. Table 5.1 summarizes the prototype parameters.

This prototype was tested on a laboratory shaker (sinusoidal input waves from 1 to 5 Hz with 0.5 Hz increments under varying resistance loads) while the induced voltage was measured. Fig. 5.9 shows the voltage, power, and acceleration results for this test

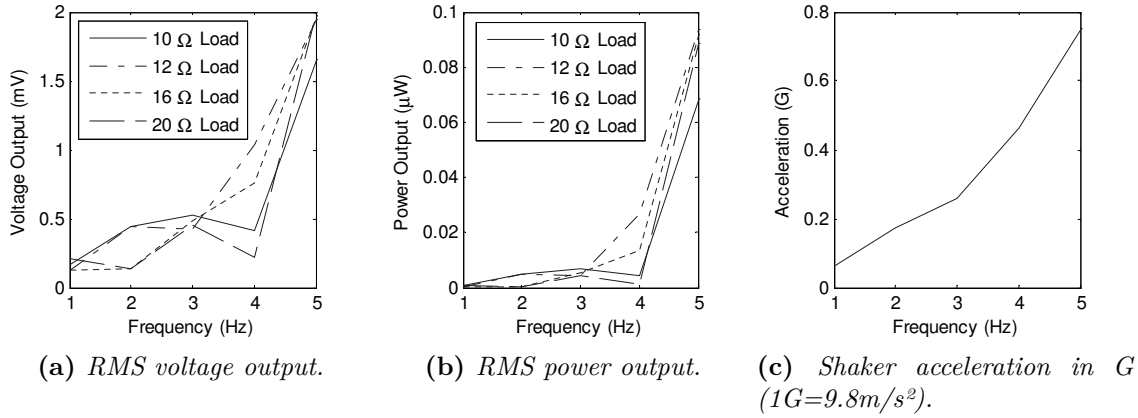


Figure 5.9: Test results for the μ VPG-0.5 prototype on a laboratory shaker.

(acceleration varied from 60 mG to 750 mG, where $1\text{ G}=9.8\text{ m/s}^2$). The voltage and power are larger for frequencies closer to the generator natural frequency, 1.94 mVrms and 0.093 μW at 5 Hz and 12 Ω ($\sim 0.14\text{ }\mu\text{W}/\text{cm}^3$ of power density), although shaker acceleration increased almost proportionally to frequency. The instantaneous voltage output at 5 Hz and 12 Ω load, is shown in Fig. 5.10, presenting a maximum peak voltage of 6.3 mV and maximum peak power of 0.096 μW . Coil fabrication was challenging with diameter dimensions smaller than 2 mm, and thicknesses smaller than 1 mm. Planar coils are considered to offer cost-effective fabrication since they do not require dedicated tooling or equipment for testing multiple geometries.

As a comparison, the mechanism of a self-winding wristwatch with an electrical generator (Seiko wristwatch, Kinetic brand, Fig. 5.11) was also examined on a laboratory shaker (voltage from the generator was measured under sinusoidal input waves from 1 to 5 Hz, and varying resistance loads). Results for this experiment are shown in Fig. 5.12. It can be seen that there is little variation in voltage output under varying loading, although power transfer is higher for a load matching the coil resistance (330 Ω), from Eq. 4.53. Given the proof mass dimensions (27 mm diameter, 4.7 g), the natural frequency is estimated to be 3.8 Hz. This might explain the larger voltages between 3-5 Hz, although this design does not oscillate freely due to cogging torque². Frequencies between 3-5 Hz produce more than three times the power results obtained at 2 Hz, although acceleration content also increased more than 10 times for this test. This commercial generator does not seem to be optimized for the ~ 2 Hz range of body motion for average walking speeds. At 2 Hz with acceleration of 120 mG the power output is near 30 μW , while it peaks at 4 Hz and 620 mG producing 580 μW of power.

²Cogging torque is due to the interaction between the permanent magnets of the rotor and the iron (soft-magnetic material) of the stator.

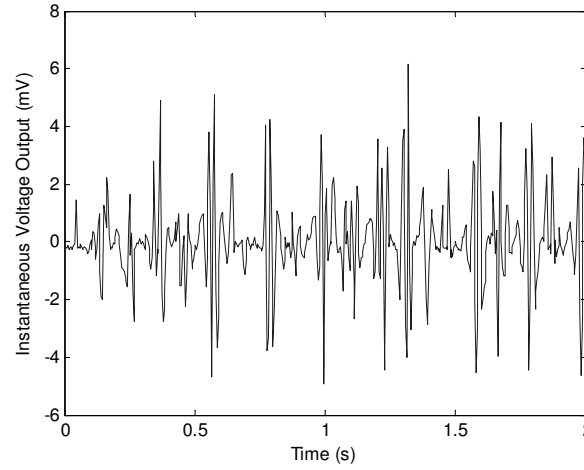


Figure 5.10: Instantaneous voltage for the μ VPG-0.5 prototype on a laboratory shaker at 5 Hz and 12Ω load.

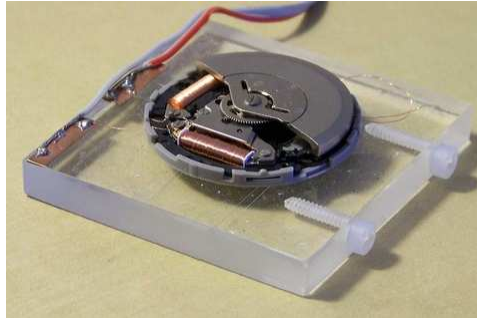
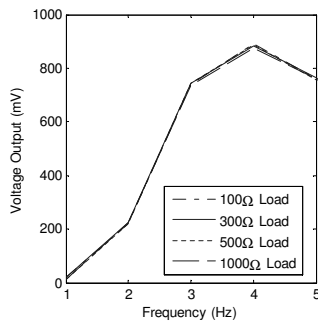
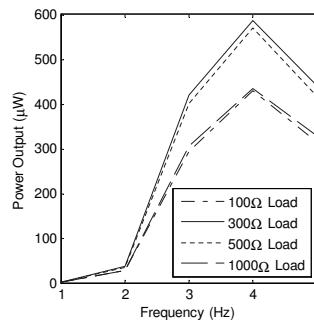


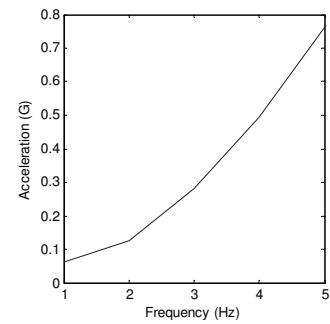
Figure 5.11: Commercial self-winding wristwatch generator (Seiko wristwatch, Kinetic brand).



(a) RMS voltage output.



(b) RMS power output.



(c) Acceleration peak variation in G ($1\text{ G}=9.8\text{ m/s}^2$).

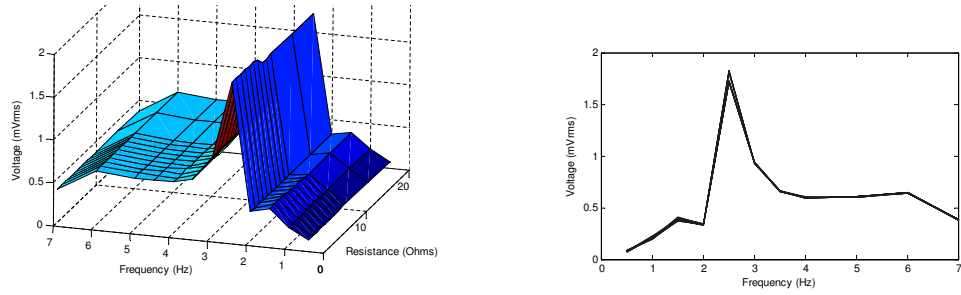
Figure 5.12: Test results from a commercial wristwatch on a laboratory shaker.

5.3.2 Second Prototype: μ VPG-1.0

Since the μ VPG-0.5 prototype was tested successfully as an energy generator, a second prototype was fabricated in order to determine new design topologies. A complete circular rotor was selected to double the number of magnets and coils for energy generation (doubling the induced voltage when compared to the first prototype). One mm cube magnets were used instead of disk magnets. A soft-magnetic material sheet was used to facilitate the assembly of the rotor magnets since the 1mm cube magnets repel each other when placing two in a row for a 2 mm radial magnet segment. Planar coils were fabricated by photolithography to create thinner geometries and simplify manufacturing, changing the design from several individual coils to one coil. The diameter was arbitrarily chosen to be 25 mm, and one ball bearing set was used to complete the assembly for a volume of 1.5 cm^3 (considering only the rotor, proof mass and planar coil). The separation between the rotor and stator was required to be at least 1mm at the widest point to avoid friction between the rotor and the coil due to rotor tilt. The tilt was produced by torque of the eccentric mass along the shaft when using a single ball bearing set. A subsequent prototype used dual ball bearings to avoid this assembly problem.

The μ VPG-1.0 prototype, as shown in Fig. 5.7, was also tested on a laboratory shaker (sinusoidal input, 1-7 Hz with 0.5 Hz increments, varying load conditions). Fig. 5.14 shows the laboratory shaker setup used with the generator mounted on the second shaker. Fig. 5.13 shows the induced voltage output results for a L200U05M-1L-20P1R2x1MM assembly (linear coil ends, 200 μm linewidth coil, 18 μm thick copper, 0.5 mm nominal radial-wire length, 1-layer coil, 20 pole-pairs, one 25 mm diameter PM ring rotor, and 2x1x1 mm magnet sets by using 1 mm magnet cubes). The coil resistance was measured as $3.2\ \Omega$. A 2 g proof mass was used for this test providing a calculated resonant frequency of 2.7 Hz for this system. Due to the 0.5 Hz frequency increments, there is an optimal point at 2.5 Hz for this generator when the external frequency matches the resonant frequency of the pendulum arrangement. A sub-harmonic appears to be present at a frequency of 1.5 Hz.

Power output results are presented in Fig. 5.15. Although results are less than $1\ \mu\text{W}$, power output increased twice (to $0.26\ \mu\text{W}$ from $0.093\ \mu\text{W}$) while the operating frequency was reduced in half (to 2.5 Hz from 5 Hz) with a smaller acceleration (to 150 mG from 750 mG) when compared to the first prototype. Acceleration increased almost proportionally with frequency, with two outliers at 2 and 7 Hz. The 2 Hz test, although having a higher acceleration content than the 1.5 and 2.5 Hz test points does not seem to have any influence the voltage generation results since the induced voltage was smaller. At 7 Hz the influence is evident; a smaller shaker acceleration induced a smaller voltage. Power output was the highest for a matching load of $3\ \Omega$. Voltage peaked at 2.5 Hz with 1.8 mVrms while it was fairly constant at higher frequencies with a voltage slightly larger than 30% from the peak value. This suggests



(a) 3D plot with varying load and frequency.

(b) Induced voltage vs. frequency with overlapped loads.

Figure 5.13: Voltage output results for the μ VPG-1.0 prototype on a laboratory shaker.



Figure 5.14: Laboratory shaker setup.

the possibility of non-harmonic energy generation at frequencies higher than the resonant frequencies with a power generation of 10% of the peak value. The wide peak shape in the voltage output result plot is indicative of the non-linear behavior of the system. Since the generator resembles a pendulum, it is a non-linear system when driven to large amplitude oscillations. In addition, the shape of the resonance curve becomes distorted (foldover effect). This nonlinear resonance³ produces some effects that modify the shape of the resonance curves that can explain the wide shape.

5.3.3 Third Prototype: μ VPG-1.1

μ VPG-1.1 prototype was built with dual ball bearing sets in order to avoid the shaft tilt observed in the single bearing design. The use of two radial ball bearings

³Elmer, Franz-Josef, *Nonlinear Resonance*, <http://www.elmer.unibas.ch/pendulum/nonres.htm> Retrieved in 2010-06-27.

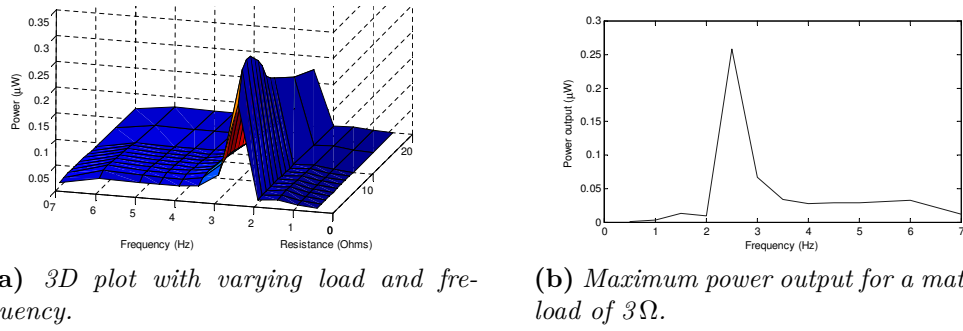


Figure 5.15: Power output results for the μ VPG-1.0 prototype on a laboratory shaker.

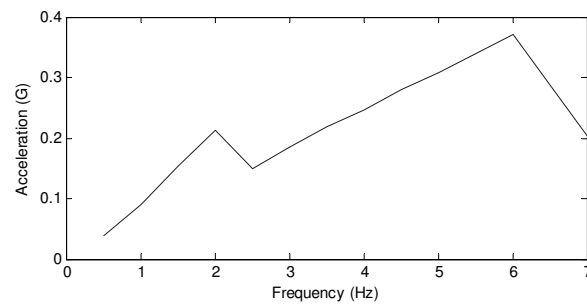
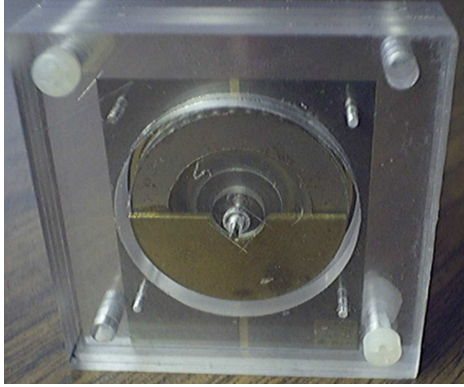


Figure 5.16: Shaker acceleration in G for the μ VPG-1.0 prototype ($1\text{ G}=9.8\text{ m/s}^2$).



(a) A soft-magnetic material can be observed on the rotor under the eccentric brass mass.



(b) Rotor detail with the 1mm cube magnets placed radially. The ball bearing set can be observed near the tip of the shaft.

Figure 5.17: μ VPG-1.1 prototype photos.

with the eccentric mass placed in between was deemed as a practical solution to avoid the tilt and place the magnet surface closer to the coil, as shown in Fig. 5.17. The rotor diameter continued to be 25 mm with a 2 g eccentric mass (calculated resonant frequency of 2.6 Hz). A soft-magnetic material sheet was used to facilitate the assembly of the rotor magnets since the 1 mm cube magnets repel each other when placing two in a row for a 2 mm radial magnet segment (see detail in Fig. 5.17). Separation between the rotor and stator was 0.5 mm.

The μ VPG-1.1 prototype was tested on a laboratory shaker (sinusoidal input, 1-6 Hz with 0.5 Hz increments, varying load conditions). Fig. 5.18 and Fig. 5.19 present the induced voltage for a L200U20M-4L-20P1R2x1MM assembly (linear coil ends, 200 μ m linewidth coil, 2 mm nominal radial-wire length, 4-layer coil, 20 pole-pairs, one PM ring rotor, and 2x1x1 mm magnet sets by using 1 mm magnet cubes). The coil internal resistance was measured as 15.9 Ω .

As with the previous prototype, the 0.5 Hz frequency increment provides a maximum voltage at 2.5 Hz while the resonant frequency was calculated as 2.7 Hz. The coil tested had near twice the radial wire length covered by the magnets for 1.5X increase in the induced voltage (when compared to the L200U05M coil), and since a 4-layers were employed instead of one, the increase was estimated to be 6X when compared to the L200U05M-1L-20P1R2x1MM test from the previous prototype (to ~ 12 mVrms peak from ~ 2 mVrms peak) and found to be ~ 6 X. Power was calculated to be 2 μ W at 2.5 Hz for a load of 15 Ω , that is near 6X the previous prototype power peak (0.3 μ W). Voltage output for frequencies larger than 2.5 Hz was higher than 50% of the peak RMS voltage, while the power generation was slightly higher than 25% of the peak power.

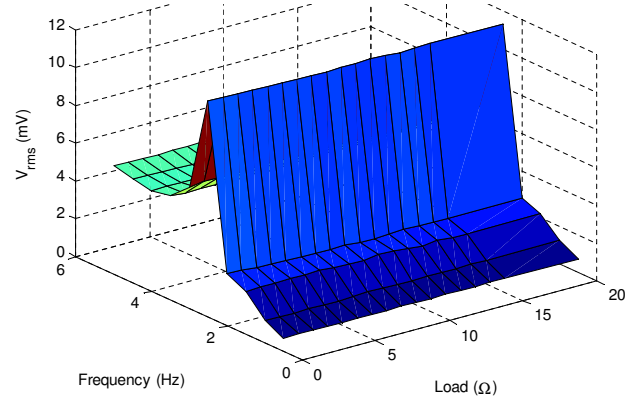


Figure 5.18: Voltage output results for the μ VPG-1.1 prototype on a laboratory shaker for varying frequency and loading conditions.

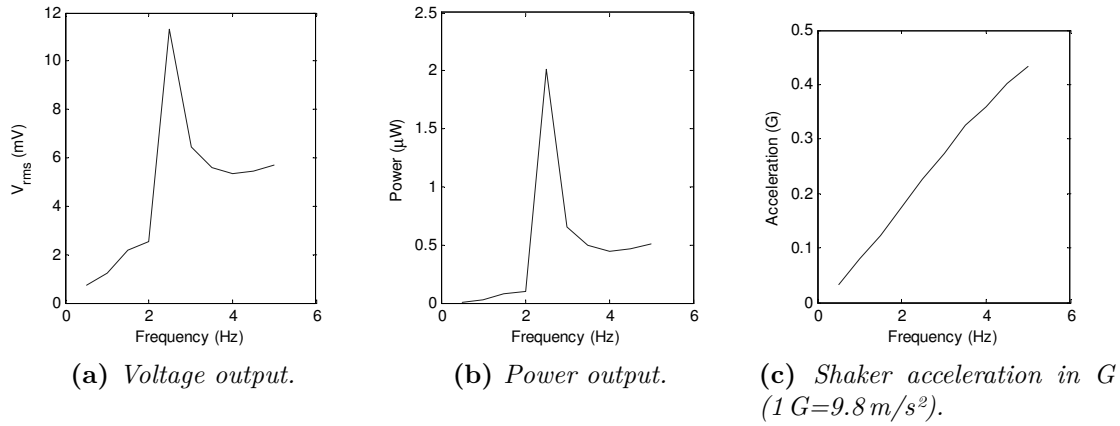


Figure 5.19: Results for the μ VPG-1.1 prototype on a laboratory shaker for a load of 15Ω with 0.5 Hz frequency increments.

A preliminary test to determine the viability of the design for energy generation from the human body was performed with the generator placed at several body locations (knee, hip, abdomen, chest, wrist, and forehead) while free walking along a hallway. The results are shown in Fig. 5.20. Only open-circuit voltage was measured. There were three distinct energy generation zones according to the RMS voltage readings: The highest induced voltage location was the knee with 7.4 mVrms; the second was composed by the wrist, elbow, and forehead with induced voltages at 3 mVrms; the third was formed by the chest and abdomen at ~ 1.5 mVrms. The induced voltage values are found to correlate well with the results from the availability of power from body motion in Chapter 3.

A test of a planar coil with a smaller linewidth dimension was performed to evaluate this prototype and to determine the induced voltage for a coil with double the amount of radial wires. The L100U20M9T-2L coil was used (linear ends, 100 μ m linewidth, 20 mm nominal radial length, 9 turns, and 2-layer coil). Results for a varying load and frequency (0.5-5 Hz with 0.5 Hz increments, and with 0.1 Hz increments in between 2-3 Hz) are presented in Fig. 5.21, 5.22, and 5.23. When compared to the L200U20M4T-4L coil, the voltage output and power output are essentially the same, although voltage was slightly larger (14 mVrms) since the L100U20M9T-2L coil had an extra wire turn per layer. Power was slightly smaller since the internal coil resistance was larger ($29\ \Omega$), as shown in Fig. 5.22. The shaker acceleration (Fig. 5.23) was similar to the previous test up to 3 Hz, it was almost constant with respect to frequency at higher frequencies. Power output was reduced to near 20% of its peak value at 3 Hz while being close to 10% of the peak value at 5 Hz. The natural resonant frequency was determined to be 2.7 Hz with a second peak located at 1.5 Hz, which seems to correspond to a sub-harmonic located near 1.35 Hz. Power generation was found to be larger at frequencies higher than the resonant frequency as compared to frequencies below it, except at the subharmonic point where it was close to 30% of the peak value.

The L100U20M9T-2L coil was tested again to determine the nature of the subharmonic behavior. Results for open-circuit voltage with varying frequency (0.5-5 Hz with 0.1 Hz increments) are presented in Fig. 5.24. It can be observed that the frequency behavior for this generator gave a natural resonant frequency peak at 2.7 Hz, a first subharmonic at 1.5 Hz and a second subharmonic at 1 Hz. The acceleration was maintained fairly constant for this test, although it was the highest for the test 1 at 1 Hz, which can explain why this peak is as high as the 1.5 Hz peak while it was smaller in the previous test (Fig. 5.21). Fig. 5.25 shows the power calculated for the Test 3. Power generation is identical to Fig. 5.22 except that the shaker acceleration was near 0.12 G while in the previous test it was increased to 0.27 mG, which explains the lower voltage and power output results.

Another test was performed with a 10-layer coil to evaluate the voltage generation with thicker coils. A L200U20M4T-10L coil with 0.5 mm thickness was used

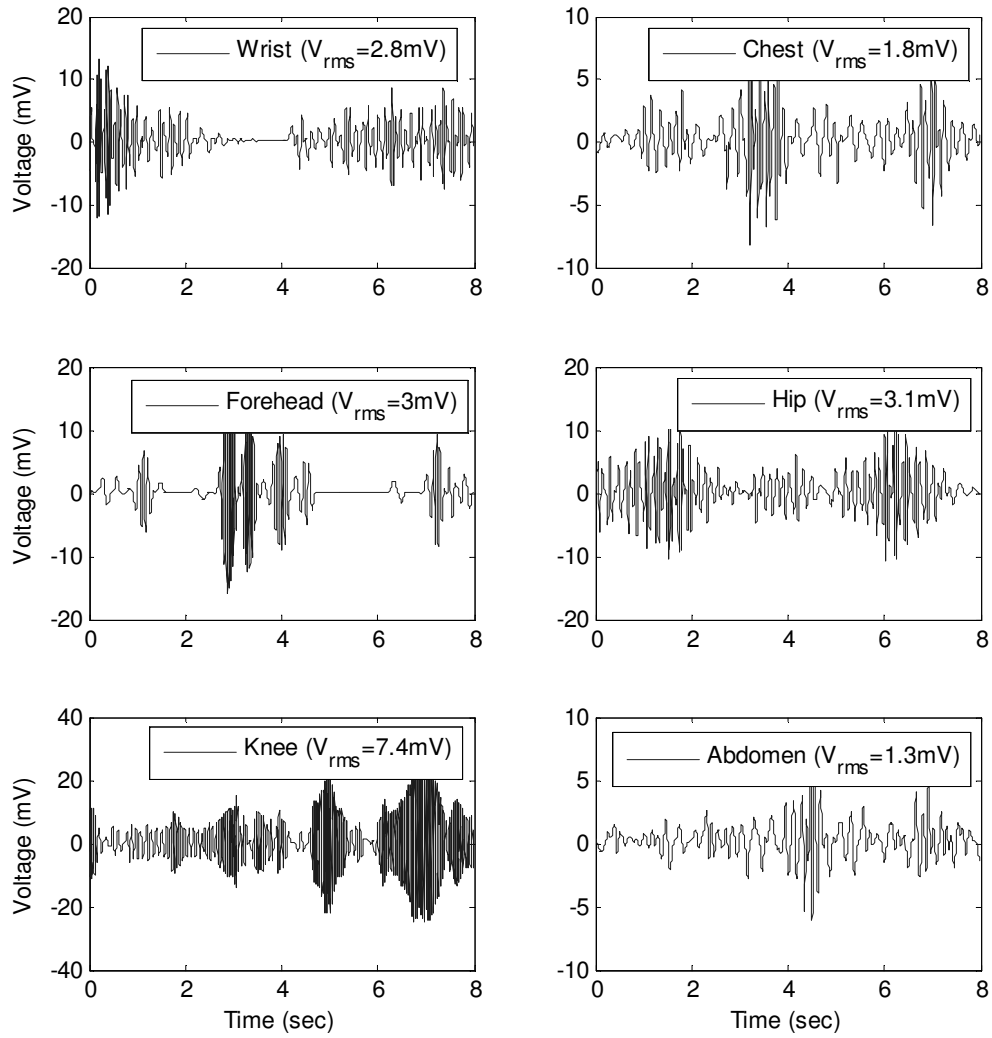
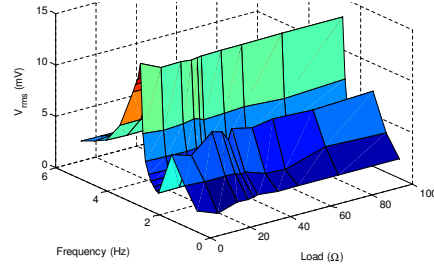
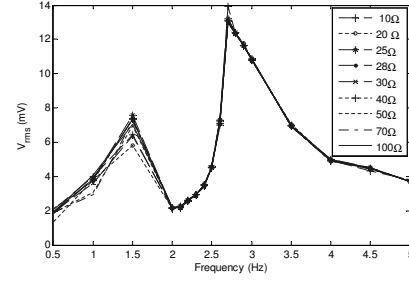


Figure 5.20: Results for the μ VPG-1.1 prototype while free walking.

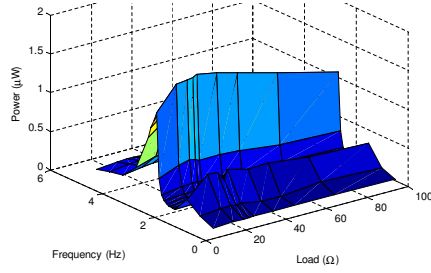


(a) 3D plot with varying load and frequency.

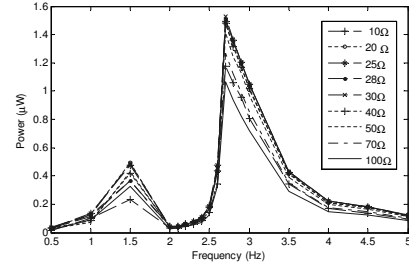


(b) Induced voltage vs. frequency with overlapped loads.

Figure 5.21: Voltage output results for the μ VPG-1.1 prototype on a laboratory shaker for varying frequency and loading conditions.



(a) 3D plot with varying load and frequency.



(b) Maximum power output for a matching load.

Figure 5.22: Power output results for the μ VPG-1.2 prototype on a laboratory shaker.

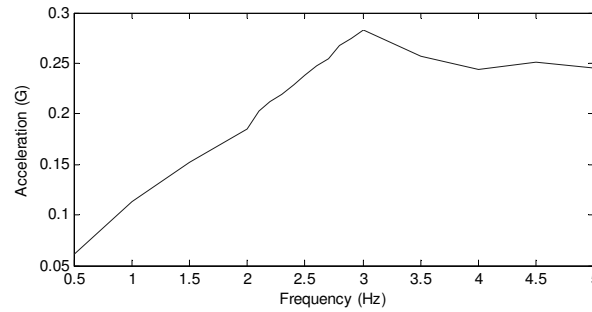
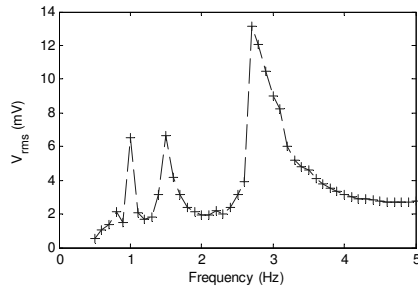
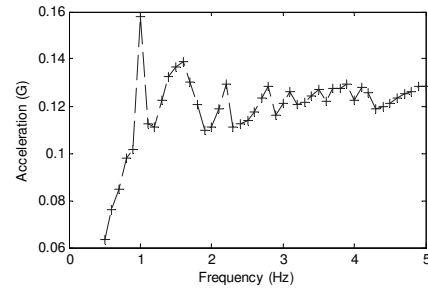
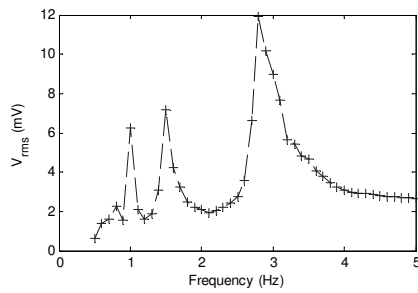


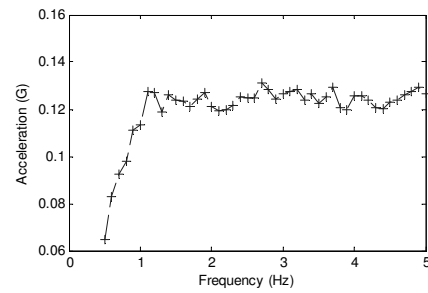
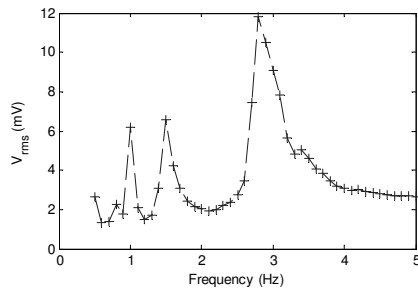
Figure 5.23: Shaker acceleration in G for the μ VPG-1.1 prototype using the L100U20M9T-2L coil ($1\text{ G}=9.8\text{ m/s}^2$).



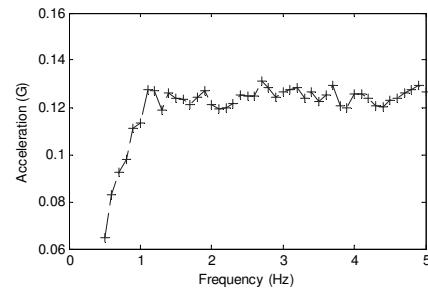
(a) Open-circuit voltage test 1.

(b) Test 1 shaker acceleration in G ($1 G = 9.8 m/s^2$).

(c) Open-circuit voltage test 2.

(d) Test 2 shaker acceleration in G ($1 G = 9.8 m/s^2$).

(e) Voltage for test 3.

(f) Test 3 shaker acceleration in G ($1 G = 9.8 m/s^2$).**Figure 5.24:** μ VPG-1.1 prototype using the L100U20M9T-2L coil.

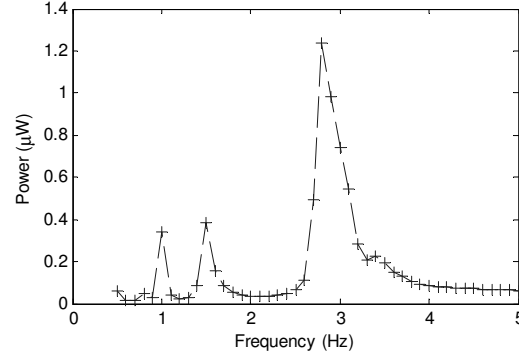


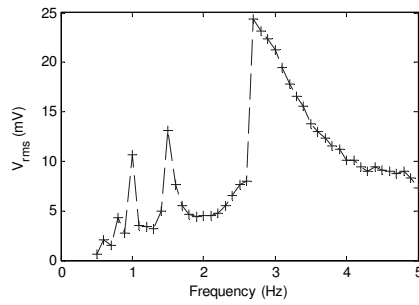
Figure 5.25: Power output for the test 3 with a load of 28Ω .

(44Ω measured coil resistance). Voltage output was expected to increase 2.5X when compared to the 4-layer coil, although the increase in coil thickness was expected to reduce the magnetic flux on the more distant coil layers. Frequency varied from 0.5-5 Hz with 0.1 Hz increments, as shown in Fig. 5.26 for the open-circuit and loaded case. The voltage output peaked at 2.7 Hz with 24.5 mVrms and 0.3 mG of shaker acceleration.

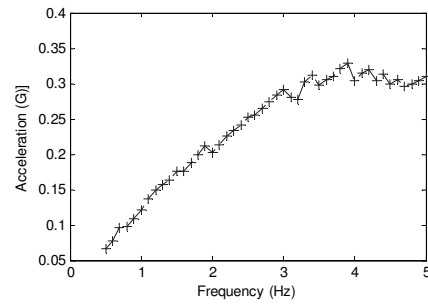
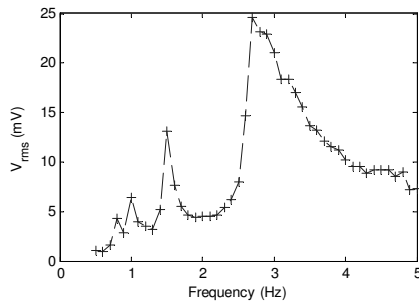
The nonlinear effects of the large amplitude pendulum oscillations also bring in another effect, the subharmonic resonance⁴. These are additional peaks appearing at driving frequencies that are fractions of the resonant frequency. Therefore, the peaks presented at 1.5 Hz, 1 Hz, 0.8 Hz, which seem to correspond to the frequencies $1/2\omega_n$, $1/3\omega_n$, and $1/4\omega_n$, where ω_n is the resonant frequency of the generator, seem to be a product of the superharmonic resonance. Voltage output increase 2.1X rather than 2.5X when compared to L200U20M4T-4L coil results, the difference is due to the increased coil thickness that produces a reduced voltage on the more distant coil-layers. Fig. 5.27 shows the power calculated. A peak power of $3.45\ \mu\text{W}$ at 2.7 Hz and a second peak of $1\ \mu\text{W}$ (30% from the peak value of $3.45\ \mu\text{W}$) at 1 Hz was found. Power produced for frequencies larger than 2.7 Hz was larger than $0.5\ \mu\text{W}$ for frequencies up to 4.6 Hz.

⁴The term is known as superharmonic resonance, but here it is described as subharmonic since subharmonic frequencies are involved, and also to avoid the confusion with the word superharmonics. The resonance with one of the higher harmonics is called superharmonic resonance when the driving frequency is a fraction of the resonant frequency. Since nonlinear oscillators do not oscillate sinusoidally, the final oscillation is a sum of harmonic oscillations with frequencies that are integer multiples of the resonant frequency. This is explained by the Fourier series where a periodic function can be represented by the (infinite) sum of sines and cosines functions.

Elmer, Franz-Josef, *Nonlinear Resonance*, <http://www.elmer.unibas.ch/pendulum/nonres.htm> Retrieved in 2010-06-27



(a) Open-circuit voltage.

(b) Shaker acceleration in G for the open-circuit voltage test ($1 G = 9.8 \text{ m/s}^2$).

(c) Loaded circuit.

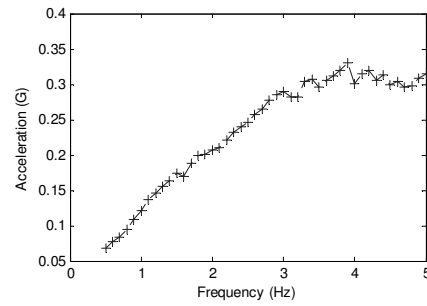
(d) Shaker acceleration in G for the loaded test ($1 G = 9.8 \text{ m/s}^2$).

Figure 5.26: Voltage output results for the $\mu\text{VPG-1.1}$ prototype on a laboratory shaker for the $L200U20M4T-10L$ coil with varying frequency and a 44Ω load.

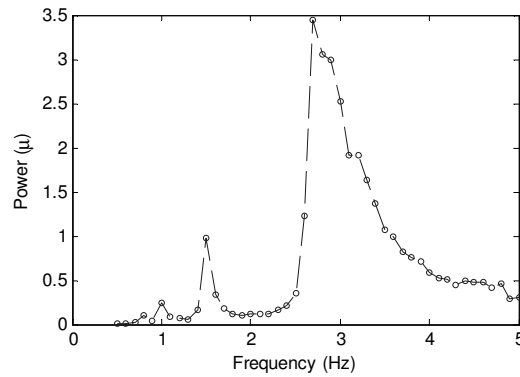
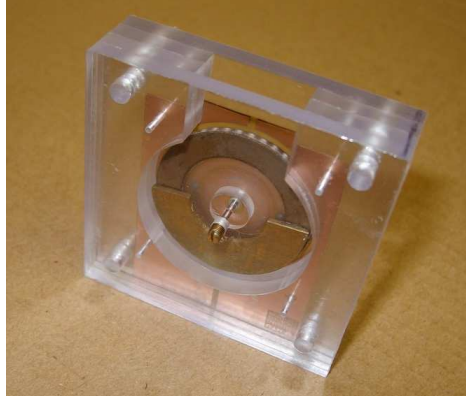
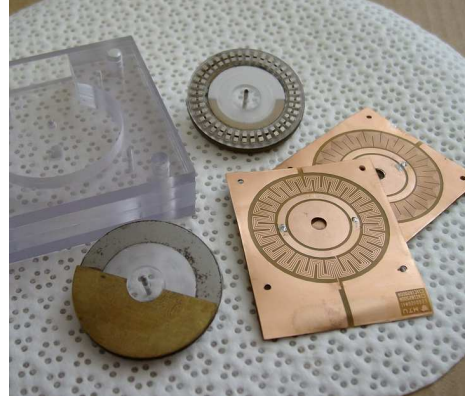


Figure 5.27: Power output results for the $\mu\text{VPG-1.1}$ prototype on a laboratory shaker for the $L200U20M4T-10L$ coil with varying frequency and a 44Ω load.



(a) A brass vee jewel assembly (the brass screw on the shaft) for adjustment can be observed on the prototype.



(b) Prototype components including rotors with different mass and two different coils.

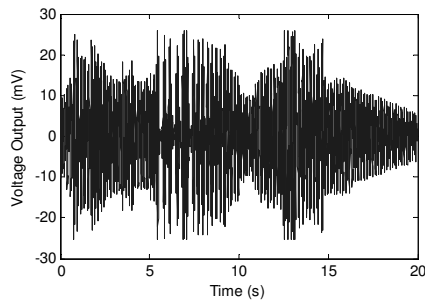
Figure 5.28: μ VPG-1.2 prototype photo.

5.3.4 Fourth Prototype: μ VPG-1.2

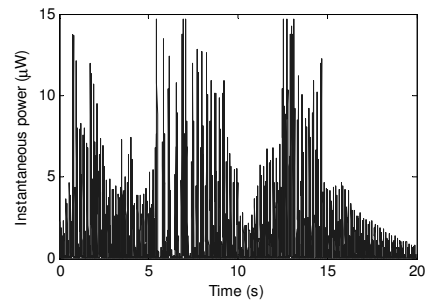
The prototype μ VPG-1.2 was built to test the jewel bearings as opposed to the ball bearing sets. Jewel bearings are used in the wristwatch industry and in sensitive measuring equipment for their low friction, with friction coefficients as low as 0.10-0.15 for steel on sapphire⁵. The watch industry has used them for more than a century for low-load and low-speed applications, and they are also considered as maintenance-free bearings in precision mechanisms. Preliminary tests showed that the oscillation time was least twice what it was when compared to the previous prototype under the same conditions. This prototype is shown in Fig. 5.28.

This prototype was tested for suitability of energy generation from body motion. A preliminary test was performed using a L200U20M4T-2L coil at two body locations, hip and ankle. Results are presented in Fig. 5.29 for a coil with a measured internal resistance of $10\ \Omega$ and an external load of $10\ \Omega$. RMS voltage output was found to be slightly larger than the previous walking test, although only a 2-layer coil was used. Power output was calculated to be $1.5\ \mu\text{W}$ at the hip location while free walking and $2.3\ \mu\text{W}$ at the ankle location. A larger number of coil layers, larger magnet area, and larger number of wires per coil (with reduced wire linewidth) should increase the induced voltage and the power generated in future prototypes.

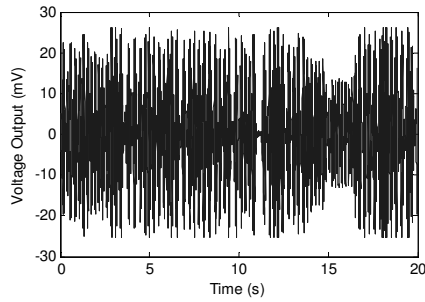
⁵<http://www.birdprecision.com/PDFs/jewelbearings.pdf>, Retrieved in 2010-06-27.



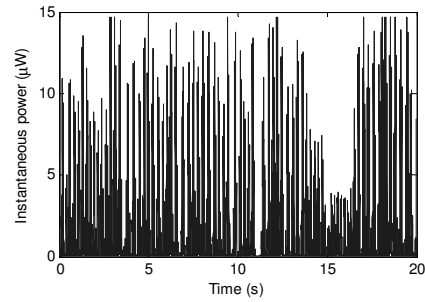
(a) *Instantaneous voltage output at the hip. Average voltage was 8.3 mV.*



(b) *Instantaneous power output at the hip. Average power was 1.5 μW.*



(c) *Instantaneous voltage output at the ankle. Average voltage was 10.4 mV.*



(d) *Instantaneous power output at the ankle. Average power was 2.3 μW.*

Figure 5.29: *μVPG-1.2 prototype results while free walking.*

5.3.5 Fifth Prototype: μ VPG-1.3

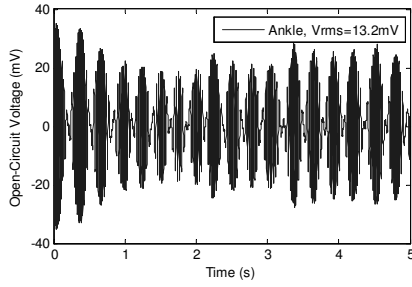
After evaluating the increase in induced voltage due to increasing wire length and number of turns per coil, a fifth prototype with larger magnets was examined. Discrete 5.1x1.1x1.1 mm magnets as opposed to the 2x1x1 mm previous magnets should provide better area coverage resulting in a higher induced voltage. A coil with 2 mm nominal radial length had wires that measured 3.1 mm whereas the previous prototype's rotor arrangement only provided a radial coverage of 2 mm in length. The new rotor was expected to provide at least a 50% increase in the induced voltage.

A free walking test with the generator placed on several body locations (ankle, knee, hip, wrist, and elbow) for 10 seconds was performed. A L200U20M4T-2L coil and a single rotor, 1.6 g proof mass, and 20 pole-pairs with 5x1mm individual magnets (20P1R5X1MM) finalized the generator components. These results are presented in Fig. 5.30. The locations with higher energetic figure of merit, σ_ω , presented the highest induced voltages. The leg locations presented the higher induced voltages (the ankle being the highest, and the hip the lowest), while the arm locations (with the elbow being the highest) were second. The induced voltage from the wrist location during free walking was the smallest, and this seems to indicate that this topology is not the best design for this location, although, if forcibly shaken, induced voltage can surpass the ankle result.

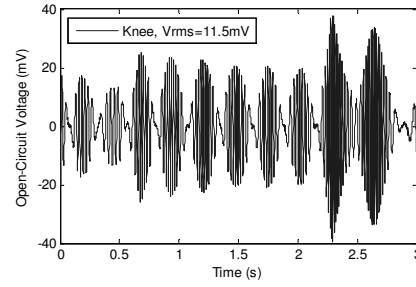
Power output results from the Fig. 5.31 indicate at least a 50% increase in power generated was obtained when compared to Fig. 5.29 for the previous prototype. For example, the power output was as high as 3.9 μ W for the ankle (from 2.3 μ W for Fig. 5.29). Therefore, further prototypes with a planar coil having larger radial dimensions and/or dual-rotors for increased flux density and higher proof-mass should produce a higher power output.

5.3.6 Sixth Prototype: μ VPG-1.4

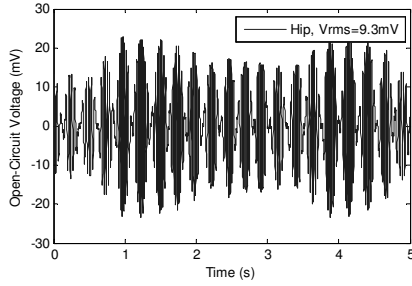
Fig. 5.32 shows the μ VPG-1.4 prototype built with a generator volume of 2 cm³ (the volume of the stator and rotor without the casing) and with two rotors to increase the magnetic flux (as indicated by the results from Section 4.3.1 on page 69). Twenty PM pole-pairs for the rotor assembly were made of discrete NdFeB magnet pieces (1.1x1.1x5.1 mm) inserted radially in a slotted 25 mm CNC machined PMMA disk. Two eccentric proof masses (1.6 g each, made of brass) were added to the two-rotor assembly. Two PMMA casing structures were fabricated with a cavity for the generator parts. This prototype was assembled by placing a planar coil in between the two rotors (1 mm gap separation) using an alignment fixture. Jewel bearings were used to provide low-friction rotor support. Coil resistance for each layer was calculated as 4.4 Ω (200 μ m linewidth), but measured as 4.9 Ω . The difference is explained by copper undercutting while etching as evidenced by micrograph analysis, as shown in



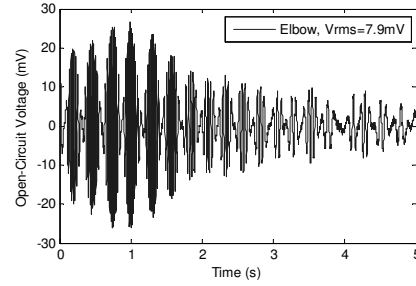
(a) Voltage output at the ankle.



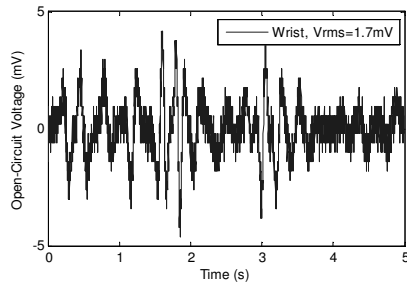
(b) Voltage output at the knee.



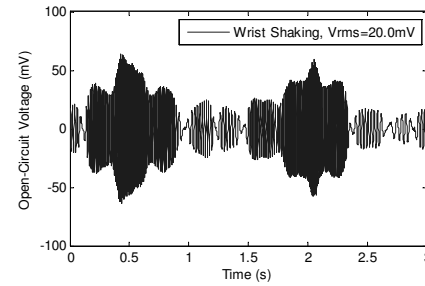
(c) Voltage output at the hip.



(d) Voltage output at the elbow.



(e) Voltage output at the wrist.



(f) Voltage output at the wrist while hand shaking.

Figure 5.30: Open-circuit results for the μ VPG – 1.3 prototype while free walking.

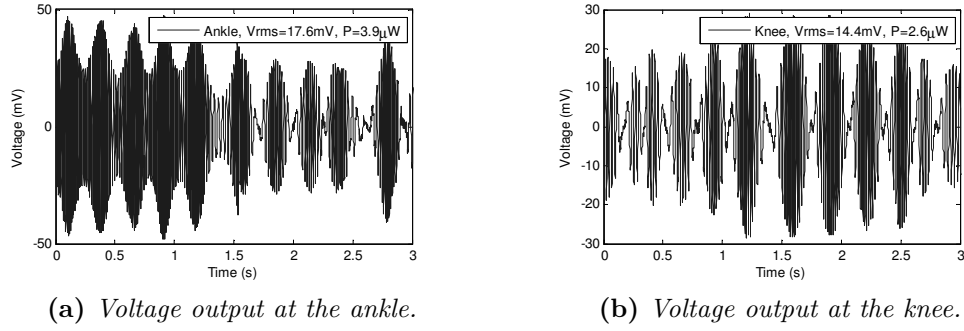


Figure 5.31: μ VPG – 1.3 prototype generation results with a 10Ω load while free walking.



Figure 5.32: μ VPG-1.4 prototype photo (L200U20M4T-2L-20P2R5X1MM).

Fig. 5.33. On average, the nominal $200\mu\text{m}$ linewidth was reduced to around $180\mu\text{m}$, while the nominal spacing increased to $120\mu\text{m}$ from $100\mu\text{m}$ for this design.

This prototype was tested on the body locations described in Fig. 3.5 on page 37: ankle, knee, hip, chest, wrist, elbow, upper arm (named shoulder for simplicity), side of the head, and back of the head of one individual. In order to provide a better comparison platform, the tests were performed on a motor-driven treadmill (Stairmaster 2100 Treadmill) at several walking speeds 1.0, 1.5, 2.0, 2.5, 3.0, 3.5 and 4.0 mph (0.45, 0.67, 0.89, 1.12, 1.34, 1.56, 1.79 m/s). The DATAQ DI-710-ULS wearable sensor platform, described in the Section 3.4.1 on page 36, was used to record the waveforms. A L200U20M4T-4L (linear end, $200\mu\text{m}$ linewidth, 20mm nominal radial length, 4 turns, and 4-layers) coil with internal resistance of 20Ω was used. Generated voltage measurements were recorded for periods of 60 seconds for each

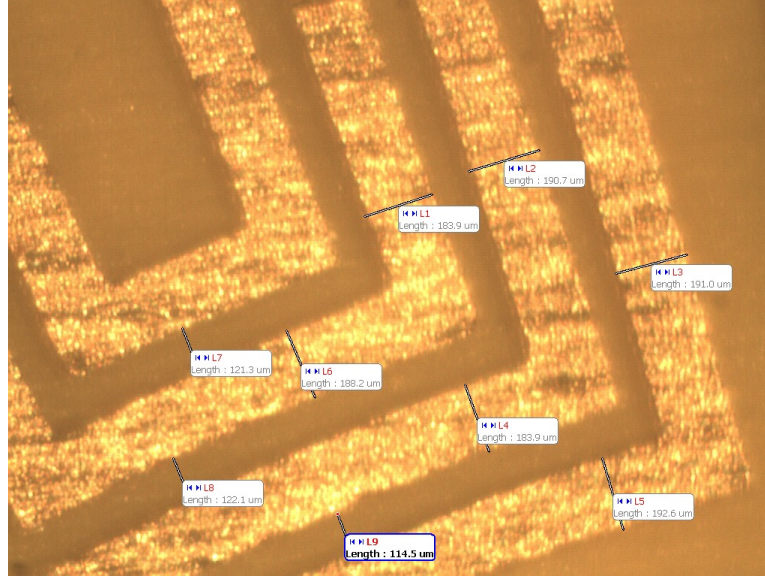


Figure 5.33: Micrograph analysis for a L200U20M4T coil, 5X magnification.

treadmill speed for a matching load of 20Ω . The device was encased in a custom-made package which was strapped to the body.

Results are presented in Fig. 5.34 and Fig. 5.35. The results exhibit three distinct zones for energy generation (high, medium, and low energy zones). The high energy zone is composed by the ankle and knee locations; the medium energy region is made at the hip, chest, elbow, and shoulder locations; while the low energy part is constituted at the wrist, side of the head, and back of the head. At walking speeds between 1mph to 4mph the voltage varied from 1 to 10 mV for the lower region, and ranged from 10 to 50 mV for the medium zone, and from 40 to 100 mV for the upper region.

Fig. 5.35 includes a shaded area describing the average walking speeds for younger (14-64 years old) and older (more than 65 years old) pedestrians for establishing further comparisons. At the evaluated walking speeds (1mph to 4mph) the generated power ranged from 0.01 to $1\mu\text{W}$ for the less energetic region (wrist, side of the head, and back of the head), and varied from 1 to $20\mu\text{W}$ for the medium energy zone (hip, chest, elbow, and shoulder), and from 20 to $100\mu\text{W}$ for the highest generating region (ankle and knee). A maximum power of $234\mu\text{W}$ ($137\text{mV}_{\text{rms}}$) was obtained when walking at 3mph (1.34m/s) with the generator placed vertically on the ankle (for a power density of $117\mu\text{W}/\text{cm}^3$). Fig. 5.36 shows the results for the ankle location with 382 mV peak and 1.84 mW peak,

Power generation for the average walking speeds is summarized in Table 5.2. It can be observed that the tested generator produced between $100\text{-}200\mu\text{W}$ of power at the ankle location, from $50\text{-}70\mu\text{W}$ at the knee, from $4\text{-}20$ at the hip, $\sim 2\mu\text{W}$ at

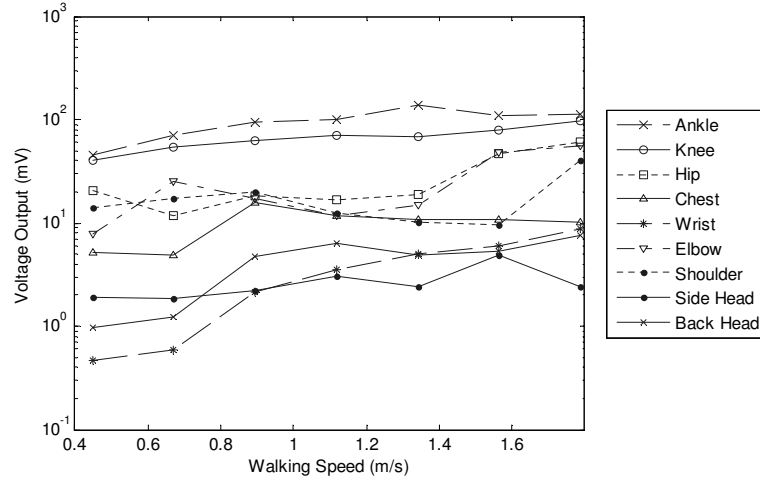


Figure 5.34: RMS voltage output results for the treadmill test of the μ VPG-1.4 prototype.

the chest, $\sim 0.3 \mu\text{W}$ at the wrist, $2\text{--}20 \mu\text{W}$ at the elbow, $\sim 2 \mu\text{W}$ at the upper arm (shoulder), $\sim 0.1 \mu\text{W}$ at the side of the head, and 0.4 at the back of the head. Upper body locations produced power on the order of $1 \mu\text{W}$, except the elbow that can produce up to $20 \mu\text{W}$. Leg locations were able to produce up to $200\times$ higher values.

As expected from the energetic figure of merit analysis from Chapter 3, the more energetic the location, the more power produced. This explains why the lower limbs (ankle being first and knee being second) produced a larger amount of power in comparison to the upper body. The lower than expected power output at the wrist location might be due to the generator orientation. On most body locations the generator was placed vertically without much deviation from a vertical-plane and aligned to the sagittal or frontal plane as described in Fig. 3.5 on page 37, but this orientation could not be maintained on the wrist while walking. This in turn, reduced the generator proof-mass movement decreasing the power generation. This seems to confirm that this kind of topology is not adequate for the wrist location because it is highly dependent on its orientation being as parallel as possible to the sagittal or frontal planes.

5.3.7 Seventh Prototype: μ VPG-1.5

The results in Fig. 5.35, indicate that optimized generators should be able to generate a larger amount of power than has been found in the above examples. Therefore, μ VPG-1.5 prototypes were built with a coil with a larger radial dimension, 5.1mm , matching the length of the commercial magnets. A new coil, termed as L200U51M4T (linear ends, $200 \mu\text{m}$ linewidth, 5.1mm radial length, 4 turns) was fabricated. Fig.

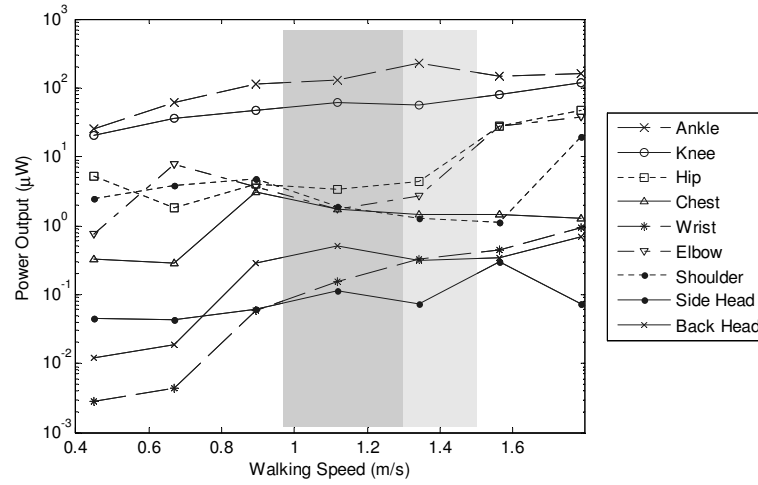
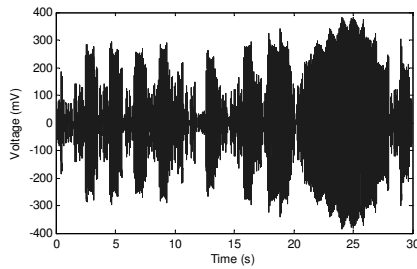
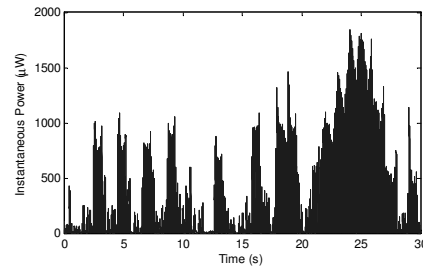


Figure 5.35: Power output results for the treadmill test of the μ VPG-1.4 prototype. Darker-shaded region is for older pedestrians walking speeds (0.97-1.3 m/s), while the lighter-shaded area is for younger pedestrian walking speeds (1.3-1.5 m/s). Average walking speeds of older and younger pedestrians from [56].



(a) Voltage output, 382 mV peak.



(b) Power output, 1.84 mW peak.

Figure 5.36: Results for the generator located at the ankle while walking at 3 mph.

Table 5.2: *Power generation from Fig. 5.35 for the average walking speeds.*

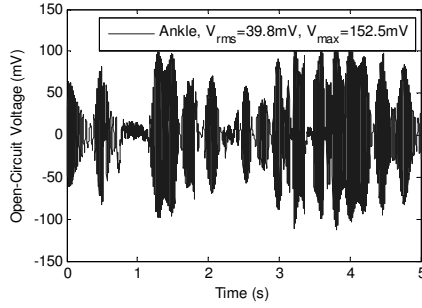
Body	Older pedestrian (0.97-1.3m/s)	Younger pedestrians (1.3-1.5m/s)
Location	Power generation (μ W)	Power generation (μ W)
Ankle	110-200	200-180
Knee	50-60	60-70
Hip	4-5	5-20
Chest	3-2	2-1.5
Wrist	0.09-0.3	0.3-0.5
Elbow	3-2	2-20
Shoulder	4-2	2-1
Side of the Head	0.08	0.08-0.2
Back of the Head	0.4	0.4

5.37 and Fig. 5.38 show the results from free walking using a 100 μ m thick 2-layer coil with the generator at several body locations. Induced voltages were as high as 39.8 mVrms (152.5 mV peak) for the ankle location and 30.5 mVrms (100.2 mV peak) for the knee location. The hip and chest produced similar results with \sim 13.5 mVrms (\sim 76 mV peak), elbow and shoulder also generated similar voltages with \sim 20 mVrms (\sim 75 mV peak), and finally the wrist and side of the head were found to provide similar results too, \sim 4 mVrms (\sim 25 mV peak). If a 10-layer 100 μ m linewidth coil is used under these conditions, the induced voltages should increase around 10 times. Therefore, the leg locations could provide more than 300 mVrms (>1 V peak), hip and chest could provide more than 100 mVrms (>700 mV peak), elbow and shoulder could generated \sim 200 mVrms (>700 mV peak), while the head and wrist could provide \sim 40 mVrms (>250 mV peak). This makes the leg and arm locations (except the wrist) potential candidates for generators that could provide a DC voltage via semiconductor rectification with Schottky diodes since their threshold voltages are on the order of 200 mV.

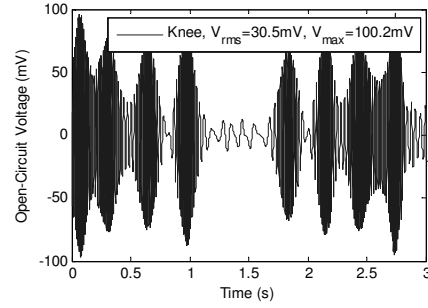
5.4 Summary

Fabrication

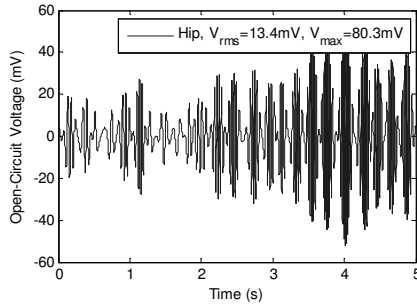
- Multiple layer coils were fabricated by photolithography from commercial copper-clad polyimide film. Coils were stacked and bonded with cyanoacrylate to manufacture multi-layer assemblies. Two-layer coils were as thin as 80 μ m thick while a 10-layer coil was up to 430 μ m thick (18 μ m thick copper and 20 μ m thick polyimide).



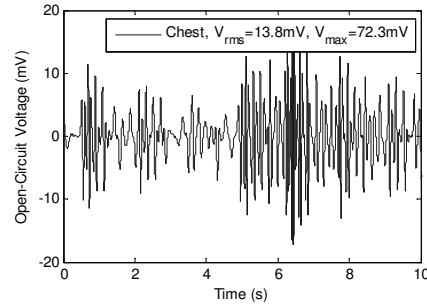
(a) Open-circuit voltage results at the ankle.



(b) Open-circuit voltage results at the knee.

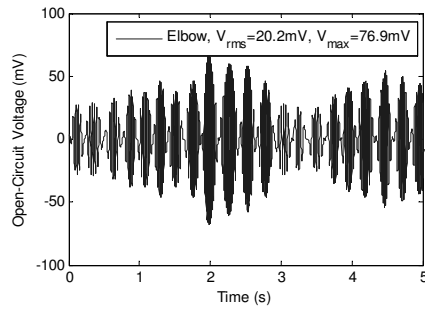


(c) Open-circuit voltage results at the hip.

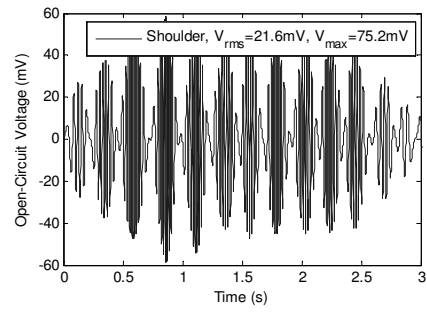


(d) Open-circuit voltage results at the chest.

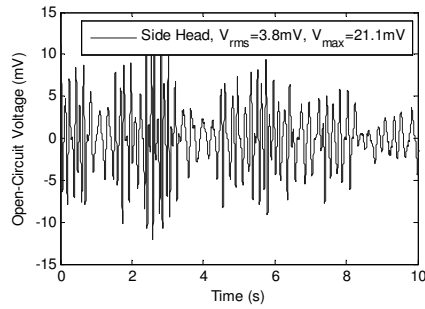
Figure 5.37: Free walking results for the μ VPG-1.5 prototype at the leg and chest locations.



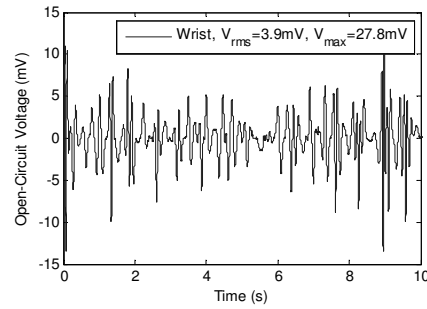
(a) Open-circuit voltage results at the elbow.



(b) Open-circuit voltage results at the upper arm (shoulder).



(c) Open-circuit voltage results at the side of the head.



(d) Open-circuit voltage results at the wrist.

Figure 5.38: Free walking results for the μ VPG-1.5 prototype at upper body locations.

- The rotors and the packaging were machined from PMMA and/or polycarbonate using CNC milling processes. Commercially available prismatic magnets were used for the rotor assembly; brass was used for the proof mass while jewel bearings completed the assembly.

Prototypes

- $\mu VPG - 0.5$: Tested for proof of concept using two semicircular rotor discs with disc magnets and wire-wound coils. Higher power output was found near the resonant frequency using a matching load on a laboratory shaker test ($0.09 \mu W$ at 5 Hz).
- $\mu VPG - 1.0$: A single layer planar coil (1.3 mm radial wire length), single rotor (20 pole-pairs and $2 \times 1 \times 1$ mm magnets), and single ball bearing design achieved $0.3 \mu W$ of power on a laboratory shaker near its resonant frequency (2.5 Hz). The design was found to require an additional ball bearing to avoid an observed shaft tilt.
- $\mu VPG - 1.1$: This prototyped used two ball bearing sets as suggested by the previous design. A 6X increase in power output was found for this design when compared against the previous prototype (up to $2 \mu W$ employing 1.5X larger radial wires and a 4-layer coil, 3.3 mm radial wire length).
- $\mu VPG - 1.2$: This design used jewel bearings for reduced friction when compared to ball bearings. A 2-layer coil prototype produced $1.5 \mu W$ at the hip location and $2.3 \mu W$ at the ankle location when tested while free walking.
- $\mu VPG - 1.3$: This prototype used $5.1 \times 1.1 \times 1.1$ mm permanent magnets. Radial wire length coverage by the new magnets increased to 3.3 mm from 2 mm, for a calculated 50% increase in induced voltage. A 2-layer coil test at the ankle location provided $3.9 \mu W$ when free walking.
- $\mu VPG - 1.4$: This design used two permanent magnet rings with a 4-layer planar coil placed in between. At the average walking speed of 1.3 m/s (~ 3 mph) power was found to be as high as $200 \mu W$ at the ankle, $60 \mu W$ at the knee, $5 \mu W$ at the hip, $2 \mu W$ at the chest, $0.3 \mu W$ at the wrist, $2 \mu W$ at the elbow and shoulder, $0.08 \mu W$ at the side of the head, and $0.4 \mu W$ at the back of the head.
- $\mu VPG - 1.5$: This prototype was tested with a 2-layer planar coil having 5.1 mm radial length wires. Voltage peaks as high as 152 mV were obtained when free walking with the device placed at the ankle location, and 100 mV at the knee location.

Next chapter will evaluate the results from the prototype testing and compare them to the modeling analysis from Chapter 4.

Chapter 6

Discussion of Results

Power generation for this generator topology was found to be proportional to the square of the induced voltage, and the induced voltage was described to be proportional to the kinematics (angular velocity), the magnetic field, and the geometry/configuration (the number of pole-pairs, the number of wires, and the radial wire length) in the theoretical analysis of our electromagnetic generator design. The experimental evaluation of these parameters and its relationship to the theory and models in Chapter 4 is discussed in this section.

6.1 Model and Experiment Comparison

Due to the complexity of the pendulum design kinematics, the modeling and experimental comparisons were made for a proof mass released at a known angle and followed until the oscillations were damped out for the generator placed vertically. This approach provided useful information about the relationship between the generator geometry and its kinematics.

Fig. 6.1 compares the model and the experimental results for a proof mass released from a 45° angle (Fig. 6.2 shows an enlarged detail) while Fig. 6.3 presents the results from an initial amplitude of 90° (Fig. 6.4 shows an enlarged detail). The induced voltage follows the model given in Eq. 4.16 (on page 68), where it is proportional to the generator angular velocity (kinematics), magnetic flux intensity, and coil configuration/geometry (number of pole-pairs, number of layer and radial wire dimensions). The model was elaborated for the L200U20M4T-4L coil, with 20 pole-pairs, 0.2T of magnetic field intensity (from FEA analysis), and a damping factor $\zeta = 0.035$.

It can be seen from Figures 6.1 and 6.2 that the simulated voltage waveform describes well the experimental results, although the estimated voltage was 27% larger than the measured value which led to a theoretical calculated power output 60%

larger. For the 90° test, the expected voltage was 31% larger than the recorded value, leading to a 72% higher power output.

It can also be observed in Fig. 6.1 and Fig. 6.3 that the modeled signal takes longer to decay than the experimental data. One can hypothesize that this difference could be due to air damping, bearing friction, and electromagnetic damping, all of which were not included in the model. This explains the larger calculated RMS voltage (and larger power output) from the simulation when compared to the test results. The different rate of decay between the experimental results and the model can be explained by an increase in friction between the rotors and stator due to slight misalignment of the generator components while performing the test. Therefore, a model that includes this friction should account for a better simulation, but, of course, the best solution would be to minimize this friction by better alignment of the generator components. Further, friction from air damping can be minimized by packaging the generator in vacuum.

Since this test was performed for an initial amplitude of 45° , there is less than 4% deviation in the pendulum period. The model assumes a constant period while the actual period is varying, as discussed in Chapter 4 (page 63). This variation can be better appreciated when the proof mass is released with a larger initial amplitude, as shown in Figures 6.3 and 6.4, for an initial amplitude of 90° . Fig. 6.4 clearly presents this frequency shift.

The model is also found to describe the beating due to the interference of the oscillating pendulum frequency and the induced voltage frequency resulting from the 20 pole-pairs count (for a 360° generator rotation there are 20 voltage peaks due to the 20 pole-pairs). Thus, for smaller pendulum amplitudes there are a smaller number of these voltage peaks. This is more clearly depicted in Fig. 6.2. The slight mismatch variations between the model and the test are thought to be due to the varying period and to initial misalignments (the initial angle not being exactly 45° or 90° ; and the proof mass being released from an angle that does not necessarily made the permanent magnet pole-pair position coincide with a coil pole-pair placement).

6.1.1 Kinematics

One of the prototypes ($\mu VPG-1.4$) was also tested in order to compare the experimental results with the large amplitude nonlinear pendulum model. To evaluate this, a recording with a high speed camera (Fastcam APX RS with Photron software) was made using a 60 mm lens at 1000 frames per second (FPS) and shutter speed of $1/1000$ s. The prototype was assembled without a planar coil (to determine the mechanical damping) and released at a 90° angle. MATLAB was used for the processing of the recorded images. The nonlinear pendulum model from Eq. 6.1 (on page 133) was used to compare the results but using $\omega_0^2 \sin(\theta)$ as the restoring term leading to

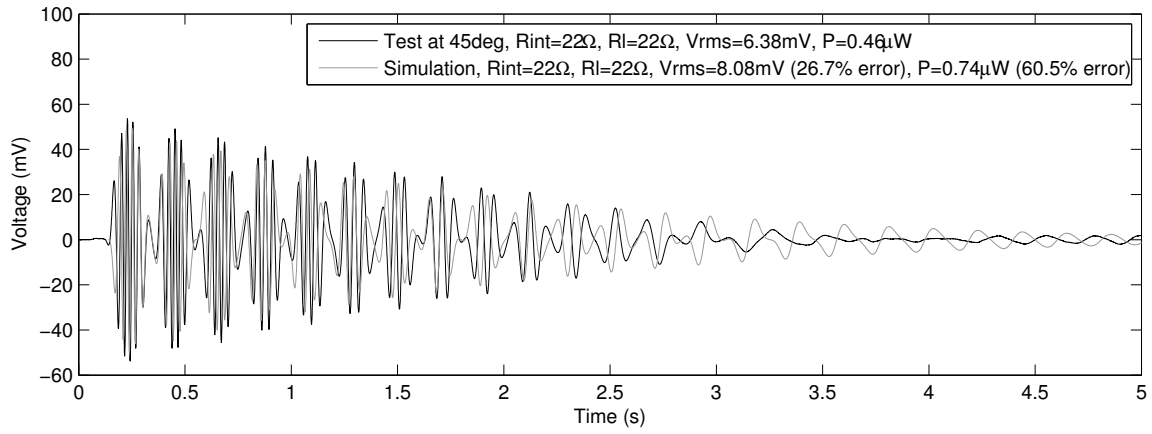


Figure 6.1: Comparison for a proof mass released at 45° (μ VPG-1.3, L200U20M4T-4L-20P2R1X5MM) with the developed model.

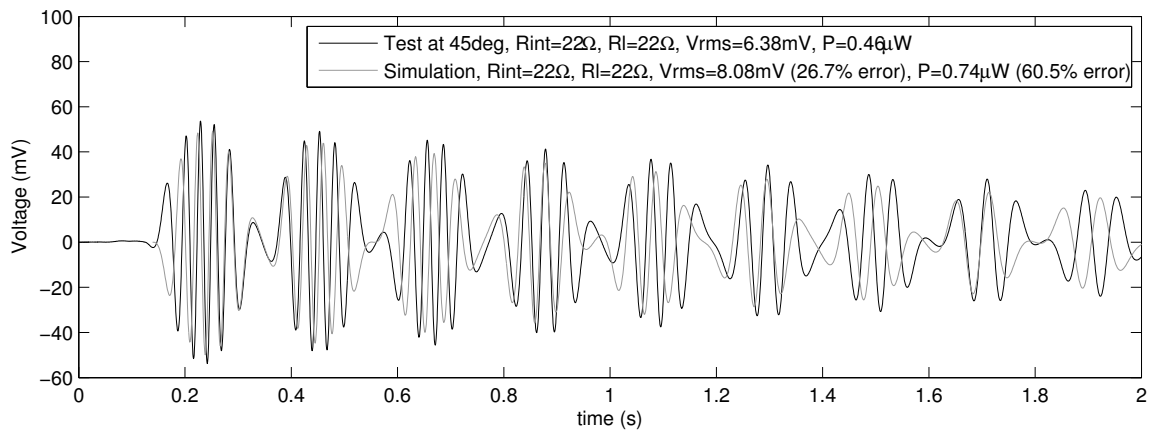


Figure 6.2: Detail of the comparison for a proof mass released at 45° (μ VPG-1.3, L200U20M4T-4L-20P2R1X5MM) with the developed model.

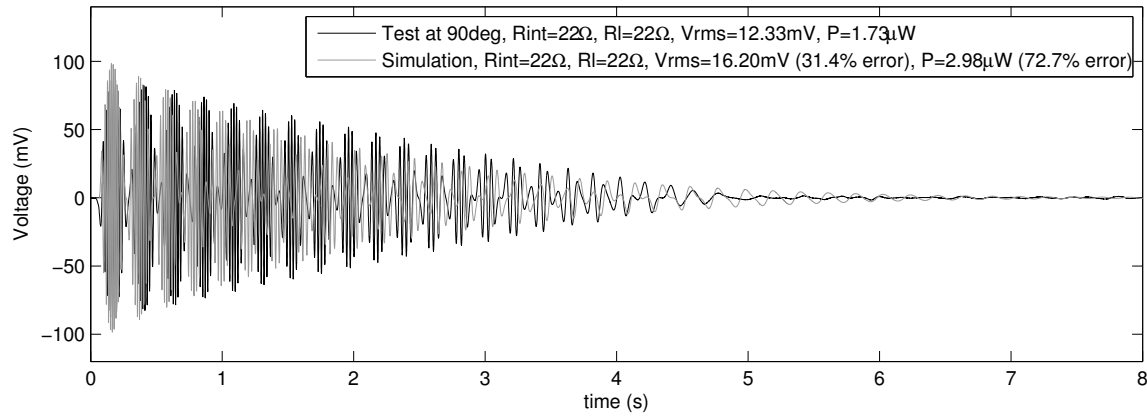


Figure 6.3: Comparison for a proof mass released at 90° (μ VPG-1.3, L200U20M4T-4L-20P2R1X5MM) with the developed model.

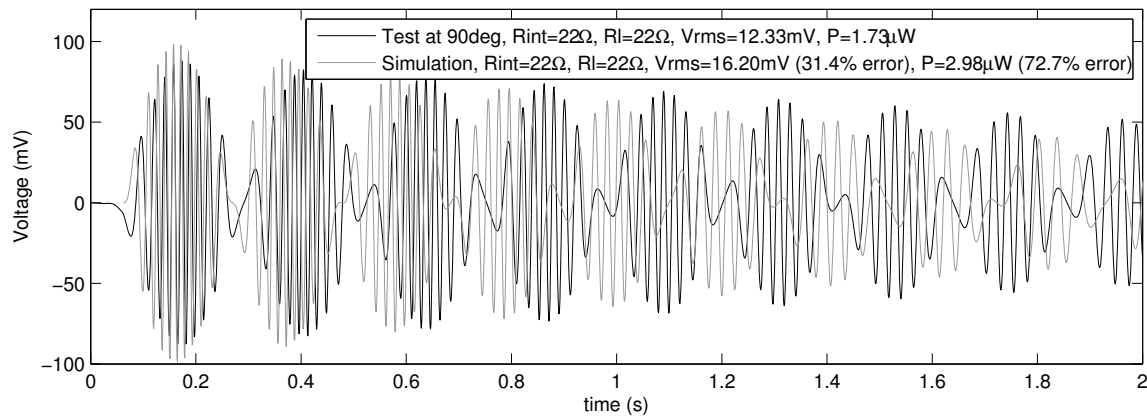


Figure 6.4: Detail of the comparison for a proof mass released at 90° (μ VPG-1.3, L200U20M4T-4L-20P2R1X5MM) with the developed model.

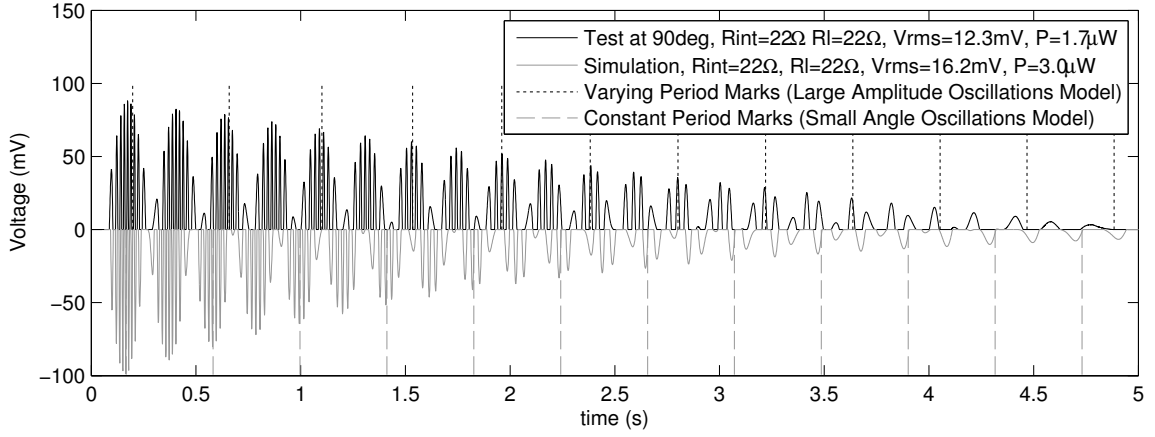


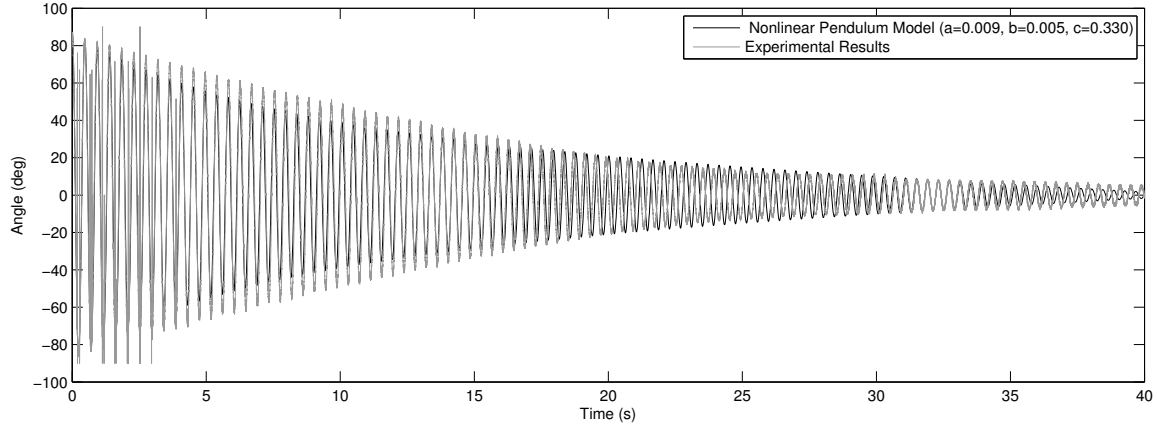
Figure 6.5: Comparison of variable vs. constant frequency for a proof mass released at 90° .

$$\frac{d^2\theta}{dt^2} + a \left| \frac{d\theta}{dt} \right| \frac{d\theta}{dt} + b \frac{d\theta}{dt} + c \operatorname{sign} \left(\frac{d\theta}{dt} \right) + \omega_0^2 \sin(\theta) \quad (6.1)$$

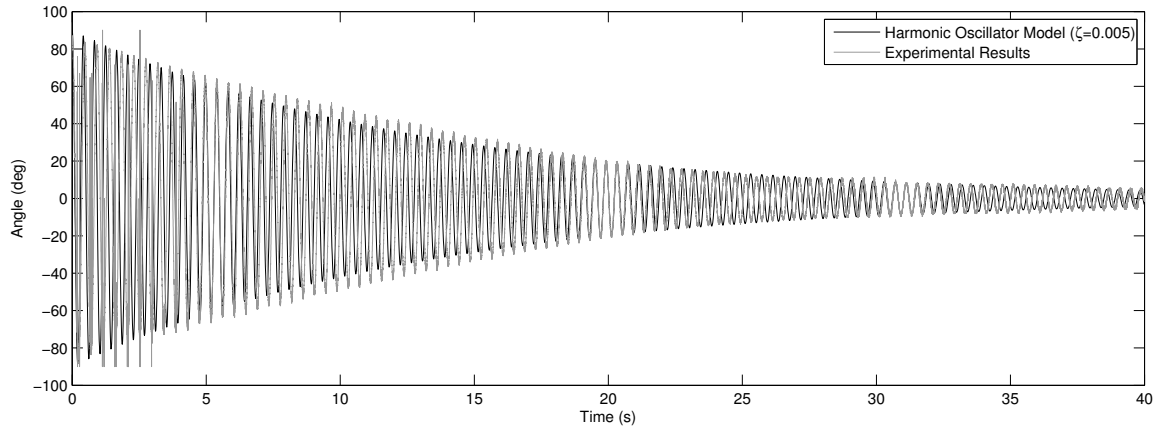
which needs to be evaluated by numerical methods in order to determine the angular displacement as a function of time.

The experimental results are presented with the best model match from Eq. 6.1 in Fig. 6.6a. Other than the mentioned artifacts the experimental results seem to follow the model well. Although the frequency is not perfectly matched, the damping coefficients found in the experiment do not accurately match the predicted displacement. The data showed up to an 11% difference between the model and the experimental results (the model being smaller). This might suggest that the damping coefficients vary with amplitude rather than being constant for this generator design. Based on the description provided in Section 4.3.2, the coefficient a is associated with turbulent air damping, b with viscous damping and c with bearing friction. The modeling then indicates a high dry friction damping coefficient with turbulent and viscous damping contributions to a lesser extent.

A simplified analysis was performed using Eq. 4.26 (on page 75) for a damped harmonic oscillator, as shown in Fig. 6.6b (with a constant damping ratio). Although this model has a constant frequency (the output waveforms do not match) the matching of the output displacement is slightly better than the nonlinear pendulum model (up to 7% difference between the model and the experimental data, with the model being smaller). Therefore, the simplified model of the harmonic oscillator can be used to describe the kinematics of the large amplitude pendulum model.



(a) Comparison of the pendulum oscillations from a proof mass released at a 90° angle and the large amplitude nonlinear pendulum model. The experimental results show some artifacts (sharp peaks) due to the image processing algorithm used.



(b) Comparison of the pendulum oscillations from a proof mass released at a 90° angle and the harmonic oscillator model. The experimental results show some artifacts (sharp peaks) due to the image processing algorithm used.

Figure 6.6: Pendulum oscillations from a proof mass released at a 90° angle compared against the nonlinear pendulum and the harmonic oscillator model.

6.1.2 Magnetic Field

Several tests were performed to evaluate the average magnetic field for the fabricated coils. A vertical milling machine was used to provide a constant speed source and adjustable vertical distance.

The induced voltage was found to be proportional to the rotational speed, as expected from Eq. 4.16 (on page 68), indicating a constant magnetic field. Since the L200U20M4T coil had 18% longer radial wires when compared to the L200U15M4T coil, then according to the Eq. 4.16 the induced voltage should be 18% larger, as shown in the comparison between Figures 6.7a and 6.7b. The comparison of the magnetic flux distribution for Figures 6.7a and 6.7b was found to differ by 7%. This variation might be due to inaccuracies while setting the initial air gap separation. The error bars show up to a 17% variation on the calculated magnetic flux values. This larger variation could be due to vertical movement of the planar coil due to aerodynamic effects (possibly by pressure difference resulting in an upwards lift force from the rotor moving at high speeds over the coil) since the planar coil was not held in place at the center region (it was secured with tape at the periphery).

Fig 6.8 presents the results for a 4-layer and a 6-layer coil design. Each 2-layer coil set had an average thickness of 100 μm , the two sets of 2-layer coil (4-layer set) were thicker than 200 μm , while the three sets of 2-layer coils (6-layer set) were thicker than 300 μm (the increase in thickness was due to the tape used to hold them in place). Since every 2-layer set had a thickness of 100 μm , the second set for the 4-layer arrangement received a smaller magnetic field, while the third set being the most distant had the least strong magnetic field. It was calculated that the second set of the 4-layer coil test had 15% less induced voltage than the set closest to the magnets, and the third set for the 6-layer coil test produced 15% less voltage than the previous coil set. This corresponds to a set of coils spaced farther apart than the suggested 300 μm assumption, near the 400 μm for the third coil set of the 6-layer coil test. Therefore, separation distance between coil layers must be kept at a minimum to induce a larger voltage.

Another coil was evaluated and compared against the previous results. A 6-layer (TC200U51M4T-6L) coil with 5.1 mm radial length and a total thickness of 250 μm was tested. The average magnetic field was calculated for the 6-layer coil using Eq. 4.17 (on page 68), the results are presented in Fig. 6.9. Since the coil thickness was 250 μm , there is little variation between the magnetic flux from the bottom-most and top-most layer and thus the calculated magnetic field was similar to that presented in Fig. 6.7. This indicates that Eq. 4.17 can be used to calculate the induced voltage (induced voltage is proportional to radial wire length and generator geometry) when the angular velocity is known.

In addition, the radial wire length for the TC200U51M4T coil is 54% longer than the L200U20M4T coil for a 54% increase in the induced voltage (measured as 45%).

This increment can be observed when comparing the results for the 6-layer coil tests from Fig. 6.8b for the L200U20M4T-6L test and the Fig. 6.9 for the TC200U51M4T-6L coil. This 9% in difference (to 45% from 54%) can be partially due to inaccuracies while setting the initial air gap separation for both tests, and possibly by the previously commented aerodynamic effects.

The magnetic field at a gap distance of 500 μm was found to be near 0.2 T, which is similar to the results presented from the finite element model (0.19 T) in Section 4.3.1 (on page 69). Although these results were calculated for 5.1x1.1x1.1 mm permanent magnets, it verified the magnetic field solution for a single rotor with similar configuration.

6.1.3 Q factor

The quality factor or Q factor is the dimensionless parameter that describes the ratio of the stored energy to the energy dissipated in one cycle (or the ratio of proof mass displacement to external displacement). It can be determined by the ratio of resonant frequency to the bandwidth at half the energy level (described in Fig. 6.10) as

$$Q = \frac{f_0}{\Delta f} \quad (6.2)$$

or by the evaluation of the parameters from Eq. 3.13 ($Q = 1/(2\zeta)$).

From the results in Fig. 6.6b, $\zeta_m = 0.005$ (subscript m for mechanical) represents a Q factor of 100 for the generator without a planar coil or by dry friction damping. For instance, the Q factor of a high precision mechanical clock is larger than 10,000 and between 100 and 300 for standard mechanical wristwatches¹. Thus, the Q factor of the generator without electromagnetic damping is on the order of those from mechanical wristwatches.

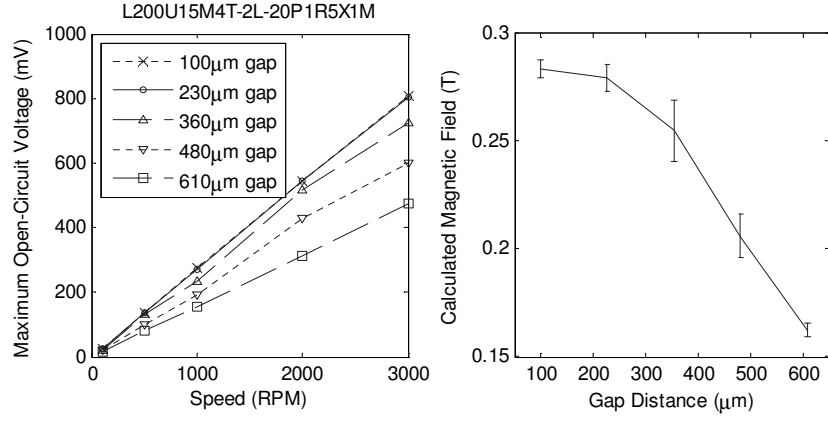
The model presented in Fig. 6.3 was based on the harmonic oscillator from Eq. 4.26 with a total damping factor (ζ_t) of 0.035 (from Fig. 4.14a). Therefore, the electromagnetic damping factor for this system is estimated to be $\zeta_e = 0.030$ ($\zeta_t = \zeta_e + \zeta_m$) for an overall Q factor of 14.

Following the definition of Eq. 3.15 (on page 33) and evaluating its last term leads to the electrical Q factor term (Q_e) of

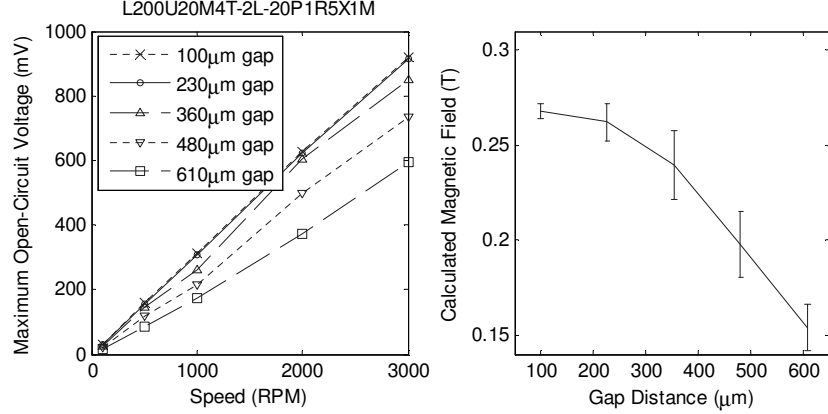
$$Q_e = \frac{\zeta_e}{2(\zeta_m + \zeta_e)} \quad (6.3)$$

From the previous results, this Q_e is found to be 0.4. Then, when replacing this term into the expression from Eq. 3.20 (on page 35) leads to

¹<http://www.orologeria.com/english/magazine/magazine004.html>, Retrieved 2010 07 20

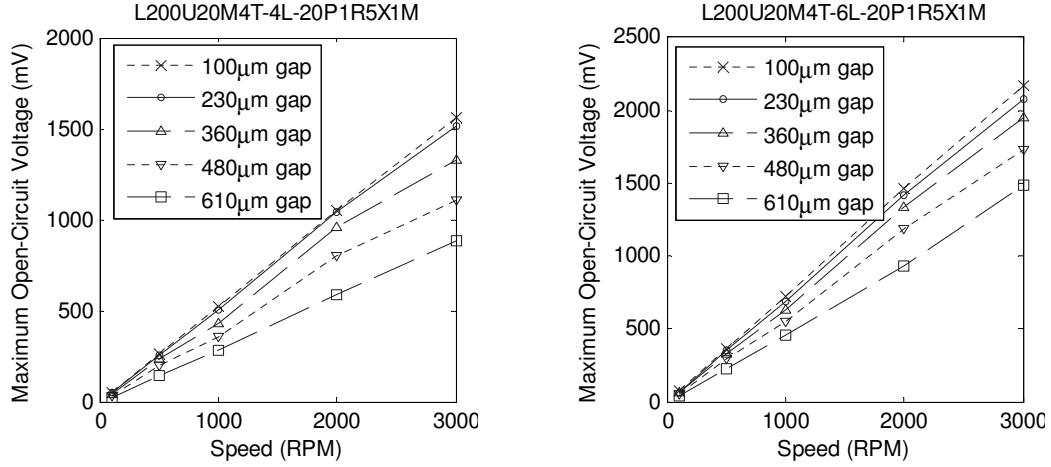


(a) L200U15M4T-2L coil at constant speed test. Nominal radial length is 1.5 mm (2.8 mm actual radial length). Error bars represent one standard deviation.



(b) L200U20M4T-2L coil at constant speed tests. Nominal radial length is 2.0 mm (3.3 mm actual radial length). Error bars represent one standard deviation.

Figure 6.7: Coil evaluation at constant speeds for two different wire lengths.



(a) *L200U20M4T-4L* coil at constant speed tests. (b) *L200U20M4T-6L* coil at constant speed tests.

Figure 6.8: Coil evaluation at constant speeds for four and six layer stacks.

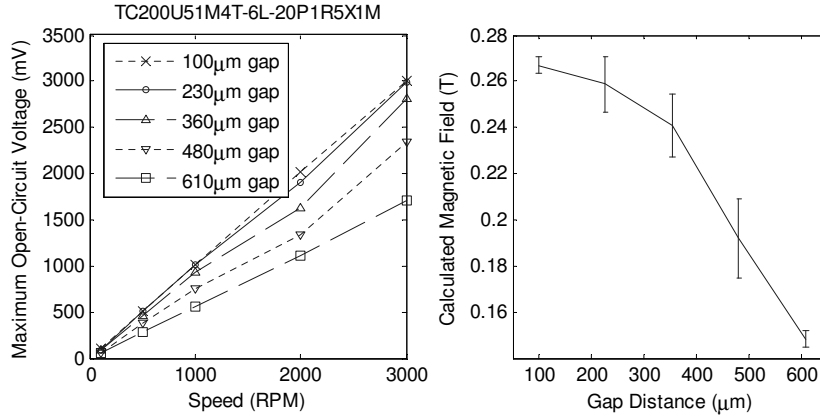


Figure 6.9: Coil evaluation at constant speeds for a 6-layer coil (*TC200U51M4T-6L* coil).

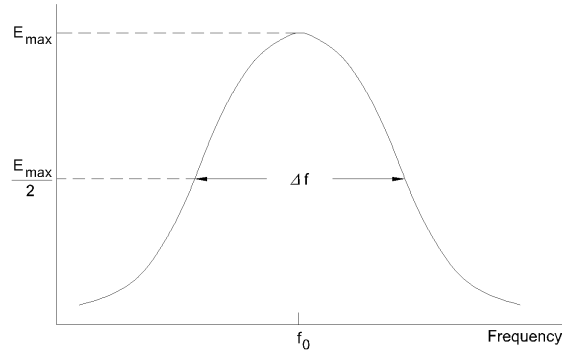


Figure 6.10: *Energy versus frequency plot.*

$$P_{max\ gen} \simeq \frac{1}{8}m\sigma\omega \quad (6.4)$$

Equation 6.4 refers to the maximum electrical power that this generator can produce under optimal conditions. This Q factor was obtained from a system released from an angle until the oscillations were completely damped. Different conditions provide different Q factors. For instance, the evaluation of the Q factor from a sinusoidal input source at a constant frequency (laboratory shaker test) using Eq. 6.2 in Figures 5.15, 5.19, 5.22, 5.25, and 5.27 reveals Q factors from 3.5 to 7.

Using this generator design at frequencies different than the resonant frequencies would result in lower power generation. From Fig. 5.27, the operation of the prototype at a frequency of 1.9 Hz produces approximately 5% of the peak power. The 1.9 Hz frequency was chosen since it is associated with average walking speeds as described on in previous chapters. However, the frequency components of body motion cover a wide band as shown in Fig. 6.11, and will vary from individual to individual and will vary as the activity (such as walking speed) varies. This figure shows the FFT analysis from the acceleration results (forward axis) at the ankle on the treadmill test at several walking speeds (1-4 mph). Because of this, a generator with a larger frequency bandwidth (or a smaller Q factor) could harness more energy from different gait frequencies, rather than a generator optimized for a single narrow band of frequencies based on average gait.

Considering that the actual generator topology is highly dependent on the generator resonant frequency (or its high Q factor) a design with a broad frequency range (or smaller Q factor) would be desirable since its power generation will not be highly dependent on a specific frequency. Generator topologies such as the commercial self-winding wristwatch studied (Kinetic brand from Seiko wristwatches) provide useful information. Applying the Eq. 6.2 to the experimental results presented in Fig. 5.12 (on page 105) reveals a Q factor of ~ 2 . This topology provides a relatively high

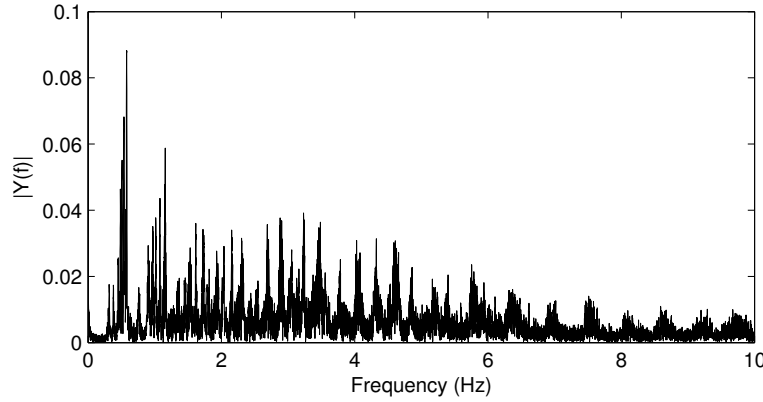


Figure 6.11: *FFT analysis of the acceleration (forward axis) at the ankle location while walking (1-4 mph).*

power output for frequencies from 3 to 5 Hz, with a peak near 4 Hz, but with power generation being less than 10% of the peak at frequencies below 2 Hz.

When comparing the Q factors of the fabricated prototypes against the self-winding wristwatch design, it is evident that a small Q factor is preferable over a larger Q factor because of the larger frequency bandwidth. Although a relatively large Q factor means a higher power output near its resonant frequency, a broader frequency input would include most body motion activities. Then a Q factor near 2 would generate energy more uniformly over a larger frequency bandwidth as observed from the self-winding wristwatch generator. Since the proposed prototype is based on a pendulum mechanism it has a relatively high Q factor (~ 100 without electromagnetic damping and 3.5-7 with electromagnetic damping), then generator topologies such as the self-winding wristwatch could be useful. The relatively low Q factor of the self-winding wristwatch could be due to the cogging torque between the permanent magnet on the rotor and the iron on the stator. Further investigation would be required to determine the low Q factor parameters for this design.

6.1.4 Power Loss by Eddy Currents

Based on the analytical model presented in Eq. 4.54 on page 85 (on page 4.54), the eddy current losses were evaluated for a round conductor with an identical area as the rectangular cross-section area coil wires. The electrical frequency was calculated by multiplying the device's resonant frequency (3 Hz was used for simplicity) by the number of pole-pairs (20). Table 6.1 shows the parameters used while Table 6.2 shows the calculated results. Only the steady-state case (constant speed) was considered, but actual results can be different since angular velocity on a pendular-design is not constant. It is evident that the eddy current losses are significant, up to $5.6 \mu\text{W}$ for

Table 6.1: *Eddy current loss parameters.*

Parameter	Value
Wire Length (mm)	2, 5
Wire Linewidth (μm)	100, 200
Equivalent diameter (μm)	48, 68
Peak Magnetic Field (T)	0.2
Electrical Frequency (Hz)	60
Copper Resistivity (Ωm)	1.68×10^{-8}

Table 6.2: *Eddy current loss for various coil configurations at constant rotational speed.*

Coil Condition	Eddy Current Loss (μW)	
	2-layer coil	10-layer coil
2 mm wire and 100 μm linewidth	0.22	1.1
2 mm wire and 200 μm linewidth	0.45	2.2
5 mm wire and 100 μm linewidth	0.56	2.8
5 mm wire and 200 μm linewidth	1.12	5.6

a 10-layer coil. However, as mentioned in the section 4.3.4 (on page 84), the eddy current loss can have a larger component than Eq. 4.54 predicts and the actual loss can be as high as twice the ideal model values summarized in Table 6.2. In the case of the $\mu\text{VPG-1.4}$ prototype placed on the ankle (walking on the treadmill), an eddy current loss of 2 μW for a L200U20M4T-2L coil from a maximum of 234 μW represents a 1% loss (for an ideal model at constant rotational speed). Since power generation is proportional to the rotational speed, then eddy current losses are expected to be proportional as well and be a small fraction of the generated power. In this case, the modeling of an oscillating pendulum (a varying rotational speed model) would provide different results under more realistic conditions

6.1.5 Summary

The induced voltage for this generator topology was found to be proportional to the kinematics (angular speed), the magnetic field, and the generator configuration (the number of wires, and the radial wire length). This is summarized as:

- Kinematics: The modeling of the kinematics from 4 was found to describe well the pendular movement for a proof mass released at a known angle. The nonlinear pendulum model described the varying frequency for a large amplitude pendulum model, while the damped harmonic oscillator model provided a simple description. Both models were found to match the experimental results.

- *Magnetic field:* The FEA analysis from Chapter 4 described a magnetic field of ~ 0.2 T at a distance of 0.5 mm over the magnet surface (20 pole-pairs, single rotor design). The experimental evaluation of a 20 pole-pair single rotor at a distance of 0.5 mm was also found to be ~ 0.2 T. Thus, FEA modeling can be used to determine the magnetic field of more complex geometries.
- *Generator configuration:* The magnetic field evaluation testing also compared the induced voltage for several numbers of coil layers, and two different radial wire lengths. It was found that the induced voltage was proportional to the number of stacked layers of coils. The induced voltage was also found to be proportional to the radial wire length over the range of 1.3 mm to 3.3 mm.

6.2 Evaluation

Chapter 3 described that the available power density for the ankle location was close to 30 mW/cm^3 during walking at 3 mph, yet only $234 \text{ }\mu\text{W}$ was produced when actual measurements were made. Using the power density definition from Eq. 3.21 (on page 35), the power density reached was $468 \text{ }\mu\text{W/cm}^3$ (0.5 cm^3 proof mass volume) or approximately 0.5 mW/cm^3 . This is $\sim 60\text{X}$ smaller than the theoretical limit, assuming a sinusoidal driven input motion.

In addition, the theoretical limit was calculated assuming a Q factor of one and with a design with a resonant frequency equal to the driving frequency. However, the tested prototype had a resonant frequency other than the gait frequency. Considering that body motion has a relatively broad frequency spectrum, energy harvesting from body activities would benefit from designs that produce energy under a relatively broad bandwidth (small Q factors).

A Q factor of 1, in the case of a linear generator, means that if the external motion source moves 1 m the generator's proof mass moves 1 m as well which is challenging for a small generator design. The theoretical limit will be smaller depending on the achievable Q factor for this kind of topology. When the generator was evaluated under a sinusoidal input waveform on a laboratory shaker the Q factor was found to be relatively high (>4). Relatively high Q factors make energy harvesters better suited for fixed frequencies, while body motion energy harvesters would benefit from lower Q factors.

Sasaki et al. [109] described a similar mechanism based on the Seiko wristwatch. The energy generation process was described as being produced by oscillatory or swinging motion, by transient rotation due to wristwatch posture change, and by self-excited rotation (the self-excited rotation mode happens when the rotor continues to rotate due to an initial impulse). It was suggested that the primary mode for energy generation in this wristwatch type was due to postural change rather than by the

inertial forces of the arm's motion. This can explain the reduced power output when this wristwatch mechanism was used in places different than the wrist, as noted by Gorge et al [41] when positioned on the chest.

Sasaki et al. [109] also described that the power output for this wristwatch mechanism can be up to 10 times larger when the rotations are maintained by means of self-excited rotations. This also seems to partially answer the increased power output when forcibly shaken as mentioned by Paradiso and Starner [87]. This self-excited rotation seems to explain the power peak presented in Fig. 5.36 near the 25 s mark, where the power output was twice the average peak magnitude. Therefore, in designing a device with the parameters from Eq. 2.4 on page 13, at least twice the average power output can be expected as evidenced by the self-excited rotations in Fig. 5.36.

6.3 Challenges

There are limitations that challenge energy scavenging at small scales such as the energy generation efficiency, energy density, rectification, energy storage and management, manufacturing, longevity, and packaging. A summary of these challenges is discussed to highlight some of the difficulties that need to be resolved in the near future for energy harvesting to be a practical energy source for portable, embedded, or implantable applications.

6.3.1 Power Generation and Efficiency

Energy generation from inertial approaches at smaller scales faces limitations due to the reduced mass sizes because power is directly proportional to mass. For example, a proof mass with a volume of 1 mm^3 , according to the Fig. 3.4, has a maximum available power of $1 \mu\text{W}$ (volumetric power density of 1 mW/cm^3) for a generator attached to a walking person. Yet, only a few reported devices are close to that figure of the volumetric power density. Hence, generator size, placement, and power requirements must be evaluated. Parallel-plate electrostatic generators need to have air-gap displacements between 0.5 and hundreds of μm in order to generate power comparable to electromagnetic or piezoelectric devices, as estimated by Roundy [104]. This displacement range severely challenges the implementation and stability of electrostatic generators. Electrical generators usually are more efficient with increasing sizes, this means that efficiency does not scale well with smaller dimensions. Furthermore Roundy showed that electromagnetic, piezoelectric, and electrostatic generation have the possibility of high coupling coefficients (0.6 to 0.8). Therefore, the main challenge is to design miniature energy harvesters with efficiencies as high as the models predict. Electrical generators are typically more efficient the larger they are, but trying to recreate high efficiencies at smaller scales is a difficult task. Finding materials with

the same properties as the bulk materials with tight tolerances, and same reliability as the larger counterparts while being cost competitive is also difficult. Rectification is still the biggest obstacle since the threshold voltages represent a large fraction of the low voltages produced, and this fraction of these voltages is lost.

6.3.2 Fabrication

Electromagnetic generators at the MEMS-scale are typically limited by the permanent magnet (PM) fabrication since MEMS-compatible processes cannot replicate bulk PM material properties. For example, sputtering and electroplating are limited to produce μm -sized thin films that exhibit weaker magnetic fields than the permanent magnets used in this project. Research in this area aims to resolve this limitation. Chin [23] showed that films made of PM powder have the potential for MEMS fabrication, and Niarchios [81] reported the development of PM materials and processes (including biomedical device applications). Considering that NdFeB is one of the more frequently used PM materials due to its properties, there is broad research for using this material at MEMS-scale. Pawlowski et al. [88, 89] reported NdFeB thick films (100-800 μm) by tape-casting (NdFeB power mixed with a polymer). Rieger et al. [98] covered a vacuum-plasma-spraying process that fabricates up to 1.2mm thick NdFeB PM with remeance as high as 600 mT. Topfer and Christoph, and Achotte et al. [127, 128, 1] have demonstrated mm-sized pole patterns.

Linear generators with free-sliding masses and rotational devices are also limited by low-friction technology to minimize the mechanical damping. Rotational devices are the most susceptible since low-friction MEMS-based bearings are needed. Several new technologies are being developed to overcome this limitation: micro ball bearings [38, 37, 138], rotating pivots [144], and magnetic bearings [28, 39]. In addition, generators under vacuum present fewer losses due to air damping, but create the need for special packaging. Packaging is also a constraint for devices operating in harsh conditions, such as bio-implanted applications.

Fabrication techniques at the micro scale are well established for piezoelectric and electrostatic generators because of the uncomplicated geometries they present. On the other hand, electromagnetic generators are limited by the availability of high-performance magnets and high-density coils at the micro scale, although they are preferred for energy generation at larger sizes. Piezoelectric and electrostatic generators are also characterized by their relatively high-voltages and low currents, whereas electromagnetic generators provide the opposite. Therefore, the selection of one of the transduction techniques is dependent on the energy source and the desired output characteristics for specific applications.

Reliability is a point to consider since this energy harvester uses a moving part (the rotor) and no long term studies were undertaken. Wristwatch technology can be employed since the mechanics of the generator are similar to those from the wristwatch

industry. Although being relatively complex mechanical devices, wristwatches are considered a reliable and proven technology. Therefore, wristwatch bearing system assemblies might be used and adapted to rotational energy harvesters to improve reliability and performance.

6.3.3 Rectification

The output for most energy harvesters is usually a time-variant AC signal, however DC rectification and voltage regulation are needed to power most electronic circuits. The forward-bias voltage for diodes on bridge rectification circuits (>200 mV for Schottky diodes) can be high for the low-voltage generated from some devices. In these cases, voltage multipliers have been employed to increase and rectify the output voltages.

Some of the limitations faced by the use of semiconductor p-n junctions can be overcome by the use of active electronics. Power-on-reset techniques and self-timed circuits have been proposed to avoid the threshold voltages from diodes [114, 5]. Other techniques, such as Application-Specific Integrated Circuits (ASICs) using low-threshold voltage diodes with voltage multipliers can have footprints as small as 1mm^2 [70]. Another approach that employs low energy dissipation circuits using a piezoelectric transducer, an on-off switch, and a two-diode bridge (called Synchronized Switch Harvesting on Inductor, SSHI) has been reported to increase the energy output by 120% [67]. A recent approach utilizing CMOS technology proposes an active two-stage rectifier (a negative voltage converter and an active MOS diode) [90]. The negative voltage converter uses four CMOS transistors to transform the negative part of the output into a positive potential, while the MOS diode controls the current direction. This circuit had a power consumption of $1\text{ }\mu\text{W}$ (1 Hz to over 100 kHz) with a voltage drop less than 20mV for a rectifier efficiency over 95% for input voltages in between 1.25-3.75 V. Mechanical rectification has also been investigated at MEMS-scale for electrostatic devices [79]. A prototype used an electret parallel-plate design where one of the plates also operated a mechanical switch for rectification purposes.

6.3.4 Energy Storage

Since the energy generation process from energy harvesting is heavily dependent on the availability of the external energy source, the produced energy must be stored for use when the energy source is unavailable. Capacitors and rechargeable batteries are the traditional energy storage elements that have been used for this purpose. Rechargeable batteries are preferable because of their high energy storage capacity, but they have a limited number of charging cycles. Capacitors can be charged quickly an infinite number of times, although the energy storage capacity is relatively low.

On the other hand, electrochemical double-layer capacitors (supercapacitors or ultracapacitors) provide almost unlimited recharges with relatively high energy storage capacity. Supercapacitors with sizes resembling a postage stamp with capacities of 5-19 F have been presented [31, 133]. Thin-film lithium batteries can also reduce the size of rechargeable power sources for biomedical applications [11, 45, 2, 15]. Studies reporting the successful use of rechargeable batteries using piezoelectric energy harvesters have also been carried out [118, 117].

Chapter 7

Societal Implications

7.1 Introduction

Any thought about electronics and their marvelous progress in the last few decades, brings to mind the need to carry a power cord or a battery pack for its use along with the device. However, the increasing cost of electricity and the pollution associated with fossil fuels remind us of the price of that progress. In addition, the technical marvels of modern life usually end up discarded in landfills, and the batteries that power most electronic portable devices are an environmental concern for the hazardous chemicals employed. Although recycling programs already are in operation around the globe, several thousand of tons of batteries are still discarded in landfills in the United States alone. What can be expected from the developing world? How sustainable can the future be if the pollution and the consumption of non-renewable energy resources continue their current trend? Environmental technology, or green technology, promises an answer.

History shows that technology has helped advanced societies use fewer resources, pollute less, and improve the standard of living. In the search for alternative technologies, energy harvesting is emerging as a new technology to continue this progress. The main advantage of this technology is that devices powered by energy harvesters have the possibility to diminish or even avoid battery use. This approach also provides a longer lifetime for portable electronic systems, as well as reducing the number of batteries and chemicals disposed into the environment.

Energy harvesting, or energy scavenging, is the process of transforming energy from external sources (such as wind, thermal, solar, or mechanical motion) into mainly electrical energy for powering portable autonomous devices. Although this technique has been employed recently in new technological developments for energizing miniature or portable electronics (e.g. shake-driven flashlights, solar-powered calculators, crank-driven radios), the history dates back to the waterwheel and the

windmill. The first energy harvester in history that is known to power a portable device is the self-winding watch. In this watch, a spring is wound by a mechanism using an eccentric mass that moves as the person walks. This idea was first described by Swiss watchmaker Abraham Louis Perrelet in 1770¹, but it wasn't until the 1960s that this mechanism became better known.

New technologies have profound implications to society because, in addition to the direct benefits they bring, sometimes there are some unexpected consequences or environmental concerns, such as the case for oil, pesticides, or nuclear power plants for their realized and potential hazards. Therefore, it is likely that society will embrace promising new technologies but will also question them for their potential unwanted outcomes. At this point of technology development, past experiences can be used to highlight possible future scenarios for the case of energy scavenging and systems they would power. Learning from history can help us understand the societal implications and avoid missteps in the introduction of new technologies.

7.2 The Environmental Battery Reality

With the advent of the 20th century came power lines and power cords, then came freedom from the cables only to be attached to batteries. This new marvelous wireless world in the 21st century has brought simplicity and portability in the shape of battery-operated devices (e.g. cellular phones, digital cameras, wireless keyboards and mice, portable videogames and music players), but this approach has made the world addicted to batteries (disposable or rechargeable). Although battery technology has evolved incredibly in the last decades since the voltaic pile in 1800 by Alessandro Volta, it has not kept pace with other technological industries as shown in Fig. 1.1 (on page 4).

A battery is a combination of electrochemical galvanic cells that store chemical energy to be released as electrical energy. They commonly are classified into disposable (primary cells) and rechargeable (secondary cells). Zinc-carbon and zinc-manganese (alkaline) are the most used materials for primary cells. Battery components consist of an anode, a cathode, and an electrolyte, which are made of an array of potentially hazardous materials such as copper (Cu), zinc (Zn), lead (Pb), mercury (Hg), cadmium (Cd), nickel (Ni), manganese (Mn), and lithium (Li).

In the past, zinc-carbon battery technology used to employ lead, cadmium, and mercury, even though cadmium is one of the most hazardous elements. By 1995 more than 80% of the rechargeable batteries were made from NiCd. Although this chemistry is being replaced by an environmentally-friendly one, nickel-metal-hydride (NiMH), this newest system has higher manufacturing costs as mentioned by

¹<http://www.hautehorlogerie.org/en/players/famous-watchmakers/18th-century/abraham-louis-perrelet.html> Retrieved September 29 2009

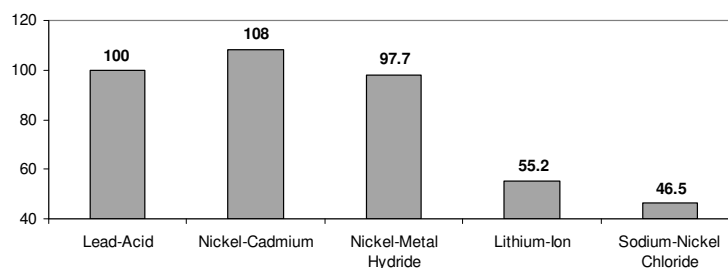


Figure 7.1: *Relative environmental score vehicle battery technologies, chart adapted from [131].*

Bernardes et al [14] based on the work of Putois about the market of NiCd batteries [93]. A European study presented in 2005 by Van den Bosshe et al [131] provided an assessment of the environmental impact for sustainable battery technologies used in electric vehicles (see Fig. 7.1). Lead-acid, the traditional car battery, was used as a reference to compare against the others types. As a result, traditional chemistries (Pb-acid, NiCd and NiMH) were found to have twice as much environmental impact as the newest types (Li-ion and NaNiCl). Although the newest chemistries are promising, several technical limitations delay their widespread adoption (safety, stability, and cost for Li-ion, and the need to keep a high operating temperature close to 300°C for the NaNiCl, even when not in use).

When batteries are depleted most are disposed of directly into sanitary landfills, stabilized (chemically treated before disposed in landfills), incinerated, or recycled. The problem with batteries in landfills is that heavy metals can dissolve and leach into soil, leading to groundwater contamination, which can be a significant problem. Recycling, on the other hand, can be difficult to build into consumer habits. For instance, a study published by Bernardes et al. [14] in 2004 documented consumer research in Germany, The Netherlands, and Belgium that showed 80-90% of the population knew about battery collection systems in place, but only 30-50% of the population used them. This is reflected in European battery collection rates of 32-54% [13]. The volume of batteries produced can give an idea of the magnitude of the battery disposal problem. For example, Europe produced 5 billion battery units in year 2000 [14], whereas nearly 3 billion batteries were sold in the United States circa 2001 of which close to 180,000 tons ended up in landfills [33].

In the US, the Environmental Protection Agency (EPA) has issued regulations concerning hazardous waste (universal waste) to be separated from municipal waste and managed in appropriate systems. As a result, most of the states have their own waste programs. The Resource Conservation and Recovery Act (RCRA) is the legislation that governs the disposal of hazardous wastes materials (such as nickel-cadmium and lead-acid batteries), but household batteries containing no cadmium,

lead, or mercury are not regulated by RCRA. They can still end up in sanitary landfills, depending on state regulations [13]. In emerging economies and developing countries, the situation is more apparent. In Brazil, for example, only 2% of municipal waste goes into a recycling process, and this is a country that consumes a billion batteries per year (~30% alkaline batteries, and 2% automotive batteries). Brazil is one of the few countries in South America with regulations for battery disposal, but little is done to enforce the laws [13].

Therefore, the environmental situation around the world for the disposal of billions of batteries is not ideal. Proven solutions that avoid using batteries that are disposed of later can provide an environmental advantage. Since the world relies on two choices for electrical power (either the power grid or batteries), alternatives that overcome the limitations of being wired to a power grid or using batteries are more than welcome. Maybe the 21st century will free the world from power cords and batteries; maybe devices will be operated by scavenging energy from the surroundings.

Some examples of this technology have been available for some time. Examples are the solar-powered calculator and the electronic self-winding wristwatch, which produce enough energy to power themselves. Thus, the technology exists, but is limited to the low power requirements of electronic devices (as shown in Fig. 1.3 on page 6). Solar cells and thermoelectric generators are more environmentally-friendly but provide a lesser amount of power. They also depend on the availability of enough solar light and temperature gradients to generate energy. However, they have been found practical for less power hungry devices. On the other hand, the human body provides a much smaller amount of power, but enough to be usable for some applications where fuel-based devices, solar cells, or thermoelectric generators cannot be employed.

Energy harvesting technology can help minimize battery dependency and, thus, minimize environmental disposal problems. Energy harvesting from human activities is one interesting research area because it can use body motion to energize portable, wearable, or implantable electronic devices. This has real potential to increase the use of biomedical sensors and instrumentation for monitoring patient health and treatment, including wireless body sensor networks for health-monitoring as mentioned by Jovanov et al. [50] and Hao and Foster [44]. Jovanov et al describes the Wireless Body Area Network (WBAN) as a new enabling technology for health monitoring. In order to showcase this approach, a prototype WBAN was built with off-the-shelf components for physical rehabilitation applications and ambulatory monitoring. It was claimed as an inexpensive, unobtrusive, and unsupervised ambulatory monitoring technique. Hao and Foster in a study presented in 2008 [44] a comprehensive review of the developments in wireless technology for monitoring human physiological responses. As a result, it is expected that this WBAN technology will make healthcare more ubiquitous at home while lessening the load for clinicians in hospitals.

7.3 Miniaturization, Pervasiveness, and Public Perception

New developments in low-power consumption electronics increase the operating life of devices while reducing overall dimensions. Hence, the merging of energy harvesting, low-power electronics, and reduced sizes promises new applications for health, environmental, and surveillance monitoring. Energy harvesting can also facilitate wide deployment of sensors and autonomous systems for monitoring tasks that otherwise would be too costly for battery-operated devices. Therefore, the pervasiveness of electronic devices is something that can be expected in the near future. For instance, advances in electronics, sensors, and wireless communications have made it possible to integrate devices for Wireless Body Area Network. This WBAN technology is being developed for patient health monitoring, computer-assisted physical rehabilitation applications, and ambulatory monitoring. This type of system constantly monitors the wearer's condition and sends information wirelessly to a central unit. It provides a relatively inexpensive, unsupervised, and wearable monitoring device for remote patient observation since it does not require specialized personnel. In addition, as mentioned by Jovanov et al [50], the privacy of wireless communication of health-related information (between sensors or between a sensor and an interrogating device) can be a sensitive issue since legal regulation will be required for this.

Wireless networks, pervasive computing, smart networks, intelligent sensors networks, smart computing, mesh networks, cloud computing, or the "Internet of things" are some of the terms often used in what is expected to be the next technological revolution where electronic devices will be interconnected. Wireless devices and Radio Frequency Identity Chip (RFID) tags are today the precursors of the intelligent sensors networks of the future. The world will contain more and more electronic devices that communicate wirelessly and transfer information about the object or about ourselves.

However, the same technology that helps to shape the world with its pervasiveness can face privacy implications due to the surveillance capabilities it poses. In addition, continuous scale downsizing and price reduction of electronic devices makes the public aware of the feasibility of the *Big Brother*² or *Panopticon*³ scenario.

²The *Big Brother* is a character of fictional novel *Nineteen Eighty-Four* by George Orwell, where society is under complete surveillance by the authorities, and people are constantly reminded of this by the phrase "Big Brother is watching you" on telescreens.

³The panopticon is a prison building designed by philosopher and social theorist Jeremy Bentham in 1785 where prisoners can be observed without them knowing if they are being observed. It is also being used as a metaphor for the surveillance by closed-circuit television (CCTV) cameras in public spaces. This metaphor is also used by Shoshana Zuboff in his book *In the Age of the Smart Machine: The future of Work and Power*, about how the information panopticon makes the user more vulnerable [148].

It is the tracking, the surveillance possibilities, and the misuse resulting from this nascent technology, either direct or indirect, that concerns people and their sense of identity and security, as discussed by Toumey about the pre-existing patterns of technology-and-privacy [129], or by van den Hoven in his privacy implications of RFID and nano-electronics, or the surveillance as a social sorting discussed by Lyon [66]. In this scenario the public should be able to enforce its privacy if they are aware of the presence of monitoring devices. Thus, users and manufacturers dealing with this kind of technology will have to worry about privacy in order to make it visible and detectable in order to take appropriate measures. This is the case for the large-scale video surveillance technology deployment in London initiated by the mid 1980s, as summarized by the House of Commons report in [84] or by the crisis of London essay from Thornley [126]. This *Big Brother* scenario, however, would be the price to pay in order to enjoy the benefits of constant health, environment, and surveillance monitoring.

Privacy concerns go hand-in-hand with new technologies such as the RFID tag tracking. RFID tags are small integrated circuits with antennas for radio reception and transmission of information either powered by batteries (active RFID tags) or by RFID readers (passive RFID tags). RFID tags are expected to replace bar codes in the future to speed up handling and facilitate tracking of goods. As technology progresses, self-powered circuits can be a reality by means of energy harvesting from environmental sources. This, combined with the ever decreasing size and low prices, can open the door for mass production and mass adoption. Thus, tracking of individuals can be an indirect result of the technology, where wireless technology, while facilitating life, keeping medical records, or personal information handy, could undermine privacy. Van den Hoven [132] summarizes some of the actual tagging possibilities, such as the FDA approval in 2004 for implantable RFID tags for hospital patients, the trace of Japanese school children with subcutaneous chips, the tracking of government officials in Mexico in case of kidnapping, the use of implantable chips to simplify ID verification in clubs and to trace runaway pets in the US, and even an RFID tracking system has been suggested to monitor the movements of legal immigrants in the US.

Public reaction and public trust are now at center stage when developing new technologies. For instance, as mentioned when technology and society face each other by Keller [54], the risk perception of nuclear power in the US has delayed development for more than 30 years while public acceptance in France and Japan has been practically the opposite (the US generates close to 20% of its electricity from nuclear power, whereas France is close to 80%). Another well-known case is the sensationalist news headlines of *Frankenfoods*⁴ (genetically-modified organisms) that has

⁴*Frankenfoods* is a term coined against genetically modified foods after Frankenstein's character in the novel of the same name.

been in the eye of the hurricane of public perception as mentioned by Kulinowski because of the controversies that some technologies have faced [57]. In the case of *Frankenfoods*, a critical report was published in *Nature* by Losey in 1999 and titled as "Transgenic pollen harms monarch larvae" [63]. After that, genetically-modified (GM) foods were under intense scrutiny by the public, especially in Europe, as mentioned by Kulinowski. This controversy has been based on concern about the safety of the products, or the health risks they can pose, and the benefits they promote, although no adverse health effects have been documented to date. A book published in 2004, and titled as "The Frankenfood Myth: How Protest and Politics Threaten the Biotech Revolution", relates how activists against GM foods have been spreading unfounded and inaccurate stories to continue the controversy [75].

Often the public perception molds society decisions, otherwise how can we explain the differences between nuclear power development among the US and France? Studies have suggested that the public relies on heuristics, or intuitive judgments, in order to evaluate new technologies, as summarized by the study of Scheufele and Lewenstein [110]. Citing their work: "people form opinions and attitudes even in the absence of relevant scientific or policy-related information." In addition, the information often provided by the mass media influences the public opinion on new technologies to the point that it determines the level of support for funding research. A rigorous regulatory system is often seen as a way to gain the public confidence in new technologies, yet the system can be so rigorous that sometimes it can delay improvements, such as the lengthy FDA regulatory process for new drugs approval⁵ that can take between 8-12 years, as summarized by Lipsky and Sharp [64].

Roco and Bainbridge [101] provided an insight of what future technology development will mean from the view of societal implications. Although the analysis is specifically elaborated for nanotechnology, the perspective of the implications of new technologies can be used for other areas as well. They focused on the benefits of nanotechnology to humanity; but also the risk, uncertainty, legal aspects, and public interaction. Technology is seen as a tool to help solve some social problems, such as healthcare, fertility, poverty and inequality, natural resources, and economic development, where new developments will directly improve the life quality, and help to boost the prosperity of nations. For instance, nanotechnology has been heralded as a solution for solving many problems in the developing world where the developed world see technological innovation as the main solution to alleviate poverty, as mentioned by Salamanca et al [108], Barker et al [10], and Canton [19]. On the other hand, there are situations where the social context is more important than the technology itself, as pointed by Invernizzi and Foladori [47], Keller [54], Meaney [73], and Freeman [32].

⁵The FDA drug approval process starts with preclinical testing with an investigational new drug (IND) application filed. After that, if successful, clinical trials follow later with three phases. Again, if successful, the final step is to submit a new drug application (NDA) containing all the information obtained previously. If approved, post market studies are conducted later.

Thus, public perception, public trust, and technology awareness must be considered when accepting or rejecting a new technology.

Micro Electro Mechanical Systems (MEMS) is an example of a relatively young technology that had a turning point in 1982 when attention was centered on silicon microstructures. Sensors have become a major point of MEMS devices, with pressure and acceleration sensors the best known examples. Disposable blood-pressure sensors have made their way into patient diagnostic surgical procedures, where their social impact is direct, as summarized by Bryzek [18]. History has also shown that new technologies involve a close relationship with society. Society is affected by the introduction of new technologies, and society also affects how technology is developed and perceived. MEMS and nanotechnology are not exceptions to this rule. For instance, since nanotechnology has a broad potential of applications such as medicine, biomaterials, electronics, energy generation, and others, it has opened the debate to future implications of this technology. The implications are so intricate that ethical, social, medical, legal, and environmental concerns have raised questions about the benefits and potential risks, as commented upon by Smiley-Smith et al [116], Schuler [111], Moor and Weckert [78], and Robison [100]. That is why it is important to learn from past lessons. History often offers insights of sensitive social issues, unexpected consequences, and pitfalls on how technology develops.

7.4 Energy Harvesting Implications

Energy harvesting by itself is a technology that enables some applications to run without batteries or to extend battery life for others while diminishing the number of batteries and the hazardous chemicals disposed in landfills. Energy harvesters represent a clean energy alternative because they don't require consumables to function and do not release byproducts from its operation. Since these generators employ environmental energy sources (such as light, temperature changes, or motion) there is little to no interaction between the generator, the carrier, and the environment. Since it has been challenging to get consumers to recycle household items such as batteries [13], energy harvesting seems a viable alternative. In addition, this makes this type of technology attractive, environmentally-friendly, and relatively safe to use. However, since the use of this technology seems to be focused for biomedical application or portable electronics, the potential market can be small or a niche market, then the environmental benefits of using energy harvesters can be reduced.

Although power output for generators based on body energy is relatively low (Fig. 1.2 on page 5), it is clear that the power envelope depends on specific applications (Fig. 1.3 on page 6). Therefore, the target market for this kind of technology is in low-power electronics and/or biomedical devices. The advantages of this energy generation approach are multiple, from the simplicity of operation, the reduced main-

tenance, and a longer battery lifespan, up to the elimination of battery substitution. Users of medical devices would need less frequent battery replacement, especially for those with surgically-implanted devices.

Environmental monitoring is another area that can be the direct beneficiary of this approach. Environmental monitoring requires the deployment of multiple sensors commonly powered by batteries, but battery-powered devices need to be regularly serviced for battery replacement. Deployment of sensors into remote or difficult-to-access locations is therefore limited. Energy harvesting is then a technology that can enable broader monitoring capabilities for environmental purposes.

However, the possibility of a wider deployment of monitoring sensors brings to mind the surveillance and privacy fears discussed earlier. It is expected that the WBAN technology for medical monitoring of patient whereabouts will raise privacy questions as well. This is also a concern inherent in existing battery-powered devices for continuous sensing and monitoring, not for a battery-replacement technology such as energy harvesters. The development on electronics has enabled the reduction of devices' physical dimensions, but most of them are still limited as autonomous systems. In these independent systems the battery still dictates the final size. Although energy scavengers are intended to assist or replace batteries, their physical size can be in the same order of magnitude as the batteries they intend to replace. Only autonomous systems operating for several years could have reduced sizes since there is no need for a large battery. In addition, power generation scales proportionally with size: large harvesters produce a relatively large power output, while smaller scavengers will produce a fraction of that. Particularly, motion-based energy harvesters do not downscale favorably at reduced sizes. These scavengers generate energy proportional to their internal proof mass, if the mass has dimensions 10X smaller then the energy generation gets reduced by 1000X of the initial value. Although smaller generators can drive smaller devices, their capabilities are reduced accordingly. Therefore, miniaturization shouldn't be a concern for this technology since it will have similar physical constraints as batteries, and devices can be smaller but not invisible.

Conversely, RFID tags (active or passive) are a more pervasive technology. Ethical aspects generally arise from misuse of a technological system not the individual technological aspects by themselves, as mentioned by Toumey [129] and Van den Hoven [132]. In the case of implanted biomedical devices, energy harvesters do not differ much from batteries since both are energy sources but they use different energy generation principles.

One important area to consider is the cost, from how much it costs to manufacture to how expensive can be a final device. Low-cost devices can make a difference for wide deployment of sensors or for portable electronics if the cost is competitive with batteries (including its low environmental impact cost). New industries can be derived from applications of this technology or new related services can prosper. However, the commercial aspect also requires us to know how reliable is the technology,

especially for medical applications. This also brings the question of how accessible the technology can be. Will it be for medical-related products or for consumer devices? Although the technology is created for specific purposes, unexpected uses could appear later.

It is important to carefully examine the advantages, as mentioned earlier, of energy scavengers over the technology it intends to replace: batteries. There is clean energy generation with zero-to-little environmental impact, while making it possible to create battery-less electronic devices. Since this technology is only a component of a system, it is expected that society recognizes it as a useful technological tool that can enable new applications to enhance life quality as pointed out by Keller[54] and Kulinowski [57]. That is why public perceptions of this technology are what builds public trust, and in the end, it is the public perception which dictates the success of new technologies. The summary of findings include:

Advantages

- *Environmental:* Can alleviate the battery disposal problem, since less batteries would be disposed in landfills. This would make it a green technology for portable and/or medical devices.
- *Extended operation:* Since devices can be battery-less or hybrids (energy harvester + rechargeable battery), the operational lifespan can be extended almost indefinitely. Due to the extended operation or enhanced capabilities of autonomous systems, technologies such as WBAN, could have increasing applications for health services.
- *Cost:* Since batteries are not required or less-frequently replaced, the servicing cost or operational cost of electronic devices is expected to decrease. In the case of surgically-implantable biomedical devices, health care cost would be reduced.
- *Research:* Energy harvesting could increase the research interest for new related technologies or new set of solutions can be envisioned for multiple applications. This could also lead to new industries and diversified markets.

Potential Obstacles

- *Privacy:* As new technologies enable wider monitoring, there is always the cost of privacy. Especially if there is the need of a constant monitoring of a person whereabouts. History has provided multiple examples about this topic to consider.
- *Reliability:* Since this is a new technology, there is the need to know how reliable it is in order to be accepted or evaluated. However, the generator presented

shares similitude in operation to the wristwatches which can be helpful, but not enough if it is not a tested technology.

- *Accessibility:* Depending on the applications, there is always the question of how accessible is the technology to the public. If the applications are directly focused into medical areas, it is highly likely that the cost will be high, but if consumer products are the main target, the public will have better access to them.
- *Unexpected consequences:* This is always a difficult point, since unexpected uses can be given where implications were not envisioned ahead. There are always unanticipated consequences of technology implementation.

The results from this technology and the societal implications are not deemed unsafe, but there are some potential issues that could arise depending on the final application. Since it is difficult to know all the side effects until a technology is in the consumer's hands, the only approach that is certain from history is that there will be unanticipated consequences, either positive or negatives. This suggests the need to avoid the traditional *hype* when a new technology is introduced, but recognize the benefits associated for humanity while still being aware of possible future concerns after implantation.

Chapter 8

Conclusion

Body motion is an attractive energy source for powering portable, wearable, or surgically-implantable devices. Although energy harvesting research has been conducted before, little has been presented on energy generation from body motion. Energy harvesters can also make it possible to use hybrid designs for powering electronic devices. Such hybrid designs, consisting of a rechargeable battery and an energy scavenger, can enhance the operation of actual devices for longer operation without replacement.

The Conclusion Chapter is divided in three sections: The first section describes the overall general summary and derived conclusions; the second part provides specific findings, while the last section draws recommendations for future work.

8.1 Conclusion

This dissertation has investigated the possibilities of harvesting energy from body motion and has developed a generator to generate electrical energy from body movements. In order to do that, a review of the field was performed to determine the best techniques for energy harvesting from body motion, models were elaborated to establish the power generation limits from walking and running at different body locations, and a generator was designed and fabricated to study and evaluate the device performance. In addition, this research is not limited to body motion applications since movement from the natural environment (such as ocean waves or animals on the wild) or others that are low frequency and irregular can be used for energy harvesting.

Electromagnetic and piezoelectric transduction techniques were both found to produce a relatively high power output, with power densities as high as $1\text{mW}/\text{cm}^3$ from body motion. A preliminary study was performed on 10 test subjects walking and running on a motor-driven treadmill to evaluate the available energy from several body locations (ankle, knee, hip, chest, wrist, elbow, shoulder, side and back of the

head). The treadmill provided an analysis of the energetic figure of merit, σ_ω , which is the acceleration-squared-to-frequency (*ASTM* for simplicity) term. The larger the acceleration changes when performing an activity, such as walking, the higher the energetic figure of merit. As a result, leg locations, especially the ankle, were found to have higher energetic figure of merits, σ_ω . In contrast, upper body locations with smaller displacements, such as the head, were found to have smaller σ_ω values. High energetic figure of merit, σ_ω , is an indicator of body locations for energy harvesters with relatively high power output generation.

The treadmill analysis suggest that power densities on the order of hundreds of $\mu\text{W}/\text{cm}^3$ for the upper body locations, and several mW/cm^3 for the leg locations are available from walking at average speeds for single-axis (linear) generators, whereas the running tests suggest power densities 10X larger when compared against the same locations while walking. The results also suggest that harnessing motion from two axes at the same time should provide at least twice the output of a single axis design.

Results from the state-of-the-art survey and the treadmill analysis suggest the availability of power densities on the order of hundreds to thousands of $\mu\text{W}/\text{cm}^3$ from body motion. A generator design was then chosen to evaluate the power generation potential. A rotational design was chosen in order to have a small footprint and to harness angular motion from body joints. Electromagnetic generation was preferred since it was easier to implement for a rotational design as opposed to piezoelectric transduction that needed a mechanical deformation. The pendular-based mechanism chosen was found suitable for body motion since it oscillated with light external motions and body position changes. Physically, the chosen design resembled that from self-winding wristwatches. The generator has two main components an iron-less stator and a rotor with an eccentric mass. The stator was realized by stacking layers of planar coils, while the rotor was composed of rare earth neodymium (NdFeB) permanent magnets with an eccentric mass attached. The assembly was finalized with jewel bearings and a PMMA package.

The prototype evaluated was able to harvest kinetic energy from human walking. Generators placed on body locations with high σ_ω values presented larger power output. An average of $234 \mu\text{W}$ of power while walking with the generator placed on the ankle was found, for a power density of $117 \mu\text{W}/\text{cm}^3$.

8.2 Summary of Findings

The research presented in this document investigated techniques for energy harvesting while choosing a technology that would allow the generation of electrical energy from normal movements of the human body. The main contributions of this dissertation are the description of available power density at several body locations while walking and running at several speeds, and the pendular-based rotational electromagnetic

generator design for harvesting energy from body motion. The summary of findings includes:

Available Power

- A study of the field showed that electromagnetic and piezoelectric generation can produce power densities as high as $1\text{mW}/\text{cm}^3$ from body motion.
- Available power from a system can be estimated from Eq. 3.19 on page 34 ($P_{avail} = 1/2m\sigma_\omega Q$) for a given mass m , the energetic figure of merit σ_ω (acceleration-squared-to-frequency term), and the Q factor. From these terms, the mass m and the Q factor are design parameters for the generator, whereas the σ_ω term represents the energy source. Therefore, the energetic figure of merit σ_ω can be used to evaluate locations or systems for energy harvesting.
- Acceleration waveform recordings from 11 test subjects on a motor-driven treadmill were evaluated. Nine body locations were chosen located preferably at the joints (ankle, knee, hip, chest, wrist, elbow, shoulder, side and back of the head) for energy availability assessment. Measurement were made for walking tests from 10 subjects at several speeds (1-4mph), running tests were elaborated on 10 subjects at several speeds (2-5 mph).
- The energetic figure of merit, σ_ω , was evaluated from the walking and running tests. The σ_ω values ranged from small values as $0.1\text{m}^2/\text{s}^3$ at the head while walking at 1mph up to as large as $27\text{m}^2/\text{s}^3$ at the ankle while running at 5 mph. Leg locations were found to have larger σ_ω than upper body locations, especially the ankle. Larger σ_ω indicated body locations where energy harvesters could produce a relatively high power output.
- The energetic figure of merit analysis for power generation suggests the availability of power densities from average walking on the order of hundreds of $\mu\text{W}/\text{cm}^3$ for upper body locations, and several mW/cm^3 at the leg locations (for single-axis generators). The running test suggests power densities 10 times larger than that from the same locations while walking.

Prototype Generator

- An oscillating (pendular-based) rotational design was selected because of its small footprint. The pendular design is sensitive to oscillation from body joints rotations. Electromagnetic generation was chosen for its compatibility with a rotational design.

- The generator optimization was elaborated in two stages. The first phase optimizes the generator geometry to match a resonant frequency and to maximize the generator's potential energy. The second stage optimizes the coil and permanent magnet geometry to maximize the power generation. The findings were:
 - *First:* Stacked proof mass designs were found to provide similar power levels as protruded proof mass designs. Thinner applications can use protruded designs at the expense of a larger footprint while stacked designs can be employed for smaller areas allowing thicker profiles. Generators harnessing energy from walking were determined to require a resonant frequency of 1.9 Hz while for running this design frequency was determined to be 2.5 Hz. Larger generators were found to produce a larger power output.
 - *Second:* Optimal radial length for a 25 mm diameter rotor was determined to be 6.3 mm, and this varies proportionally with the rotor diameter as shown in Fig. 4.18 (on page 83).
 - *Third:* The optimal number of pole-pairs number was found to be 10, for an optimized 25 mm diameter coil, as shown in Fig. 4.20 (on page 85).
- Seven different prototype iterations were designed and fabricated. The findings were:
 - *First:* Wire-wound coils are difficult to fabricate in a cost-effective way with overall dimensions smaller than 2 mm and with shapes other than circular. Planar coils were considered to provide a cost-effective fabrication technique for coils with thicknesses less than 1 mm.
 - *Second:* Power generation was found to be higher when the driving frequency matches the generator's natural resonant frequency. Due to the non-linearity of the system (pendular-based with large amplitudes presenting a foldover effect), 50% of the energy can be extracted at a frequency ± 0.5 Hz from the resonant frequency. Power generation for frequencies higher than the resonant frequency was found to be 10% of the peak value.
 - *Third:* Subharmonics near $1/2$, $1/3$, and $1/4$ of the generator resonant frequency offered up to 50% of the peak energy. Power generation was found to be as high as 25% for frequencies higher than the resonant frequency. Induced voltage was found to be proportional to the total radial wire length, to the number of coil layer, and to the number of turns per coil.
 - *Four:* Jewel bearings were found to provide less friction than ball bearing sets while proving relatively smaller structures.

- *Fifth:* Larger magnets were found to increase proportionally the induced voltage. When compared to the previous prototypes (3.1 mm wire radial length) the larger magnets (1.1x1.1x5.1 mm) provided a 50% increase in induced voltage over the previous set (1x1x2 mm).
 - *Sixth:* Dual rotors with the coil in between provided a 50% increase in the induced voltage due to the increase in magnetic flux for this geometry. A test performed with the generator attached to the body while walking at several speeds on a treadmill provided a power output of 234 μW (137 mVrms) for a power density of 117 $\mu\text{W}/\text{cm}^3$ (2 cm^3 generator volume) using a 4-layer coil.
 - *Seventh:* Optimized coils (10-layer 100 μm linewidth) should provide RMS-voltages over 250 mV (>700 mV peak) for semiconductor rectification.
- The generator power output increases proportionally with the generator mass.
 - Multi-stacked coils were fabricated with thicknesses as low as 430 μm for a 10 layer coil.
 - The generator produced a higher power output when the external motion frequency matched the pendulum-based generator natural frequency. Generators operating at frequencies other than the resonant frequency were found to produce ~5% of the power at the resonant frequency.
 - Generators placed on the lower body were able to produce ~10 times as much power as devices located on upper body locations.
 - The induced voltage output was as high as 137 mVrms (382 mV peak) and the power was as high as 234 μW (117 $\mu\text{W}/\text{cm}^3$) for a four-layer coil generator placed at the ankle while walking.

Societal Implications

- Public perception is an important component that usually determines the success of new technologies. History usually helps us to understand the societal implications when embracing promising new technologies, as the case of energy harvesters for body motion. Some advantages and potential obstacles are highlighted.
- *Advantages:* A direct environmental benefit is the reduction of batteries discarded in landfills; almost indefinitely operation of electronic devices; reduction in cost since there is no need to frequently service devices for battery replacement; and increased research in alternative energy sources and/or applications of new derived technologies.

- *Potential Obstacles:* Privacy cost for surveillance or monitoring applications; reliability of the new technology; the accessibility to the public; and the unexpected consequences for not foreseen implications.

8.3 Recommendations

Energy harvesting could be an ideal solution to continuously power portable electronic devices or surgically-implantable biomedical applications. Although this field encompasses more than motion-to-electricity conversion for portable or wearable energy generation, there is a wide variety of applications that could benefit from this research. However, this research only represents a first contribution to low-frequency and non-resonant energy scavenging and highlights the work that can be done to advance the field. Some recommendations for future work are presented below.

- *Generator Design:* Since only one prototype configuration was evaluated (a free-rotating rotor with an iron-less design) other design configurations could potentially produce a higher power output. Designs such as the ones presented by Wang et al [139] or the ETA watch mechanism presented by [87] are able to produce higher power output, although operating in burst modes. Therefore, some designs with a soft-magnetic material could be envisioned.
- *Higher-density coil:* A higher density planar coil can produce larger induced voltages. In the actual prototypes, limited coil density was achieved due to the use of commercial copper-clad polyimide substrates. Since the planar coil is etched from the copper-clad laminate, enough gap space between the wires must be left to avoid undesired undercutting. Techniques such as micro electrodeposition can be used to fabricate the planar coil structures with smaller gaps and more uniform cross-sectional area to further reduce the electrical resistance.
- *Multiple-poles magnet:* A permanent magnet axially magnetize rotor with multiple-poles offers a simplified fabrication design. Due to proof-of-concept evaluation purposes, only rotors with individually placed magnets were employed, thus axially magnetize magnets with the proper pole pair distribution will simplify the design while providing better area coverage for the permanent magnet material. The permanent magnet modeling section from the generator design chapter suggests a 20% increase in magnetic flux when using sector-shaped area magnets over prismatic magnets.
- *Microfabrication:* Microfabrication can allow tighter tolerances for increased power generation. As magnetic field decreases with distance, a smaller air gap between the planar coil and the permanent magnet surface could provide a higher magnetic field for an iron-less coil design. Bearing systems from the

wristwatch industry were employed for the proof of concept evaluation. These types of bearings are also used in sensitive measuring equipment because of their low friction and their ability to operate without lubrication. Although these systems were found to perform better than commercial ball bearings, they might not be suitable to keep air gaps on the order of tens to hundreds of micrometers for an increased power output. Recent research on microball bearings, as presented in [38, 37], can fill this gap.

- *Mass production:* Prototypes were built using standard precision engineering techniques with hand assembly, which translates to relatively high fabrication costs. Mass production may be used to reduce this cost. The generator consists of three main components, stator, rotor, and packaging. The stator can be mass produced following the same fabrication steps and materials as flexible printed circuit boards. Packaging can be also mass produced by injection molding of the parts. The rotor can also be mass produced since it is composed of a permanent magnet ring, which can be axially magnetized as described in Section 6.3.2, with a shaft and eccentric mass attached. Therefore, a final device could be mass produced with relatively low fabrication cost and capital investment for commercial applications.
- *Low-power rectification:* Since electromagnetic-based energy harvesters produce low AC voltages that need to be rectified, standard rectification circuits with semiconductor technology cannot deliver high efficiencies. For instance, Schottky diodes have threshold voltages over 200mV, thus generated voltages below the threshold voltage are not rectified. Several techniques can be employed to overcome this problem as mentioned previously in the Section 6.3.3.
- *Dynamic electro-mechanical performance:* Further analysis for the dynamic behavior can be studied in order to study the effects of the mechanical damping, the electromagnetic damping, and the electric loading system circuitry. This study is necessary to develop an adequate electrical system to maximize the generate power output under several loading conditions.
- *Generator reliability:* Although no analysis or studies were realized for the reliability of prototypes fabricated, the generator should be highly reliable. Since the prototypes use technology developed for the watch industry, and because the generator operation is at low rotational speeds with similar conditions as wristwatches, then it is highly likely that the reliability similar to that of wristwatches should be able to be achieved. Further generator improvements such as precision and reliability can be adapted from the wristwatch industry.
- *Generalized body motion analysis:* The research presented in this dissertation only focused on walking and running activities, but activities such as walking

comprise only a fraction of the everyday actions of the human body. Other types of motions or activities, physical condition, or age range can provide a more accurate description of how much energy is available daily at different body locations for an energy harvester. This can help to determine appropriately the power generation for a given user condition.

One of the expected revolutions in computing technology is the widespread deployment of low cost and low-power wireless sensor networks, as mentioned by Rabaey et al [94]:

“One of the most compelling challenges of the next decade is the ‘lastmeter’ problem—extending the expanding data network into end-user data-collection and monitoring devices.”

However, in order to make it a reality a cost effective way to power them must be achieved. Although batteries have been successfully used, battery replacement is not cost-competitive for large sensor deployment. In order to solve this problem, energy harvesting technologies to power autonomous systems must be developed. Body motion is one energy source that can be employed to power autonomous systems or even body sensor networks

Bibliography

- [1] N. Achotte, P. A. Gilles, O. Cugat, J. Delamare, P. Gaud, and C. Dieppedale. Planar brushless magnetic micromotors. *Microelectromechanical Systems, Journal of*, 15(4):1001–1014, 2006.
- [2] F. Albano, M. Chung, D. Blaauw, D. Sylvester, K. Wise, and A. Sastry. Design of an implantable power supply for an intraocular sensor, using power (power optimization for wireless energy requirements). *Journal of Power Sources*, 170(1):216–224, June 2007.
- [3] R. Amirtharajah and A. P. Chandrakasan. Self-powered signal processing using vibration-based power generation. *Solid-State Circuits, IEEE Journal of*, 33(5):687–695, 1998.
- [4] R. Amirtharajah, J. Collier, J. Siebert, B. Zhou, and A. Chandrakasan. DSPs for energy harvesting sensors: applications and architectures. *Pervasive Computing, IEEE*, 4(3):72–79, 2005.
- [5] R. Amirtharajah, J. Wenck, J. Collier, J. Siebert, and B. Zhou. Circuits for energy harvesting sensor signal processing. In *Design Automation Conference*, pages 639–644, 2006.
- [6] J. F. Antaki, G. E. Bertocci, E. C. Green, A. Nadeem, T. Rintoul, R. L. Kormos, and B. P. Griffith. A gait-powered autologous battery charging system for artificial organs. *ASAIO journal (American Society for Artificial Internal Organs : 1992)*, 41(3), 1995.
- [7] Y. Arakawa, Y. Suzuki, and N. Kasagi. Micro seismic power generator using electret polymer film. In *Power MEMS 2004*, pages 187–190, 2004.
- [8] D. P. Arnold. Review of microscale magnetic power generation. *Magnetics, IEEE Transactions on*, 43(11):3940–3951, 2007.
- [9] G. L. Baker and Blackburn J. A. *The Pendulum: A Physics Case Study*. Oxford University Press, 2005.

- [10] T. F. Barker, L. Fatehi, M. T. Lesnick, T. J. Mealey, and R. R. Raimond. Nanotechnology and the poor: Opportunities and risks for developing countries. In P. Lin F. Allhoff, editor, *Nanotechnology & Society: Current and Emerging Ethical Issues*, pages 243–263. Springer Netherlands, 2008.
- [11] J. B. Bates, N. J. Dudney, B. Neudecker, A. Ueda, and C. D. Evans. Thin-film lithium and lithium-ion batteries. *Solid State Ionics*, 135(1-4):33–45, November 2000.
- [12] S. P. Beeby, M. J. Tudor, and N. M. White. Energy harvesting vibration sources for microsystems applications. *Measurement Science and Technology*, 17(12):R175–R195, 2006.
- [13] A. M. Bernardes, D. C. R. Espinosa, and J. A. S. Tenorio. Collection and recycling of portable batteries: a worldwide overview compared to the brazilian situation. *J. Power Sources*, 124:586–592, 2003.
- [14] A. M. Bernardes, D. C. R. Espinosa, and J. A. S. Tenorio. Recycling of batteries: a review of current processes and technologies. *J. Power Sources*, 130:291–298, 2004.
- [15] N. B. Bharatula, R. Zinniker, and G. Troster. Hybrid micropower supply for wearable-pervasive sensor nodes. In *Ninth IEEE International Symposium on Wearable Computers (ISWC’05)*, pages 196–197, 2005.
- [16] J. S. Boland, J. D. M. Messenger, K. W. Lo, and Y. C. Tai. Arrayed liquid rotor electret power generator systems. In *Micro Electro Mechanical Systems, MEMS 2005*, pages 618–621, 2005.
- [17] C. V. C. Bouten, K. T. M. Koekkoek, M. Verduin, R. Kodde, and J. D. Janssen. A triaxial accelerometer and portable data processing unit for the assessment of daily activity. *IEEE Trans. Biomedical Eng.*, 44(3):136–147, 1997.
- [18] J. Bryzek. Impact of mems technology on society. *Sensors and Actuators A, Physical*, 56:1–9, 1996.
- [19] J. Canton. The emerging nanoeconomy, key drivers, challenges and opportunities. In M. C. Roco and W. Brainbridge, editors, *Nanotechnology, Societal Implications, Individual Perspectives*, pages 32–40. Springer, 2006.
- [20] F. Caricchi, F. Crescimbin, O. Honorati, G. L. Bianco, and E. Santini. Performance of coreless-winding axial-flux permanent-magnet generator with power output at 400 hz, 3000 r/min. *Industry Applications, IEEE Transactions on*, 34(6):1263–1269, 1998.

- [21] D. Carroll and M. Duffy. Demonstration of wearable power generator. In *Power Electronics and Applications, 2005 European Conference on*, pages 10 pp.+, 2005.
- [22] B. Cavallier, P. Berthelot, H. Nouria, E. Foltete, L. Hirsinger, and S. Ballandras. Energy harvesting using vibrating structures excited by shock. In *Ultrasonics Symposium, 2005 IEEE*, volume 2, pages 943–945, September 2005.
- [23] T. Chin. Permanent magnet films for applications in microelectromechanical systems. *Journal of Magnetism and Magnetic Materials*, 209(1-3):75–79, February 2000.
- [24] L. Day and I. McNeil. *Biographical Dictionary of the History of Technology*. Routledge, 1995.
- [25] M. Duffy and D. Carroll. Electromagnetic generators for power harvesting. In *Power Electronics Specialists Conference, PESC 04*, volume 3, pages 2075–2081 Vol.3, 2004.
- [26] M. El-Hami, P. Glynne-Jones, N. M. White, M. Hill, S. Beeby, E. James, A. D. Brown, and J. N. Ross. Design and fabrication of a new vibration-based electromechanical power generator. *Sensors and Actuators A: Physical*, 92(1-3):335–342, August 2001.
- [27] J. Feenstra, J. Granstrom, and H. Sodano. Energy harvesting through a backpack employing a mechanically amplified piezoelectric stack. *Mechanical Systems and Signal Processing*, 22(3):721–734, April 2008.
- [28] V. Fernandez, J. Fandino, C. Sauvey, J. P. Yonnet, G. Reyne, and O. Cugat. A design methodology for permanent magnet microbearings. *Magnetics, IEEE Transactions on*, 36(4):1919–1922, 2000.
- [29] B. Flipsen, A. Bremer, A. Jansen, and M. Veefkind. Towards a selection method for designing alternative energy systems in consumer products. *Proc. TMCE 2004*, pages 1–8, 2004.
- [30] S. F. J. Flipsen. Power sources compared: The ultimate truth? *Journal of Power Sources*, 162(2):927–934, November 2006.
- [31] S. P. J. Flipsen. *Alternative Power Sources for Portables & Wearables, Part 1: Power Generation & Part 2: Energy Storage*. Delft University of Technology, 2005.

- [32] R. B. Freeman. Non-nano effects of nano-technology on the economy. In M. C. Roco and W. Brainbridge, editors, *Nanotechnology, Societal Implications, Individual Perspectives*, pages 68–74. Springer, 2006.
- [33] Frost and Sullivan. San francisco supervisor takes aim at toxic battery waste. Environmental News Network, and U.S. Battery Markets, Report No. 5949, July 1999, July 2001. Frost and Sullivan 2001, San Francisco Supervisor Takes Aim at Toxic Battery Waste, and Environmental News Network, July 11, 2001; and U.S. Battery Markets, Report No. 5949, July 1999, Figure 1-1.
- [34] G. J. Gage, K. A. Ludwig, K. J. Otto, E. L. Ionides, and D. R. Kipke. Naïve coadaptive cortical control. *Journal of Neural Engineering*, 2(2):52+, June 2005.
- [35] P. X. Gao, J. Song, J. Liu, and Z. L. Wang. Nanowire piezoelectric nanogenerators on plastic substrates as flexible power sources for nanodevices. *Advanced Materials*, 19(1):67–72, 2007.
- [36] L. A. Gavrilov and P. Heuveline. Aging of population. In P. Demeny and G. McNicoll, editors, *The Encyclopedia of Population*, pages 32–37. Macmillan Reference, 2003.
- [37] N. Ghalichechian, M. McCarthy, M. I. Beyaz, and R. Ghodssi. Measurement and modeling of friction in linear and rotary micromotors supported on microball bearings. In *Micro Electro Mechanical Systems, MEMS 2008*, pages 507–510, 2008.
- [38] N. Ghalichechian, A. Modafe, M. I. Beyaz, and R. Ghodssi. A rotary micro-motor supported on microball bearings. In *Solid-State Sensors, Actuators and Microsystems Conference, TRANSDUCERS 2007*, pages 1123–1126, 2007.
- [39] M. K. Ghantasala, L. Qin, D. K. Sood, and R. B. Zmood. Design and fabrication of a micro magnetic bearing. *Smart Materials and Structures*, 9:235–240, 2000.
- [40] S. Gil, A. E. Legarreta, and D.E. Di Gregorio. Measuring anharmonicity in a large amplitude pendulum. *American Journal of Physics*, 76(9):843–847, 2008.
- [41] G. Gorge, M. Kirstein, and R. Erbel. Microgenerators for energy autarkic pacemakers and defibrillators: Fact or fiction? *Herz*, 26(1):64–68, February 2001.
- [42] H. Goto, T. Sugiura, Y. Harada, and T. Kazui. Feasibility of using the automatic generating system for quartz watches as a leadless pacemaker power source. *Medical and Biological Engineering and Computing*, 37(1):377–380, December 1999.

- [43] H. Goto, T. Sugiura, and T. Kazui. Feasibility of the automatic generating system (AGS) for quartz watches as a leadless pacemaker power source: a preliminary report. In *Proc. of Engineering in Medicine and Biology Society*, pages 417–419 vol.1, 1998.
- [44] Y. Hao and R. Foster. Wireless body sensor networks for health-monitoring applications. *Physiological Measurement*, 29:R27–R56, 2008.
- [45] J. Harb, R. M. Lafollette, R. H. Selfridge, and L. L. Howell. Microbatteries for self-sustained hybrid micropower supplies. *Journal of Power Sources*, 104(1):46–51, January 2002.
- [46] E. Hirasaki, S. T. Moore, T. Raphan, and B. Cohen. Effects of walking velocity on vertical head and body movements during locomotion. *Experimental brain research*, 127(2):117–130, July 1999.
- [47] N. Invernizzi and G. Foladori. Nanomedicine, poverty and medicine. *Development*, 00:1–5, 2006.
- [48] A. J. Jansen and A. L. N. Stevels. Human power, a sustainable option for electronics. In *Electronics and the Environment, ISEE -1999*, pages 215–218, 1999.
- [49] M. D. Johnson, K. J. Otto, J. C. Williams, and D. R. Kipke. Bias voltages at microelectrodes change neural interface properties in vivo. In *Engineering in Medicine and Biology Society, 2004. IEMBS '04. 26th Annual International Conference of the IEEE*, volume 2, pages 4103–4106, 2004.
- [50] E. Jovanov, A. Milenkovic, C. Otto, and P. C. de Groen. A wireless body area network of intelligent motion sensors for computer assisted physical rehabilitation. *Journal of NeuroEngineering and Rehabilitation*, 2:1–6, 2005.
- [51] M. J. Kamper, R. J. Wang, and F. G. Rossouw. Analysis and performance evaluation of axial flux air-cored stator permanent magnet machine with concentrated coils. In *Electric Machines & Drives Conference, IEMDC '07*, volume 1, pages 13–20, 2007.
- [52] D. Katz and Akiyama T. Pacemaker longevity: The world’s longest-lasting vvi pacemaker. *Annals on Noninvasive Electrocardiology*, 12:223–226, 2007.
- [53] J. J. Kavanagh and H. B. Menz. Accelerometry, a technique for quantifying movement patterns during walking. *Gait and Posture*, 28:1–15, 2008.
- [54] K. H. Keller. Nanotechnology and society. *Journal of Nanoparticle Research*, 9:5–10, 2007.

- [55] T. S. Keller, A. M. Weisberger, J. L. Ray, S. S. Hasan, R. G. Shiavi, and D. M. Spengler. Relationship between vertical ground reaction force and speed during walking, slow jogging, and running. *Clinical Biomechanics*, 11(5):253–259, 1996.
- [56] R. L. Knoblauch, M. T. Pietrucha, and M. Nitzburg. Field studies of pedestrian walking speed and start-up time. *Transportation Research Record No. 1538*, pages 27–38, 1996.
- [57] K. Kulinowski. Nanotechnology: From "wow" to "yuck"? *Bulletin of Science, Technology & Society*, 24:13–20, 2004.
- [58] J. Kyminsis, C. Kendall, J. Paradiso, and N. Gershenfeld. Parasitic power harvesting in shoes. In *Wearable Computers*, pages 132–139, 1998.
- [59] B. E. Lewandowski, K. L. Kilgore, and K. J. Gustafson. Design considerations for an implantable, muscle powered piezoelectric system for generating electrical power. *Annals of Biomedical Engineering*, 35(4):631–641, April 2007.
- [60] Q. Li, V. Naing, J. A. Hoffer, D. J. Weber, A. D. Kuo, and J. M. Donelan. Biomechanical energy harvesting: Apparatus and method. In *Robotics and Automation, 2008. ICRA 2008*, pages 3672–3677, 2008.
- [61] J. Liu, P. Fei, J. Zhou, R. Tummala, and Z. L. Wang. Toward high output-power nanogenerator. *Applied Physics Letters*, 92(17), 2008.
- [62] N. F. Lombard and M. J. Kamper. Analysis and performance of an iron-less stator axial flux pm machine. *Energy Conversion, IEEE Transaction on*, 14(4):1051–1056, 1999.
- [63] J. E. Losey, L. S. Rayor, and M. E. Carte. Transgenic pollen harms monarch larvae. *Nature*, 399:214–215, 1999.
- [64] J. E. Losey, L. S. Rayor, and M. E. Carte. From idea to market: The drug approval process. *American Board of Family Medicine*, 14(5):362–367, 2001.
- [65] Y. I. Luchakov and A. D. Nozdrachev. Mechanism of heat transfer in different regions of human body. *Human and Animal Physiology*, 36(1):53–57, 2009.
- [66] D. Lyon. *Surveillance as Social Sorting: Privacy, Risk and Automated Discrimination*. Routledge, 2002.
- [67] K. Makihara, J. Onoda, and T. Miyakawa. Low energy dissipation electric circuit for energy harvesting. *Smart Materials and Structures*, 15(5):1493–1498, October 2006.

- [68] V. S. Mallela, V. Ilankumaran, and N. S. Rao. Trends in cardiac pacemaker batteries. *Indian pacing and electrophysiology journal*, 4(4):201–212, 2004.
- [69] N. Maluf and K. Williams. *An introduction to Microelectromechanical Systems Engineering*. Artech-House, 2004.
- [70] M. Marzencki, Y. Ammar, and S. Basrour. Integrated power harvesting system including a mems generator and a power management circuit. *Sensors and Actuators A: Physical*, 145-146:363–370, 2008.
- [71] A. Mason, N. Yazdi, A. V. Chavan, K. Najafi, and K. D. Wise. A generic multielement microsystem for portable wireless applications. *Proceedings of the IEEE*, 86(8):1733–1746, 1998.
- [72] K. McCarthy, M. Bash, and S. Pekarek. Design of an air-core linear generator drive for energy harvest applications. In *Applied Power Electronics Conference and Exposition, APEC 2008*, pages 1832–1838, 2008.
- [73] M. Meaney. Lessons from the sustainability movement, toward an integrative decision-making framework for nanotechnology. *Journal of Law, Medicine and Ethics*, 34(4):682–688, 2006.
- [74] P. Miao, P. D. Mitcheson, A. S. Holmes, E. M. Yeatman, T. C. Green, and B. H. Stark. Mems inertial power generators for biomedical applications. *Microsyst. Technol.*, 12(10):1079–1083, August 2006.
- [75] H. Miller and G. Conko. *The Frankenfood Myth: How Protest and Politics Threaten the Biotech Revolutio*. Praeger, 2004.
- [76] P. D. Mitcheson, T. C. Green, E. M. Yeatman, and A. S. Holmes. Architectures for vibration-driven micropower generators. *Microelectromechanical Systems, Journal of*, 13(3):429–440, 2004.
- [77] P. D. Mitcheson, P. Miao, B. H. Stark, E. M. Yeatman, A. S. Holmes, and T. C. Green. Mems electrostatic micropower generator for low frequency operation. *Sensors and Actuators A: Physical*, 115(2-3):523–529, September 2004.
- [78] J. Moor and J. Weckert. Nanoethics: Assessing the nanoscale from a ethical point of view. In D. Baird, A. Nordmann, and J. Schummer, editors, *Discovering the Nanoscale*, pages 301–310. IOS Press, 2004.
- [79] S. Nagasawa, T. Suzuki, Y. Takayama, K. Tsuji, and H. Kuwano. Mechanical rectifier for micro electric generators. In *Micro Electro Mechanical Systems, MEMS 2008*, pages 992–995, 2008.

- [80] K. Najafi. Low-power micromachined microsystems (invited talk). In *ISLPED '00*, pages 1–8, New York, NY, USA, 2000. ACM.
- [81] D. Niarchos. Magnetic mems: key issues and some applications. *Sensors and Actuators A: Physical*, 109(1-2):166–173, December 2003.
- [82] P. Niu and P. Chapman. Design and performance of linear biomechanical energy conversion devices. In *Power Electronics Specialists Conference, PESC '06*, pages 1–6, 2006.
- [83] P. Niu, P. Chapman, R. Riemer, and X. Zhang. Evaluation of motions and actuation methods for biomechanical energy harvesting. In *Power Electronics Specialists Conference, PESC 04.*, volume 3, pages 2100–2106 Vol.3, 2004.
- [84] House of Commons Home Affairs Committee. *A surveillance society? : fifth report of session 2007-08*. The Stationery Office, 2008.
- [85] K. Oweiss, Y. Suhail, K. Thomson, J. Li, and A. Mason. Augmenting real-time DSP in implantable high-density neuroprosthetic devices. In *Microtechnology in Medicine and Biology, 2005. 3rd IEEE/EMBS Special Topic Conference on*, pages 108–111, 2005.
- [86] J. Paradiso and M. Feldmeier. A compact, wireless, self-powered pushbutton controller. In *UbiComp 2001: Ubiquitous Computing*, pages 299–304, 2001.
- [87] J. A. Paradiso and T. Starner. Energy scavenging for mobile and wireless electronics. *Pervasive Computing, IEEE*, 4(1):18–27, 2005.
- [88] B. Pawlowski, S. Schwarzer, A. Rahmig, and J. Topfer. NdFeB thick films prepared by tape casting. *Journal of Magnetism and Magnetic Materials*, 265(3):337–344, October 2003.
- [89] B. Pawlowski and J. Topfer. Permanent magnetic NdFeB thick films. *Journal of Materials Science*, 39(4):1321–1324, February 2004.
- [90] C. Peters, D. Spreemann, M. Ortmanns, and Y. Manoli. A CMOS integrated voltage and power efficient AC/DC converter for energy harvesting applications. *Journal of Micromechanics and Microengineering*, 18(10):104005+, 2008.
- [91] S. R. Platt, S. Farritor, K. Garvin, and H. Haider. The use of piezoelectric ceramics for electric power generation within orthopedic implants. *Mechatronics, IEEE/ASME Transactions on*, 10(4):455–461, 2005.

- [92] S. R. Platt, S. Farritor, and H. Haider. On low-frequency electric power generation with pzt ceramics. *Mechatronics, IEEE/ASME Transactions on*, 10(2):240–252, 2005.
- [93] F. Putois. Market for nickel-cadmium batteries. *Power Sources*, 57:67–70, 1995.
- [94] J. M. Rabaey, M. J. Ammer, J. L. da Silva, D. Patel, and Roundy S. Pico-radio supports ad hoc ultra-low power wireless networking. *IEEE Computer*, 33(7):42–48, 2000.
- [95] S. S. Rao. *Mechanical Vibrations*. Addison-Wesley, 1995.
- [96] M. Renaud, P Fiorini, R. van Schaijk, and C van Hoof. Harvesting energy from the motion of human limbs: the design and analysis of an impact-based piezoelectric generator. *Smart Mater. Struct.*, 18(035001):16, 2009.
- [97] M. Renaud, T. Sterken, P. Fiorini, R. Puers, K. Baert, and C. van Hoof. Scavenging energy from human body: design of a piezoelectric transducer. In *Digest of Technical Papers. TRANSDUCERS '05*, volume 1, pages 784–787 Vol. 1, 2005.
- [98] G. Rieger, J. Wecker, W. Rodewald, W. Sattler, Fr, T. Duda, and W. Unterberg. Nd-Fe-B permanent magnets (thick films) produced by a vacuum-plasma-spraying process. *Applied Physics*, 87(9):5329–5331, 2000.
- [99] T. Ritter, X. Geng, K. K. Shung, P. D. Lopath, S. E. Park, and T. R. Shrout. Single crystal PZN/PT-polymer composites for ultrasound transducer applications. *Transactions on Ultrasonics, Ferroelectrics, and Frequency Control*, 47(4):792–800, 2000.
- [100] W. Robison. Nano-ethics. In D. Baird, A. Nordmann, and J. Schummer, editors, *Discovering the Nanoscale*, pages 301–310. IOS Press, 2004.
- [101] M. C. Roco and W. S. Brainbridge. Societal implications of nanoscience and nanotechnology: Maximizing human benefit. *J. Nanoparticle Research*, 7:1–13, 2005.
- [102] L. C. Rome, L. Flynn, E. M. Goldman, and T. D. Yoo. Generating electricity while walking with loads. *Science*, 309(5741):1725–1728, September 2005.
- [103] E. Romero, R. O. Warrington, and M. R. Neuman. Energy scavenging sources for biomedical sensors. *Physiological Measurement*, 30:R35–R62, 2009.
- [104] S. Roundy. On the effectiveness of vibration-based energy harvesting. *Journal of Intelligent Material Systems and Structures*, 16(10):809–823, October 2005.

- [105] S. Roundy and P. K. Wright. A piezoelectric vibration based generator for wireless electronics. *Smart Materials and Structures*, 13(5):1131–1142, 2004.
- [106] Shadrach J. Roundy. *Energy Scavenging for Wireless Sensor Nodes with a Focus on Vibration to Electricity Conversion*. PhD thesis, University of California, Berkeley, 2003.
- [107] C. R. Saha, T. O'Donnell, N. Wang, and P. McCloskey. Electromagnetic generator for harvesting energy from human motion. *Sensors and Actuators A: Physical*, 147(1):248–253, 2008.
- [108] F. Salamanca-Buentello, D. L. Persad, E. B. Court, D. K. Martin, A. S. Daar, and P. A. Singer. Nanotechnology and the developing world. *PLoS Med*, 2(5):0100–0103, 2005.
- [109] K. Sasaki, Y. Osaki, J. Okazaki, H. Hosaka, and K. Itao. Vibration-based automatic power-generation system. *Microsyst. Technol.*, 11(8):965–969, August 2005.
- [110] D. A. Scheufele and B. Lewenstein. The public and nanotechnology: How citizens make sense of emerging technologies. *J. Nanoparticle Research*, 7, 2005.
- [111] E. Schuler. Perception of risks and nanotechnology. In D. Baird, A. Nordmann, and J. Schummer, editors, *Discovering the Nanoscale*, pages 279–284. IOS Press, 2004.
- [112] M. Seok, S. Hanson, Y. S. Lin, Z. Foo, D. Kim, Y. Lee, N. Liu, D. Sylvester, and D. Blaauw. The phoenix processor: A 30pw platform for sensor applications. In *VLSI Circuits, 2008 IEEE Symposium on*, pages 188–189, 2008.
- [113] N. S. Shenck and J. A. Paradiso. Energy scavenging with shoe-mounted piezoelectrics. *Micro, IEEE*, 21(3):30–42, 2001.
- [114] J. Siebert, J. Collier, and R. Amirtharajah. Self-timed circuits for energy harvesting AC power supplies. In *Low Power Electronics and Design, ISLPED '05*, pages 315–318, 2005.
- [115] Peter Slob. *The Human Power Chart Sustained comfortable cranking*. PhD thesis, Delft University of Technology, 2000.
- [116] S. E. Smiley Smith, H. D. Hosgood, E. S. Michelson, and M. H. Stowe. Americans' nanotechnology risk perception, assessing opinion change. *Journal of Industrial Ecology*, 12(3):459–473, 2009.

- [117] H. A. Sodano, D. J. Inman, and G. Park. Comparison of piezoelectric energy harvesting devices for recharging batteries. *Journal of Intelligent Material Systems and Structures*, 16(10):799–807, October 2005.
- [118] H. A. Sodano, D. J. Inman, and G. Park. Generation and storage of electricity from power harvesting devices. *Journal of Intelligent Material Systems and Structures*, 16(1):67–75, January 2005.
- [119] P. T. Squire. Pendulum damping. *American Journal of Physics*, 54(11):984–991, 1986.
- [120] T. Starner. Human-powered wearable computing. *IBM Syst. J.*, 35(3-4):618–629, 1996.
- [121] T. Starner and J. A. Paradiso. Human generated power for mobile electronics. In *Low Power Electronics Design*, volume 45. CRC Press, 2004.
- [122] N. G. Stephen. On energy harvesting from ambient vibration. *Journal of sound and vibration*, 293(1-2):409–425, May 2006.
- [123] K. L. Steudel-Numbers and C. M. Wall-Scheffer. Optimal running speed and the evolution of hominin hunting strategies. *IEEE Trans. Biomedical Eng.*, 56(4):355–360, 2009.
- [124] R. Tashiro, N. Kabei, K. Katayama, E. Tsuboi, and K. Tsuchiya. Development of an electrostatic generator for a cardiac pacemaker that harnesses the ventricular wall motion. *Journal of Artificial Organs*, 5(4):0239–0245, December 2002.
- [125] G. W. Taylor, J. R. Burns, S. A. Kammann, W. B. Powers, and T. R. Welsh. The energy harvesting eel: a small subsurface ocean/river power generator. *Oceanic Engineering, IEEE Journal of*, 26(4):539–547, 2001.
- [126] A. Thornley. *The Crisis of London*. Routledge, 1992.
- [127] J. Topfer and V. Christoph. Multi-pole magnetization of NdFeB sintered magnets and thick films for magnetic micro-actuators. *Sensors and Actuators A: Physical*, 113(2):257–263, July 2004.
- [128] J. Topfer, B. Pawlowski, H. Beer, K. Plotner, P. Hofmann, and J. Herrfurth. Multi-pole magnetization of NdFeB magnets for magnetic micro-actuators and its characterization with a magnetic field mapping device. *Journal of Magnetism and Magnetic Materials*, 270(1):124–129, March 2004.

- [129] C. Toumey. Privacy in the shadow of nanotechnology. *Nanoethics*, 1:211–222, 2007.
- [130] T. Tsutsumino, Y. Suzuki, N. Kasagi, and Y. Sakane. Seismic power generator using high-performance polymer electret. In *Micro Electro Mechanical Systems, MEMS 2006*, pages 98–101, 2006.
- [131] P. Van den Bossche, F. Vergelsb, J. Van Mierloc, J. Matheysc, and W. Van Autenboerc. Subat: An assessment of sustainable battery technology. *J. Power Sources*, 162:913–919, 2005.
- [132] J. Van den Hoven. The tangled web of tiny things: Privacy implications of nano-electronics. In F. Allhoff and P. Lin, editors, *Nanotechnology & Society: Current and Emerging Ethical Issues*, pages 147–62. Springer, 2008.
- [133] R. H. Van Donk. Design of an alternatively powered remote control. Master’s thesis, Delf University of Technology, 2000.
- [134] U. Varshney. Pervasive healthcare and wireless health monitoring. *Mobile Networks and Applications*, 12(2-3):113–127, 2007.
- [135] T. von Büren, P. Lukowicz, and G. Troster. Kinetic energy powered computing - an experimental feasibility study. In *Wearable Computers, 2003. Proceedings*, pages 22–24, 2003.
- [136] T. von Büren, P. D. Mitcheson, T. C. Green, E. M. Yeatman, A. S. Holmes, and G. Troster. Optimization of inertial micropower generators for human walking motion. *Sensors Journal, IEEE*, 6(1):28–38, 2006.
- [137] T. von Büren and G. Tröster. Design and optimization of a linear vibration-driven electromagnetic micro-power generator. *Sensors and Actuators A: Physical*, 135(2):765–775, April 2007.
- [138] M. C. Waits, B. Geil, and R. Ghodssi. Encapsulated ball bearings for rotary micro machines. *Journal of Micromechanics and Microengineering*, 17(9):S224–S229, 2007.
- [139] J. Wang, W. Wang, G. W. Jewell, and D. Howe. Design of a miniature permanent-magnet generator and energy storage system. *Industrial Electronics, IEEE Transactions on*, 52(5):1383–1390, 2005.
- [140] R. J. Wang and M. J. Kamper. Calculation of eddy current loss in axial field permanent-magnet machine with coreless stator. *Energy Conversion, IEEE Transaction on*, 19(3):532–538, 2004.

- [141] R. R. J. Wang, M. J. Kamper, K. Van der Westhuizen, and J. F. Gieras. Optimal design of a coreless stator axial flux permanent-magnet generator. *Magnetics, IEEE Transactions on*, 41(1):55–64, 2005.
- [142] Z. L. Wang. Self-powered nanotech. *Scientific American*, pages 82–87, January 2008.
- [143] Z. L. Wang, X. Wang, J. Song, J. Liu, and Y. Gao. Piezoelectric nanogenerators for self-powered nanodevices. *Pervasive Computing, IEEE*, 7(1):49–55, 2008.
- [144] J. A. Williams. Friction and wear of rotating pivots in mems and other small scale devices. *Wear*, 251(1-12):965–972, October 2001.
- [145] N. Yazdi, A. Mason, K. Najafi, and K. D. Wise. A generic interface chip for capacitive sensors in low-power multi-parameter microsystems. *Sensors and Actuators A: Physical*, 84(3):351–361, September 2000.
- [146] E. M. Yeatman. Energy harvesting from motion using rotating and gyroscopic proof masses. In *Proceedings of the I MECH E Part C Journal of Mechanical Engineering Science*, volume 222, pages 27–36, 2008.
- [147] E. M. Yeatman, P. D. Mitcheson, and A. S. Holmes. Micro-engineered devices for motion energy harvesting. In *Electron Devices Meeting, IEDM 2007*, pages 375–378, 2007.
- [148] S. Zuboff. In *The Age Of The Smart Machine, The Future Of Work And Power*. Basic Books, 1989.